Development and Application of *in vivo* ^{2}H Magnetic Resonance

Author: Daniel Cocking

Thesis submitted to the University of Nottingham

for the degree of Doctor of Philosophy

Sir Peter Mansfield Imaging Centre

School of Physics and Astronomy

University of Nottingham

April 2024

Abstract

Use of deuterium (^{2}H) as a tracer combined with Magnetic Resonance (MR) Imaging/Spectroscopy could potentially replace diagnostic techniques that use ionising radiation such as Positron Emission Tomography (PET) imaging. Proton (^{1}H) MR scanning is used clinically and in research, but ^{2}H comes with a decreased Signal-to-Noise Ratio (SNR). However, thanks to the reduced T_1 relaxation times of ^{2}H, much of the SNR loss can be compensated by rapid averaging to allow for reasonable scan times. In this thesis deuterium magnetic resonance has been implemented in healthy human participants *in vivo* on both 3T and 7T MR scanners to investigate metabolism and key inherent MR parameters of ^{2}H.

7T Multi-Echo Gradient-Echo (MEGE) images at a range of Repetition Times (TR) values were used to obtain relaxation times (T_1 and T_2^*) in CerebroSpinal Fluid (CSF), Grey Matter (GM) and White Matter (WM) in subjects who had ingested heavy water (D_2O) to increase the ^{2}H concentration by $\sim$x100 times. The ^{2}H signal time-course was also measured following initial loading and compared to estimated changes in ^{2}H concentration based on consideration of body water mixing.

Glucose with two or seven attached ^{2}H atoms (glucose-d_2/d_7 respectively) was ingested by healthy human participants. The change in *in vivo* downstream ^{2}H metabolite maps of semi-heavy water (HDO), glucose, Glx (combination of glutamate and glutamine) and lactate was tracked in different brain regions using Magnetic Resonance Spectroscopic Imaging (MRSI) at 7T. An increased SNR was noted for all metabolites following glucose-d_7 ingestion. Time-courses for each metabolite were obtained and d_7/d_2 signal ratios were explained by the differing numbers of labels.

Lipid metabolism and the quadrupolar splitting of ^{2}H signals *in vivo* was investigated using a clinical 3T scanner in subjects who had ingested D_2O. An increase in ^{2}H lipid signal was detected. Quadrupolar splitting was quantified in skeletal muscle at different angles with respect to the B_0 field, along with the isolation of a Double Quantum Filtered (DQF) signal.

Acknowledgements

First I would like to thank my supervisor Prof. Richard Bowtell for his support and his direction throughout my PhD which has allowed me to become the researcher I am today. Learning under such a well respected mentor that is motivated, hardworking and incredibly intelligent was an honour I am grateful for.

I would also like to thank Dr. Robin Damion, Prof. Dorothee Auer, Dr. Matthew Clemence and Dr. Andrew Peters for their help in making a difficult project run smoothly. Without them this project would not have been half as successful or as enjoyable as it has been to work on. And to the Beacon Precision Imaging for funding the work here and my PhD.

Next I would like to thank the whole of the SPMIC for creating such a welcoming and enjoyable working environment, that has showed if you work hard you can play hard. I would like to namely thank Abi Spicer, Dr. Caitlin Connolly, Dr. Natalie Rhodes and Dr. Alex Daniel for their friendship and pushing me to be the best physicist I can be, and forcing me to take the time to enjoy and experience life during a PhD.

There is no way I could have done this without the lifelong support of my family (Rita, Graham, Rob, Gareth, John, Gemma, Evie, Kiera) for always being proud of me and supporting me, making a long drive seem only down the road is not an easy task and I could not have done it without you all. I would like to make a special thank you to my Mum Tina, you have always pushed me to put everything into whatever I am doing and to always 'back yourself' which is what has made this Thesis possible so I am lucky to call you Mum.

If I was not already fortunate enough to have such an amazing family, having such incredible friends has continuously made me feel blessed. Alfie, Flint, Josh, Liam, Matt, Sarah, Elle and Rachel to be able to say that we have been this close for so long is one hell of an undertaking, you have been there for me through it all and without you I do not see how any of this would have been possible. Yvonne, you introduced me to the world

of mathematics which kick-started this whole journey, and for that I will always be hugely grateful. To Graham and Oliver the help you have given my mum and I is beyond comprehension, and to say I am grateful is an understatement. To all listed here you will forever and always be additions to my family and I could not have done this without you.

Lucy, my fiancée, when I look at you I can see an incredible future together and that has always been a driving motivator throughout my PhD. You have encouraged me to be the best version of myself, whether that's pushing me though long hours or taking well earned rests you have been in my corner at every second of this PhD. This thesis is not only my achievement but is a testament to you.

Finally, I could dedicate this work to anyone mentioned above but I would like to dedicate it to Margaret Cocking, my grandma. Though you never got to see me off into higher education I want this Thesis to be my message to you on how much I have achieved, and to say how much I love and miss you

Contents

Abbreviations

AC	Alternating Current
AD	Alzheimer's disease
AMARES	Advanced Method for Accurate, Robust, and Efficient Spectral fitting
ATP	Adenosine TriPhosphate
BMI	Body Mass Index
BW	BandWidth
CNR	Contrast-to-Noise Ratio
CSF	CerebroSpinal Fluid
CSI	Chemical Shift Imaging
DMI	Deuterium Metabolic Imaging
D_2O	Heavy Water
DNL	De Novo Lipogenesis
DQF	Double Quantum Filtered
EFG	Electric Field Gradients
EPI	Echo-Planar Imaging
FDG	FluoroDeoxyGlucose
FID	Free Induction Decay
FWHM	Full-Width at Half Maximum
FOV	Field Of View
FT	Fourier Transform
GE	Gradient-Echo
GM	Grey Matter
HDO	Semi-Heavy Water
HOSVD	Higher-Order Singular Value Decomposition
IR	Inversion Recovery
MEGE	Multi-Echo Gradient-Echo
MIDA	Mass Isotopomer Distribution Analysis
MRI	Magnetic Resonance Imaging
MRS	Magnetic Resonance Spectroscopy
MRSI	Magnetic Resonance Spectroscopic Imaging

MPRAGE Magnetization Prepared - RApid Gradient Echo

MS Multiple Sclerosis

NA Natural Abundance

NMR Nuclear Magnetic Resonance

OVS Outer-Volume Suppression

PCA Principal Component Analysis

PD Parkinson's disease

PET Positron Emission Tomography

RF Radio Frequency

ROI Region Of Interest

RQC Residual Quantum Coupling

SAR Specific Absorption Rate

SC Superior Cistern

SE Spin-Echo

SNR Signal-to-Noise Ratio

SPMIC Sir Peter Mansfield Imaging Centre

SQF Single Quantum Filtered

SVD Singular Value Decomposition

TA Tibialis Anterior

TCA TriCarboxylic Acid

TE Echo Time

TG TriacylGlycerols

TR Repetition Times

VARPRO VARiable PROjection

WM White Matter

Chapter 1

Introduction

Magnetic Resonance Imaging (MRI) and Magnetic Resonance Spectroscopy (MRS) measure signals from atomic nuclei. The most commonly used nucleus is the hydrogen nucleus (^{1}H) which consists of a positively charged proton. This is due to the fact that ^{1}H is the most abundant nucleus in the human body, with an adult's bodyweight typically being made up of 60% water (H_2O) (more exact values can be estimated based on age, sex, height and weight [1]). This means that tissues that have a larger H_2O concentration will generally have a stronger MR signal. In order to investigate, measure and quantify metabolism it is vitally important to be able to measure small differences in the products that are created due to metabolism (metabolites). Therefore, other reference nuclei are often used to investigate metabolism. In doing this it is important to choose a nucleus that is magnetically favourable and is found in metabolites that are of interest. Carbon-13 (^{13}C) [2, 3] and Phosphorus-31 (^{31}P) [4] are often used in research to quantify metabolite concentrations *in vivo*. They have lower abundance in the human body (compared to ^{1}H), but are quite magnetically favourable for MRS studies. Their abundances are usually too low for direct MRI measurements, but the ability to separate different metabolites in each spectrum is important. Recently deuterium (^{2}H) has been shown to be a nucleus of interest when investigating metabolism in humans *in vivo* [5, 6], and the field of deuterium MR has grown at a

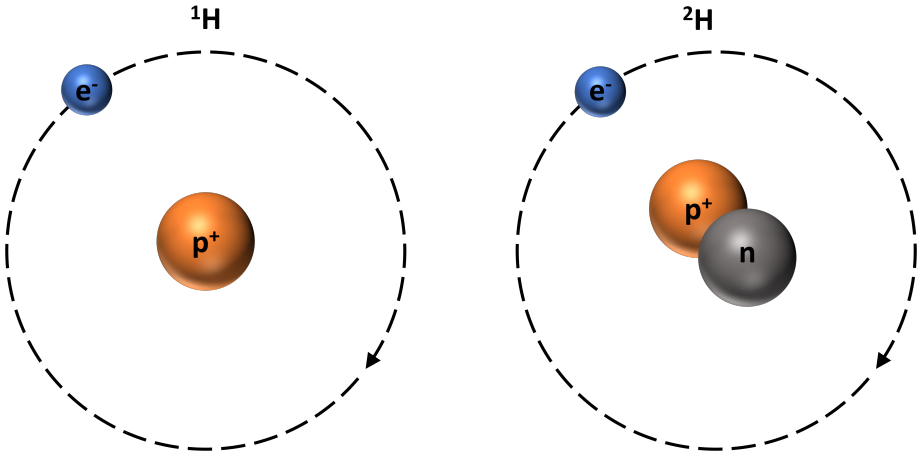

Figure 1.1: *Schematic diagram of the atomic structure hydrogen (^1H, left) and deuterium atoms (^2H, right).*

very fast rate thanks to its potential capabilities for investigating brain tumours [6], along with its relatively simple implementation. It has the potential to visualise increased tumour metabolism through increased glucose concentration through the Warburg effect [7] as well as different forms of metabolism through concentrations of downstream metabolites. It could also be used to track metabolism changes through the course of therapy thanks to the non-ionisation of MR techniques.

1.1 Metabolism

Disrupted metabolism is a key aspect of many life-altering diseases including cancer and neurodegenerative diseases, such as Alzheimer's disease (AD), Parkinson's disease (PD) and Multiple Sclerosis (MS) [8]. AD has a European age-standardized prevalence of 4.4% among people aged over 65 [9]. One of the most prevalent and fatal metabolic diseases is cancer. In 2017 there were ∼375,000 new cancer cases in the UK [10], with ∼3% of them being attributed to tumours in the brain and other parts of the central nervous system (CNS) [11]. The mortality rate of these cancers has remained significant and constant for the last decade [11]. It is

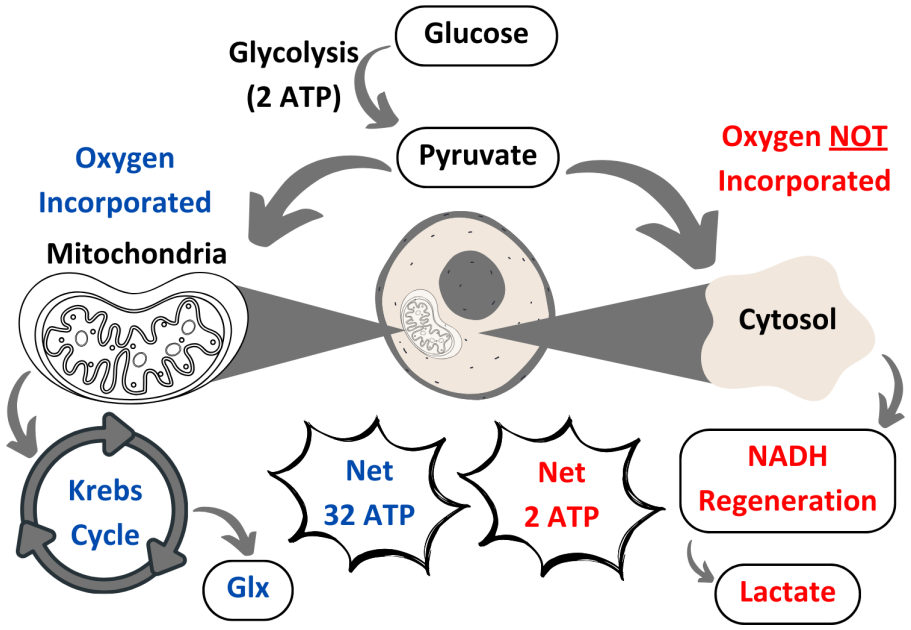

Figure 1.2: *Flow Chart demonstrating how glucose is metabolised into Adenosine TriPhosphate (ATP) with (aerobic, blue) and without (anaerobic, red) oxygen being present. Healthy cells favour aerobic respiration whilst cancerous cells prefer anaerobic respiration.*

important therefore to develop tools for investigating metabolism *in vivo*, and more specifically in brain tumours.

Cancer is often considered to be a metabolic disease because as part of their growth, tumours affect and impair normal metabolism. The nucleic acid ATP is used as energy currency in cells. In mammalian cells pyruvate is generated from glucose via glycolysis and produces two molecules of ATP per each molecule of glucose. In healthy cells there are then two options for metabolism depending on the supply of oxygen to the cell, if oxygen is readily in supply a process called oxidative-phosphorylation takes place. Oxidative-phosphorylation is where pyruvate enters the mitochondria and enters the citric acid cycle, also known as the TriCarboxylic Acid (TCA) or Krebs cycle, where as many as thirty-two more ATP are produced. This complete process is often referred to as aerobic respiration. The other option, when oxygen is not readily in supply, involves conversion of pyruvate into lactate in the cytosol of the cell through NADH regeneration. The

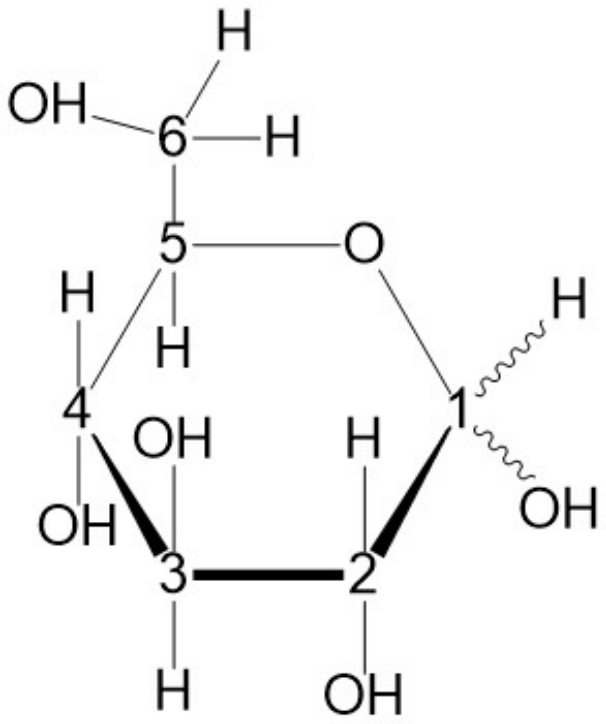

Figure 1.3: *A chemical diagram of glucose indicating the position of different carbon positions as numbers.*

complete process for the creation of lactate is known as lactic acid fermentation. Aerobic respiration is much more efficient in its energy production producing around sixteen times more ATP per mole of glucose compared to lactic acid fermentation [12].

By replacing atoms found on a glucose molecule with atoms whose presence can be tracked, it is possible to track the metabolic products of the glucose molecule. If the replaced atoms make their way through metabolism into downstream metabolites such measurements it can therefore inform on the metabolic pathway taken. There are seven hydrogens (not including those in hydroxyl groups) in a glucose molecule which can be replaced with ^{2}H atoms. During oxidative-phosphorylation, glutamate and glutamine are produced (the combination of the two is referred to as Glx) and of the seven hydrogen atoms only three are transferred to glutamine/glutamate. During lactic fermentation three of the hydrogen atoms are also transferred to lactate. These hydrogens come from the C1, C6 and C6' positions in the

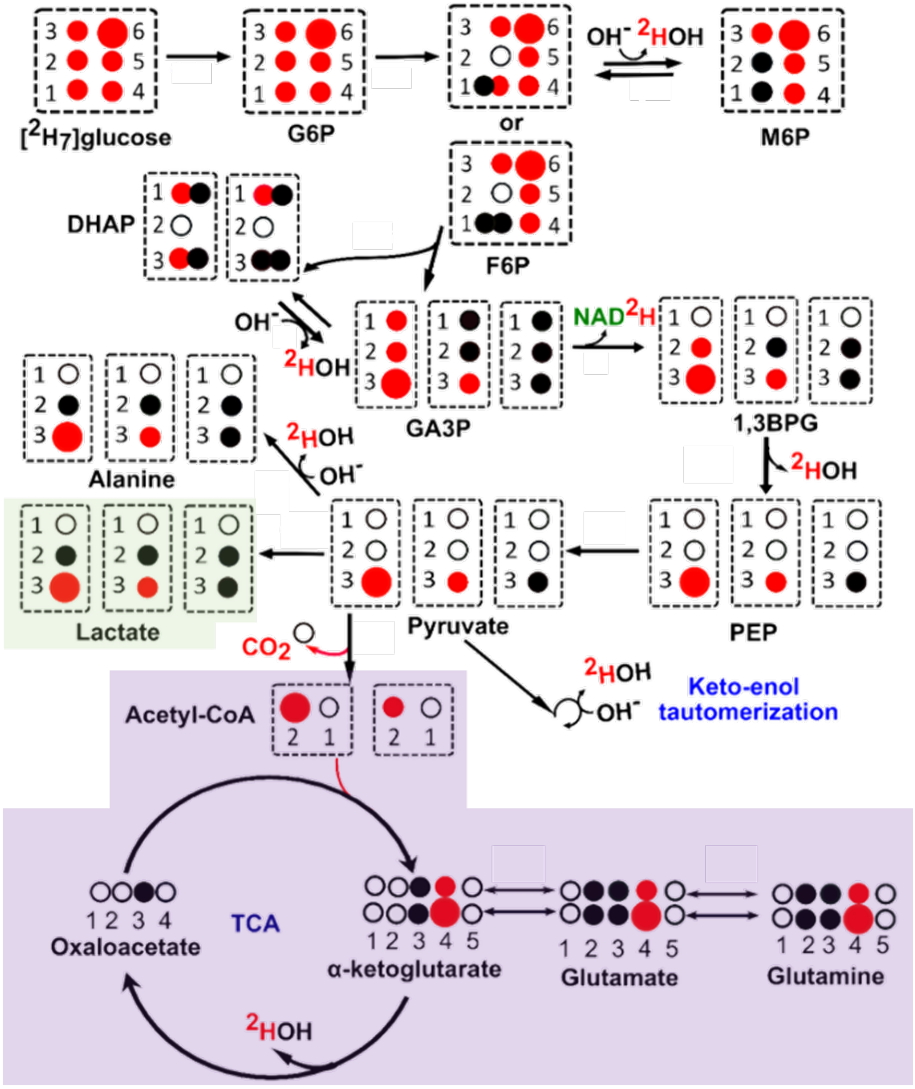

Figure 1.4: *Metabolic pathway for ^2H-labelled glucose, where all available sites for ^2H labelling have been used. The small red circles represent individual ^2H atoms, the large red circles represent two ^2H atoms at the C6 and C6' sites. The black-filled and empty circles represent ^1H and quarternary carbons, respectively. The TCA cycle is labelled on the diagram, and the specific pathway for formation of glutamate and glutamine which results from oxidative phosphorylation, is highlighted in purple. The specific pathway for the formation on lactate resulting from lactic acid fermentation is highlighted in green. The glycolysis steps are shown from the glucose molecule to the pyruvate molecule. This figure is adapted from Figure 5 in [13].*

glucose molecule. The rest of the labels (C2, C3, C4 and C5) are lost in the production of water during lactic acid fermentation and aerobic respiration. The specific metabolic pathway undertaken after fully ^{2}H-labelled glucose has been ingested is outlined in Fig. 1.4, which shows how each ^{2}H label makes it way into downstream metabolites and also indicates where the ^{2}H label can be lost. It is important to note that unlabelled lactate, glutamate and glutamine can be formed from deuterated metabolites in glycolysis and by multiple iterations of the TCA cycle. All processes take place in the cell and the labelled glucose travels to the desired location in the blood vessels.

Otto Warburg observed in the 20$^{\text{th}}$ century that tumours had a higher rate of glucose uptake [7, 14]. There were originally quite a few theories suggesting that cancerous cells had impaired mitochondria. It is now thought that the reason behind this effect is that cancerous cells are able to metabolise by either oxidative-phosphorylation or by fermentation regardless of how much oxygen is present to the cell. Lactic fermentation is favoured compared to oxidative-phosphorylation even though it is less energy/ATP efficient. This leads to an increase in lactate and a decrease in Glx [12].

Currently the most reliable way to accurately diagnose and monitor most cancers and metabolic diseases (such as AD [15] and PD [16]), in a non-invasive way, is by using PET [17]. Unfortunately this technique involves the use of a radioisotope inside the body which can put patients at further health risks, whilst a technique that is based on MRI would be non-invasive and not require the use of ionising radiation. Cancerous cells have a much higher glucose uptake during metabolism than normal cells. This is the basis behind PET imaging of cancer using ^{18}F-labelled FluoroDeoxyGlucose (FDG). Increased uptake of FDG in a specific region gives an indication of the presence a cancerous tumour. FDG PET works by attaching a positron emitting atom to the glucose analog, FDG. Once ingested it travels to the tissues where glucose is needed most. Inside cells the FDG is phosphorylated but cannot undergo further metabolism, and so

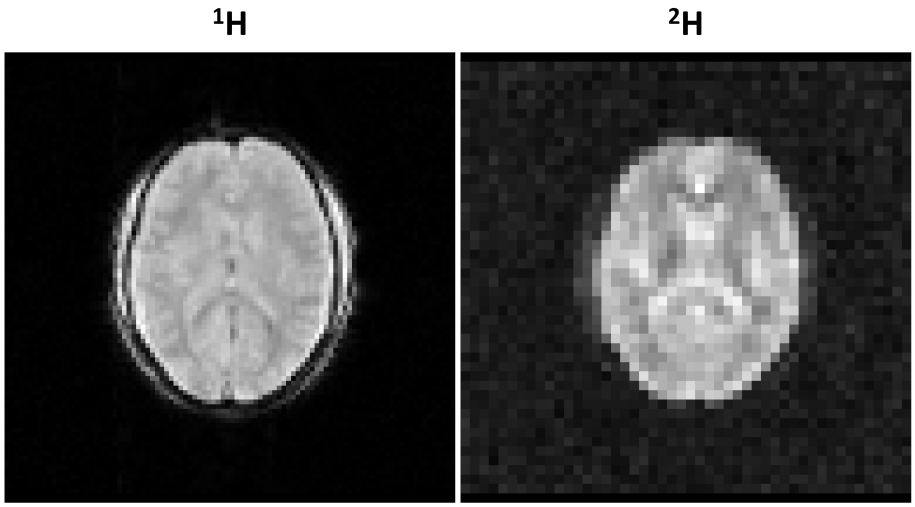

Figure 1.5: *Images of the brain acquired using different nuclei, in the same scan session for the same participant using similar gradient echo sequences. Left is a* ^{1}H *image with 3*x*3*x*2.5* mm^3 *voxels acquired in 232 s. Right is a* ^{2}H *image obtained with 6*x*6*x*10* mm^3 *voxels with a scan duration of 354 s. It is important to note that the participant's* ^{2}H *level is 100*x *natural abundance as they have consumed heavy water (*D_2O*) as part of a study.*

accumulates in metabolically active cells. When the ^{18}F-label decays, the emitted positrons annihilate with electrons, creating two photons travelling in opposite directions. These photons can be detected giving information on the location of the glucose and therefore information as to where cancer is present. A limitation of FDG PET is that because it only detects the presence of ^{18}F it does not provide information on any downstream metabolites. Since the brain is constantly metabolically active it can often be difficult to distinguish increases in metabolism compared to baseline, this is why it is important to choose a tracer with a low abundance. Metabolite signal/concentration maps from PET are often displayed overlaid on high resolution anatomical images to provide accurate spatial distributions.

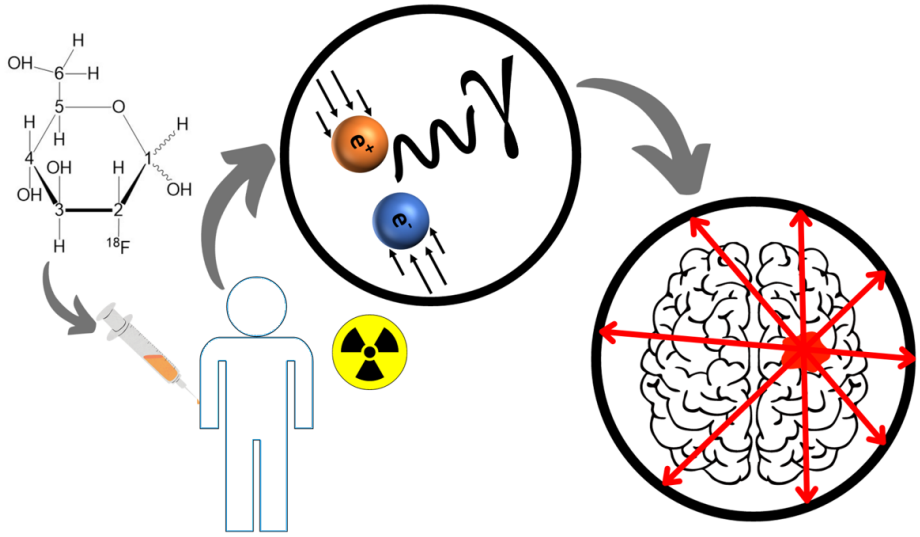

Figure 1.6: *Diagram showing how PET scanning works. Where the labelled 18FDG (left) is injected into participants/patients, and emitted positrons collide with electrons (middle). And how the resultant detected signals inform on areas of increased metabolism.*

1.2 History of ^{2}H Usage in Studying Metabolism

1.2.1 Pre-1980

^{2}H was discovered in 1932 [18] from consideration of the apparent mass difference of hydrogen when measured chemically and with a mass spectrograph. It was rapidly realised that this stable isotope could be used to measure metabolism. Many papers were published demonstrating this [19, 20] for example via deuterating naturally occurring compounds such as fatty acids, feeding them to animals and then analysing the amount of deuterium found in bodily fluids. Shortly after this, the relaxation properties of ^{2}H in NMR were quantified in a solution of heavy water [21]. One possible explanation as to why it then took so long for this technique combined with NMR to become popular is due to the rising interest (at the time) [22] in use of radioactive isotopes ^{3}H [23] and ^{14}C [24] for metabolic studies. The health concerns around use of radioactive isotopes led to a

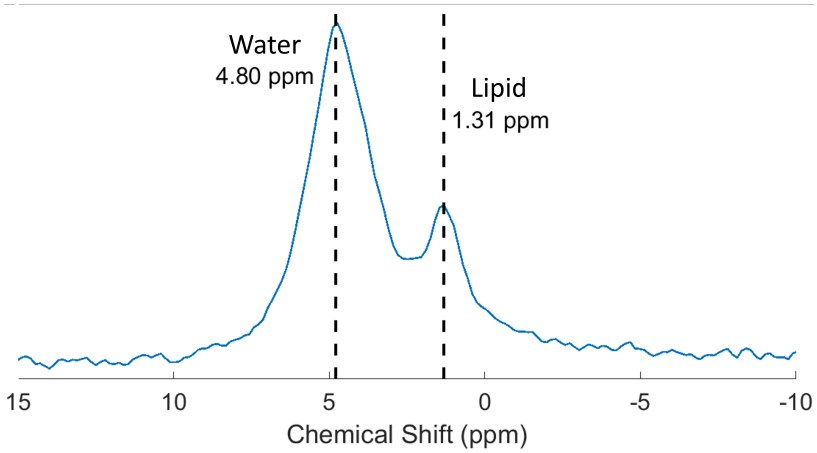

Figure 1.7: *Non-localised ^{2}H spectra obtained from the calf in vivo showing signals from water at a chemical shift of 4.8 ppm and fat/lipid signals at 1.3 ppm.*

resurgence of ^{2}H metabolism research in the 1980's.

1.2.2 1980 to the 21st Century

The first *in vivo* ^{2}H NMR study was performed in 1986 [25] in mice. Heavy Water (D_2O) ingestion was used to increase ^{2}H abundance, and an increase in fat/lipid signal was measured. Shortly after this, numerous pre-clinical studies were published that involved using heavy water as a tracer, looking at: the brain [26], blood flow and perfusion [27] and iron stores [28]. Other deuterated compounds then started to be used such as labelled choline [29], with the first instance of deuterated glucose being used being in 1986 [30]. This started a trend of other studies using deuterated glucose to investigate bacterial metabolism [31] and liver gycogen synthesis [32]. All the aforementioned studies involved animal models. The number of studies that involved ^{2}H then slowed down before a long hiatus. One potential reason for this hiatus was the success of *in vivo* ^{1}H [33], ^{13}C [34] and ^{31}P [35] measurements. However, there has recently been a resurgence in ^{2}H MR research and more specifically its use in studying metabolism.

1.2.3 The Last Seven Years

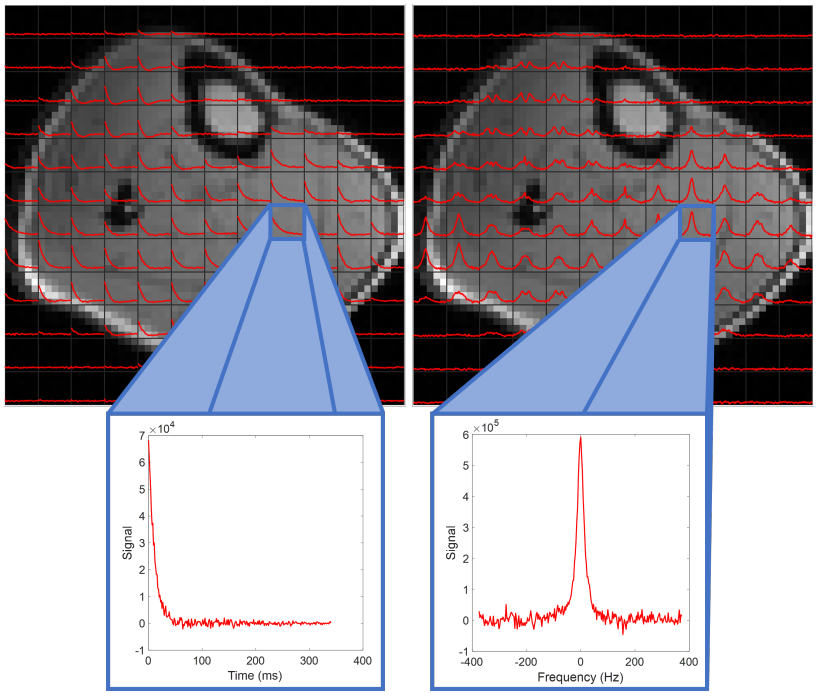

Figure 1.8: *Example NA MRSI data overlayed onto an anatomical image of the calf. The left shows the localised Free Induction Decay (FID) data from voxels with one voxel blown up. The right shows the corresponding localised spectroscopic data (Fourier transform of the FID shown on the left) with data from one voxel blown up.*

[6,6'-$^2H_2$]-glucose (also known as glucose-d_2) was first used in an *in vivo* MR study in an animal model [5] in 2017, where both the ^{1}H atoms at C6 are replaced with ^{2}H. And soon after this technique was applied *in vivo* in humans, where it was demonstrated that differences between normal and tumour tissue could be seen in maps of ^{2}H signals from downstream metabolic products of the labelled glucose [6]. This form of glucose is currently the most commonly used deuterated tracer in research [6, 22, 36–38]. In the brain at NA only a deuterated water (HDO) peak/signal is visible in a typical spectrum, because the noise level is higher than the ^{2}H signals from other ^{2}H in other molecules. In most other organs and muscles a lipid signal is also visible. After ingestion of glucose-d_2, peaks from deuterated

glucose (Glc), a combination of glutamine and glutamate (Glx) and lactate (Lac) appear. Chemical Shift Imaging (CSI) or other MRSI methods, can be used to produce maps of each of these metabolites. Production of maps of the ratio of the Glx and Lac concentration have been shown to provide a good delineation of cancerous tissue [6, 39]. Other deuterated compounds have been used to measure different metabolic pathways. These include [$^2H_3$]-acetate (acetate-d_3) [6, 40], [6,6'-$^2H_2$]-fructose (fructose-d_2) [41], as well as other forms of deuterated glucose. For example [2,3,4,6,6'-$^2H_5$]-glucose (glucose-d_5) [42] has recently been found to be cheaper to produce than glucose-d_2.

1.3 Aims

The aims of the work described in this thesis are to develop ^{2}H MRI and MRSI scanning at the Sir Peter Mansfield Imaging Centre (SPMIC) at the University of Nottingham at both clinical high field (3T) and ultra-high field (7T). Work outlined in this thesis is relevant for the implementation of ^{2}H at a range of field strengths. The more specific primary aim of the work described in this thesis is to set the ground for scanning patients with brain tumours using DMI at 7T.

All the work that is outlined in this thesis involves the use of ^{2}H MRI and MRSI techniques and includes: measuring the relaxation times of semi-heavy water (HDO) in different healthy *in vivo* brain tissues; assessing the increase in ^{2}H abundance as D_2O is ingested in different healthy *in vivo* brain tissues; using different amounts of ^{2}H labelling of glucose to assess *in vivo* metabolism in the brain of healthy participants; evaluating whether the ingestion of D_2O in conjunction with ^{2}H MR can be used to investigate lipid turnover and using ^{2}H MR following ingestion of D_2O to assess the quadrupolar HDO splitting in anisotropic and isotropic tissues using regular MRI and MRSI, as well as double-quantum-filtered MRI and MRSI.

1.4 Description of Work

Chapter two covers the theory underlying the work that was undertaken in this thesis. This includes the theory behind MRI and MRSI and more specifically the difference between ^{1}H and ^{2}H NMR including magnetisation, relaxation and pulse sequences. This chapter also describes the extra hardware adaptations that are needed for ^{2}H signal detection, ranging from amplifiers to Radio Frequency (RF) coil construction.

Chapter three reports the first measurements of ^{2}H signals from the brain in subjects who had ingested heavy water. A D_2O ingestion routine is outlined, as well as a scanning routine undertaken to allow the quantification of ^{2}H relaxation times in the human brain using MEGE scans with different TR-values. Similar scans were then also used for some participants to track the ^{2}H increase that occurs immediately following the ingestion of D_2O. It was shown that the ^{2}H increase from MRI/MRS follows what is expected from blood sampling, and the relaxation times for different tissues are reported with statistical significance shown.

Chapter four describes the first measurements of metabolism in human subjects using Deuterium Metabolic Imaging (DMI) with glucose-d_7. The methodology used so healthy participants can ingest deuterated glucose is outlined as well as the scanning routine with parameters for CSI scanning. Increases in signal levels for all downstream metabolites resulting from the glucose-d_7 were found, suggesting that better Contrast-to-Noise Ratio (CNR) between healthy and tumour tissue would be possible, despite the more complicated analysis.

Chapter five describes the importance of measuring lipid turnover and the limitations of the present methodology involving heavy-water loading and biopsy, and suggests a new routine that uses ^{2}H MRI/MRS instead. A new routine of ingesting D_2O is given as well as a regular scanning routine that is repeated once every $\sim$14 days. Increases in ^{2}H lipid signal were detected, but new advances/improvements are needed to make this

technique clinically viable.

Chapter six describes an investigation of the quadrupolar splitting seen in the ^{2}H signal from water in muscle, where the orientation of the muscle relative the external magnetic field affects the splitting amplitude. After participants have their ^{2}H abundance increased by ingesting D_2O, MRSI and DQF MRSI has been used to show the relationship between the anisotropy and quadrupolar interaction in the forearm and the calf.

Finally, chapter seven brings together all the work that has been conducted in this thesis, and gives direction on any future work that may follow from it.

Chapter 2

Theory

2.1 How NMR Works

2.1.1 Quantum Behaviour

Many subatomic particles have a quantum 'spin' and it is important to note that whilst this means the particles do not necessarily 'spin' in the macroscropic sense, a strong analogy can be made to macroscopic spin to explain the behaviour in the quantum world. This spin is linked to a quantum total angular momentum defined by the operator $\mathbf{J}$, which is made up of quantum orbital angular momentum ($\mathbf{L} = \mathbf{r} \times \mathbf{p}$, $\mathbf{r}$ is quantum position $\mathbf{p}$ is quantum momentum) as well as quantum spin angular momentum ($\mathbf{S}$ for total spin and m_s for z-component). This spin operator often refers to fermions such as electrons that have two spin-states ($m_{1/2}$ and $m_{-1/2}$), for nuclear spin angular momentum the spin operator $\mathbf{I}$. The spin of subatomic particles is associated with a magnetic moment. The atomic nucleus can therefore be represented as a magnetic dipole (which is analogous to an electric dipole) which tend to align with external magnetic fields. The magnetic moment ($\boldsymbol{\mu}$) of a nucleus is dependent on its spin and is expressed as

$$\boldsymbol{\mu} = \frac{g_s q}{2m}\mathbf{S} \tag{2.1}$$

Here, **I** is the nuclear spin, q is the charge, g_s is dimensionless and is known as the spin g-factor and m is the mass. The constant of proportionality linking the magnetic moment to the spin is known as the gyromagnetic ratio (γ) and is a constant for each type of nucleus, the mathematical expression for γ is

$$\gamma = \frac{g_I q}{2m} \tag{2.2}$$

which when combined with Eq. 2.1 gives

$$\boldsymbol{\mu} = \gamma \mathbf{I} \tag{2.3}$$

When a nucleus is exposed to an external static magnetic field (**B**) it will possess an energy which is also dependent on $\boldsymbol{\mu}$ according to

$$E = -\boldsymbol{\mu} \cdot \mathbf{B} \tag{2.4}$$

In 1922 an experiment was undertaken [43] which showed that spin only takes specific discrete values (m_I = 0, 1/2, 1, 3/2 ...) when placed in a static external magnetic field (B_0), which gives eigenvalues for the angular momentum operator along a specific direction, (e.g. I_z) as $\hbar m_I$. Where m_I can take values of $-I$ to $+I$ in integer steps. Therefore, the magnetic moment along a particular direction and the energy will also take specific discrete energy levels equal to

$$E = -m_I \hbar \gamma B_0 \tag{2.5}$$

This is evident in Fig. 2.1. The energy of an electromagnetic photon is directly proportional to its frequency (ν), with a constant of proportionality equal to Planck's constant h, this is known as the Planck relation. Therefore, for a photon to be absorbed, it will need an energy equal to the separation between quantized energy states. This relationship is expressed as

$$\Delta E = h\nu = \frac{h}{2\pi}\gamma B_0 \tag{2.6}$$

The magnetic moment of the nuclei of interest in an applied magnetic field **B** will tend to align with the field. However, due to the angular momentum of the nuclei they will instead precess around the magnetic field, with an associated frequency of precession. The frequency of precession is referred to as the Larmor frequency (ν) [44]. The Larmor frequency can also be shown as an angular frequency by $\omega = 2\pi\nu$, which is measured in rads^{-1}. the Larmor frequency is therefore directly proportional to the magnitude of the applied external magnetic field (B_0), with γ being the constant of proportionality (meaning this frequency is also specific to each nucleus). This therefore shows that for a nucleus with spin, the energy, frequency and applied magnetic field share a quantum relationship, which is analytically expressed as

$$\nu = \frac{\gamma B_0}{2\pi} \tag{2.7}$$

This gives a good overview of how individual spins act and behave in magnetic fields, however our bodies contain a collection of spins of different nuclei. Therefore, it is important to apply these relationships to a collection of spins which will give an overview of macroscopic behaviours that make up the theory of NMR.

2.1.2 Macroscopic Behaviour

The molecules of interest for MRI are in the liquid state which means the motion of the spin is largely random and due to Brownian motion, thermal energy then becomes the dominant driving force and therefore quantum effects become negligible. When particles have a large enough temperature (T) and there are enough particles, the distribution over multiple energy levels can be described according to the Boltzmann distribution [46]. The probability p_i of a single particle being in a specific state is shown explicitly

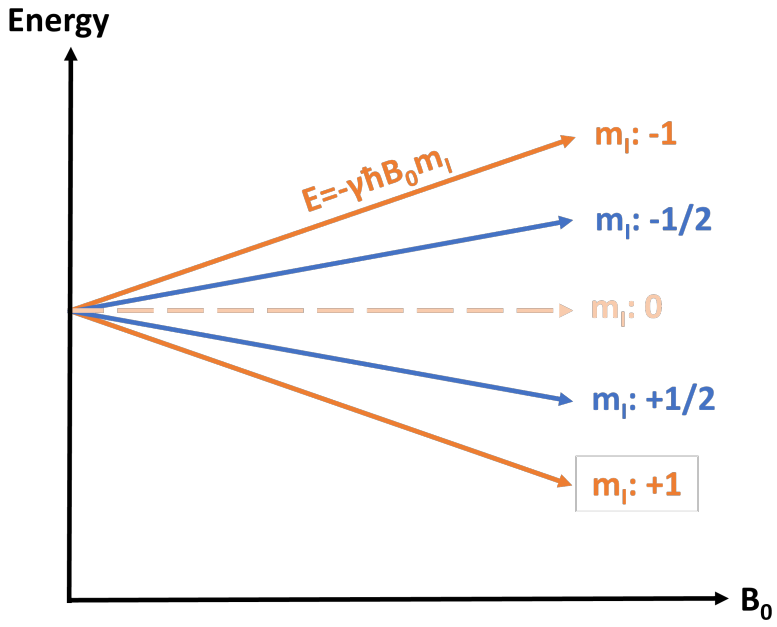

Figure 2.1: *Figure demonstrating the change in spin energy levels due to increasing magnetic field B_0, for spin-1/2 and spin-1 nuclei. Demonstrating the Zeeman Effect [45].*

as

$$p_i = \frac{\exp\left(\frac{-E_i}{k_B T}\right)}{\sum_{j=1}^{M} \exp\left(\frac{-E_j}{k_B T}\right)} \tag{2.8}$$

where i indicates the specific energy level and M is the total number of available states for a specific nucleus. The overall magnetic field that results from a large group of spins can be described by a vector called the magnetisation (M). Most of the spins' contributions will cancel so the contribution to the magnetisation vector arises from the difference in the populations of the different energy levels. A generalised summationcan be made that yields the equilibrium magnetisation

$$M = N \sum_{j=1}^{M} p_j \mu_j \tag{2.9}$$

where N is the number of spins of interest.

A major assumption that can be made, is that the thermal energy at room temperature is much larger than the nuclear magnetic energies ($E_j = \gamma\hbar B_0 \ll k_B T$). Therefore, the exponential terms can be simplified to $1+m_j\gamma\hbar B_0/k_B T$ based on the Taylor Expansion. The only variable that changes in the sum is m_j. The denominator of Eq. 2.8 becomes $2I+1$, and with the substitution of the magnitude of Eq. 2.3, Eq. 2.9 becomes

$$M = \frac{\gamma^2\hbar^2 N B_0}{(2I+1)k_B T}\sum_{j=1}^{M} m_j^2 \tag{2.10}$$

The summation here can be simplified to $I(I+1)(2I+1)/3$, and by substituting back into Eq. 2.10. A generalised form for M can be obtained for any spin that depends on the spin quantum number I, gyromagnetic ratio γ, N number of spins, B_0 strength of applied static longitudinal magnetic field and the temperature T. The analytical form of this is shown here

$$M = \frac{I(I+1)\gamma^2\hbar^2 N B_0}{3k_B T} \tag{2.11}$$

most nuclei that are of interest for NMR have a spin-1/2, which give two distinct energy levels. Equation 2.12 calculates the equilibrium magnetisation for spin-1/2 nuclei, the equilibrium magnetisation for spin-1 nuclei such as ^{2}H is

$$M_0 = \frac{\gamma^2\hbar^2 N B_0}{4k_B T} \tag{2.12}$$

The equilibrium magnetisation is responsible for the signal produced in NMR experiments. It is proportional to the total number of spins and inversely proportional to temperature (measured in kelvin). The temperature will mostly remain constant for experiments performed in humans *in vivo*. Also, M is proportional to the magnitude of any applied external magnetic field applied (B_0). The presence of equilibrium magnetisation alone is not enough for NMR/MRI to produce vital *in vivo* information about the human body. It is also important to be able to manipulate the magnetisation [47].

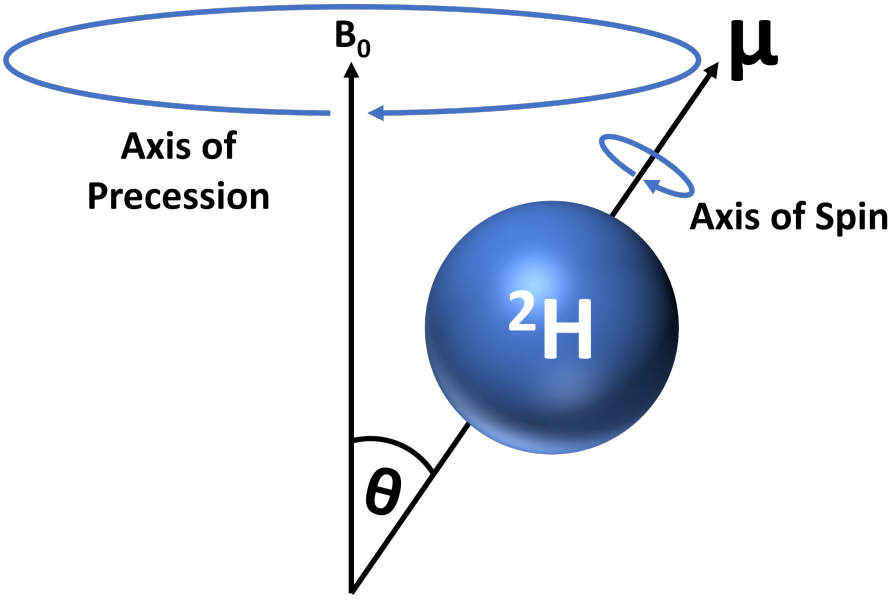

Figure 2.2: *A diagram of a ^2H nucleus spinning and precessing around an applied external magnetic field B_0. Its magnetic moment μ and both axes are labelled, along with the angle the magnetic moment vector makes to B_0.*

Whilst the magnetisation at thermal equilibrium is described above, it is possible for spins to move between spin states. In this case spin ladder operators (I_- and I_+) are used to describe this phenomenon, which are made up of the spin operators in the transverse plane. The mathematical form of the ladder operators are given as

$$\begin{aligned} I_+ &= I_x + iI_y \\ I_- &= I_x - iI_y \end{aligned} \tag{2.13}$$

The ladder operators are further explored in Chapter 7.

2.1.3 Manipulating Magnetisation

The direction of the equilibrium magnetisation vector is the same as the applied field. In general, magnetisation is made up of two main components, the longitudinal and the transverse. The longitudinal component is parallel to the applied field, with the transverse component being a combi-

nation of the two other orthogonal directions. Often the applied magnetic field, and analogously the magnetisation, is defined as $\mathbf{B} = B_0\mathbf{z}'$ and therefore the longitudinal component is in the z'-direction, which makes the transverse component a combination of the x' and y' components. The transverse magnetisation ($M_{x'y'}$) is zero at equilibrium, due to incoherence of the phases of spins. After a large enough period of time in an applied field the longitudinal magnetisation will reach the value outlined in Eq. 2.12 (M_0), whilst the transverse component will remain at zero. The evolution of the longitudinal and transverse components of the magnetisation is described by the Bloch equation [48] analytically expressed as

$$\frac{d\mathbf{M}}{dt} = \gamma\mathbf{M} \times \mathbf{B} + \frac{M_0 - M'_z}{T_1}\mathbf{z}' - \frac{\mathbf{M_{x'y'}}}{T_2} \tag{2.14}$$

The first term in Eq. 2.14 describes the evolution of the magnetisation in the presence of a magnetic field $\mathbf{B}$. The second term describes the evolution of the longitudinal magnetisation due to longitudinal relaxation, where T_1 is the longitudinal or spin-lattice relaxation time constant. This relaxation, results from spins interactions with the surrounding 'lattice'. The final term describes how the transverse magnetisation evolves over time, where T_2 is the transverse or spin-spin relaxation time constant. It arises from dephasing due to each spin's interaction with neighbouring spins.

The transverse relaxation time described here relates to the case where the applied field is perfectly homogeneous. However in reality this is rarely the case. In the presence of field inhomogeneity spins dephase more rapidly and the relevant relaxation is T_2^* which can be calculated according to

$$\frac{1}{T_2^*} = \frac{1}{T_2} + \frac{1}{T_2'} \tag{2.15}$$

Here T_2' is dependent only on the homogeneity of the field. This means that T_2^* can change between scans and scanners. The relaxation times T_1 and T_2 are specific for each nuclei, tissue type and field strength. In spec-

troscopy the Full-Width at Half Maximum (FWHM) of each peak, which is a measure of the broadness of peak, is related to the total transverse relaxation (FWHM= $1/\pi T_2^*$).

The NMR signal arises from the longitudinal magnetisation, however this is very small and can be dominated by magnetisation from electron currents within atoms and molecules. By applying an orthogonal magnetic field in the transverse plane, it is possible to 'tip' the magnetisation into the transverse plane. Here it will undergo precession and is able to induce a voltage in a current carrying loop thanks to Faraday's law of induction. This voltage will precess at the same angular frequency as the transverse field applied (ω). As the frequency of this applied field is usually in the RF range, this is usually referred to as an RF pulse when t is finite. This transverse applied field is referred to as $\mathbf{B_1}$ which is defined as

$$\mathbf{B_1}(\mathbf{t}) = B_1 \cos(\omega t)\mathbf{x}' + \sin(\omega t)\mathbf{y}' \tag{2.16}$$

The precession of magnetisation can be difficult to conceptualise/visualise in a stationary laboratory reference frame (x', y', z') due to the complex 3D motion. Therefore it is beneficial to consider the system in a rotating frame of reference (ie. as if the observer rotates around the z'-axis). The common reference frame used is one that rotates at the angular frequency of the applied RF around the z'-axis (ω), called the rotating reference frame. This means that the axis in this frames also rotates at ω angular frequency and is denoted as x, y and z. In the rotating reference frame the mathematical description of the applied RF pulse changes, and can now be described as composing of two circularly polarised components (B_1^+ and B_1^-) that rotate in opposite directions. The B_1^+ component rotates in the same direction as the rotating frame and hence would appear static, whilst B_1^- appears to rotate in the opposite direction with twice the angular frequency (-2ω). It is the B_1^+, known as the transmit field, that is responsible for the 'tipping' of magnetisation. The use of the transverse B_1, B_1^+ and B_1^- and the hardware that is used to produce these fields is described in more detail in

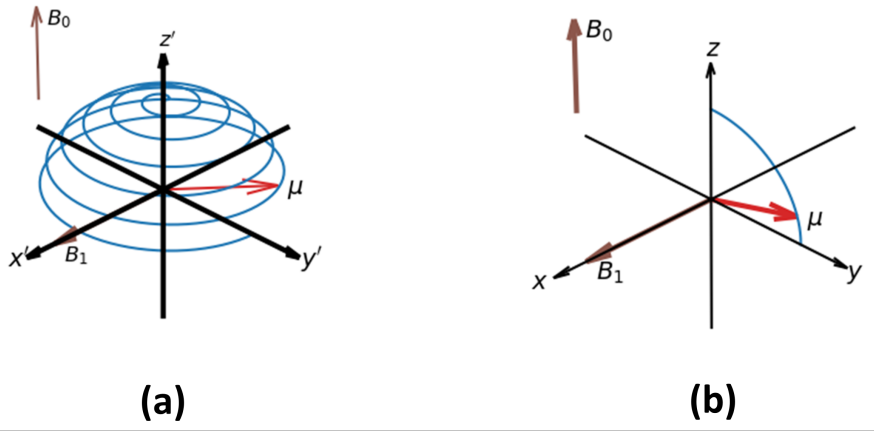

Figure 2.3: Diagram demonstrating how the precession of a magnetic moment following a RF field B_1 (brown arrow) in a static B_0 fields appears to evolve differently in the laboratory frame (a) and in the rotating frame.

Chapter 3.

An example of how a precessing magnetic moment appears to evolve differently in the laboratory frame and the rotating frame is shown in Fig. 2.3. The rest of this thesis will use the rotating reference frame in order to simplify calculations and assumptions.

Quite often in cases where there is rotational symmetry it can be easier to describe operators as spherical tensors, as the rotational operator $R(\theta, \phi)$ acts on the tensor T_k^q. In this case the spherical tensor T_k^q is said to have a rank k which has $2k + 1$ components and q ranges from $-k$ to k. In the case of a spherical spin tensor the q refers to the coherence of the tensor, which represents the transitions in the spin state. If the rank of the tensor is 0 ($k = 0$), therefore there is only one coherence available ($q = 0$). In the rank one case ($k = 1$) there are three available coherence's ($q = -1, 0, 1$), where $q = 0$ this corresponds to the I_z operator and does not change under the rotation operator. The T_1^{+1} and T_1^{-1} correspond to the spin ladder operators I_+ and I_-. Rank two tensors ($k = 2$) corresponds to the tensor that arises from interactions between the spin and the electric field gradient, which is the quadrupole moment which is present in $I = 1$ nuclei such as

^{2}H. These spherical tensors that arise from the quadrupole moment are further explained in Chapter 7.

The rotating reference frame also changes the mathematical description of the Bloch equations for the evolution of magnetization in the rotating reference frame (x, y, z) according to

$$\frac{dM_x}{dt} = \Delta\omega M_y - \frac{M_x}{T_2} \tag{2.17}$$

$$\frac{dM_y}{dt} = \Delta\omega M_x + \omega_1 M_z - \frac{M_y}{T_2} \tag{2.18}$$

$$\frac{dM_z}{dt} = -\omega_1 M_y + \frac{M_0 - M_z^{'}}{T_1} \tag{2.19}$$

Here, $\omega_1 = \gamma B_1$ and $\Delta\omega$ is the difference between the Larmor angular frequency (ω_0), which is the rate at which the reference frame rotates, and the angular frequency of the nuclei precession (ω), and represents any off resonance effects. Therefore, if the RF is applied at ω_0, $\Delta\omega = 0$ and these terms disappear. If only the static field case is being considered, the ω_1 terms disappear as well, which leaves only the relaxation dominant terms. If short and rectangular RF pulses are considered the solutions to Eqs. 2.17 - 2.19 describing the evolution of magnetisation after the pulse are shown here

$$M_x(t) = \exp(-t/T_2)\,(M_x(0)\cos\Delta\omega t \;+\; M_y(0)\sin\Delta\omega t) \tag{2.20}$$

$$M_y(t) = \exp(-t/T_2)\,(M_y(0)\cos\Delta\omega t \;-\; M_x(0)\sin\Delta\omega t) \tag{2.21}$$

$$M_z(t) = M_z(0)\exp(-t/T_1) \;+\; M_0\,(1 - \exp(-t/T_1)) \tag{2.22}$$

RF pulses are used to rotate the longitudinal magnetisation into the transverse plane. In between short applied fields (RF pulses) it is often necessary to wait a large enough period of time for the magnetisation to relax back into its longitudinal state before repeating the process to acquire more data.

2.1.4 Flip Angles, Phase and Signal

The flip angle (θ) generated from a short RF pulse (excitation) is dependent on the B_1 magnetic field strength and the pulse duration (τ) can be calculated from the equation here

$$\theta = \gamma B_1 \tau \tag{2.23}$$

Where θ is the angle the magnetisation is rotated through after excitation, also known as the flip-angle. If starting from the equilibrium situation, the closer this flip-angle is to 90° the larger the amount of longitudinal magnetisation that is rotated into the transverse plane. The signal produced by precessing transverse magnetisation can be described as a complex signal such that $f(t) = R(t) + I(t)i$. This is known as a FID, $R(t)$ is the real component of FID, $I(t)$ is the imaginary component and $f(t)$ is the combination. The signal induced in the receiver coil after a 90° pulse is applied to equilibrium magnetisation can be written as

$$R(t) \propto M_0 \cos(\omega_0 t + \phi) \exp(-t/T_2^*) \tag{2.24}$$

$$I(t) \propto M_0 \sin(\omega_0 t + \phi) \exp(-t/T_2^*) \tag{2.25}$$

where ϕ is the phase of the signal and represents the angle the transverse magnetisation makes to the x' axis after excitation, i.e a phase of 90° would be aligned parallel to the y-axis. M_0, ω, ϕ and $1/T_2^*$ are parameters that were mentioned in the previous section (amplitude, angular frequency, phase and relaxation rate) respectively. The real and imaginary components can be combined using Euler's formula to give the following

$$\nu(t) \propto M_0 \exp(-\omega_0 i t) \exp(-t/T_2^*) \exp(i\phi) \tag{2.26}$$

This signal is described in the time-domain. To separate different frequency contributions to the signal, it is useful to transform this signal into the frequency domain, which can be performed using a Fourier Transform (FT) [49]. A similar equation can be used for moving in the other

direction (from frequency to time domain) and this is known as the Inverse Fourier Transform (IFT). Both equations are listed analytically here

$$F(\nu) = \int_{-\infty}^{+\infty} f(t) \exp(-2\pi\nu i t)\, dt \tag{2.27}$$

$$f(t) = \int_{-\infty}^{+\infty} F(\nu) \exp(2\pi\nu i t)\, d\nu \tag{2.28}$$

where $F(\nu)$ is the frequency domain spectrum. An important aspect of these equations is that they can be used without affecting the original signal such that $\mathrm{IFT}(\mathrm{FT}(X)) = X$, where X is any signal. Whilst the limits on the integrals are listed as infinity (∞) this is not applicable to a real MR signal, here the signal begins at $t = 0$ where the non-zero magnetisation begins, so therefore the limits will start there. By applying a FT to the FID where signal is only present for $t > 0$ Eq. 2.29 is obtained, which depends on the same four parameters as the FID. The relationship between the T_2^* and the FWHM has already been described: as the T_2^* gets longer, the peak becomes narrower. It is important to note however that the integral/area under the peak is independent of T_2^*. The integral only depends on the amplitude (A) of the signal. Therefore, the shorter the T_2^* the smaller the peak height and *vice versa*, and therefore maximising A and T_2^* maximises the available SNR in the spectrum with $R_2^* = 1/T_2^*$, the equation for a frequency domain spectrum is given as

$$F(\nu) = A \exp(i\phi) \frac{R_2^* - i2\pi(\nu - \nu_0)}{R_2^{*2} + 4\pi^2(\nu - \nu_0)^2} \tag{2.29}$$

SNR is used to measure the quality of the obtained signal, currently multiple definitions and methods of calculating SNR exist, one of the most famous is given formally as ratio of the peak height to the root mean square of the noise [50]

Using NMR to measure signals from pure samples with only one nuclear magnetic resonance will produce spectra with single peaks. However in general samples contain a range of different molecules, in which the

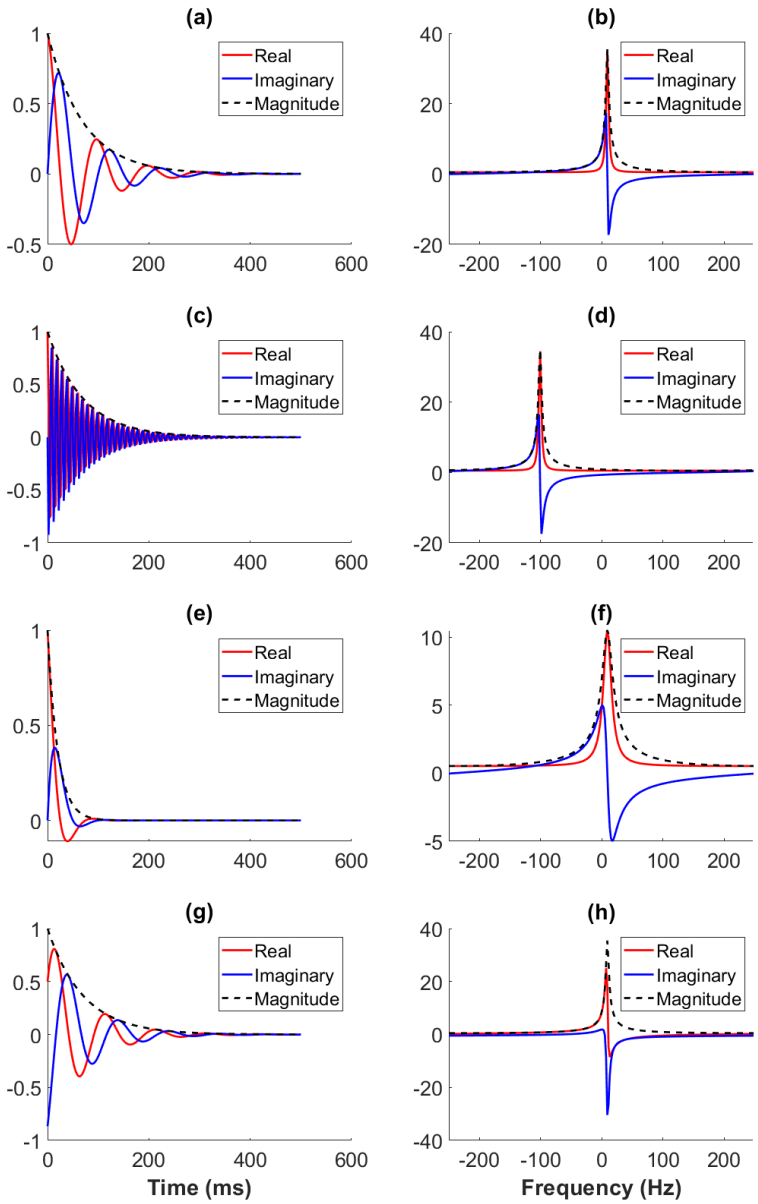

Figure 2.4: *Plots of FIDs (left) and corresponding lineshapes (right) for different frequency offsets (ν_0), transverse relaxation times (T_2^*) and phases (ϕ), all FIDs have an amplitude (A) of 1. The parameters for (a) and (b) are ν_0=-10 Hz, T_2^*= 70 ms and ϕ=0, one parameter is changed in each row. (c) and (d) have a different ν_0 of +100 Hz. (e) and (f) have a shorter T_2^* of 20 ms. (g) and (h) have a phase of ϕ=-π/3.*

atoms of each atomic species can be in different chemical environments. This is certainly the goal for MRS measurements on living systems. The shielding of the magnetic field at the nucleus by the surrounding electron cloud changes the magnetic field at the nucleus, which in turn changes the resonant frequency of precession for nuclei. Therefore, nuclei that have different chemical environments will precess at different frequencies which means that the NMR signal will be found at different frequency positions in an NMR spectrum. Therefore by identifying the positions of peaks in an NMR spectrum and finding the amplitudes of the peaks, it is possible to probe the chemical structure of the compounds found in the sample. This is useful in studies of medical conditions and diseases. The main unit of measure for frequency is hertz (Hz), however the values here will change greatly depending on the nuclei of interest and the field strength being used. Therefore a different unit of measurement is often used to characterise the frequency in an NMR spectrum to make it more general and therefore applicable to all nuclei and field strengths. The chemical shift (δ) of each signal is measured in parts-per-million (ppm). The equation to calculate chemical shift from frequency is shown here

$$\delta = \frac{\nu - \nu_{\text{ref}}}{\nu_{\text{ref}}} \times 10^6 \tag{2.30}$$

Where ν_{ref} is a reference frequency, usually this is set such that the water peak is centered at 4.8 ppm. The specific value is controlled by the scanner operator.

2.1.5 Introduction of Gradients

So far it has been outlined how to obtain an NMR signal in samples and in the body using MRS. However, sometimes it is not enough to only obtain information on the chemical structures/composition of the body and spatial information is also needed to interrogate chemical compositions of specific areas in the body. The most common way to do the required spatial

encoding is to use magnetic fields that vary spatially [47].

According to Eq. 2.7 the frequency of precession is dependent on the applied magnetic field. Therefore if the magnetic field varies with spatial position the frequency of precession will also vary with spatial position. In particular a magnetic field gradient corresponding to the linear variation of field with position, produces a linear variation of frequency with position. For example when a gradient is applied in the z-direction, the variation in the z component of B_0 (B_{0z}) is given as the product of the z-component of the gradient $\mathbf{G}$ and the position on the z-axis $\mathbf{z}$, mathematically expressed as

$$B_{0z} = \mathbf{G} \cdot \mathbf{z},\ \nu = \frac{\gamma \mathbf{G} \cdot \mathbf{z}}{2\pi} \tag{2.31}$$

Previously, we considered the situation where a static spatially-homogeneous B_0 was applied to a sample and an RF pulse was used to tip the magnetisation of all the spins into the transverse plane. However if a gradient is applied along with B_0, only the spins with the same frequency as the RF pulse will be tipped. The magnetic field in the presence of a gradient (G) is described by Eq. 2.32, with the frequency that is spatially dependent is shown in Eq. 2.33. Both equations are explicitly shown here

$$B(r) = B_0 + \mathbf{G} \cdot \mathbf{r} \tag{2.32}$$

$$\nu(r) = \frac{\gamma}{2\pi}(B_0 + Gr) \tag{2.33}$$

Here $\mathbf{r}$ is used to represent any cartesian spatial vector. Therefore only a spatially localised 'slice' will be excited and any signal received will be specifically from that slice. By changing the frequency of the applied RF pulse different slices can be excited. If the pulse contains a range of frequencies (bandwidth) all the frequencies in the bandwidth will be excited, this results in a slice being excited that has a finite thickness. If this process is repeated, signals can be acquired from multiple slices and therefore the

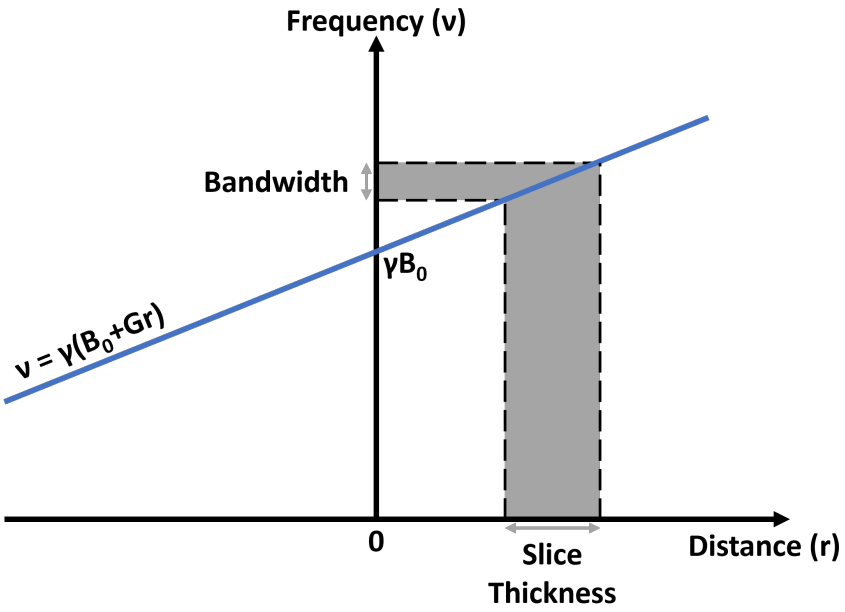

Figure 2.5: *The relationship between frequency of precession (ν) and thickness of an acquired slice when a gradient (G_{slice}) is applied.*

changes in signals can be compared to position in the body of which the slice was acquired. The link between magnetic field/frequency and position using gradients is demonstrated visually in Fig. 2.5.

If the chemical composition of what is being investigated is not important it is possible to acquire entirely spatial information and create a volumetric image based on multiple slices. To perform this process gradients are applied in more dimensions than just the slice-selective gradient [51]. Phase encoding and readout encoding will be explained in Section 2.3.1 below.

2.2 Differences for ^{2}H

Deuterium (^{2}H) is a stable isotope of hydrogen. The nucleus of a ^{2}H atom is called a deuteron. Large elements are formed in supernovas [52], whilst lighter elements up to iron are made in the cores of stars during fusion. However, ^{2}H is destroyed very quickly in fusion within stars [53] therefore almost all the ^{2}H that exists naturally is formed from Big Bang Nucle-

osynthesis [54]. The 0.015% ^{2}H abundance found in the Earth's oceans is similar to what has been found in comets, which adds evidence that ocean water originates from comets [55]. Most of the natural ^{2}H content occurs as HDO, and the ^{2}H content of different water sources (oceans, rainwater etc) can be used to track the water cycle [56]. Our bodies consequently have a very low natural abundance (NA) ∼0.015% of ^{2}H, which makes ^{2}H appealing for tracer studies, as small concentration increases are easy to detect above baseline. The addition of a neutron to the nucleus of ^{2}H means the gyromagnetic ratio (γ) is smaller than that of ^{1}H (6.54 vs 42.6 MHzT^{-1}) which reduces the Larmor frequency of ^{2}H according to Eq. 2.7. A magnetic moment is a vector quantity that is used to describe magnetic fields and interactions that arise from charges. Dipolar moments arise from charge distributions and point dipoles, a quadrupolar moment is a second rank expansion of the dipolar moment and is used to describe non-spherical charge distributions. ^{2}H has an integer spin of 1 and due to the non-symmetric distribution of charge within the nucleus also has a quadrupolar magnetic moment of 0.286 fm^2e. The nuclear quadrupolar moment interacts with local electric field gradients, and fluctuations in this interaction cause relaxation, thus reducing both the longitudinal and transverse relaxation times of quadrupolar nuclei. Deuterium's spin of 1 also introduces an extra Zeeman energy level more than for ^{1}H, with allowed values of m_I = -1, 0 and 1. Considering that the magnetisation is the net vector sum of μ the net magnetisation is due to the population differences across energy levels. Using Eq. 2.9 and/or 2.11 a simplified equilibrium magnetisation can be found

$$M_0 = \frac{2\gamma^2\hbar^2 N B_0}{3k_B T} \tag{2.34}$$

Whilst the magnetisation appears to be 8/3 larger for ^{2}H compared to ^{1}H in Eq. 2.34, it is important to note M_0 is also dependent on the gyromagnetic ratio squared along with the number of spins. The gyromagnetic ratio squared is ∼42 times smaller for ^{2}H. Also assuming the mass

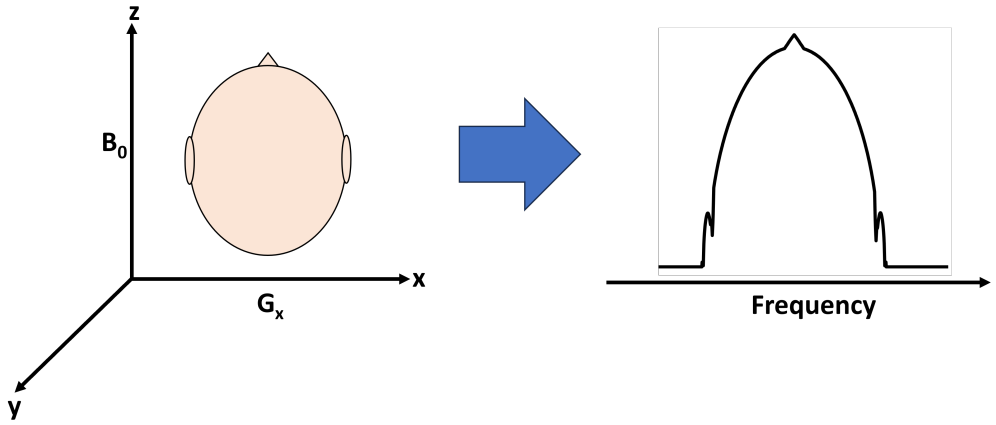

Figure 2.6: Diagram showing how a 1D projection of an image is created using a gradient applied in the x direction.

and volume of the sample/tissue being scanned/investigated is at NA the number of spins will be ~6.7x10^{-3} smaller for ^{2}H. The lower value of γ also reduces the Larmor frequency, leading to a further reduction in the NMR signal. This reduction in γ means stronger gradients are needed to produce the same amount of spatial encoding. Some of the loss in signal of ^{2}H can thankfully be recovered due to the reduction in relaxation times. This is because the signal will return to equilibrium more rapidly and therefore the scans can be more rapidly repeated and averaged, increasing the number of averages that can be acquired per unit time. The decrease in SNR for ^{2}H compared to ^{1}H makes MRI difficult at NA, which is why spectroscopic techniques are much more common for ^{2}H.

2.3 Scanning

2.3.1 Imaging

The use of gradients during RF pulse excitation to excite signals selectively within a thin slice of the object, known as slice selection, is the first step in using magnetic fields to obtain images. In addition to slice selection two more directions also need to be encoded. If a gradient is applied immedi-

ately after the excitation, the FID and corresponding spectrum will contain spatial information, as the frequency shift of peaks will inform on location of the signal in a similar way to the slice selection. The spectrum then represents a 1D projection of the spin density of whatever is being scanned. The spectral width of the obtained signal therefore identifies the width/size of the image which is often linked to the required Field Of View (FOV) of an image. This method of encoding an additional dimension is known as frequency encoding using a readout/frequency gradient (G_{read}/G_{freq}), with the obtained 1D spectrum being known as the readout profile.

Whilst frequency encoding does work to obtain an additional dimension, there are real world limitations that can hinder this process. The main limitation is the gradient switching as the turning on/off of the gradient cannot occur instantaneously therefore the first few FID points might be acquired during a time-varying gradient which could lead to errors in the data, which will persist into the spectrum after an FT is applied. A method of getting around this is to remove first few points from the FID, however these contain the highest signal and therefore could reduce the available SNR. The realistic method to navigate around this problem is to create an signal at a later time point by taking advantage of dephasing and rephasing, the later signal is referred to as an echo. If the echo is created using a 180° pulse it is referred to as a Spin-Echo (SE), if the echo is created by manipulating gradients it is referred to as a Gradient-Echo (GE). When a perfect FID is created, the signal starts with any phase between 0 and 2π which depends on the RF pulse used. As the magnetisation evolves in the transverse plane it begins to accumulate phase. Therefore by applying a negative G_{read} which encourages the dephasing, followed by a positive G_{read} the phase accumulation reverses in direction during the positive G_{read} and reaches 0 again. Acquiring data at this point allows a full FID to be obtained with the maximum signal occurring during the G_{read}. The echo occurs at a time referred to as the Echo Time (TE). It is important to note that the rephasing only recovers the dephasing caused by the negative

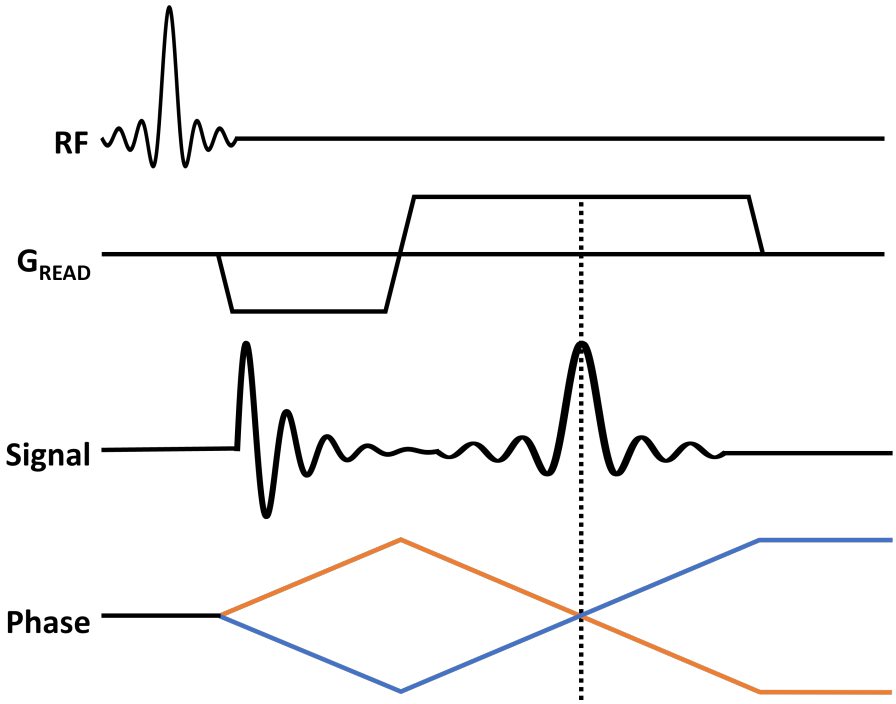

Figure 2.7: Diagram showing how phase accumulation varies with dephasing lobes of the read gradient, along with the received RF signal. The blue and orange lines demonstrate the phase changes of two different spins in two different spatial locations. The peak signal during the echo occurs when the phase net phase change for spins is zero, indicated by the dotted line.

G_{read}, it does not recover signal lost from T_2 or T_2^* relaxation processes. Another type of echo formation exists, called a SE or Hahn-echo [57] which involces application of a 180° RF pulse after the first set of gradients to rephase the signal, the use of GE are often preferred to SE in terms of imaging thanks to the the lower flip angles, shorter TE and shorter TR that can be achieved. The TR is the time from the end of the RF pulse until the scan can be repeated. Repeating/averaging the scan allows the SNR to be improved.

The final spatial dimension is often encoded using a phase-encoding gradient (G_{phase}) which is applied before the signal is acquired under the read gradient. This gradient only affects the phase of the signal in a way

which is dependent on its position in real-space. By linearly changing the magnitude of the applied phase encoding gradient a set of 1D spectra are acquired which can be represented in a 2D matrix. The data in the 2D matrix is therefore a collection of spatial frequencies with dimensions u and v, in each dimension the central spatial frequency is 0. A low spatial frequency describes the general trend of an image whilst the high spatial frequencies define the sharp edges. This frequency space where the data is stored is called k-space, and applying a 2D inverse FT to this data produces an image [58, 59]. Which is a 2D matrix of values in directions x and y. The equations used to perform 2D IFT and FT are similar to the 1D FT and IFT in Eqs. 2.27 and 2.28, and are shown here

$$F(u,v) = \int_{-\infty}^{+\infty} \int_{-\infty}^{+\infty} f(x,y) \exp(-i2\pi(ux+vy))\, dx\, dy \tag{2.35}$$

$$f(x,y) = \int_{-\infty}^{+\infty} \int_{-\infty}^{+\infty} F(u,v) \exp(i2\pi(ux+vy))\, du\, dv \tag{2.36}$$

The collection of RF pulses and gradients is called a pulse sequence, and the pulse sequence described so far is called gradient-echo imaging, and can be viewed in Fig. 2.8.

It has been shown that the introduction of gradients can be used to acquire more spatial dimensions of an image. They can also be used to destroy/null signal in a specific region, for example it can be beneficial to null signal at the end of each TR period. These gradients are referred to as 'spoiler' gradients and work by de-phasing the transverse magnetisation spins. If signal can be nulled outside a 3D volume before imaging this can remove the need for slice selective gradients during imaging. This nulling is usually performed with the use of selective RF pulses that excite magnetisation outside of the 3D volume, followed by the use of spoiler gradients. This is often referred to as Outer-Volume Suppression (OVS) and is commonly used to acquire reduced FOV image data [60].

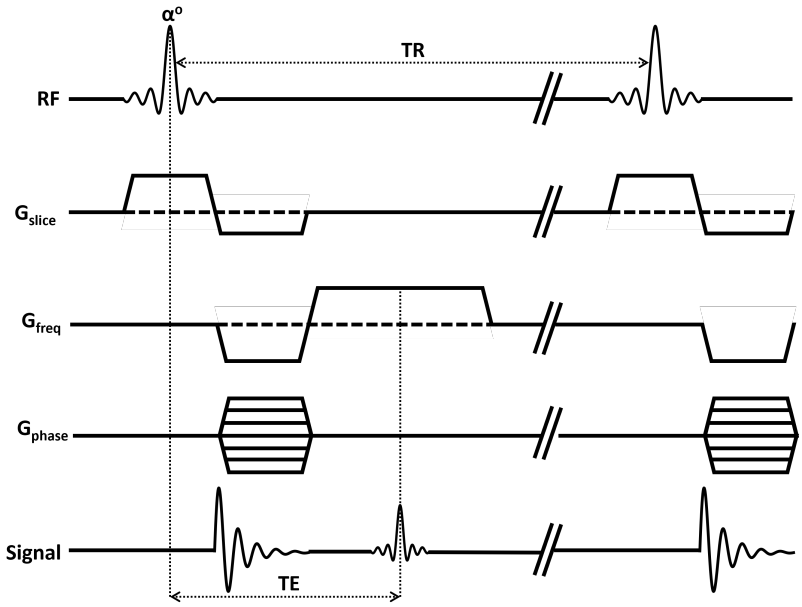

Figure 2.8: *Example pulse sequence diagram for a GE imaging sequence, with the TE indicated.*

Longitudinal and transverse relaxation time constants vary depending on the type of tissue. Therefore, when a particular pulse sequence is used the choice of TR and TE will effect the the contrast in the image. The image signal in a GE varies with flip-angle, TR and TE, which drives the contrast. The expression for signal S is shown empirically here as

$$S = M_0 \sin(\alpha) \exp(-\mathrm{TE}/T_2^*) \frac{(1 - \exp(\mathrm{TR}/T_1)}{(1 - \cos(\alpha) \exp(-\mathrm{TR}/T_1))} \tag{2.37}$$

There are three main types of contrast in an image: T_1-weighted, T_2-weighted, T_2^*-weighted and spin density weighted. The contrast in spin-density images comes from the difference in the density of spins in a particular tissue being emphasised. Remembering that most commonly the spin of interest is ^{1}H, it is the ^{1}H proton density that gives the contrast. The contrast in T_2-weighted images is emphasised by differences in T_2 times of different tissues, in order to produce these images long TRs and long TEs are used which minimises effects from different T_1s. Blood flow of oxygenated and deoxygenated blood changes the T_2^* (known as the blood-

oxygen-level-dependent (BOLD) signal) which can give rise to T_2^*-weighted images, shown in Eq. 2.37. Finally in T_1 weighted images the contrast is dominated by differences in the T_1 times of different tissues. This contrast is produced by choosing short TRs and TEs which minimise effects from different T_2 times.

The SNR obtained from a specific pulse sequence often depends on how quickly data can be acquired. One of the biggest aspects of scanning that affects the time taken is how data in k-space is obtained (k-space traversal). By traversing k-space more efficiently, scan time can be reduced which can make scanning more comfortable or can be used to improve SNR by increasing the number of averages in a fixed scan duration. One of the biggest improvements in the traversing of k-space came with the development of Echo-Planar Imaging (EPI) [61].

2.3.2 MRSI

Acquiring MR spectra allows molecular concentrations to be obtained by comparing the magnitudes of peaks/signals at different chemical shifts, whilst MR images provide good contrast for structural differences. It is possible simultaneously to acquire information on chemical/molecular concentrations as well as structural information using a technique called MRSI, which is effectively a combination of MRS and MRI. This technique provides individual spectrum from small volumes that are packed together into a 2D/3D grid that covers a larger volume/tissue. The voxels are often much larger than what would usually be acquired using MRI, but maybe smaller than what would be acquired using MRS strategies. By calculating concentrations for the visible molecules in each spectra the spatial distribution of each molecule can therefore be represented as a coarse image. This is often overlaid onto an anatomical image so that the corresponding regions can be easily identifiable. Concentration changes in specific tissues can therefore be used as bio-markers for disease. In order to obtain this type of data different pulse sequences that use different combinations of

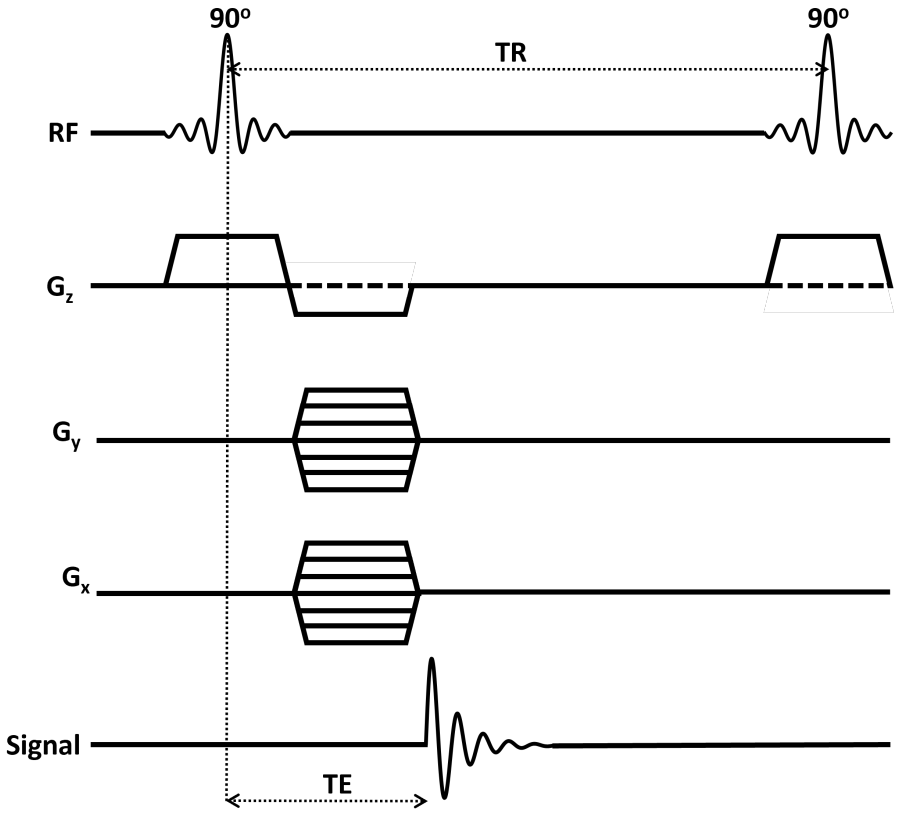

Figure 2.9: *Example pulse sequence diagram for a 2D CSI, which includes two 90° RF pulses seperated by TR applied at the same time as a slice selective gradient G_z, which is followed by a rephasing lobe. During this rephasing, G_x and G_y gradients are also applied to spatially localise the resulting via phase encoding FID, the time between the centre of the pulse and the start of the FID sampling defines the TE.*

RF pulses and gradients are used.

Chemical Shift Imaging

The simplest and quickest method to acquire a spectrum is to apply an RF pulse in a static magnetic field and acquire data from the FID immediately after the pulse. Application of a gradient during the RF excitation will localise the data from a specific slice in the body. Often this gradient is applied in the z-direction to localise the signal from a transverse slice through the body. However any direction of gradient can be used to excite

a region. For example a sagittal or a coronal slice can be excited instead. The combination of gradients increases the number of dimensions in which spatial position can be localised, as has been shown with gradient echo imaging in Fig. 2.8. By applying a phase encoding gradient along one axis before it is possible to make the phase of the signal dependent on the position in the gradient direction. Repeating the FID acquisition with different phase encoding gradient amplitude and then applying a Fourier transform the stacked spectra produces a one dimensional chemical shift image. If phase encode gradients are independently applied in two or three directions. Fourier transformation of the resulting FIDs in two or three dimensions produces 2D or 3D chemical shift images. This pulse sequence is called CSI, a diagram of the pulse sequence used to acquire a 2D CSI is shown in Fig. 2.9.

CSI has been used for different nuclei (^{13}C, ^{31}P and ^{2}H) to create maps that show the distribution of different metabolites. Acquiring this type of data takes a long time which can be a problem is functional data was to be acquired, which motivates work to decrease the acquisition time for MRSI data.

2.4 Analysis

2.4.1 Quantification of MRS data

When analysing MRS data it is important to be able to accurately track changes for each metabolite. The oldest method of doing this is peak integration whereby the spectral points spanning a peak are summed together. An integration range of at least two FWHM's wide is usually enough to obtain accurate quantification [62]. The spectral peak integration value can also be obtained from the time-domain signal as the first point in the absorption spectra (for a spectrum with a single peak), as well as from the product of the FWHM, π and the spectral peak-height in the frequency

domain [51]. This technique is simple to implement computationally and takes little time, however it requires correctly phased spectra as any incorrect phasing will give the incorrect amplitude. Most biological tissues and processes involve complex chemical environments with many different compounds which will produce different MR signals appearing at different frequencies (also known as chemical shifts). This does not necessarily affect the peak integration method as long as each peak/signal has a large enough frequency offset relative to each other. However this is commonly not the case especially in ^{1}H spectroscopy [63].

Therefore, a different methodology is needed to overcome this issue, which comes in the form of fitting spectral signals to lineshapes, such as Lorentzian [64], Gaussian and Voigt [62] lineshapes. In order to correctly perform the fitting a methodology is needed to mathematically quantify the quality of the fit, using the difference between the model and the data. One of the most common mathematical models is the least-squares [65] whereby the sum (R^2) of the squared differences between the experimental data and a model (residuals) is minimised [66], once its deemed the result is minimised then the data is fit. Mathematically this is demonstrated as the following summation

$$R^2 = \sum_{i=1}^{n} \left|[y_i - f(x_i, a_1, a_2, ..., a_m)]\right|^2 \tag{2.38}$$

Where i represents each data point with n data points, and the range of values a_1 to a_m covers the amount of fitting parameters such as linewidth (similar to FWHM), frequency position, phase and most importantly amplitude. R^2 is said to be minimised when the following differential relationship for each fitting parameter is met, the derivative is referred to as the Jacobian and is shown here

$$\frac{\partial(R^2)}{\partial a_i} = 0 \tag{2.39}$$

The fitting then begins by using initial parameter guesses and applies this

to the least squares model and finds the sum of squared residuals. An optimisation algorithm is then used to update the parameter values iteratively, until a certain threshold in the R^2 value is met or the max number of iterations is reached.

It is possible to fit MRS data in both the time and frequency domain, and each can be better depending on the scenario [67]. To model experimental MRS data in the time domain a series of exponentially damped sinusoids are used. Since the full spectra comprises the sum of many individual damped sinusoids. The more signals present in the spectra the more difficult computationally this becomes. There is consequently a strong motivation to reduce the number of parameters, reduce the computational load and therefore increase the reliability of the fitting [62]. It has been shown that one way to improve the reliability of fitting spectra that suffer from overlapping signals, which is the case for ^{31}P MRS data, is to use prior knowledge [68]. Some of the overlapping signals while distinctly different can share common ratios between some of their fitted parameter. One of the first fitting algorithms to include prior knowledge was the VARiable PROjection (VARPRO) method [65] which has successfully been used to analyse ^{31}P data [69, 70]. Whilst VARPRO was successful as an improved fitting methodology, a new technique was developed called Advanced Method for Accurate, Robust, and Efficient Spectral fitting (AMARES) which fits more reliably and accurately, as well as having increased functionality, including lineshape choice, fitting of echo signals and imposition of upper and lower bounds on fitting parameters [71]. AMARES is used regularly in MRS analysis and is included in software packages such as JMRUI [72] and OXSA [73], which have previously been used to analyse ^{2}H MRS data [74–76]. The model of summed damped sinusoids that is used in the AMARES package is the trust region-reflective optimisation algorithm, which is mathematically shown here

$$y_n = \hat{y_n} + e_n = \sum_{k=1}^{k} a_k \exp(i\phi_k) \exp(-d_k(1 - g_k + g_k t_n)t_n) \exp(i2\pi f_k t_n) + e_n \tag{2.40}$$

Here k is the number of sinusoids, ϕ_k is the phase, d_k is the damping factor, g_k determines the lineshape (1 for Gaussian, 0 for Lorentzian), t_n is the time for each point, f_k is the frequency offset and e_n describes complex white Gaussian noise. Eq. 2.40 and Eq. 2.26 are similar and therefore it can be seen that d_k has the same effect on an FID as R_2^* and is therefore equal to $\pi\times$ FWHM of the frequency domain spectrum. The caret indicates the model as opposed to actual measurement.

Even AMARES has its limits and signal fitting can struggle when many peaks are present especially in terms of overlapping signals, which can be a big problem in ^{1}H MRS data. Therefore, a new methodology was developed to overcome this called linear combination and was made into a toolbox that is called LCModel [77]. This works by fitting total spectra for each metabolite (called basis sets) instead of individual peaks, this reduces the number of model parameters and leads to increased reliability in fitting. The basis sets can be acquired by either phantom *in vitro* experiments or by numerical simulation [62]. The creation of basis sets makes LCModel more technically challenging to fit, compared to AMARES. Also, because of the technical challenge LCModel offers users less control of fitting parameters. Because of this it is more complicated to set up so it is yet to be used commonly for the more simplified and sparse spectra from ^{13}C, ^{31}P and ^{2}H, although it has been used in analysing data for the indirect detection of ^{2}H glucose by looking at the loss in ^{1}H signal [40, 78, 79]. In ^{1}H spectra a rolling baseline as well as contributions from macromolecules and lipids can be an issue. Therefore the ability to fit the baseline as well as the macromolecules as part of the linear-combination are benefits compared to AMARES.

2.4.2 Post-Processing Improvement of SNR

The low SNR of ^{2}H is often a problem during scanning and as scanning times have to be kept short for participant/patient comfort this can be a problem in spectroscopy with any nuclei. Whilst fitting in the frequency domain can provide accurate fitting and quantification, it is now common practice to fit data in the time-domain which can have the ability to provide more accurate and reliable fitting [80]. In order to increase the reliability and reproducibility of values obtained from analysis it is important to maximise the SNR. A popular method of increasing the SNR of spectra is to apply spectral filtering in the form of apodisation. Common lineshapes that are used in the filtering are exponential and Gaussian [81]. An exponential filter is commonly used as it matches the exponential decay due to T_2^*. However, this strategy increases the linewidths of the spectra where it is applied, which is why it is often called line-broadening. This line-broadening effect has been shown to reduce the accuracy of fitting especially in cases of complex spectra where signals overlap spectrally [82]. Apodisation has also been shown to effect metabolite concentration quantification [81] and as a result, apodisation is not used as a de-noising tool and is often only used for the displaying of spectral data. Lots of alternatives exist in terms of denoising including Principal Component Analysis (PCA) [83] and low rank approximation [84] that have been shown to provide improved SNR without limiting quantification [85].

Singular Value Decomposition (SVD) is a linear algebra technique that breaks down a 2D matrix into its key components, and is used to reduce a matrix without affecting the data. An example would be a 2D matrix A that is $m \times n$ in size will have $m \times n$ values, if this can be decomposed into two vectors that are orthogonal such that $A = \mathbf{u}\mathbf{v}^{\mathrm{T}}$ the total number of values in these vectors is $m+n$. Therefore large data sets can be compressed into a smaller storage size without compromising the data itself. The use of SVD is similar to an eigenvalue problem, the eigenvalue problem only works

when A is a square matrix, if A is a rectangular matrix the eigenvectors become square matrices, U and V. Here each column of v and each row of u diagonalises the matrix A similar to an eigenvalue problem. The eigenvalues then form the diagonal elements of the matrix Σ called the 'core matrix', the eigenvalues are called the singular values and the size represents the importance for reconstructing A. By rearranging the matrices Eq. 2.41 is created for the matrix A [86] and is expressed mathematically as

$$A = U\Sigma V^{\mathrm{T}} = \sum_{k=1}^{r} \mathbf{u_k} \sigma_k \mathbf{v_k}^{\mathrm{T}} \tag{2.41}$$

However, a full reconstruction does not necessarily need to be performed, if the core matrix is arranged by size and the lower singular values are removed, A can be reconstructed using only the more important features. When this technique is applied to MRS data this will de-noise the data as the noise will be represented by the lower singular values [3]. This technique can also be also used to fit MRS data, as the results can be converted into the regular fitting parameters [87], as well as to remove water signal in post-processing [88].

This approach only works with 2D matrices, which is an issue for MRSI data which commonly has up to five dimensions (one spectral, three spatial, and a temporal domain). However, a similar technique can be used when more dimensions are present called Higher-Order Singular Value Decomposition (HOSVD). This is similar to regular SVD but has the ability to work with higher dimension data. Here the original matrix A that has size $I \times J \times K \times L$ is converted to a tensor $\mathcal{A}$. This is decomposed into the product of the core tensor $\mathcal{S}$ and the unitary orthogonal matrices U, each matrix U has a specific mode which is indicated by the subscript. Each U is a square matrix that has the size of the corresponding mode of $\mathcal{A}$, for example U_2 will have a size $J \times J$. An example of the mathematical form of the HOSVD of $\mathcal{A}$ that has size $I \times J \times K \times L$ shown here

$$\mathcal{A} = \mathcal{S} \times U_1 \times U_2 \times U_3 \times U_4 \tag{2.42}$$

This gives a core tensor that is the same size in each dimension, which can be truncated in a similar way to SVD, so that when the original tensor $\mathcal{A}$ is reconstructed the less important components are removed. For MRSI data this de-noises the data as the lower singular values again represent the noise. The core tensor here will have the same size in each dimension, which is not optimal for MRSI data as often the spectral dimension will be much larger than the spatial or temporal dimensions. To overcome this a Tucker decomposition is used which allows a core tensor of any size to be constructed [89], this gives much more control over the level of de-noising that is applied. If the core tensor has a size $W \times X \times Y \times Z$, the matrices U will have corresponding size of mode of $\mathcal{A}$ by the size of the mode of S, for example U_2 will have the size $J \times X$. This whole method is called a Tucker-Tensor decomposition and it has been used previously to de-noise DMI data [75, 90]. This strategy has been implemented in this work using a MATLAB toolbox [91].

Chapter 3

Building RF Coils

RF coils have two functions: first to apply a B_1 field to tip the magnetisation, and second to receive a signal from precessing magnetisation due to Faraday's law of induction. The profile of the applied B_1 field depends on the design/shape of the coil, the sensitivity of the coil also depends on the electronic components used for tuning and matching. The frequency of the applied B_1 depends on the applied waveform. The key point in designing/building the RF coil is to maximise the B_1 per unit voltage by tuning the coil to resonate at the Larmor frequency and matching the coil's impedance to whatever it is connected to. This shows how important design and building of RF coils is. Lots of different companies exist from whom it is possible to buy RF coils. This can be expensive due to the experience and time that goes into coil building. Therefore it is useful when starting new research with a new nucleus of interest (such as ^{2}H) to be able to build home-made coils. The coils described in this chapter are interfaced using a T/R switch that is already built into our Philips Achieva 3T MRI scanner along with a Philips preamp interface.

3.1 Theory

3.1.1 Coil Electronics

The simplest way to build an RF coil is to shape a wire into a loop (inductor) and connect a capacitor in parallel. This forms what is known as an LCR circuit which is often used to create a resonance. The LCR circuit will have a natural resonance angular frequency (ω_0), therefore when the angular frequency of the applied voltage is the same as this natural frequency the circuit is considered on resonance ($\omega = \omega_0$). For a circuit to resonate reactance (X), needs to be minimised. X is the imaginary component of the impedance given as $Z = R + iX$, for components in series the total impedance is the sum of the individual components, for components in parallel the reciprocal of the total impedance is equal to the sum of the individual components which is shown mathematically here

$$\begin{aligned} Z_{\text{Series}} &= Z_1 + Z_2 + ... + Z_N \\ \frac{1}{Z_{\text{Parallel}}} &= \frac{1}{Z_1} + \frac{1}{Z_2} + ... + \frac{1}{Z_N} \end{aligned} \tag{3.1}$$

For N number of components. For an LCR circuit the impedance is composed of two components the inductive reactance (X_L) and the capacitive reactance (X_C). The total reactance for a series LCR is the sum of X_L and X_C, for a parallel LCR circuit the reciprocal of the total reactance is equal to the sum of the reciprocal of the individual components, in the same was the impedances were combined. The relationship between the reactances and the resonant frequency is shown here

$$\begin{aligned} X_L &= i\omega L \\ X_C &= -\frac{1}{i\omega C} \end{aligned} \tag{3.2}$$

The resonant condition of the LCR circuit is then well demonstrated by calculating the current flow, which is shown here as the ratio between the voltage and the impedance

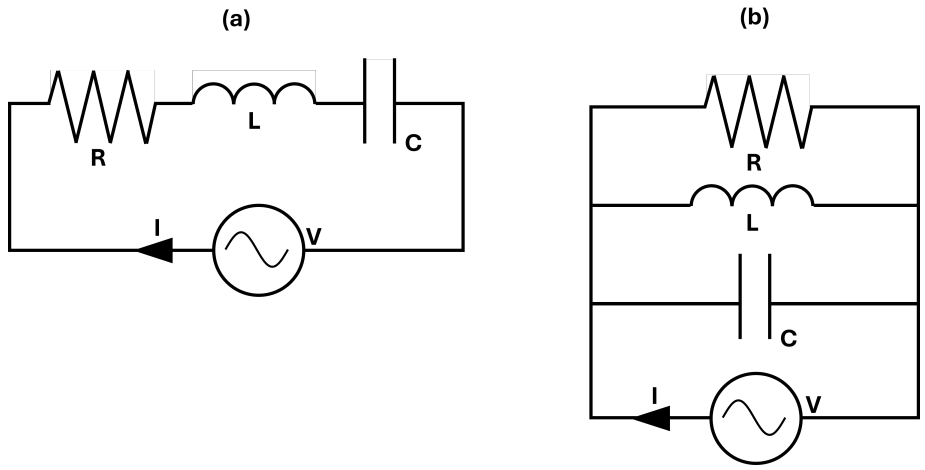

Figure 3.1: *Examples of an LCR circuit in series (a) and in parallel (b). The power source (V), current (I), resistor (R), inductor (L) and capacitor (C) are shown and labelled here.*

$$|I| = \left|\frac{V}{Z}\right| = \left|\frac{V}{R + i(\omega L - \frac{1}{\omega C})}\right| = \left|\frac{V}{\sqrt{R^2 + (\omega L - \frac{1}{\omega C})^2}}\right| \tag{3.3}$$

Examples of series and parallel LCR cirucits are shown in Fig. 3.1. The natural resonance of the circuit is shown here

$$\omega_0 = \frac{1}{\sqrt{LC}} \tag{3.4}$$

The voltage variations with time for each electrical component are shown here

$$\begin{aligned} \Delta V_R &= IR = I_{\max} R \sin(\omega t + \phi) \\ \Delta V_L &= \omega L I_{\max} \cos(\omega t + \phi) = X_L I_{\max} \cos(\omega t + \phi) \\ \Delta V_C &= -\frac{I_{\max}}{\omega C} \cos(\omega t + \phi) = -X_C \cos(\omega t + \phi) \end{aligned} \tag{3.5}$$

As an RF B_1 field is applied to the coil, current will be induced which charges the capacitor. As the B_1 is then reduced, the capacitor will then release stored energy which causes current to flow through the rest of the circuit. Energy is dissipated in the resistor and therefore the current de-

creases exponentially. Graphs of the change in voltage in this case are shown in Fig. 3.3, along with the corresponding absorption and dispersion curves. This behaviour is often referred to as a driven resonance.

If the time in which the driven resonance is applied is short the overall behaviour is the impulse response. The most common cables that are used to connect to RF coils are coaxial cables, which usually have a characteristic impedance of 50 Ω. The coaxial cable when cut open has an inside core and outer shielding both made by copper surrounded by insulating covering. The coils have two ends when constructed, one is attached to the core (indicated by small black oval in figures) and the other is connected to the shielding (wire that ends in white space of BNC in figures). When a coil is constructed and tuned to the Larmor frequency the impedance is most likely different to the impedance of the cable. The difference in impedance will cause some of the power to be reflected at the coil instead of transmitted. Therefore, the impedance of of the coil needs to be changed, which can be done by changing its reactance. The most common ways of doing this are by adding an inductor or a capacitor in parallel with the coil. The method of adding a capacitor will be discussed here and an example circuit can be seen in Fig. 3.1.

The capacitor in series with the coil is referred to as the matching capacitor (C_M) with the other capacitor called the tuning capacitor (C_T). The total capacitance is C_M+C_T. A relationship between C_M and C_T can be found that is related to the quality factor (Q) [92] which is the resonance frequency divided by the bandwidth of the coil resonance in Fig. 3.3, and is shown here

$$C_M = \sqrt{\frac{C_T}{Q\omega_0 Z}} \tag{3.6}$$

The combination of Eqs. 3.4 and 3.6 can be used to find the capacitances needed to tune and match the coil [92]. To test a fully constructed coil an Alternating Current (AC) is applied to the coil and the reflected power is plotted against frequency as a logarithmic scale measured in decibels

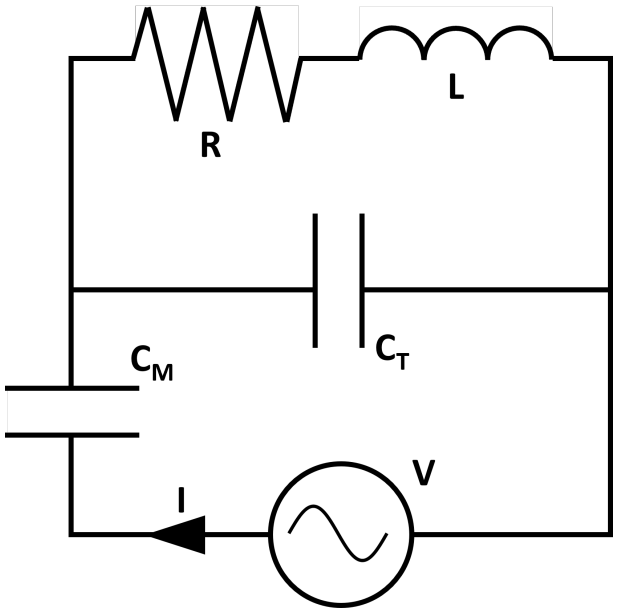

Figure 3.2: *Example diagram of an LCR circuit with both tuning (C_T) and matching capacitors (C_M), along with an AC signal generator.*

(dB), the graph will appear similar to the absorption spectra shown in Fig. 3.3. To perform this the coil is connected to a network analyser which is able to measure the scattering parameters (S), by passing an RF current through the coil and using receivers to measure the power reflected and transmitted in the coil. The sacattering parameters include the input port reflection S_{11}, the reverse gain S_{12}, the forward gain S_{21} and the output port reflection S_{22}. A $S_{11} = 1$ indicates an open circuit, $S_{11} = -1$ indicates a short circuit and $S_{11} = 0$ indicates a perfectly matched circuit. Typically $S_11 <$ -20 dB is considered acceptable for the value of reflected power, with the peak appearing at the Larmor frequency. Realistically soldering and adding components will change the circuit and the theoretical components can be wrong so will often need changing based on the measured response.

When a coil is placed over a sample or body tissue coupling occurs which changes the total impedance. This can change the matching condition as well as the resonant frequency of the coil. Therefore it is important to load the coil with a phantom that matches the loading response that will be present during scanning, when designing/building the coil.

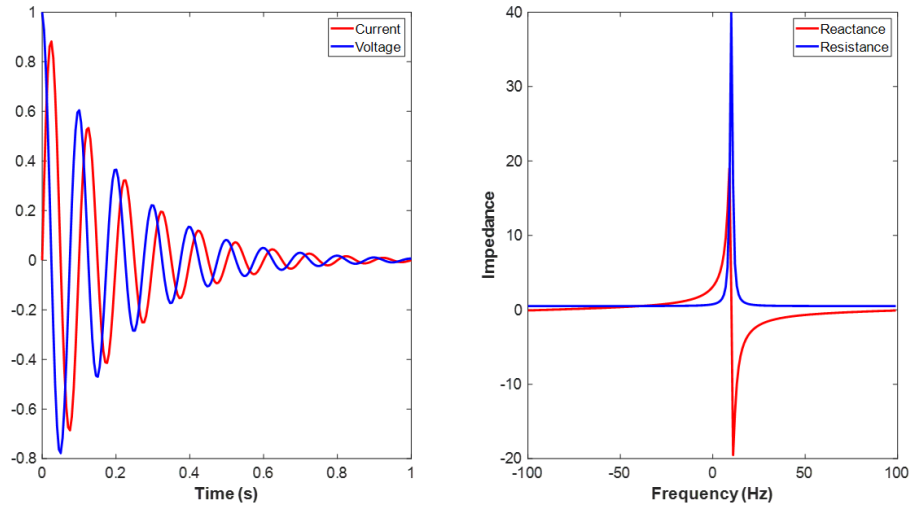

Figure 3.3: *(a) Current and Voltage graphs for a dissipating capacitor in an RLC circuit. (b) Impedance variation with frequency which demonstrate the resistive and reactive components.*

3.1.2 Transmit and Receive of B_1

As was shown in section 2.1.3 the transverse applied B_1 is made up of two circularly polarised components, known as the transmit field B_1^+ and the receive field B_1^-. The B_1^+ field rotates at the same angular frequency and in the same direction as the rotating reference frame, whilst B_1^- rotates at the same angular frequency but in the opposite direction. Mathematically, this is shown as

$$B_1(t) = B_1^+ \exp(-i\omega t) + B_1^- + \exp(i\omega t) \tag{3.7}$$

Where t is time. If the transmit and receive fields are in a singular axis, the fields are linearly polarised. In this case the B_1^+ and B_1^- equally share the power distribution of B_1, and since only the B_1^+ excites the nuclei spin states half the power is then wasted in the B_1^-. By introducing extra coils perpendicular to the original coils and driving the field 90° out of phase, it is possible to cancel out the counter-rotating B_1^-. Therefore, all of the B_1 power is deposited into the B_1^+ field. This is referred to as quadrature transmission, and the fields are circularly polarised. In this case a separate

coil channel is used for the receive element of the coil. All the coils built in this chapter are linearly polarised for simplicity. Minimising the B_1^- is not only important to ensure that as much of the available power is used to excite the spins, it is also an important aspect in the safety of RF coils. The B_1^- field is responsible for tissue heating which is explained in more detail in the following section.

3.1.3 Coil Safety

The varying magnetic field gives rise to electric fields inside the tissue being imaged outside of the coil. Due to the bodies conductivity these electric fields move ions and molecules inside the body which transfers thermal energy to the tissue, which causes the temperature of the tissue to rise. The power P absorbed by the tissue volume v is directly proportional to the electric field E and is given mathematically as

$$P = \frac{1}{2}\int_v \sigma |E|^2 dv \tag{3.8}$$

Where σ is the conductivity of the tissue. Modelling is important to ensure each coil built is safe to use with humans. The magnetic field can be modelled using the Biot-Savart law given as

$$\mathbf{B}(\mathbf{r}) = \frac{\mu_0}{4\pi}\int_v \frac{\mathbf{J}(\mathbf{r}) \times \mathbf{r}}{|\mathbf{r}|^3} dv \tag{3.9}$$

Where $\mathbf{J}$ is the current density, dV is the volume element from the coil and $\mathbf{r}$ is the position vector from dv. The electric field E can then be calculated from the A vector potential which is defined by the magnetic field B being the curl of the vector potential ($\mathbf{B} = \nabla \times \mathbf{A}$). $\mathbf{A}$ can therefore be analytically expressed as

$$\mathbf{A}(\mathbf{r}) = \frac{\mu_0}{4\pi}\int_v \frac{\mathbf{J}(\mathbf{r})}{\mathbf{r}} dv \tag{3.10}$$

E can then be found from A following

$$\mathbf{E} = -\frac{d\mathbf{A}}{dT} \tag{3.11}$$

During an MRI scan the RF power is monitored and the tissue heating is controlled by Specific Absorption Rate (SAR), which is defined as the time and volume averaged power absorbed inside the head or body. It is mathematically defined as

$$SAR = \frac{\sigma|E|^2}{2\rho} \tag{3.12}$$

Where ρ is the density of the tissue. The SAR, which is measured in W/kg, was modelled for all the coils built in this thesis. Based on these models the B_1 was adapted to ensure the coil was safe to use, by making sure the SAR values fall within safe guidelines. The International Electrotechnical Commission (IEC) and the US Food and Drug Administration (FDA) developed the first international safety requirements for MR equipment, which includes SAR limits. For local transmit coils this is 20 W/kg and for volume transmit coils it is $[10 - 8 \times r]$ where r is the ratio of the exposed body weight to the total body weight.

3.2 Coils Built

Three different coil types were constructed for use in the experiments reported here and implemented for use on a Philips 3T Achieva system. These were two surface coils, a saddle coil and a Helmholtz coil. All coils were tuned to 19.6 MHz, the Larmor frequency of ^{2}H at 3T. A 2 litre salt-water solution was used to load each coil, since each coil was used for scanning on different body parts the loading response changed slightly which was controlled by changing the salt concentration. A birdcage coil dual tuned to the Larmor frequencies of ^{1}H and ^{2}H at 7T was purchased from Rapid Biomedical for use on a 7T Philips Achieva System. The in-house built coils were used to acquire spectroscopic ^{2}H data with anatomical ^{1}H images being acquired using the whole-body RF coil in the scanner for transmission

and reception. The purchased coil is able to acquire ^{1}H anatomical images as well as ^{2}H spectroscopic data, low resolution ^{2}H images were also acquired using this coil.

After the building of each coil, the coil is placed around a phantom and spectra are acquired with a range of flip-angles (α). The spectrum with the largest SNR should correspond to 90°, if it does not it means the coil is not calibrated correctly. This is common with a new coil. This can be corrected by changing the B_1 reference scaling factor until the spectra with the largest peak is at 90°. Now when the scanner intends to send a RF pulse with a specific flip angle it will be correct. This can also be be performed at the beginning of every scan session to check the calibration, but this is not necessary. A single bulk spectra should be acquired at the beginning of every scan session, and the SNR and linewidth should be noted. Changes in these could be indicators that the RF calibration is not working or the coil is broken in some way. Doing this is called Quality Assurance (QA) of the coil, and is very important when using in-house built coils and can be overlooked too often. This form of quality assurance was performed at the beginning of every scan session reported in this Thesis.

3.2.1 Surface Coil

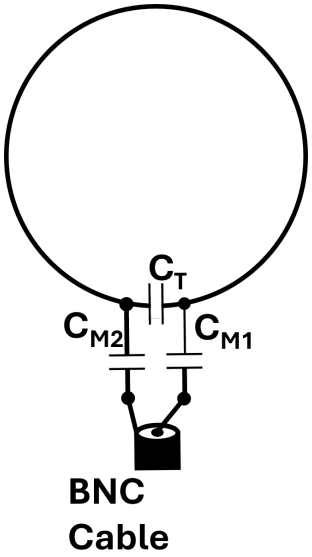

Figure 3.4: *Diagram of a typical planar surface coil with circuit elements attached, the coaxial cable attaches to a BNC connector. C_T is the tuning capacitor and C_{M2} and C_{M1} are the matching capacitors.*

A surface coil is the simplest and most basic coil to design, where the coil often forms a simple circular loop. The magnetic field is largest on axis and decreases, with distance from the coil. Therefore the field is spatially inhomogeneous which is why this coil design is often used for non-localised spectroscopy, where the localisation of the signal is down to the placement of the coil. The penetration depth of the magnetic field for a surface coil is approximately equal to the diameter of the coil [93], and therefore a surface coil is sensitive to regions closest to the coil.

The surface coils used for data collection were built for use in the study described in Chapter 6. The first coil is a small 5 cm coil with two loops of copper wire with a tuning capacitance of 173.4 pF and a matching capacitance of 11 pF which is split over both wires of the loop to keep it balanced. The coil is made small to maximise the sensitivity to signal from subcutaneous fat in the calf. Maps for the $B_y, B_\rho, |E|$ and SAR maps for this coil are shown in Fig. 3.5, the maximum SAR of this coil was <20

W/kg. This was calculated assuming the target B_1 of 40 μT occurs 4 cm from coil on coil axis, and the conductivity (σ) of the muscle is 0.64 S/m.

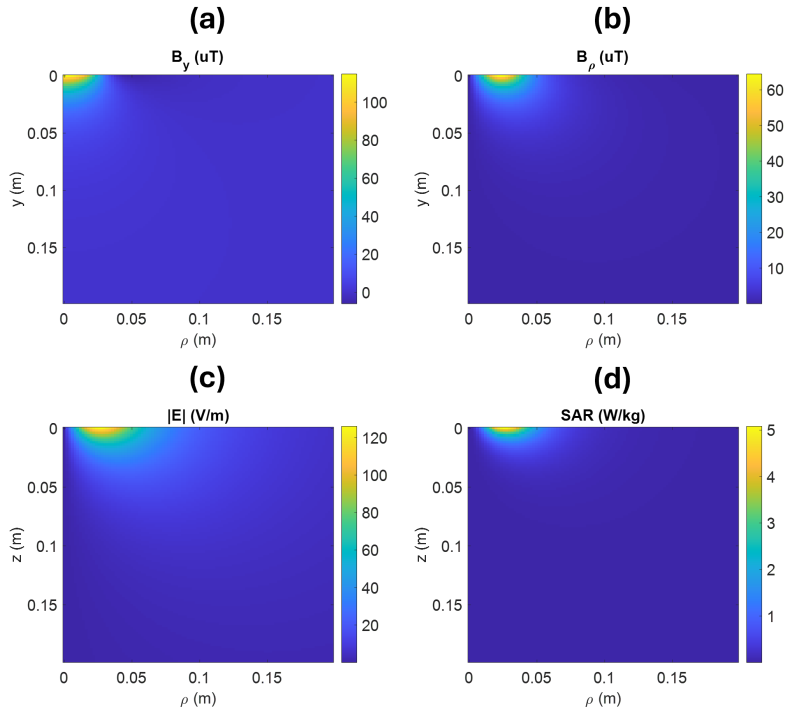

Figure 3.5: *(a) Map of B_y measured in μT, (b) map of B_ρ measured in μT, $|E|$ measured in (V/m) and (d) map of SAR measured in (W/kg). All maps show the spatial dependence up to 20 cm away from the calf coil in the z and ρ direction. Figure by Prof. Richard Bowtell.*

The second coil is 12 cm in diameter and again made out of copper wire, and is designed for imaging the liver. This coil is larger so that the penetration depth is large enough to reach the liver. The coil is slightly curved in plane in order for the coil to sit closer to the liver on one side of the abdomen and is mounted onto a holder so that the coil can be rotated whilst still being attached to the scanner bed. Maps for the $B_y, B_\rho, |E|$ and SAR maps for this coil are shown in Fig. 3.8, the maximum SAR of this coil was <20 W/kg. This was calculated assuming the target B_1 of 40 μT occurs 4 cm from coil on coil axis, and the conductivity (σ) of the muscle is 0.64 S/m. These simulations were performed by Prof. Richard Bowtell.

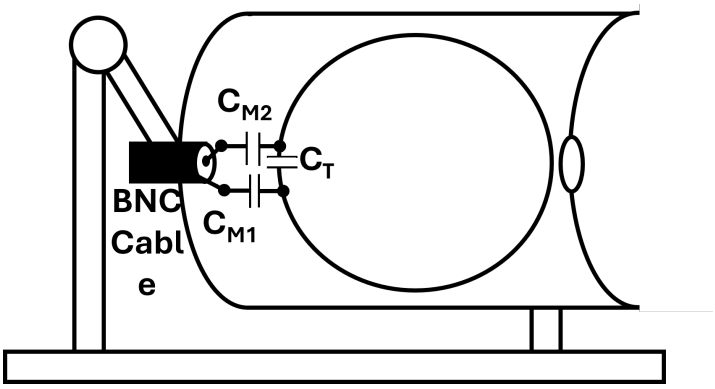

Figure 3.6: *Diagram of the circular surface C_T is the tuning capacitor and C_{M2} and C_{M1} are the matching capacitors which are attached to a BNC cable which continues of the diagram. The bottom bar of the diagram is housing which slides into the MRI bed, then the two spokes then hold the coil in plastic housing. The circular joint in the top-left of the image allows movement so the coil can be comfortable and close to the participant.*

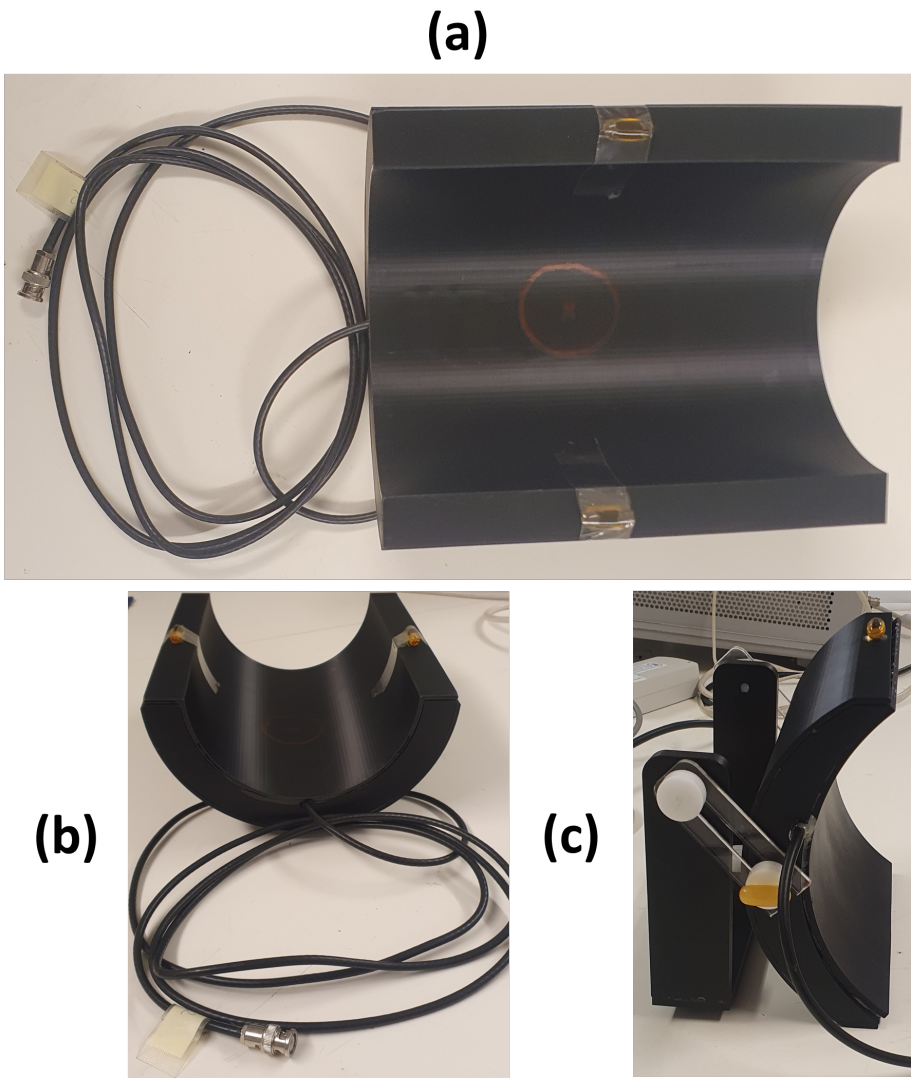

Figure 3.7: *Photos of the calf surface coil from two different angles (a & b) with a photo of the liver surface coil (c), both tuned to the ^2H Larmor frequency at 3T. The yellow tablets that can be seen in all the photos are vitamin tablets (also known as fiducial markers) used to identify where the coil is in an image.*

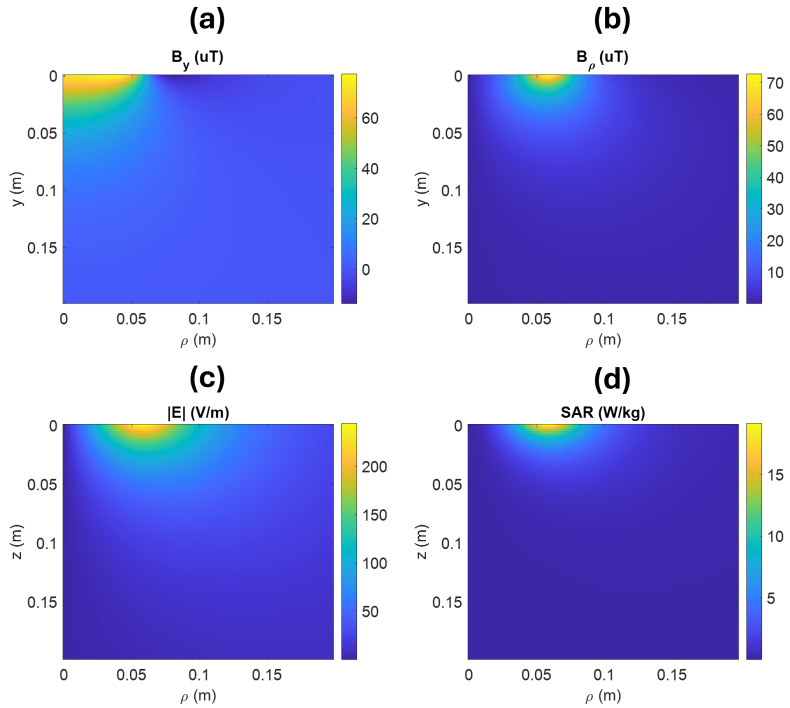

Figure 3.8: *(a) Map of B_y measured in μT, (b) map of B_ρ measured in μT, $|E|$ measured in (V/m) and (d) map of SAR measured in (W/kg). All maps show the spatial dependence up to 20 cm away from the liver coil in the z and ρ direction. Figure by Prof. Richard Bowtell.*

3.2.2 Saddle

Volumetric coils such as saddle coils have more homogeneous B_1 fields than surface coils and are able to cover a larger volume. A saddle coil derives its name from the fact that the coil elements it uses have a similar appearance to a horse's saddle. Two square loops surround a circular tube with an angular separation of 120° of the wires in each saddle. The saddle coil has optimum geometry that has been previously been found which includes the length/diameter between 1 and 2, and an angular width for each coil of ∼120° [94, 95].

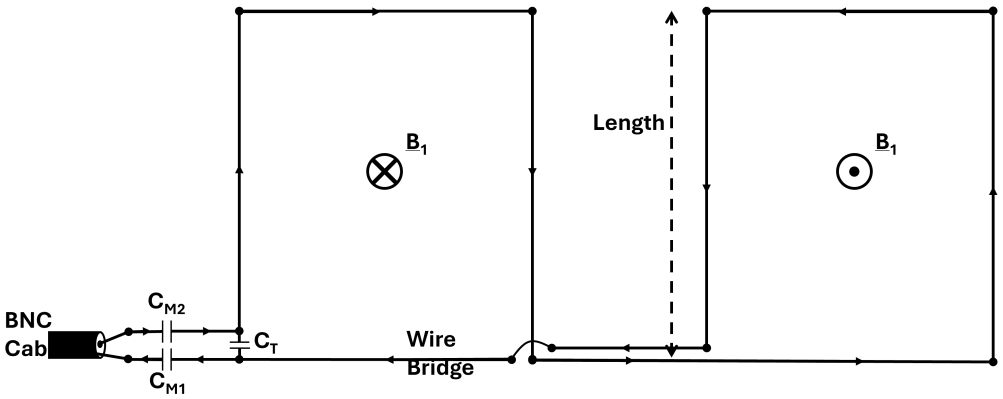

Figure 3.9: *2D circuit diagram of the saddle coil used for scanning of the calf.*

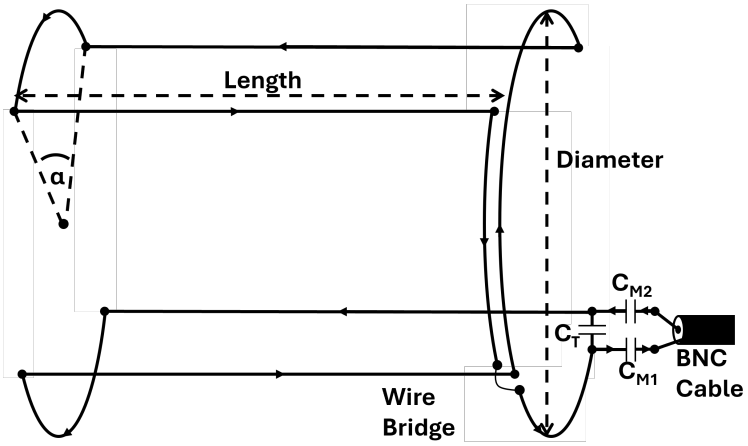

Figure 3.10: *3D circuit diagram of the saddle coil used for scanning of the calf.*

The coil built for scanning in Chapter 7 is made from copper tape and has an angular width of 120° a length of 16.8 cm and a diameter of 14.8 cm. Where the copper tape that links the two squares intersects/crosses over, an insulated wire is used to avoid a capacitor being created. Also, the wires here run close side by side so that the fields from the opposing currents will cancel. Diagrams of the circuit for the coil are shown in Figs. 3.9 and 3.10 with pictures in Fig. 3.11. The tuning capacitance is 47.3 pF, the total matching capacitance 8.8 pF. Simulations of the Biot-Savart equation were used to simulate the B_x and B_y components through

the saddle coil. Plots of the B_x and B_y at four different planes along z are shown in Fig. 3.12, these were calculated by Prof. Richard Bowtell. The vector potential A and therefore E were also simulated to calculate SAR values across the same axis, plots across four different planes along z are then shown in Fig. 3.13, which were calculated by the author. The maximum SAR value was found to be safe < 9 W/kg. These simulations were calculated assuming the target B_1 of 40 μT occurs at the centre of the coil axis, and the conductivity (σ) of the muscle is 0.64 S/m. This is a different limit for the surface coils because this is a volume coil, assuming the weight of the calf takes up 5% of the total body weight the limit here is 10 W/kg.

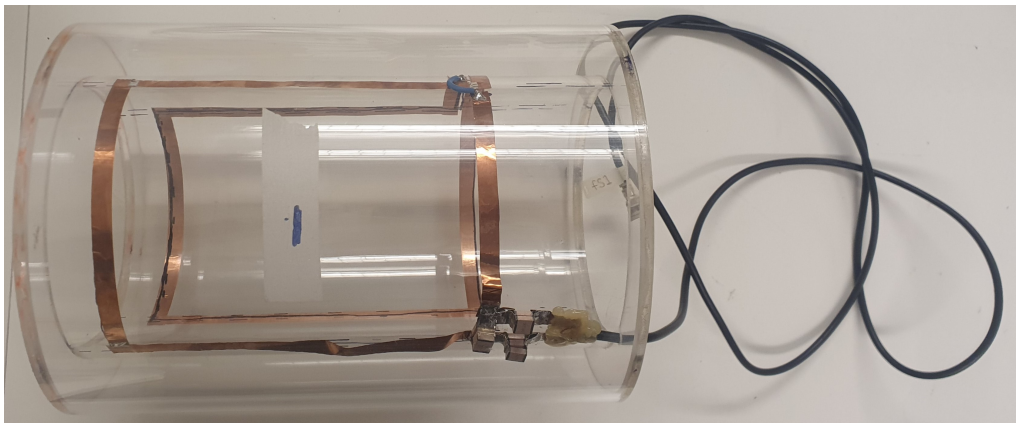

Figure 3.11: *Photo of the saddle coil used to obtain ^2H data from the calf.*

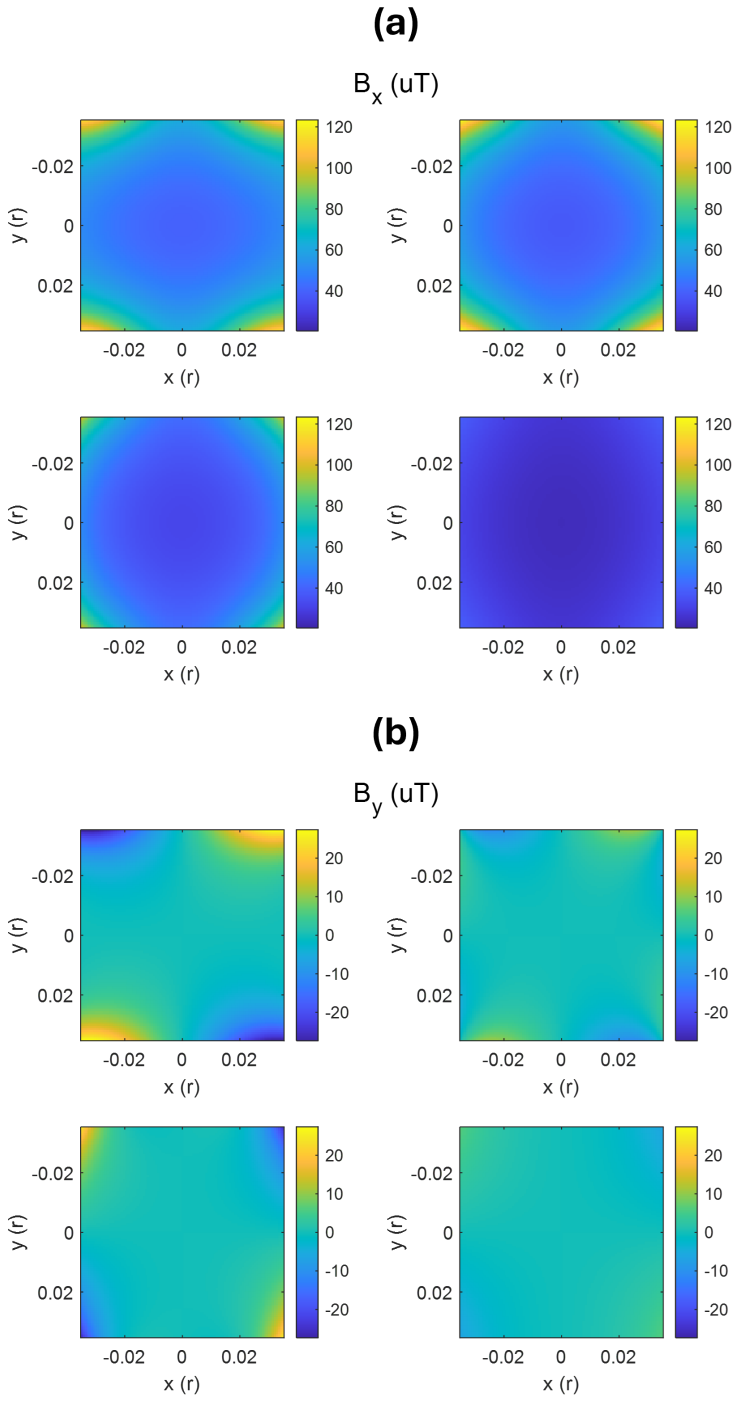

Figure 3.12: *Maps of the B_x (a) and B_y (b) components inside the saddle coil plotted against x and y in units of radius. The planes are of the z direction at the centre of the coil (top left), 2/3 of the length of the coil (top right), 4/5 of the length of the coil (bottom left) and 19/20 down the length of the coil.*

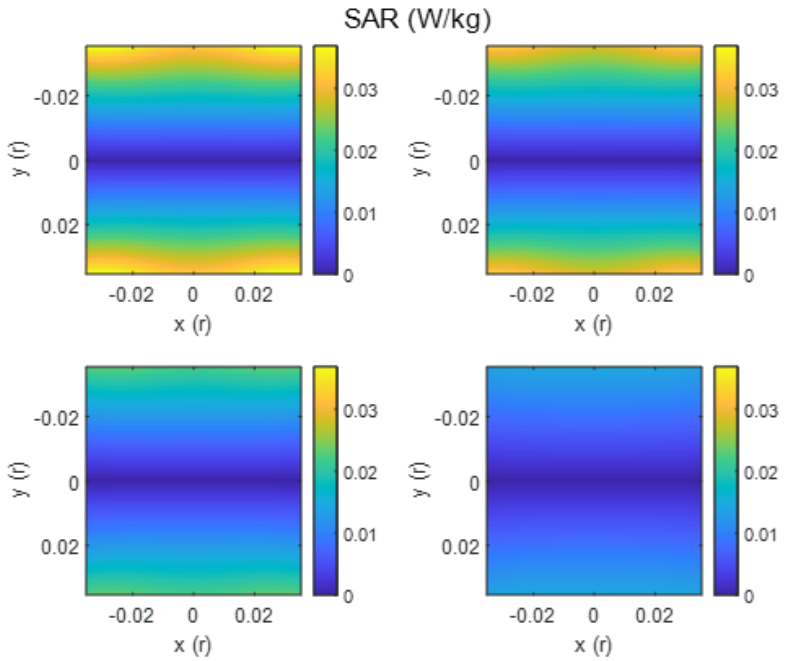

Figure 3.13: *Maps of the SAR magnitude measured in W/kg inside the saddle coil plotted against x and y in units of the coil radius. Top left is at the centre of the coil, top right is 2/3 down the length of the coil, bottom left 4/5 down the length of the coil and bottom right 19/20 down the length of the coil all in the z direction.*

3.2.3 Helmholtz coil

A Helmholtz coil is similar to to a surface coil in its circuitry. Except a second surface coil is connected to it by two crossing insulated wires, where the current in each flows in opposite directions so that the field flows in the centre of the setup. This creates a homogeneous B_1 in between the coils. The Helmholtz coil arrangement was chosen for the scanning the forearm described in Chapter 7 and needs to be easily movable and a saddle coil would roll/move to much and would be difficult to rotate in the magnet bore.

The coil setup comprises involves two octagonal loops that are ∼14 cm in diameter separated by a 12 cm gap with a tube in the centre to keep the arm still in the same position, away from the circuit elements. The tuning

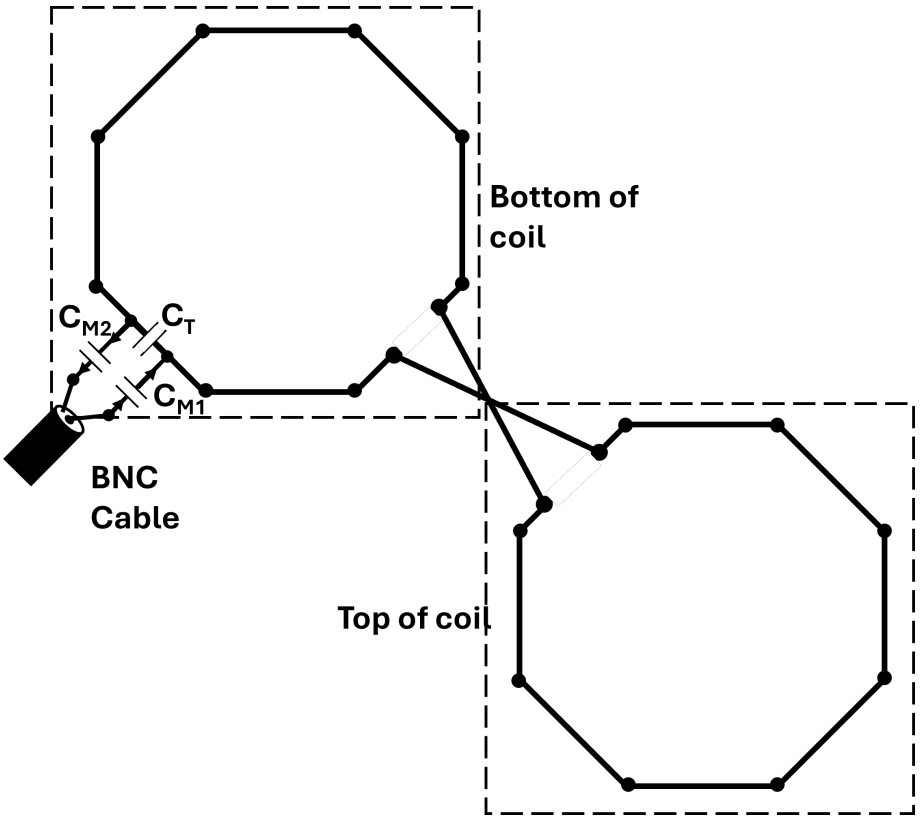

Figure 3.14: *2D circuit diagram of the Helmholtz coil used for scanning of the arm.*

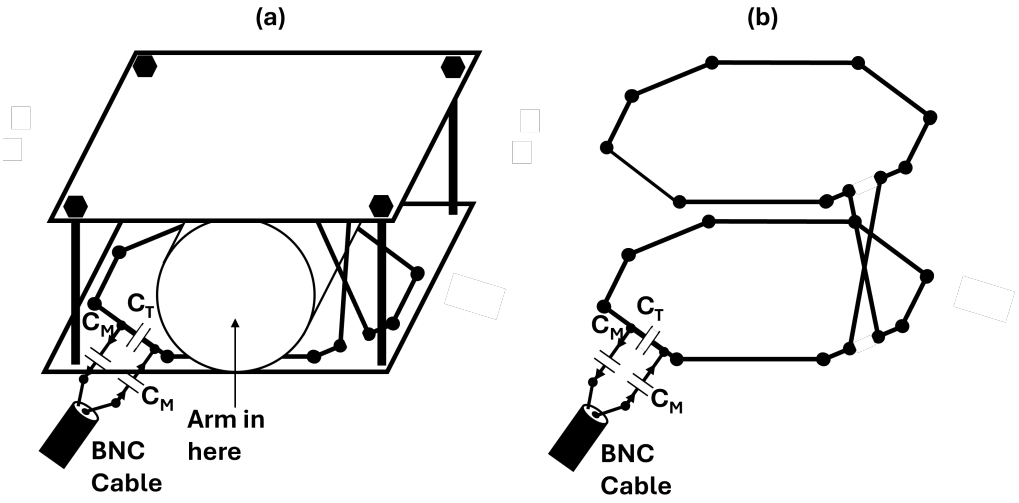

Figure 3.15: *3D circuit diagram of the Helmholtz coil used for scanning of the arm with housing (a) and without (b).*

Figure 3.16: *Photo of the HelmHoltz coil used to obtain* ^2H *data from the arm.*

capacitance is 73.3 pF and the total matching capacitance is 8.8 pF.

Chapter 4

Scanning post Heavy Water Loading

4.1 Introduction

4.1.1 Heavy Water Uses

When most people think of D_2O they usually think of the the production of nuclear energy and atomic weaponry. However, a very important use of heavy water now is as an isotopic tracer in studies of biochemical processes, such as the assessment of body composition [96] and it is now also often being used to study triglyceride [97] and lipid turnover [98]. Studies of lipogenesis in the liver are performed to investigate characteristics of liver disease [99]. This often involves giving study participants heavy water for a long period of time and then taking blood or tissue samples and analysing them *in vitro* using mass spectrometry [100, 101]. The need for invasive sampling leads to limits on how many measurements can be taken and from where they can be taken, in order to avoid patient discomfort. Deuterium magnetic resonance could potentially offer a way to characterise and investigate liver disease non-invasively.

After drinking D_2O, rapid exchange occurs between exchangeable hydrogen atoms and deuterium atoms. This produces an increase in the

concentration of HDO from that present at natural abundance (NA). This consequently produces an increase in the strength of the NMR from ^{2}H in water. Covalently bonded hydrogens that exist in the methylene group (-CH_2) of fatty acids, can also potentially be replaced by deuterium atoms derived from heavy water, which causes the naturally abundant deuterated fat (CHD) signal to increase. More details on how ^{2}H is incorporated into lipids and this increase in CHD signal can be found in Chapter 6. Therefore by using CSI over the liver whilst a participant/patient is loaded with heavy water and then tracking the change in concentration of fat/lipid signals over time, lipogenesis could in theory be studied. This approach could be useful in also studying general fat turnover not only in the liver but also in adipose and visceral fat as well. This sort of measurement was previously implemented in healthy and diabetic mice in the 1980's [25, 102].

4.1.2 Relaxation Times

DMI has been shown to be able to provide spatially resolved measurements of metabolite concentrations [5, 75]. This makes DMI of clinical importance, as the metabolite concentrations could potentially be used as bio-markers to assess metabolic disease or tumour aggressiveness, on a patient-to-patient basis. It is straightforward to compare the strengths of different metabolite signals, but to work out absolute concentrations you need a reference and also need to account for the effects of relaxation on the signal strengths.

In DMI this is performed by comparing the naturally abundant MR signal of HDO to the MR signal of other metabolites, along with an attenuation factor which is based on the sequence used for signal acquisition along with the number of deuterium labels in the metabolite. An estimate of the concentration of HDO at NA ($\sim$0.015%) in the brain is 12.6 mM. This is calculated by multiplying the number of moles in one litre of D_2O (55.4 Mol) by the water fraction of the brain $\sim$73% along with the NA of ^{2}H, remembering to take into account the two ^{2}H labels.

The attenuation factor specifically depends on the TR, flip angle (α) and the T_1 of the metabolite in question. Consequently it is of great importance to have an understanding of how T_1 changes in different tissues. Proton relaxation times have previously been reported in the literature at multiple field strengths for different tissues in the brain [103], and can be used for proton metabolite quantification. Previous measurements of HDO relaxation times in human participants used non-localised data [6, 36, 104] which means the variation of relaxation times across specific tissue compartments is not known, making tissue-specific metabolic concentration calculations difficult.

4.1.3 Aims

^{2}H MRI at 7T was used to characterise the HDO signals from the human brain in four healthy participants who increased their deuterated water content to ∼1.5% over a six-week period by drinking D_2O. The heavy water loading was carried out as part of a parallel study into immune cell proteomics. ^{2}H MRI and MRS measurements were made on all four participants. This included MEGE images acquired at a range of TR values, from which T_1 and T_2^* relaxation maps were calculated. Co-registration to higher resolution ^{1}H images allowed T_1 and T_2^* relaxation times of deuterium in HDO in CSF, GM, and WM to be reported. For two of the participants, ^{2}H MRI/MRS data was also acquired during the initial ∼eight-hour loading period to track the time-course of ^{2}H enrichment within the brain [105]. The work described in this chapter formed the basis of the peer-reviewed paper 'Deuterium brain imaging at 7T during D_2O dosing' published in the journal 'Magnetic Resonance in Medicine' [105].

4.2 Methodology

Six healthy participants in total took part in this ^{2}H-imaging sub-study which was approved by the local institutional ethics committee and the

volunteers gave informed consent. Two of the participants were scanned during a set-up phase in which we established the feasibility of ^{2}H imaging and identified favourable imaging parameters. Here, I report data from four participants (A - D) who were subsequently scanned using the optimised imaging protocols. All scanning was performed on a 7T Philips Achieva scanner (Philips Healthcare, Amsterdam, The Netherlands), operating at 45.8 MHz for ^{2}H and 298 MHz for ^{1}H. A 26.4 cm inner diameter, dual-tuned ^{1}H/^{2}H birdcage coil (Rapid Biomedical) was used for deuterium measurements, while the standard 32-channel Rx/2-channel Tx head coil (Nova Medical) was used for acquiring anatomical ^{1}H images.

The proteomics study required an initial loading regime in which the targeted enrichment was built up in around 8 hours. This was achieved by participants drinking between 12 and 16, ∼50 ml doses of 70% D_2O/30% H_2O every ∼30 minutes, with the total amount of D_2O consumed adjusted according to the participant's body weight, so that an enrichment of around 1.5% was produced. The participants subsequently drank ∼50 ml of D_2O each morning over the six-week study period to maintain a ∼1.5% enrichment. Similar enrichment levels and durations have been used in recent studies [106–108] with no adverse events reported. However some participants experienced a brief period of dizziness during the initial loading phase due to the rapid rise in body water enrichment [106].

4.2.1 Initial Loading

Two of the participants (A and B) were scanned during the initial 8-hour loading period to monitor the time-course of changes in the concentration of ^{2}H in the brain. A scanning protocol of ∼15 minutes' duration was performed before dosing and then again after 30, 90, 150, 210, 270, 360, 420 and 540 minutes. The protocol comprised, a ^{1}H scout scan for planning, followed by acquisition of ^{2}H pulse-acquire spectra from the whole head and then from a 2-cm-thick axial slice positioned over the lateral ventricles. Both used the following scan parameters: $\alpha = 90°$, 2048 samples,

BandWidth (BW) = 3000 Hz, repetition time TR = 1 s and 64 averages (acquisition time T_{scan} = 64 s). We then acquired axial, MEGE ^{2}H images (20 averages, T_{scan} = 453s, FOV = 288 × 288 × 80 mm^3, 6 × 6 × 10 mm^3 voxels, $\alpha = 33°$, TR = 62 ms, five echoes, TE = 8.9 ms and ΔTE = 8.4 ms. Axial ^{1}H GE images (T_{scan} = 232 s, 32 slices, FOV = 288 × 288 × 80 mm^3, 3 × 3 × 2.5 mm^3 voxels, TE = 5.9 ms, TR = 39 ms) were also acquired. The scanning protocol was repeated 17 days after the initial loading to obtain comparative data at steady-state enrichment.

The spectroscopy measurements made before loading provided an estimate of the signal from naturally abundant deuterium in water: scaling subsequent measurements then allowed the absolute HDO concentration to be estimated at each time-point. The HDO concentration in the body was also estimated from the ratio of the total imbibed D_2O volume to an estimate of total body water using the participant's height, weight, age and gender [1]. The temporal variation of HDO concentration in the brain was monitored by plotting the amplitude of the single peak in each non-selective and selective spectrum against the time since the first heavy water dose. The peak amplitude was obtained by fitting the complex data to a Lorentzian line shape in the frequency domain using non-linear least squares fitting.

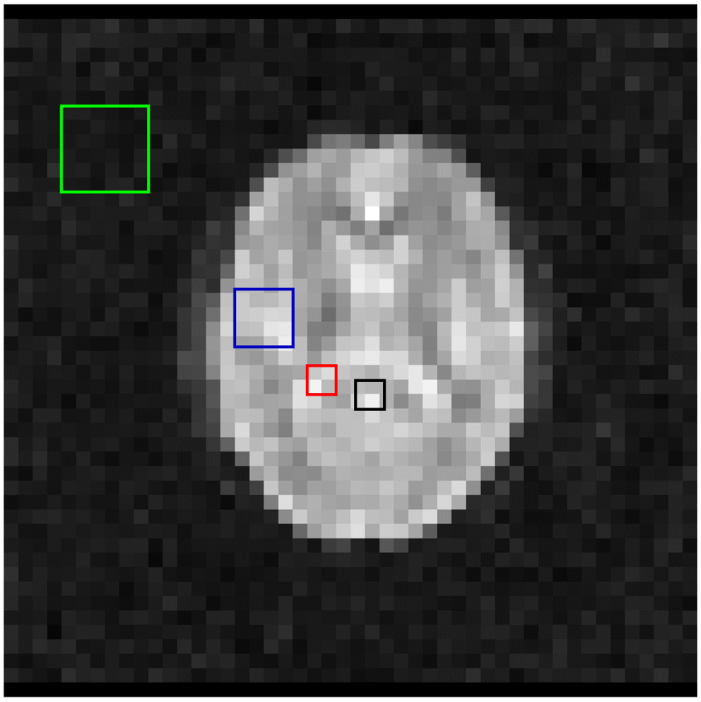

Figure 4.1: *Regions of interest used for following the time-course of signal change during D_2O loading. Black = Superior Cistern (SC); Red = lateral ventricle; Blue = brain (GM, WM and CSF); Green = background noise.*

We used the image data to track the changes in ^{2}H signal from different tissue compartments. The ^{2}H images acquired at each time-point were summed over the five echoes to form a single image data set. Then using both the ^{2}H and ^{1}H images, regions of interest (ROI) were formed for a background region, general brain tissue, the lateral ventricles and for a region of high signal intensity thought to arise from blood vessels and CSF in the superior cistern (SC). Examples of the Region Of Interest (ROI)s used are shown in Fig. 4.1. The signal intensity in each region was plotted against time from the first heavy water dose. The SNR in images acquired before loading was too low to make good estimates of NA signal strength, so values were normalized to the signal measured in the superior cistern ROI at the last time point of the initial loading period. All analysis was performed using MATLAB (Release 2020b, The MathWorks, Inc., Natick, MA, United States). Saliva samples were obtained and measured by gas

chromatography–mass spectrometry (GCMS) from Participant A and B, as part of the parent project.

4.2.2 Relaxation Time Measurements

^{2}H relaxation times for water in CSF, GM, and WM were calculated from data acquired during the six-week loading period using the dual-tuned ^{2}H/^{1}H coils. In each imaging session, ^{2}H 3D sagittal MEGE images were acquired (voxels = 6 × 6 × 10 mm^3, FOV = 288 × 288 × 240 mm^3, slices = 24) at a range of TR values, along with ^{1}H 3D MEGE images (voxels = 3 × 3 × 5 mm^3, FOV = 288 × 288 × 240 mm^3, slices = 48, 15 TEs with TE_1 = 2.5 ms, ΔTE = 2.34 ms, and TR = 41 ms).

^{2}H MEGE data from Participants A and B were acquired with five echoes (TE_1 = 4.3 ms, ΔTE = 8.4 ms), $\alpha = 60°$ and TR = 68, 136, 272 and 544 ms, with 8, 4, 2 and 1 averages so that T_{scan} = 487 s for each image. ^{2}H MEGE data from participants C and D was acquired with six echoes (TE = 4.3 ms; ΔTE = 8.4 ms) and one additional TR value (TR = 816 ms; T_{scan} = 730 s; 1 average). The number of TE and TR values were increased for participants C and D to improve fitting quality. The ^{2}H scanning sessions were performed twice on Participants C and D.

In a separate scanning session using the Nova coil, ^{1}H Magnetization Prepared - RApid Gradient Echo (MPRAGE) images (0.7 mm resolution) and ^{1}H 3D MEGE images (3 × 3 × 5 mm^3 voxels, 15 echo times, TE_1 = 2.5 ms, ΔTE = 2.57 ms, and TR = 41 ms) were acquired from each participant. These images were used for image segmentation and estimation of the ^{1}H T_2^* values.

For calculation of ^{2}H relaxation time maps, we first estimated the variation of flip angle (α) over the image volume by summing the images across TEs, at each TR, and then fitting the resulting image data voxel-wise to a saturation recovery curve (i.e., fitting signal variation with TR for α, R_1, and signal amplitude). The resulting flip-angle maps were smoothed by averaging over 5 × 5 × 5 voxel neighbourhood and the α-values used as

(a) Flip-Angle Fitting

	Amplitude	α (rad)	R_1 (Hz)
Lower Bound	0	0	0.5
Upper Bound	Inf	π	Inf
Initial Guess	A_{smooth}	0	0

(b) Main Fitting Routine

	Amplitude	R_1 (Hz)	R_2^* (Hz)
Lower Bound	0	0.5	2.5
Upper Bound	Inf	Inf	Inf
Initial Guess	Average	π/2	0

Table 4.1: *Parameters and constraints used in the Matlab fmincon fitting routines, (a) shows the parameters used to obtain the initial flip-angle (α) map and (b) shows the parameters used in the main fitting routine to obtain relaxation rates. Average indicates the average of the masked brain image, and A_{smooth} indicates the amplitude value from the smoothed map that was created after the flip-angle fitting.*

a fixed variable in dual-fitting the variation in signal intensity $S_{i,j}$ across TR_i and TE_j values. The absolute difference between the model and the obtained data was found and minimised, the mathematical form of this expression is given here

$$r = \sum_{i=1}^{n_{\mathrm{TR}}} \sum_{j=1}^{n_{\mathrm{TE}}} \left| \frac{A \sin\alpha(1-\exp(-R_1\mathrm{TR}_i)}{1-\cos\alpha\exp(-R_1\mathrm{TR}_i)} * \exp(-R_2^*\mathrm{TE}_j) - S_{i,j} \right|^2 \qquad (4.1)$$

r is the calculated value that is to be minimised. The Matlab fmincon command was used to perform the minimisation, ^{1}H R_2^* maps were obtained by similar fitting to the exponential signal decay with TE in the ^{1}H MEGE data acquired using the Nova coil. The parameters and constraints used in the fmincon fitting are given in Table 4.1.

To evaluate the relaxation times in different compartments, we seg-

mented the ^{1}H MPRAGE data using FSL FAST [109] and transformed the resulting GM, WM and CSF masks to the space of the ^{2}H relaxation time maps. Following brain extraction using FSL BET [110] and bias field correction, an affine matrix was obtained from image co-registration using FSL FLIRT [111, 112] which transformed the ^{1}H MEGE data acquired using the dual-tuned coil to the ^{1}H MEGE Nova Medical coil data, along with an affine matrix for the ^{1}H MEGE to MPRAGE transformation. Image co-registration was linear, with six degrees of freedom and used the correlation ratio cost function [113]. The MEGE data were summed across echoes and repetition times before co-registration.

The brain-extracted MPRAGE image was segmented to create binary masks for GM, WM and CSF using FSL FAST [109]. These masks were then transformed to the ^{2}H space using the previously obtained affine matrices and the outer regions of the CSF mask were manually removed so that the majority of the CSF mask come from the lateral ventricles. The new masks were binarized at a value of 0.6 for each tissue to ensure that each mask contained at least 25 voxels for averaging. The binarized masks were applied to the relaxation maps for calculation of mean relaxation times for CSF, GM and WM.

4.3 Results

4.3.1 Loading

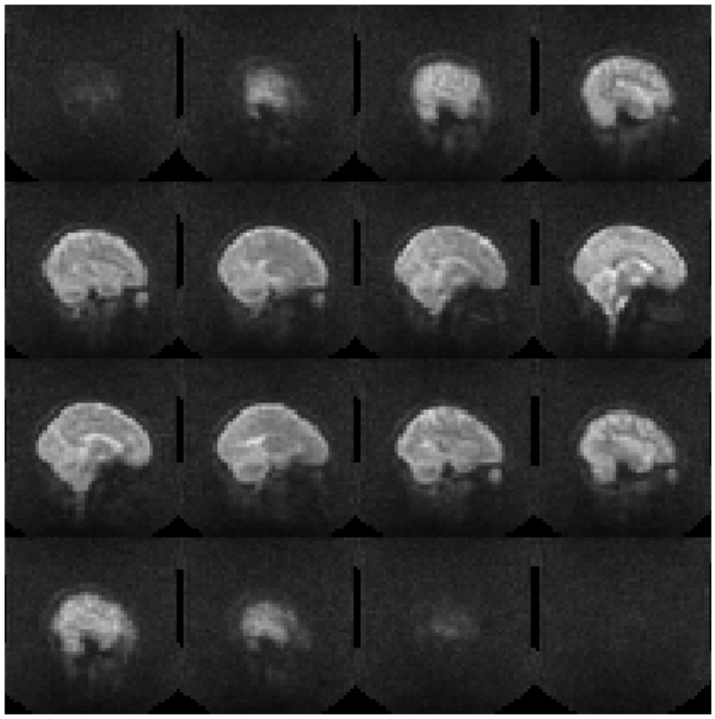

Figure 4.2: *3D MEGE ^2H image data from Participant C. Images produced by summing over six TE values and five TR values. Voxel size = 6 × 6 × 10 mm^3, in-plane FOV = 288 × 288 mm^2, T_{scan} = 485 s for each TR value.*

Figure 4.2 shows example ^{2}H 3D sagittal images obtained by summing the ^{2}H MEGE data for a single (fully loaded) subject over TE and TR values, during the steady-state loading period. The resulting images, which predominantly show T_2^* contrast, clearly depict the brain anatomy and have a similar appearance to T_2^*-weighted, ^{1}H images. The CSF in the ventricles and at the cortical surface appears hyperintense, while regions of white matter where there is little partial-voluming with CSF, such as in the corpus callosum, appear hypointense. Figure 4.3 shows the variation of image intensity with TE and TR in a central sagittal slice. The slower T_2^* decay of the CSF signal compared with that of the GM and WM signals is

evident, along with the signal saturation at reduced TR, and the reduction of contrast at low TE and TR values. In Fig. 4.4, example ^{2}H images acquired from participants A and B at different dosage times during the initial loading process are shown. As dosage increases, so does the overall SNR. The ROIs that were used to analyse the loading in different brain tissues are outlined in Fig. 4.1 (for participant A). Since the background MEGE image is obtained after the final dose for Subject A the tissues being segmented are easily discerned in the ^{2}H images. However, for the lower dosage images this is not the case, which is why the ROI's are defined on the anatomical ^{1}H image.

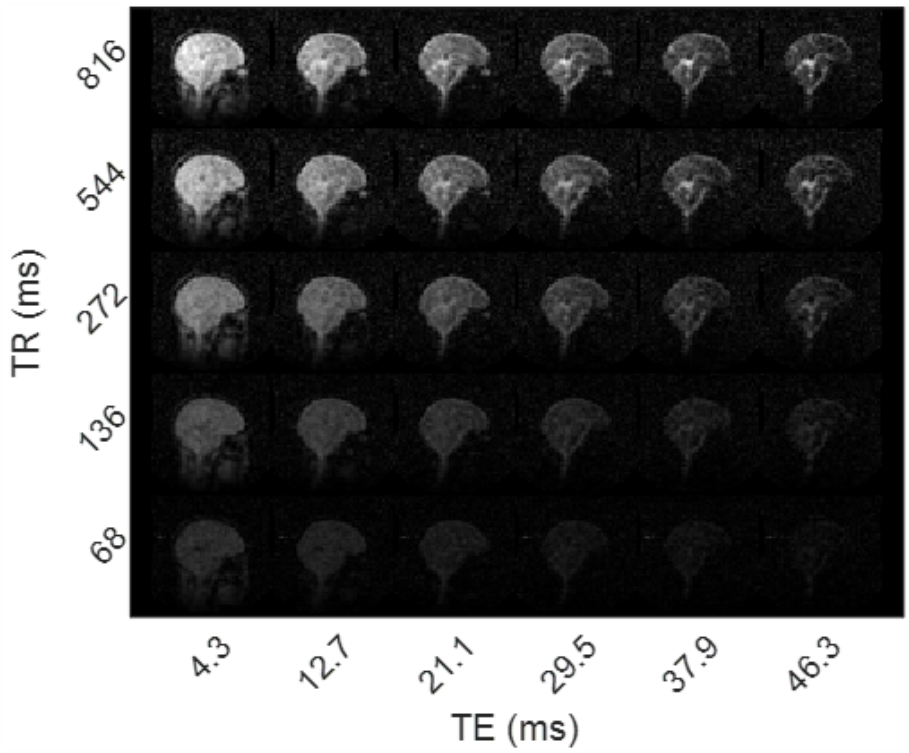

Figure 4.3: *3D MEGE ^{2}H image from one slice from Participant D. Images are displayed with TE value varying horizontally and TR-value varying vertically. Voxel size = 6 × 6 × 10 mm^3, in-plane FOV = 288 × 288 mm^2, T_{scan} = 485 s for each TR value.*

The qualitative increase in signal during the loading period in Fig. 4.4 is shown more quantitatively in Fig. 4.5, which plots the ^{2}H concentration

time course obtained from the spectroscopy data, along with the steady-state values measured after 17 days of loading. The average signal from each ROI during loading is shown in Fig. 4.6 scaled to the signal measured in the SC at the last time point, in the brain along with the steady-state values measured after 17 days of loading. Plotted values from Figs. 4.5 and 4.6 also show the ^{2}H concentration estimated from the cumulative D_2O dose and estimated total body water volume, for comparison. The results from GCMS analysis of saliva samples are also plotted here for comparison.

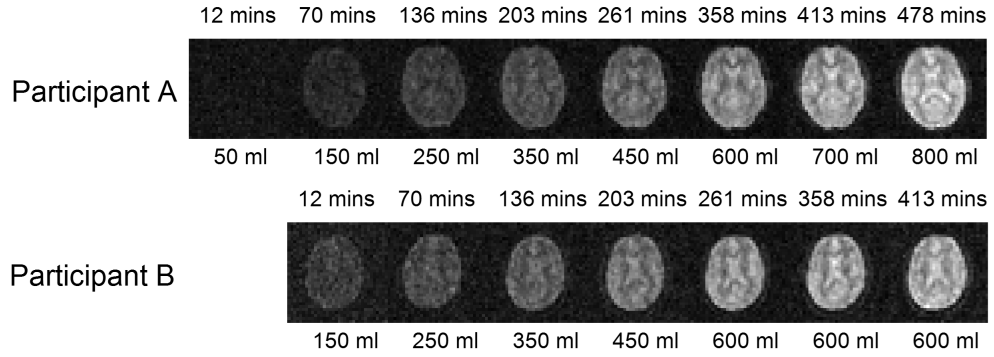

Figure 4.4: *^{2}H images acquired from two participants at different times during the initial, 8-hr heavy water loading period. The time since the first dose is indicated above each image and the cumulative dose of heavy water is indicated below. A single axial slice spanning the lateral ventricles is shown. The images shown are formed from the average over five echoes (TE_1 = 8.9 ms, ΔTE = 8.4 ms) and have a reduced in-plane FOV of 204 × 204 mm^2.*

4.3.2 Relaxation Times

Figure 4.7 shows sagittal and axial relaxation rate maps from two participants, with the dominant feature in the ^{2}H maps being the reduced R_2^* and R_1 relaxation rates in the ventricles. The elevated R_2^* values seen in deep grey matter structures in the ^{1}H maps are not evident in the ^{2}H maps. Scatter plots of the voxelwise T_1 and T_2^* relaxation times and the proton and deuterium T_2^* relaxation times, across four subjects are shown in Fig.

4.8. Table 4.2 reports the average and standard deviation of the ^{2}H T_1 and T_2^* values, along with ^{1}H T_2^* values measured measured in GM, WM and CSF in the four participants. These values were calculated by applying the binarised segmentation masks to the relaxation maps.

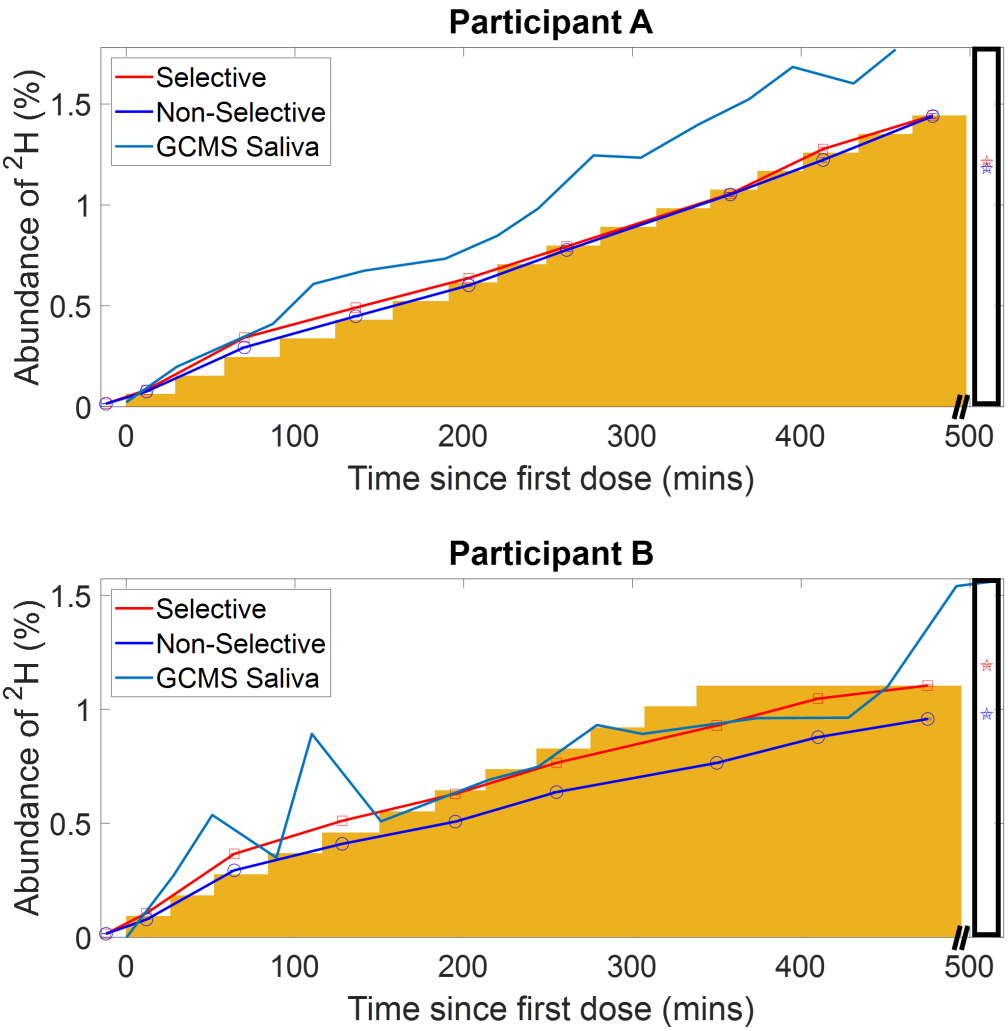

Figure 4.5: *Time course of the concentration of deuterium in the brain estimated from the ^2H spectroscopy measurements (red=from 2 cm slice at level of lateral ventricles; blue= whole head). Percentage estimated by scaling by the signal measured at NA (assumed to be 0.015%). The orange blocks indicate the concentration estimated from the cumulative D_2O dose and body weight. The measurements made at steady state (after 17 days of loading) are shown in the box at the far right. Measurements from saliva samples are given in the light-blue line.*

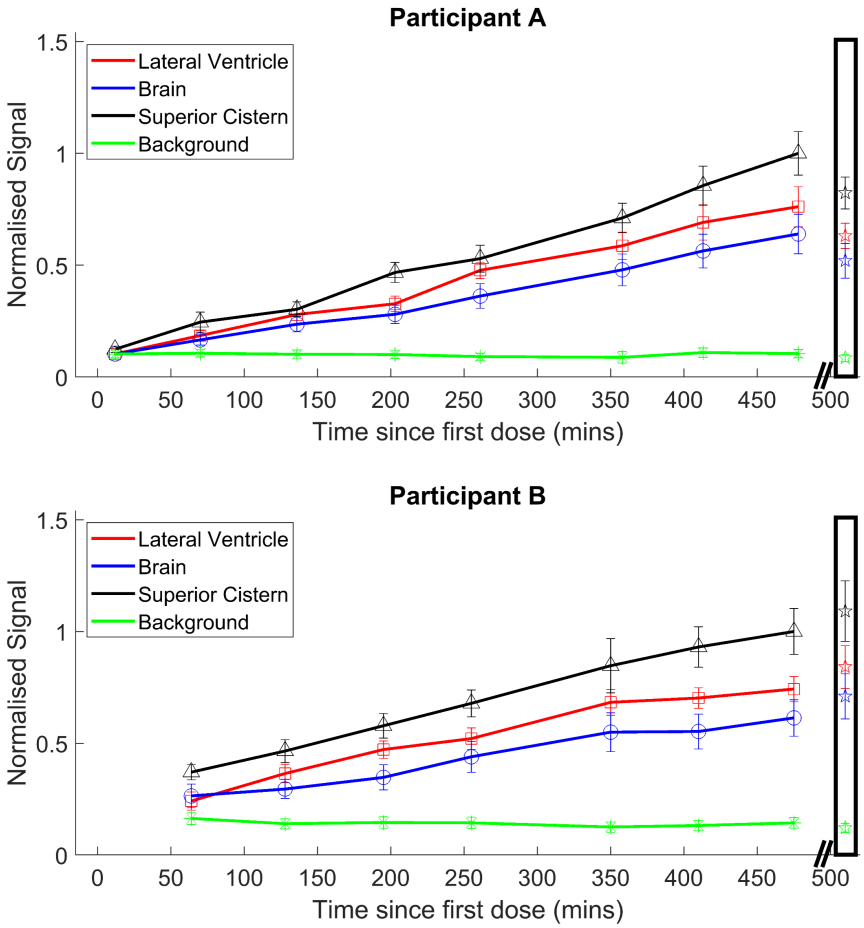

Figure 4.6: *Time course of average signal change in image ROIs (red=lateral ventricle; blue=brain tissue; black=SC; green=background noise) in two participants. Signals from all compartments are scaled by the SC signal at the final measurement time-point. Scaled signals measured at steady state (after 17-days loading) are shown in the box at the far right.*

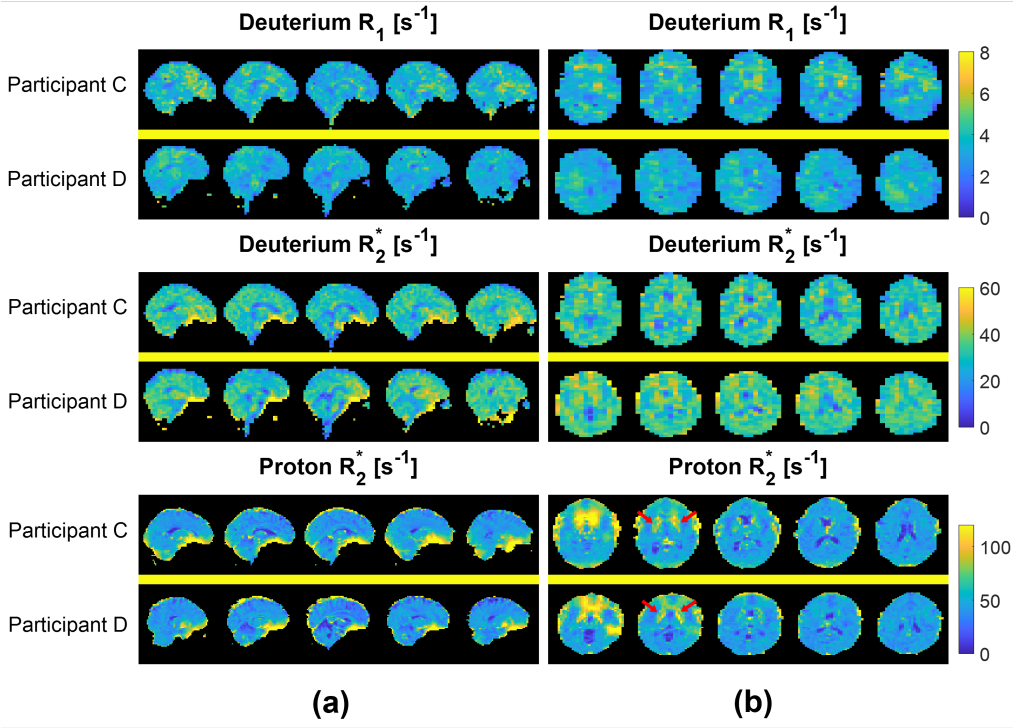

Figure 4.7: *^2H R_2^* and R_1 maps are shown along with ^1H R_2^* maps in sagittal (a) and axial (b) format. Maps show five central slices from Participants C and D. Relaxation maps were calculated from MEGE data equivalent to that displayed in Fig. 4.3. The elevated R_2^* in iron-rich deep GM structures is evident in the lower slices of the ^1H maps (red arrows), but is not seen in the ^2H maps. The images shown have a reduced FOV of 204 × 204 mm^2.*

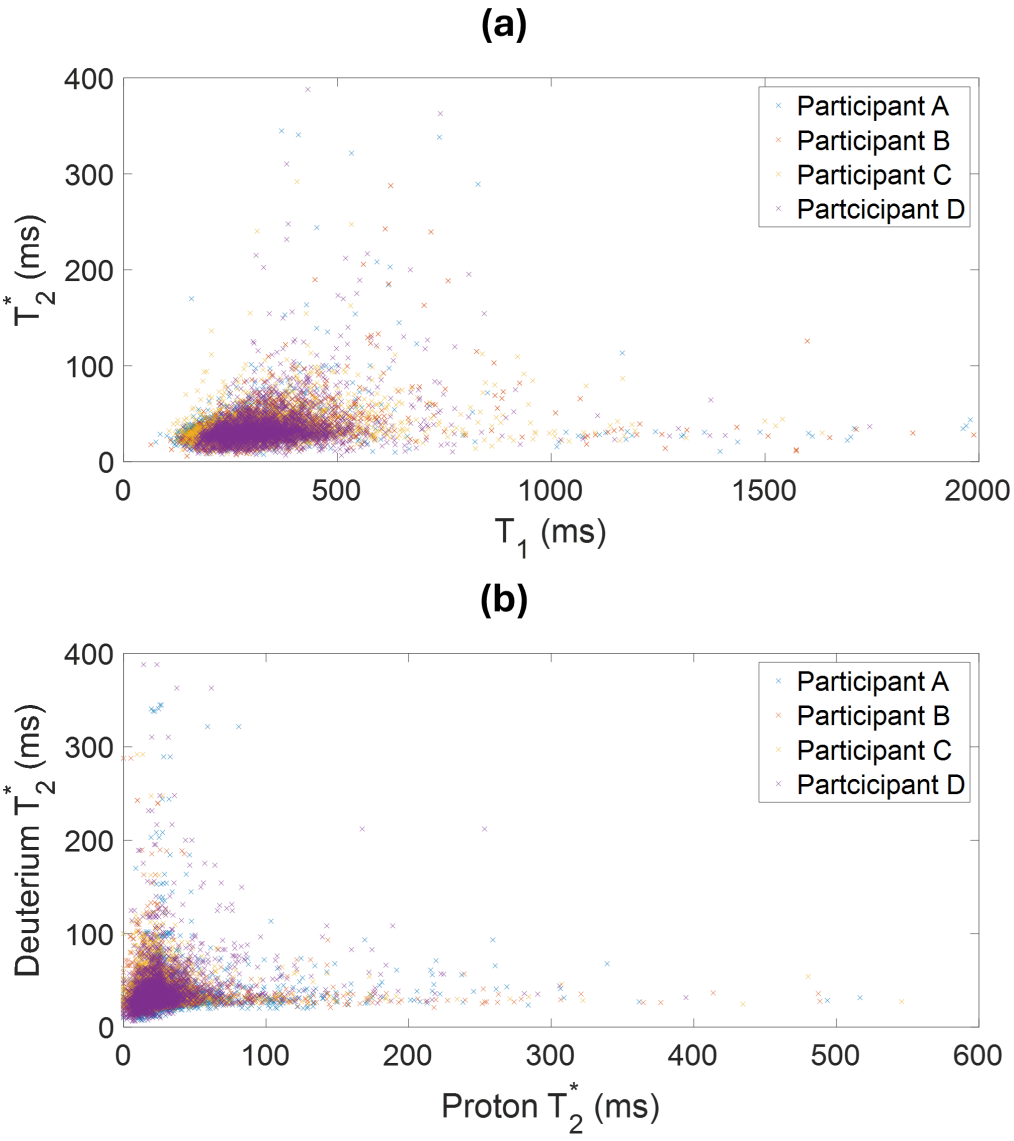

Figure 4.8: *Scatter plots of the voxelwise deuterium T_1 and T_2^* relaxation times (a) and the voxelwise proton and deuterium T_2^* relaxation times (b).*

Subject	Visit	Deuterium Relaxation Times [ms]						Proton Relaxation Times [ms]		
		CSF		GM		WM		CSF	GM	WM
		T1	T2*	T1	T2*	T1	T2*	T2*	T2*	T2*
A	1	450 ± 200	110 ± 90	280 ± 100	32 ± 8	260 ± 100	30 ± 10	106 ± 90	26 ± 20	27 ± 20
B	1	520 ± 200	83 ± 50	300 ± 100	33 ± 10	280 ± 100	32 ± 20	103 ± 90	25 ± 20	23 ± 10
C	1	460 ± 100	76 ± 40	301 ± 80	31 ± 7	290 ± 100	30 ± 10	93 ± 100	22 ± 10	21 ± 6
C	2	390 ± 100	82 ± 60	295 ± 90	32 ± 8	267 ± 90	32 ± 10			
D	1	720 ± 200	84 ± 50	420 ± 100	31 ± 6	350 ± 100	28 ± 6	87 ± 90	23 ± 10	22 ± 8
D	2	510 ± 100	110 ± 40	320 ± 80	31 ± 6	277 ± 80	28 ± 6			
Mean		510	90	320	32	290	30	97	24	23
SD		100	10	50	1	30	1	5	2	2

Table 4.2: *Average and SD of ^2H (T_2^* and T_1) and ^1H (T_2^*) relaxation times in CSF, GM, and WM for different participants and visits. These values were produced by averaging over segmented relaxation time maps, similar to those shown in Fig. 4.7. Average values and standard deviations across participants are also shown.*

4.4 Discussion

The results shown in Figs. 4.2 and 4.4 indicate that ^{2}H images of 6 × 6 × 10 mm^3 voxel size with a useful SNR can be acquired in ∼7.5 minutes at 7T with a head-sized bird-cage coil, when participants have been deuterium-enriched to ∼1.5% concentration (∼100 times NA). After summing over echo times these images (Fig. 4.4) showed SNR ∼16 in brain tissue in the steady-state condition (after 17 days of loading), the contrast in these images is dominated by T_2^*-weighting with the CSF appearing hyperintense relative to grey and white matter.

The measured relaxation times were reasonably consistent across the six measurements (Table 4.2), with CSF having significantly higher T_1 and T_2^* values than GM or WM ($p < 0.007$ for two-sample t-test). The measured T_1 and T_2^* values were consistently higher in GM than in WM, but the differences did not reach statistical significance (T_1: $p = 0.21$; T_2^*: $p = 0.08$). The relatively coarse resolution of the ^{2}H images made it difficult to avoid the effects of partial voluming, particularly of CSF and GM, and the limited range of TE and TR values reduced the accuracy of measurement

of the long T_1 and T_2^* values in CSF. The average values of the relaxation times are consistent with values reported from non-localised measurements of HDO signals in human [6, 22, 114], cat [26] and rat [5, 6] brain.

Focusing on human brain measurements, De Feyter et al. [6] reported HDO T_1 of 346 ± 5 ms at 4 T, while Ruhm et al. [114] measured 362 ± 6 ms at 9.4 T – values which lie between the values for CSF (508 ms) and GM/WM (318/285 ms) measured here at 7 T. As expected, the measured ^{2}H T_1-values are significantly shorter than the corresponding ^{1}H values at 7 T [115], due to the quadrupolar relaxation of ^{2}H. The long T_1 of HDO in CSF relative to GM/WM will lead to greater saturation in the CSF signal in short CSI measurements used for DMI (for example Ruhm et al. used TR = 155 ms [114]) which needs to be considered when quantifying signals from other ^{2}H-labelled metabolites using NA HDO signals. Bi-exponential T_2 decay was previously identified at 4 T [6] and 7 T [37] using non-localised spin echo measurements: at 7 T large (small) pools were found to have relaxation times of 29 ± 1 (412 ± 40) ms, respectively [37], consistent with our identification of short and long T_2^* values in GM/WM (32/30 ms) and CSF (90 ms).

The TE-summed MEGE images in Figs. 4.2 and 4.4 show contrast that is dominated by T_2^*-weighting, with the CSF appearing hyperintense relative to grey and white matter, as is the case in T_2^*-weighted ^{1}H images. A notable difference between the ^{1}H and ^{2}H R_2^* maps (Fig. 4.7) is that deep GM structures which appear with elevated R_2^* in ^{1}H maps due to their high iron content [115] do not appear hyperintense in the ^{2}H maps. This is a consequence of the dominance of quadrupolar, rather than dipolar, relaxation in the case of ^{2}H. The ^{1}H R_2^* maps also show larger regions of hyperintensity near the frontal sinuses due to the greater field-inhomogeneity-related intra-voxel dephasing resulting from the higher γ of ^{1}H. Signals from structures outside the brain (apart from the eyeball) are only evident in the ^{2}H images acquired with the shortest TE (Fig. 4.3) most likely because of the very short T_2^* of HDO in muscle [104, 116].

Both the imaging and spectroscopy results shown in Figs. 4.5 and 4.6 show that changes in HDO concentration on the order 0.1% can be readily monitored and tracked, with spectroscopy data being obtained in one minute. At an estimated concentration of 0.5% ^{2}H, the ratio of signal to background noise varied from ∼2.7 (brain) to ∼3.1 (SC) and these values increased approximately linearly with concentration as expected (Fig. 4.6) to steady state levels over the 8-hour loading period. The normalised values here are not normalised for flip-angle here. The concentrations estimated from the ^{2}H spectra are in reasonably good agreement with the values calculated from the cumulative D_2O dose and body mass (Fig. 4.5).

In addition, the signal amplitudes measured from ROIs in the brain have similar time-courses maintaining relatively constant ratios, dictated mainly by differences in T_2^*-weighting and water fraction in the different brain regions (Fig. 4.6). It is also important to note that as subject C stopped loading (after ∼350 minutes) a reduction in the rate of increase in ^{2}H concentration is evident in both Figs. 4.5 and 4.6, on the scale of minutes. This implies that the ^{2}H MR measurements are robust and that the dispersal kinetics of deuterium following oral ingestion of D_2O are rapid throughout the body on the timescale of the measurements. This is consistent with previous measurements based on blood sampling which indicate that the half-life of absorption into blood is around 12 min, with similar time constants for dispersal into other body water compartments [117, 118].

In our experiments the participants came out of the magnet bore between measurements, leading to the potential for changes in signal intensity due to variation of the slice position. Nevertheless the ^{2}H signals tracked the monotonically increasing dose and the values measured at maximum dose were similar to those measured 17 days later during the steady state loading period. Although both participants had approximately the same weight and target D_2O dose, Participant B was only able to ingest 600 ml during the initial loading. The deuterium concentration measured from

Participant A was consequently higher at the end of the loading period. The rest of participant B's loading was completed over the following four days, along with the daily 50 ml top-up and similar concentrations were measured from the two participants in the steady state (Fig. 4.5). The tracked GCMS analysis of saliva samples during loading is given in this figure. The saliva samples do not follow the deuterium concentration by body-weight estimates as closely as the spectroscopy measurements as well as being much more variable The GCMS measurements of the saliva at the end of the loading was 1.51% ± 0.09%, and 1.53% ± 0.17%, respectively for participants A and B.

Rapid increases in body water enrichment can lead to feelings of dizziness and nausea. These symptoms can occur at relatively low enrichments while equilibrium has not yet been achieved, and are thought to result from temporary effects on the vestibular system due to density changes in the semi-circular canals of the inner ear [119]. The rapid loading was required for the parallel study, but a more gradual increase in heavy water uptake could be used for future MR-loading experiments to minimise these effects.

4.5 Conclusion

^{2}H MR measurements at 7T have been successfully used to track the increase in concentration of ^{2}H in brain during D_2O loading to 100 times NA, in four human participants. Gradient echo images with an SNR of 16 and a voxel volume of 0.36 ml could be acquired in 7.5 minutes. ^{2}H T_1 and T_2^* relaxation times from water in GM, WM and CSF have also been measured at 7T. These relaxation times can be applied in research protocols using the NA ^{2}H signal from water for calibration and concentration calculations. This lays the ground work for further studies involving ingested D_2O in order to measure lipid turnover in Chapter 6. In future work we aim to track uptake from a single D_2O dose on a shorter time scale, using faster, interleaved acquisition of ^{2}H images and spectra.

Chapter 5

Comparing glucose-d_2 and glucose-d_7 in DMI

5.1 Introduction

DMI is a MRSI method that enables substrates and metabolic products that are labelled with the non-radioactive hydrogen isotope ^{2}H, to be mapped *in vivo*. The scientific impact of ^{2}H and usage in the real world has increased greatly since its existence was first theorised [18], and it was not long before its potential for biological applications was recognised [19, 20]. Of particular interest is the use of glucose as the administered labelled precursor molecule, as this can provide a direct probe of glucose metabolism. Whilst the most common current uses for ^{2}H for *in vivo* NMR measurements involve deuterated glucose, initially it was D_2O that was ingested to elevate ^{2}H levels for use in NMR [25, 28], particularly to investigate lipid metabolism. The most useful forms of deuterated glucose are those whose carbon-bonded hydrogen atoms in the first and sixth positions have been replaced by deuterium because these substitutions are the only ones that are transferred to pyruvate, and then to either lactate (Lac) or to a combination of glutamate and glutamine (Glx) via the TCA cycle in the mitochondria. For this reason, [6,6'-$^2H_2$]-glucose has been a common

choice of labelling (isotopologue), providing twice the number of ^{2}H labels as would [1-^{2}H]-glucose, and this form of labelled glucose has been used in many *in vivo* studies ranging from preclinical work [5, 120] to demonstration in humans [6, 37]. Lac and Glx as well as non-metabolised deuterated glucose and water (NA plus an additional amount caused by label-loss during various processes) become detectable via either choice of labelling. The detected Lac and Glx provide information about the tissue's propensity to metabolise glucose via glycolysis or the oxidative phosphorylation pathway, and thereby an important clinical potential of DMI is identified, since many tumour cells exhibit an increased tendency for glycolysis. This manifests in higher than usual lactate production; the well-known Warburg effect [7].

^{2}H NMR measurements following labelled glucose ingestion or injection allow information on downstream metabolite concentrations to be quantified to obtain metabolic flux measurements, without the use of ionising radiation. In contrast PET scans using FDG involve ionising radiation and only provide information on glucose uptake. Besides the effect of cancer and other disease states, brain metabolism is also altered locally, albeit temporarily, as part of normal function. This might occur when a part of the brain is activated by a task or stimulus, such as by visual stimulation. For example it has been previously shown many times that there is metabolic activation in the visual cortex following visual stimulation [121, 122]. Lactate increases [35, 123, 124], and glucose decreases [125] in the visual cortex following visual stimulation have been measured using ^{1}H MRS. ^{13}C [126] MRS has been used to measure TCA-related changes during activation in the visuall cortex, and ^{31}P MRS has been used to measure signal changes in lactate, phosphocreatine and inorganic phosphate in the visual cortex during stimulation[35]. Glc signals are not present in these measurements. It is important to note that significant increases in glutamate (2%) and decreases in glutamine (8%) have also been shown during activation [125].

In its simplest form, DMI is relatively straightforward to implement using a pulse-acquire CSI sequence, usually without the need for water sup-

pression because of the low concentration of naturally occurring deuterated water. In most cases, DMI spectra are also simpler to analyse than proton spectra. If using glucose as the labelled substrate, there are just four metabolites to consider: water (HDO), glucose (Glc), Glx, and Lac. This relative simplicity can be regarded as a positive attribute in the context of potential clinical translation. However, the generally low SNR of DMI is not a favourable characteristic, and means that data is often acquired with low spatial resolution, often with voxels of around 8 ml [22, 38] in volume; the smallest reported voxel size to date in humans is 2.97 ml [36], in measurements made at a high magnetic field strength of 9.4 T. Low SNR and spatial resolution can potentially be improved upon by performing DMI scans based upon indirect detection using ^{1}H MRSI [36, 79, 127, 128]. This has the benefit of not requiring deuterium-specific hardware, but this comes at the expense of often requiring a more complex acquisition scheme and post-processing analysis. Another method of increasing SNR in DMI is to implement de-noising during post-processing analysis. This has been shown to improve SNR in MRSI using low rank approximations [84]. Similar techniques using Tucker decomposition [89, 91] have been applied to DMI data with notable SNR improvements [75, 129].

Other labelled compounds than glucose-d_2 have also been used to investigate *in vivo* metabolism in conjunction with DMI in animal experiments. For example [6,6'-$^{2}H_2$]-fructose has been used to investigate liver cancer [41]. Fructose was found to have a similar spectral appearance as the glucose, with slightly different kinetics. Intravenous injection of deuterated acetate ([$^{2}H_3$]-acetate) has been used to investigate myocardial metabolism [130] and tumour metabolism [6], where acetate accumulation and Glx changes were tracked.

One important way of increasing the ^{2}H signal is to use a form of deuterated glucose with a larger number of ^{2}H labels. Since there are twelve hydrogen atoms in the glucose molecule, all twelve could potentially be substituted with ^{2}H atoms. However, atoms in the hydroxyl groups exchange

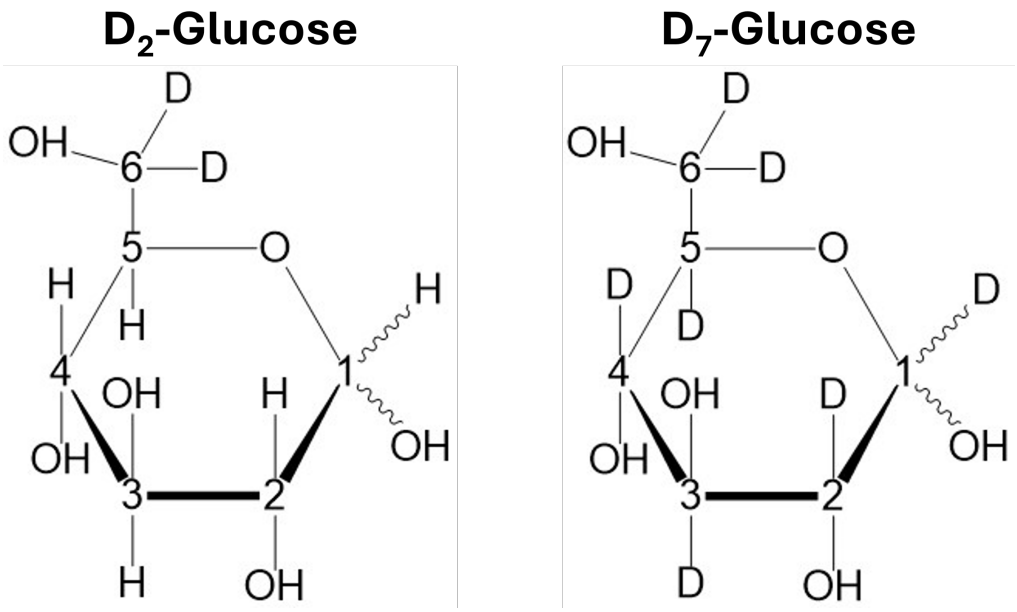

Figure 5.1: *The chemical structure of glucose-d_2 (left) and glucose-d_7, where D indicates deuterium atoms and each number refers to a different carbon atom position.*

rapidly with the surrounding water and therefore are not usually useful in metabolic applications. The seven other locations in which the ^{2}H atoms are directly carbon-bonded are less labile and potentially useful labelling sites, yielding the form [1,2,3,4,5,6,6'-$^2H_7$]-glucose (glucose-d_7). Compared with [6,6'-$^2H_2$]-glucose (glucose-d_2), the ^{2}H spectrum of glucose-d_7 should contain a factor of 7/2 times more components, many of which overlap due to the broad linewidths of ^{2}H, thus producing a gain in SNR. An example ^{2}H high-resolution NMR spectrum of 100mM of glucose-d_7 dissolved in H_2O obtained at 9.4 T, showing the overlapping spread of peaks, is shown in Fig. 5.2 which was performed by Dr. Galina Pavlovskaya.

However, glucose-d_7 is over eight times more expensive compared to glucose-d_2, per gram purchased. The ^{2}H atoms in the C1 and C6 positions (in the absence of label-loss) will be transferred to lactate or Glx molecules [131], producing a gain of 3/2 in the Glx signal. A similar gain is expected for Lac. Therefore, it is expected that the use of glucose-d_7 will increase the SNR and reliability of detected signals for Glc, Glx, and Lac, compared

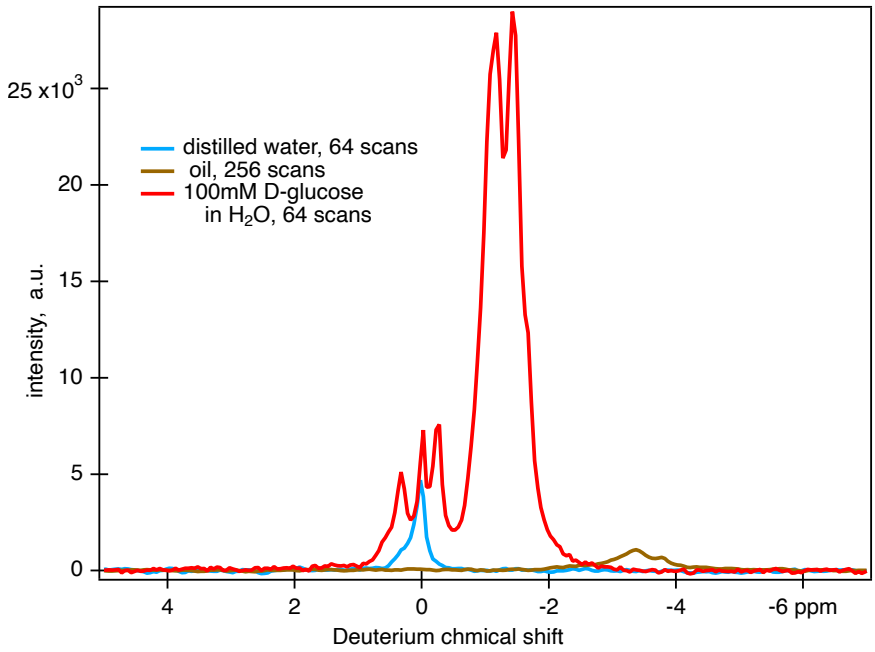

Figure 5.2: *^2H spectrum of 100mM of glucose-d_7 dissolved in H_2O obtained at 9.4T. Also, showing ^2H spectra for distilled water and oil obtained for reference. Figure created by Dr. Galina Pavlovskaya.*

to using glucose-d_2. In addition, the four remaining ^{2}H labels in the positions C2, C3, C4 and C5 of glucose-d_7 are transferred directly or indirectly to water during glycolysis, and will therefore contribute to an increased HDO signal [13, 132]. The HDO (deuterated water) signal increase that is a result from metabolism has been shown to be directly proportional to the increase in downstream metabolites (Glx and Lac) [13], which implies that regular non-spectroscopic imaging of the HDO signal increase could be used as a measure of the Warburg effect, potentially providing improved spatiotemporal resolution compared to MRSI techniques. The path of metabolism taken by glucose-d_2 and glucose-d_7 is outlined in Fig. 5.3, including the label-loss to deuterated water.

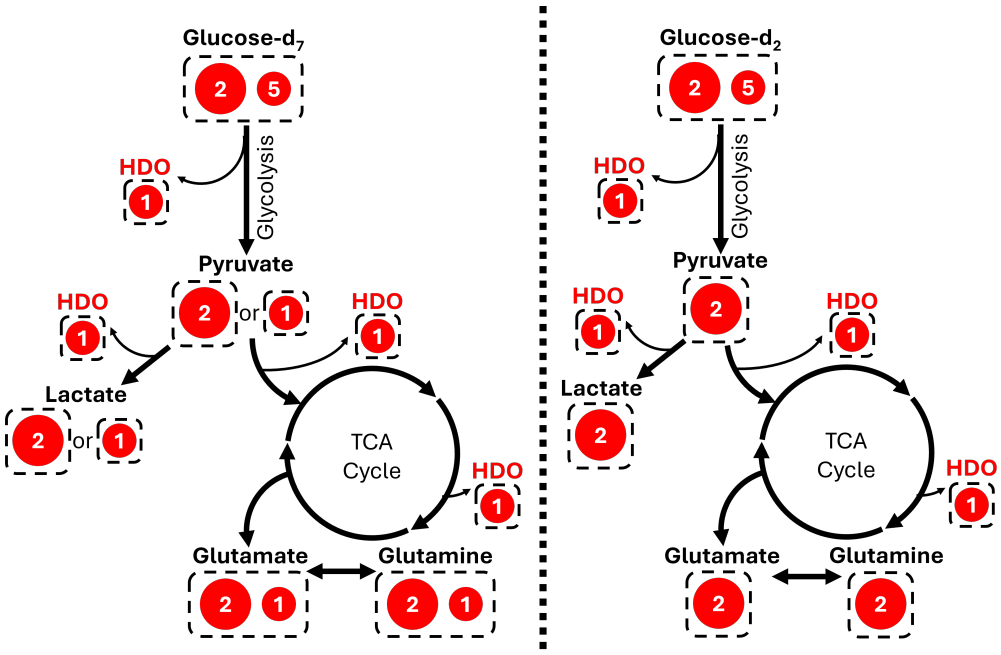

Figure 5.3: *The metabolism followed by glucose-d_2 and glucose-d_7 outlining the number of ^2H labels present in each metabolite indicated by red circles and the number in the centre. The larger circle represents the ^2H from the C6 and C6' labels.*

5.2 Methodology

The primary aim of this study is to measure the difference in vivo metabolite signal/concentration changes for HDO, Glc, Glx and Lac in the brains of healthy human participants following ingestion of glucose-d_2 or glucose-d_7. This the first instance of glucose-d_7 being used with human subjects. Each participant drank 250 ml of water containing 0.75g/kg of of dissolved labelled glucose. All the glucose was purchased from CK isotopes and is microbiological/pyrogen tested. The glucose-d_2 cost ∼£16 per gram whilst glucose-d_7 cost ∼£130 per gram. CSI scanning, de-noising and a sophisticated and robust fitting routine was used to track the change in metabolite signals. Also, the possibility of detecting differences in metabolite concentrations due to an applied visual stimulus was investigated.

5.2.1 Particicpants

Scanning was performed on a 7T Achieva scanner (Philips Healthcare), operating at 45.8 MHz for ^{2}H. A 26.4 cm inner-diameter, dual-tuned ^{1}H/^{2}H birdcage RF coil (Rapid Biomedical) was used for ^{2}H measurements and acquisition of anatomical ^{1}H images. Ethical approval was received from the Faculty of Medicine and Health Sciences Research Ethics Committee (ref. no. FMHS 306-0621) at the University of Nottingham to recruit 15 healthy participants for this study. Informed consent was received from all participants who were only recruited if they had: a Body Mass Index (BMI) < 25 kg/m^2 (or less than 27 kg/m^2 for males whose waist circumference was <94 cm), had a normal heart rate and blood pressure, a blood glucose concentration of <7.8 mM (finger-prick test), an age between 18 and 60 years, and no significant medical conditions or issues related to safety in the MR scanner. As participants are being given extra glucose it is important to minimise the risk of hyperglycaemia, which is why participants that are at risk of developing type-2 diabetes are excluded. Older participants and those taking oral medication are excluded as their metabolism can be

Parameter	MPRAGE	Bulk Spectra	Slice-Select. Spectra	CSI
Nuclei	^{1}H	^{2}H	^{2}H	^{2}H
FOV (mm3)	224 x 224 x 140	n/a	n/a	180 x 180 x 120
Voxel	1.4 mm (isotropic)	n/a	2 cm thick slice	15 mm (isotropic)
Averages		16	128	6
TR (ms)	7.1	1000	1000	230
TE (ms)	2.6	1.1	1.9	2.4
Flip Angle (°)		90	90	62
BandWidth (Hz)		3000	3000	1200
Samples		2048	2048	256
Scan Time (s)	353	17	129	670

Table 5.1: *The parameter details for each of the scans used in this study. Note that the averages for CSI are acquisition weighted, and that the 'Bulk' spectra is non-localised.*

altered. At the screening visit, participants were informed whether visual stimulation would be applied and that at least an eight hour fast would be required on the day of scanning. Blood glucose status was checked using a second blood glucose level test (finger-prick) that had to be <5.6 mM. For those receiving glucose-d_2 (n=8), 5 experienced a visual stimulus. For those receiving glucose-d_7 (n=7), 4 experienced a visual stimulus.

5.2.2 Scan Protocol

Scanning for each participant was split into two parts, the baseline NA scanning before the glucose drink (lasting approximately 20 minutes) which was used for quantification and calibration, and the 90-minute scanning session after the glucose drink was ingested. The drink was consumed in a maximum of eight minutes. Baseline measurements included a ^{1}H scout scan for planning; a ^{1}H MPRAGE scan (FOV: 224 × 224 × 140 mm^3, 1.4 mm isotropic voxels, TR: 7.1 ms, TE: 2.6 ms, T_{scan}: 353 s); a non-localised ^{2}H spectrum (16 averages, TR: 1000 ms, TE: 1.1 ms, α: 90°, BW: 3000 Hz, 2048 samples, with a scan duration of 17 s); a slice-selective ^{2}H spectra, acquired from a 2-cm-thick axial slice positioned over the lateral ventricles, using 128 averages, TR: 1000 ms, TE: 1.9 ms, α:

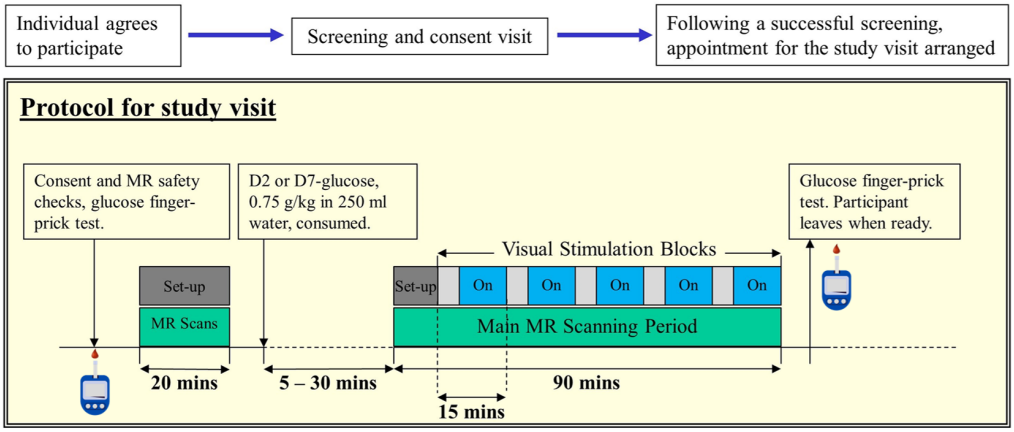

Figure 5.4: *Schematic of the scanning protocol that was used in this study. Above the box the three main steps for recruitment are outlined, in the yellow box the details of the study day are listed. The study day starts with a blood-glucose test before NA and post ingestion scanning.*

90°, BW: 3000 Hz, 2048 samples with a T_{scan}: 129 s and a 3D ^{2}H CSI covering the whole brain (FOV: 180 × 180 × 120 mm^3 , 15 mm isotropic voxels, TR: 230 ms, TE: 2.4 ms, α: 62°, BW: 1200 Hz, 256 samples, with a T_{scan}: 670 s) acquired using 6 acquisition-weighted [133] averages. All the NA scans were performed in the absence of visual stimulation and after these data were acquired the participant was then brought out of the scanner and consumed the glucose drink. This contained 0.75g/kg (bodyweight) of either glucose-d_2 or glucose-d_7 powder purchased from CK Isotopes Ltd. (microbiological/pyrogen-tested product) and Merck Life Science UK Ltd. (endotoxin-tested product) dissolved in 250 ml of water at room temperature. The participant was allowed to consume this in their own time, and when they indicated that they were ready for the second scanning session (∼30 minutes later), were guided back into the scanner.

In the second session, the two ^{1}H scans were repeated, followed by five or six repeats of the three ^{2}H scans. In the event that the participant needed to exit the scanner for a short period and re-enter, the ^{1}H scans were repeated before continuing with the ^{2}H scans. If the participant was to be visually stimulated, the display was activated during the CSI scans

only and quiescent otherwise.

Visual stimulation was produced via an 8 Hz flashing, black and white, radial checkerboard, similar to what has been used previously [124]. The visual display was projected onto a screen that the participants could observed by wearing prism glasses while lying in the scanner. Most of the participants who experienced visual stimulation (three that ingested glucose-d_2 and four that ingested glucose-d_7) were shown a checkerboard flashing pattern that was active for 50 seconds followed by 10 seconds of rest (red cross on a grey background). However, two participants (both of whom ingested glucose-d_2) experienced a checkerboard flashing pattern that was active for 30 seconds followed by 30 seconds of a red cross on a grey background. Participants who received no visual stimulation were asked to close their eyes during the scanning session. In all cases, the scanner room lights were turned off.

5.2.3 Image and spectral processing

The ^{1}H MPRAGE images were converted to a NIFTI format using MRIcroGL (www.nitrc.org), and bias-field corrected using FSL-FAST [109]. Each corrected MPRAGE image was then brain extracted using FSL-BET [110] which also bias-field-corrected the image and removed any neck voxels. The fractional intensity threshold was allowed to vary between subjects along with the gradient in the foot-head direction. This was done to ensure the brain extraction was optimised for each participant. The MNI-152 brain image dataset with 2 mm isotropic voxels (distributed with FSL [134]) was linearly registered to each image using FSL-FLIRT [111, 112] and twelve degrees of freedom. The MNI-152 brain image was then non-linearly registered to the same image to obtain the warp-field using FSL-FNIRT [135], with the affine matrix from the linear registration used as an initial guess. The warp-field was then used to non-linearly register probabilistic maps of the frontal and occipital lobes from the MNI-152 atlas to the MPRAGE space. The maps were subsequently binarised to

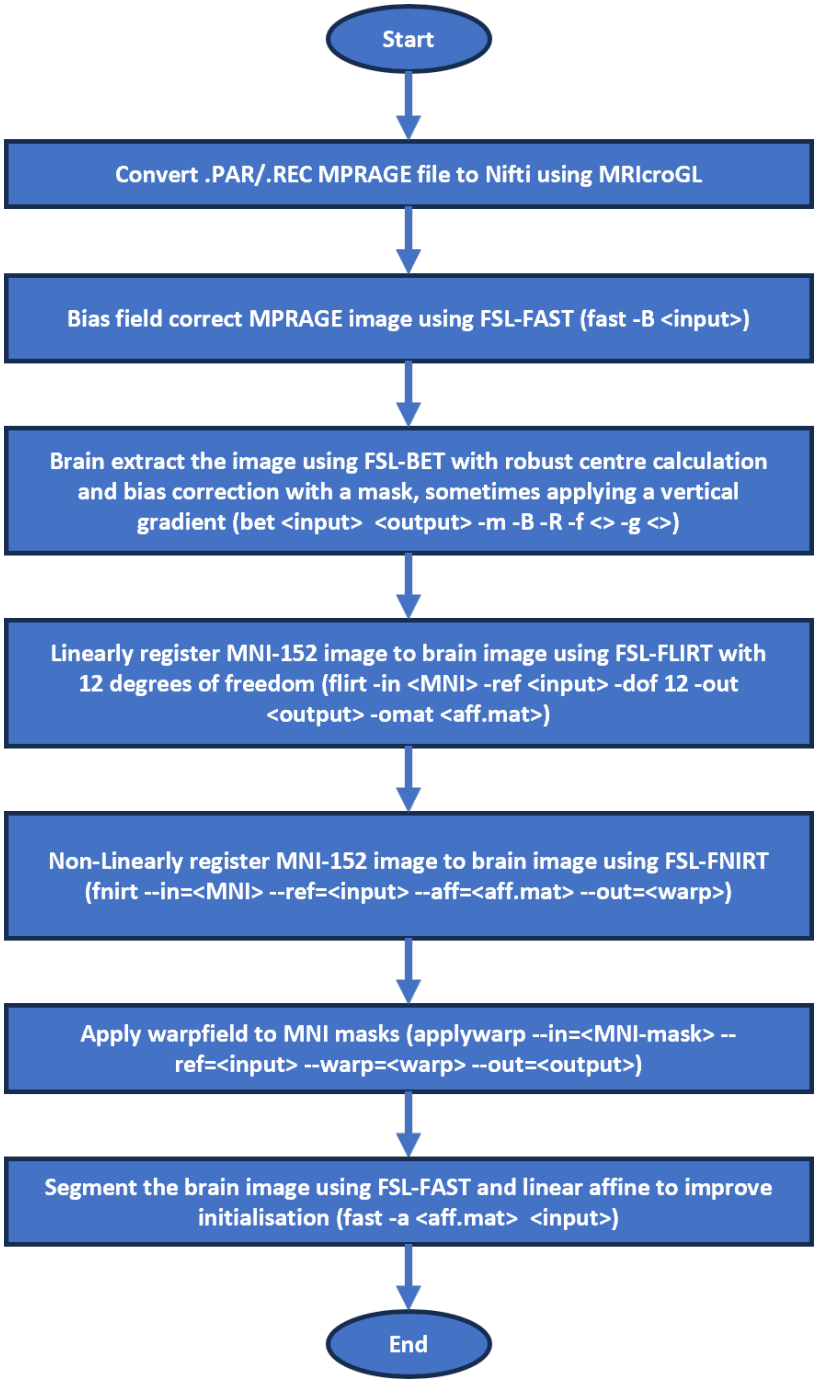

Figure 5.5: *Flowchart outlining the steps used to analyse the* ^{1}H *MPRAGE images and obtain the ROI Masks. The case-sensitive FSL commands are included in brackets.*

obtain ROI masks. These regions were chosen to test whether contrast in metabolite signals/concentrations could be detected with participants who were visually stimulated. A flowchart that outlines the analysis steps for the ^{1}H MPRAGE images and the construction of the masks can be seen in Fig. 5.5. A flowchart that outlines the steps used to analyse all the ^{2}H CSI data can be seen in Fig. 5.6. It is important to note that 'separate/group fit parameters' is where the individual metabolite parameters that are grouped/separate form a single set of amplitude, phase, linewidth and chemical shift for each metabolite .

A noise spike that affected each voxel at the same frequency position was visible. In some of the spectra the spike which generally only affected one data point in each spectrum most likely arose from baseline error. To correct this spike the data points on either side of corrupted point were averaged together and the spike was replaced with this value.

Apodisation and smoothing techniques have been shown to affect metabolite quantification in MRSI [81], which is why it was chosen to not apodise when analysing the data. Low-rank denoising has been shown to be able to use the similarities in temporal/spatial information to denoise, better than for single voxel denoising [3, 81]. Tucker decomposition also known as a HOSVD is an extended version of the simpler SVD, which is then followed by a low rank approximation. Here only the largest singular values persist, and the rest are replaced with zeros, therefore when reconstructed the data is similar except only the most prominent features persist. This works as a de-noising method as the noise will be represented as smaller singular values and will hence be removed, only leaving the metabolite peaks as described in section 2.4.2. This can be performed in either the frequency or the time domain.

Here, each CSI data-set was denoised in the time-domain using a Tucker decomposition [91] with a compression matrix size of [64 6 6 4] (spectral and 3 spatial dimensions). The core matrix size was chosen by simulating 3D *in vivo* ^{2}H CSI spectra for HDO, Glc and Glx resonances. To reflect the form

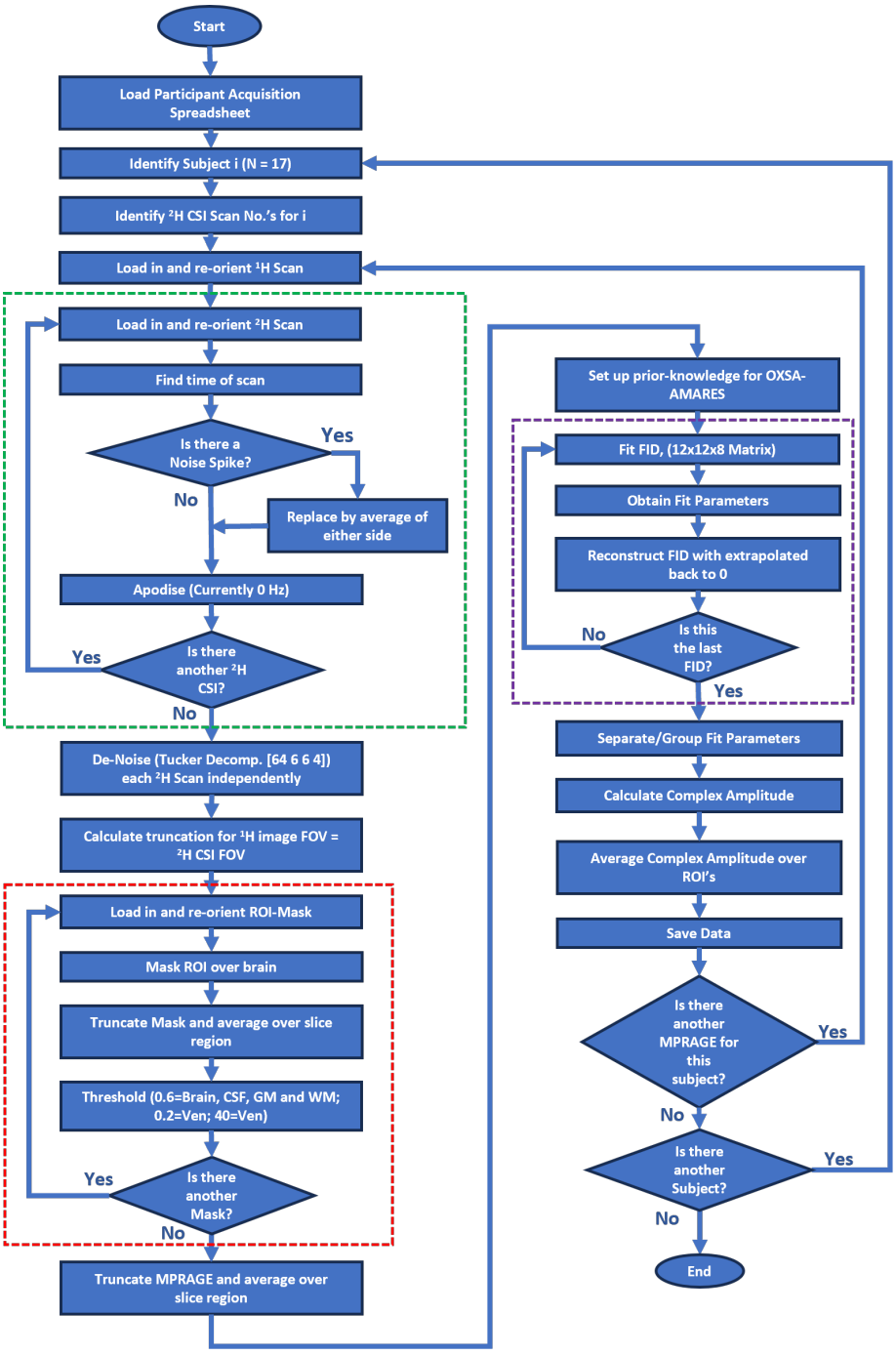

Figure 5.6: *Flowchart outlining the steps used to analyse the ^{2}H CSI spectral data (including de-noising). The dotted green box represents the pre-processing steps for the ^{2}H data, the dotted red box describes the application of the ^{1}H mask and the dotted purple box describes the fitting of each spectra.*

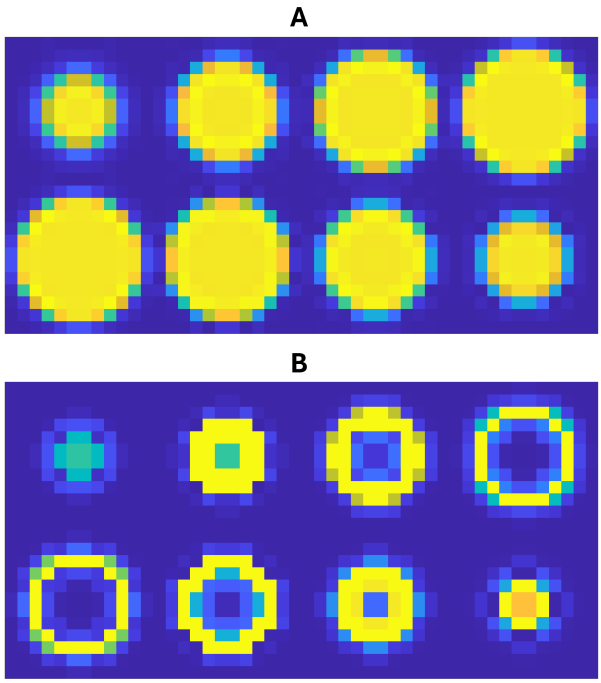

Figure 5.7: *3D simulated spherical (A) and hollow-spherical (B) signal distributions used to simulate DMI data, for testing different core matrix sizes when de-noising.*

of *in vivo* data, the amplitude distribution for water and glucose followed a spherical pattern (Fig. 5.7A) whilst the amplitude distribution for Glx followed a hollow-sphere (Fig. 5.7). Then by varying the core matrix size in a single direction (whilst keeping the others the same) and fitting the spectra, it is possible to compare the signal distribution for each metabolite at each compression size. An example of this can be seen in Fig. 5.8 as the dimensions of the core matrix in the FID sample direction are varied, with the amplitudes for HDO, Glc and Glx being displayed. A choice is then made for the compression in the selected direction that does not modify the overall distribution for each metabolite whilst still de-noising the data. This is then repeated for each of the other spatial directions until an optimal compression matrix size is obtained. The resulting compression matrix size (relative to total data size) is similar to compression matrix sizes that have been previously used with DMI [75, 129] and ^{13}C studies

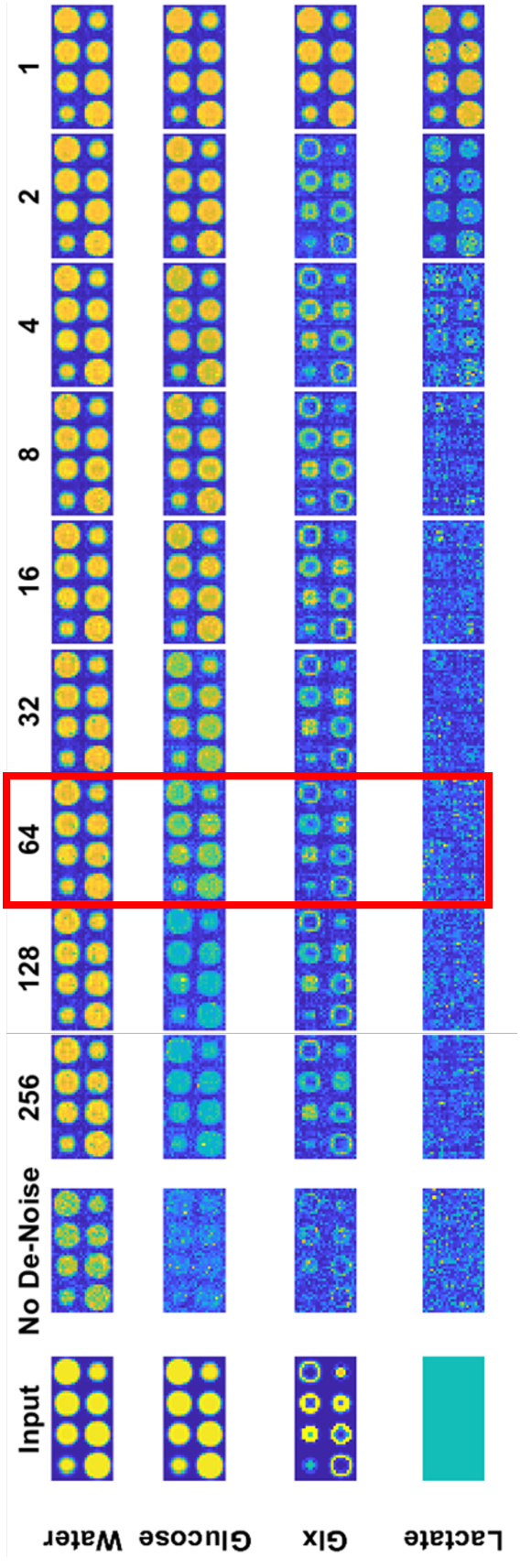

Figure 5.8: *Ground truth signal distributions for ^2H water, glucose and Glx (far left) followed by amplitudes obtained from fitting spectra to varying levels of compression in the FID sampling direction. The spatial dimensions are compressed to a core matrix size of [6 6 4]. The red box shows the choice of compression for the FID sampling direction, the spectral SNR of the centre region ∼7.5.*

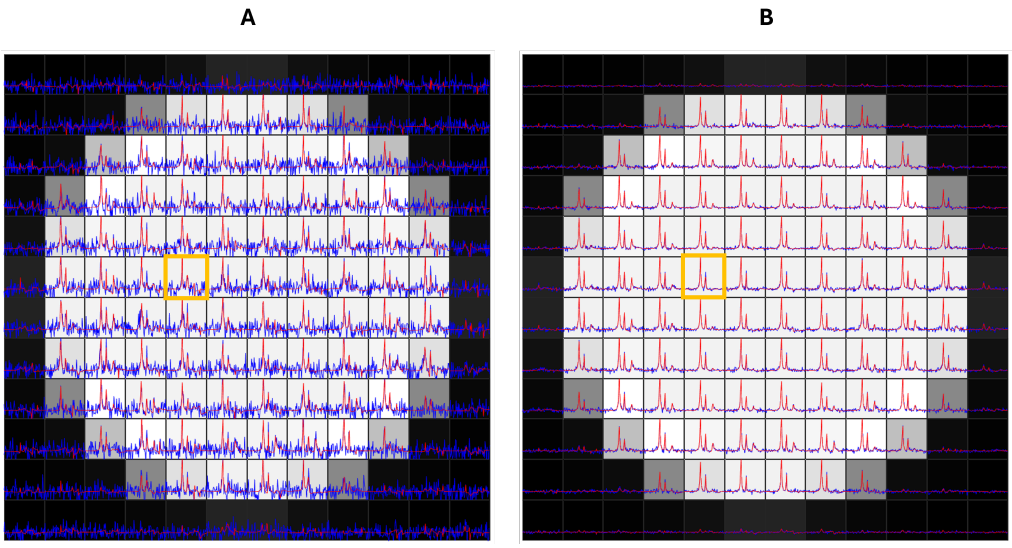

Figure 5.9: *CSI simulated data (blue) and the corresponding fits (red) for a single slice overlayed onto the sphere from Fig. 5.7A. A is the results before de-noising and B is the results after a Tucker decomposition with a core matrix of [64 6 6 4]. Here the SNR in the highlighted voxels increases from ∼7.5 to ∼16.5, by dividing the peak height of the spectra by the square root of mean squared noise regions either side of peaks of interest.*

[3]. The effect of de-noising using a Tucker decomposition with this core matrix size can be seen in Fig. 5.9.

With low SNR datasets it can be possible to bias the data using de-noising. One way to overcome this is to simulate your data and apply varying levels of de-noising which can help choose rank reduction. This was performed with our dataset which helped motivate the choice of rank reduction, which is why de-noising was only applied to each CSI and not in addition with a fifth domain of time. It was found that any level of de-noising in this domain smoothed the metabolite change curves, when compared to individual CSI de-noising. To avoid biasing the Lac peak (because of its low SNR) the simulated data had no true Lac peak present, therefore any presence of Lac above the noise floor in the amplitude maps would indicate too much of a rank reduction. It was found that a rank of eight in the spectral domain and ranks below four in the spatial domain

were too small. This can be seen in Fig. 5.8.

	ChemShift (ppm)				LineWidth (Hz)				Amplitude				Phase (°)			
Metabolite	LB	UB	IV	G	LB	UB	IV	G	LB	UB	IV	G	LB	UB	IV	G
Water	4.6	5	4.8 (0)	1	0	20	5	n/a	0	Inf	1	n/a	-180	180	0	n/a
$Glucose_{\alpha}^{1}$	n/a	n/a	0.416	1	0	25	5	2	0	Inf	0	2	-180	180	0	2
$Glucose_{\alpha}^{2}$	n/a	n/a	-1.281	1	0	25	5	2	0	Inf	0	2	-180	180	0	3
$Glucose_{\alpha}^{3}$	n/a	n/a	-1.102	1	0	25	5	2	0	Inf	0	2	-180	180	0	3
$Glucose_{\alpha}^{4}$	n/a	n/a	-1.405	1	0	25	5	2	0	Inf	0	2	-180	180	0	3
$Glucose_{\alpha}^{5}$	n/a	n/a	-0.978	1	0	25	5	2	0	Inf	0	2	-180	180	0	3
$Glucose_{\alpha}^{6}$	n/a	n/a	-0.974	1	0	25	5	2	0	Inf	0	2	-180	180	0	3
$Glucose_{\alpha}^{7}$	n/a	n/a	-1.051	1	0	25	5	2	0	Inf	0	2	-180	180	0	3
$Glucose_{\beta}^{1}$	n/a	n/a	-0.17	1	0	25	5	2	0	Inf	0	9	-180	180	0	2
$Glucose_{\beta}^{2}$	n/a	n/a	-1.57	1	0	25	5	2	0	Inf	0	9	-180	180	0	3
$Glucose_{\beta}^{3}$	n/a	n/a	-1.327	1	0	25	5	2	0	Inf	0	9	-180	180	0	3
$Glucose_{\beta}^{4}$	n/a	n/a	-1.413	1	0	25	5	2	0	Inf	0	9	-180	180	0	3
$Glucose_{\beta}^{5}$	n/a	n/a	-1.35	1	0	25	5	2	0	Inf	0	9	-180	180	0	3
$Glucose_{\beta}^{6}$	n/a	n/a	-0.918	1	0	25	5	2	0	Inf	0	9	-180	180	0	3
$Glucose_{\beta}^{7}$	n/a	n/a	-1.093	1	0	25	5	2	0	Inf	0	9	-180	180	0	3
Glx	n/a	n/a	-2.4	1	0	20	5	n/a	0	Inf	0	n/a	-180	180	0	n/a
Lactate	n/a	n/a	-3.5	1	0	20	5	n/a	0	Inf	0	n/a	-180	180	0	n/a

Table 5.2: *Prior knowledge used in OXSA-AMARES [71, 73] to fit the individual CSI datasets after glucose-d_7 ingestion, which includes the parameters chemical shift, linewidth, amplitude and phase. The acronyms are defined as LB:Lower-Bound, UB:Upper-Bound and IV:Initial-Value. The α and β subscripts represent the different glucose anomers, and the superscript represent different carbon positions on the glucose. N/a refers to non-applicable meaning the parameter is not used with this metabolite, this is because it is grouped to something else or is not grouped to any other metabolite. The 'G' column shows which peaks are grouped for each parameter.*

The FIDs were fitted using an adapted version of the OXSA-AMARES MATLAB toolbox [71, 73], which requires prior knowledge for each of the metabolites, the values used for glucose-d_7 can be seen in Table 5.2. In previous studies that have used glucose-d_2 ingestion, the glucose spectrum has

been fitted as a single peak at 3.8 ppm, since the chemical shift difference between the multiple resonance lines are usually not discernible due to the relatively broad linewidths and low SNR. However, this is not the case for glucose-d_7 [136] which has a larger number of spectral lines with a larger range of chemical shifts. Therefore, the spectrum needs to be modelled more accurately, taking into account the contribution from each deuterium label for both anomers (α and β). The chemical composition of the glucose stays the same for the different anomers, but the location of the hydroxyl group can swap with the ^{1}H on C1. When dissolved in water 1/3 of glucose will exist in the α form whilst 2/3 will exist in the β form [137].

Here, Glc is fitted as a sum of 14 peaks due to the number of label positions for both anomers. For consistency, this approach was also implemented when analysing the glucose-d_2 data, which resulted in 4 lines being fit for Glc. The ^{2}H chemical shifts of the Glc, Glx, and Lac resonances are assumed to be the same as those of the ^{1}H chemical shifts [136] and were implemented in the fitting as relative shifts to the water peak [120] at 4.8 ppm. When constructing the prior knowledge file the inputted initial values are shifted from the reference, ie. are from 0 which is 4.8 ppm in this case. The glucose peaks were fitted assuming a common scaling factor; all glucose peaks have the same phase, other than the peaks from the C1 position which have a different phase due to large differences in chemical shift. The linewidths of peaks from the same anomer share the same value. For HDO, Glx, and Lac, only single components were assumed, with independent amplitudes, phases, and linewidths.

Due to the additional prior knowledge the fitting routine takes approximately 2 to 3 times longer for the glucose-d_7 analysis compared to the glucose-d_2 analysis, the exact times can vary depending on the SNR for each metabolite during the time-course, approximate average time per spectrum to obtain fit parameters for glucose-d_2 and glucose-d_7 CSI data respectively are $\sim$0.16 s and $\sim$0.32 s (with default optimisation). The increased complexity of the fitting means it is less likely to accurately fit the FID however

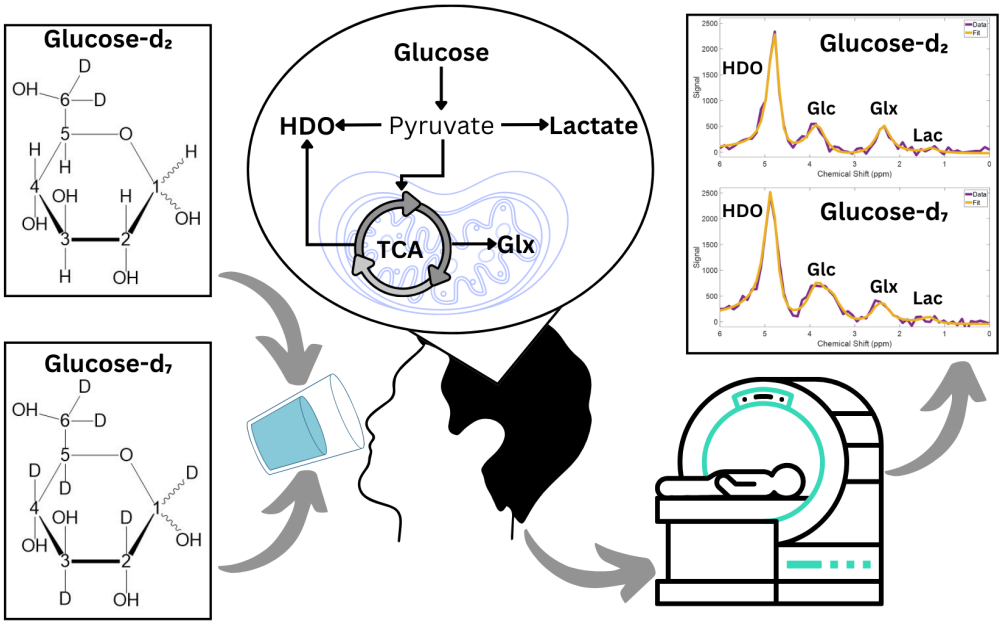

Figure 5.10: *Schematic diagram of the approach used to obtain the* ^{2} *MRSI data in this study.*

by narrowing the linewidth constraints and using more accurate initial estimates, as well as lowering the tolerance of the fit (increasing iterations and function evaluations and lowering the function and step tolerance) the fit is found to overlay the data accurately as seen in Figs. 5.11 and 5.15.

The amplitude and phase values for each metabolite peak at each voxel position were converted to complex amplitudes and interpolated to the same resolution as the MPRAGE image. These maps were then averaged over the whole-brain, occipital lobe, and frontal lobe ROI (using the binarised segmentation maps) to obtain ROI-averaged amplitudes for each metabolite for each CSI data-set. This provided amplitude time-courses as a function of time relative to glucose ingestion. These values were then either quantified into concentration values, normalised or corrected for the effect of T_1 differences and used as ratios between the two different types of glucose.

5.2.4 Concentration calculations

Concentrations C^m for each metabolite m were determined by Dr. Robin Damion using the following equation

$$C^m = \frac{A^m}{kE^m N^m}, \tag{5.1}$$

where A^m is the FID amplitude of the metabolite, N^m is the number of effective ^{2}H labels per metabolite molecule, E^m is the attenuation factor given by

$$E^m = \frac{1 - \exp(-\mathrm{TR}/T_1^m)}{1 - \exp(-\mathrm{TR}/T_1^m)\cos\alpha} \tag{5.2}$$

where T_1^m is the longitudinal relaxation time of the metabolite, TR is the repetition time, α is the flip angle, and k is a scaling constant. This constant, which is found to be ROI-dependent, is calculated by using the average NA water amplitude within a given ROI. This was calculated from the CSI data acquired before glucose ingestion assuming an isotopic percentage for deuterium of 0.015% [138], a concentration of pure water at 55.4 M, a factor of 2 because of the two hydrogen atoms in water, and an estimate of the percentage of water in each ROI. Cortical GM and WM were assumed to be 84% and 69% water [139]. The occipital and frontal ROIs were assumed to be comprised of 40% GM and 60% WM, resulting in a water content of 75%. The whole brain ROI was assumed to be 10% CSF, 36% GM, 54% WM, resulting in 77% water content.

Component of Brain	Region-Of-Interest (ROI)		
	Whole Brain	Occipital Lobe	Frontal Lobe
CerebroSpinal Fluid (CSF) (%)	10	0	0
Grey Matter (GM) (%)	36	40	40
White Matter (WM) (%)	54	60	60
Water Content (%)	77	75	75

Table 5.3: *Assumptions made for the brain tissue and overall water components or each ROI.*

Once k had been estimated for each ROI, metabolite concentrations were calculated via Eq. 5.1, with knowledge of the ^{2}H label numbers, N^m. The effective number of ^{2}H labels depends on whether glucose-d_2 or glucose-d_7 was ingested and, for Glx and Lac, also depends on label-loss. To account for label-loss, we have assumed the effective number of labels for water, Glc, Glx, and Lac is 1, 2, 1.2, and 1.7, respectively for glucose-d_2 [140]. For glucose-d_7, we have assumed 1, 7, 0.9, and 1.3 (estimated [141] assuming glutamine and glutamate are present in approximately equal amounts).

Longitudinal relaxation times for Glc, Glx and Lac were assumed to be 67 ms, 139 ms, and 297 ms, respectively [6], independent of ROI, number of ^{2}H labels, and whether glucose-d_2 or glucose-d_7 was the metabolic precursor. For water (HDO), the T_1 relaxation times were assumed to be 510 ms, 320 ms, and 290 ms for CSF, GM, and WM, respectively [105].

Metabolite	Effective Number of Labels		T_1 (ms)
	Glucose-d_2	Glucose-d_7	
Water	1	1	***
Glucose	2	7	67
Glx	1.2	0.9	139
Lactae	1.7	1.3	297

Table 5.4: *The effective number of labels (accounting for label loss) for HDO, Glc, Glx and Lac. As well as assumed T_1 relaxation times, '***' is listed as the values have been found to be tissue-dependent (510 ms, 320 ms, and 290 ms for CSF, GM, and WM, respectively [105]).*

5.3 Results

Figure 5.11 shows spectra acquired from a 2-cm thick axial slice positioned over the lateral ventricles in two participants before and after ingestion of a similar amount per bodyweight glucose-d_2 or glucose-d_7. The spectra are displayed with the same signal intensity axis scale so that the greater am-

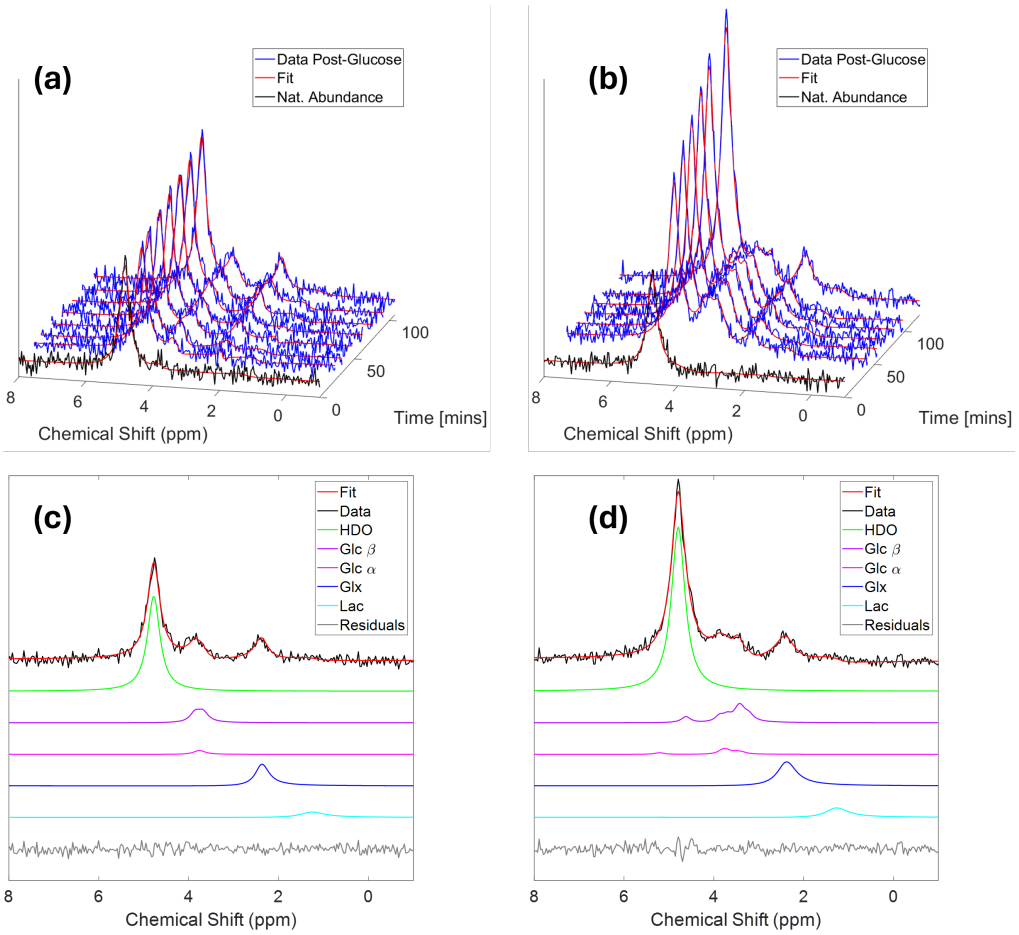

Figure 5.11: *Stacked selective spectra from a 2-cm-thick slice over the lateral ventricles from individual participants who had ingested glucose-d_2 (a) or glucose-d_7 (b). (c and d) Last spectra obtained during scanning with timepoints of ≈108 and ≈125 minutes after ingestion, for glucose-d_2 and glucose-d_7 respectively. Corresponding fits are shown for each spectra, along with separated contributions from each metabolite and the residuals after fitting.*

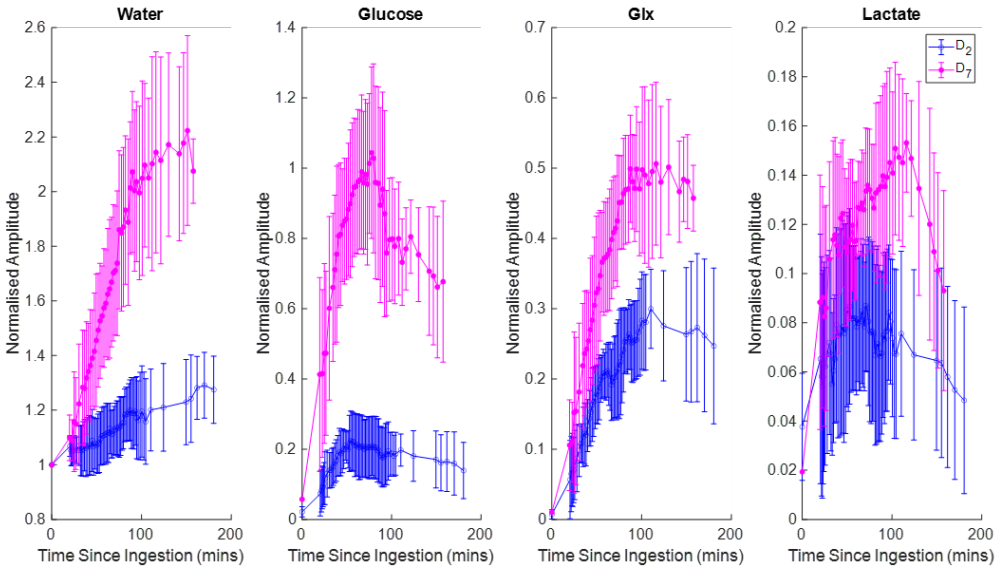

Figure 5.12: *Average time-courses of normalised metabolite signals taken from the slice selective spectra from all participants who ingested glucose-d_2 (blue, 8 participants) and glucose-d_7 (pink, 7 participants). A moving average over a number of the nearest points equal to the number of participants, with error bars representing the moving standard deviation. Time = 0 indicates the pre-ingestion scans, the HDO result is used for normalisation.*

plitudes of the signals following glucose-d_7 ingestion are evident, especially for the HDO. Single spectra obtained ∼108 minutes and ∼125 minutes after glucose-d_2 and glucose-d_7 ingestion, respectively, are also shown, along with the fits, and the individual contributions to the fit from HDO, Glc, Glx and Lac. Glc signals include contributions from both anomers (α and β) and each label position. Glucose-d_7 produces a broader peak, centred around 3.7 ppm, compared to glucose-d_2, and there are additional resonances at 5.2 and 4.6 ppm from the C1 deuterium of the two anomers in the glucose-d_7 spectra. The HDO, Glx and Lac signals show no obvious differences in linewidths and chemical shift position between glucose isotopologues or times after glucose ingestion. No obvious peak is visible above the noise floor in the residual spectrum, indicating the fitting performed well; notably this is true for the more intricate Glc from glucose-d_7.

The overall time-courses obtained from analysing all the slice-selective spectra for all participants who ingested glucose-d_2 and glucose-d_7 can be seen in Fig. 5.12. It is important to note that no line broadening/apodisation or de-noising technique has been applied here prior to fitting. The data is normalised to the NA HDO signal obtained prior to ingestion and the increase in reported signal for each metabolite can clearly be seen here. The Lac signal here could arise from lipids as it has the same chemical shift as the CHD of fatty acid chains, however it is not expected to see any ^{2}H incorporation into lipids from the labelled glucose.

Axial and sagittal slices from denoised 3D CSI data from two participants, averaged over six scans are shown in Figs. 5.13 and 5.14, with the fits to each voxel. Figure 5.13 shows data from a subject who ingested glucose-d_2, while Fig. 5.14 shows corresponding data from a subject who ingested glucose-d_7. The spectral data is overlaid on the bias-field-corrected ^{1}H MPRAGE image. A spectrum and the corresponding fit from the voxel highlighted (red) in both the axial and sagittal view are also shown. The spectra are similar in appearance to those displayed in the slice-selective spectra of Fig. 5.11. Interpolated and overlaid, axial, amplitude maps of each of the metabolites from one axial slice are also shown in Figs. 5.13 and 5.14. The FID amplitude values, for each metabolite, are obtained from fitting the averaged CSI data after denoising using OXSA-AMARES [71, 73].

Figure 5.15 shows participant-averaged metabolite time-courses (non-averaged data are shown in Fig. 5.16). These plots were generated by calculating the running average of the time-ordered data from all participants in the glucose-d_2 or glucose-d_7 cohorts, with a variable window size that always includes a number of points equal to the number of participants included in the particular data-set. This is shown in Fig. 5.15 with the errorbars being equal to the standard deviation over the number of measurements in the running average. Here, for each participant, the metabolite signals are normalised to the HDO signal at NA obtained before

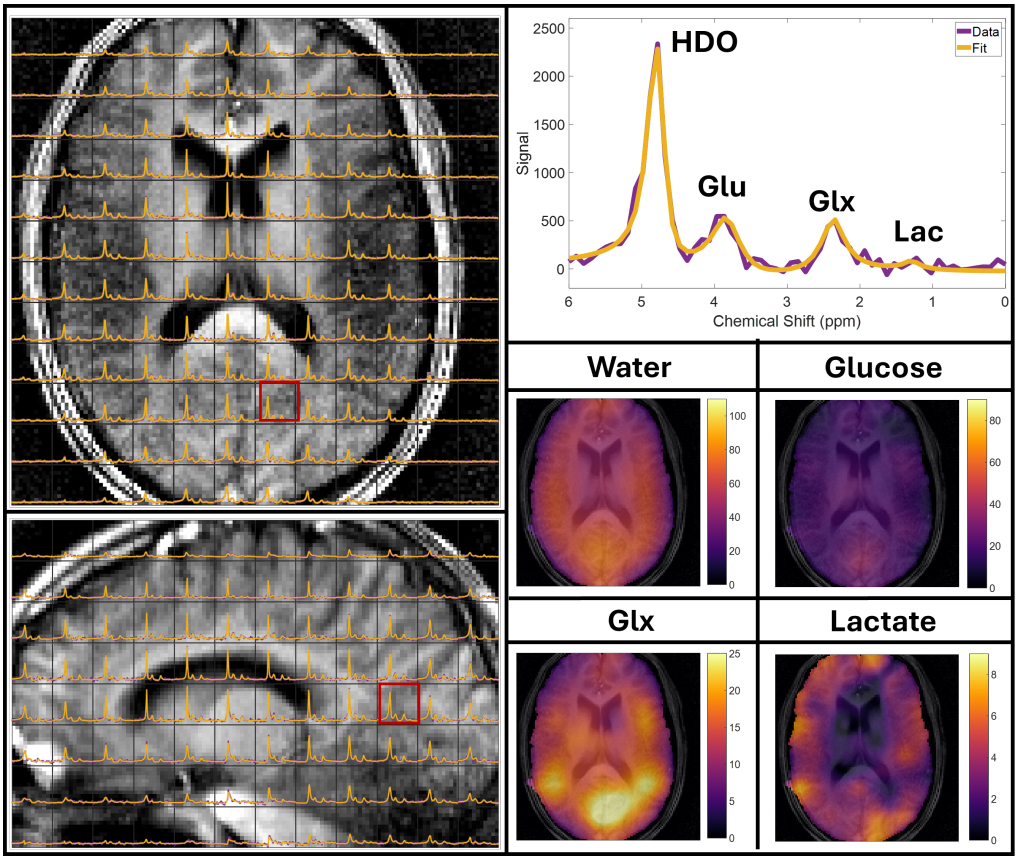

Figure 5.13: *Axial and sagittal slices from a 3D CSI data set (FOV: 180 x 180 x 120 mm^3, 15 mm isotropic resolution) acquired from a participant who had ingested glucose-d$_2$. Spectra were averaged over six scans and then denoised using a Tucker decomposition and are overlaid on the corresponding slice of the MPRAGE image acquired after ingestion. Experimental data (purple) and fit (yellow) are shown for each voxel. The spectrum from the highlighted voxel is shown in detail in the plots shown upper right. Amplitude maps for each metabolite are also shown, with the colour axis being shared with Fig. 5.14.*

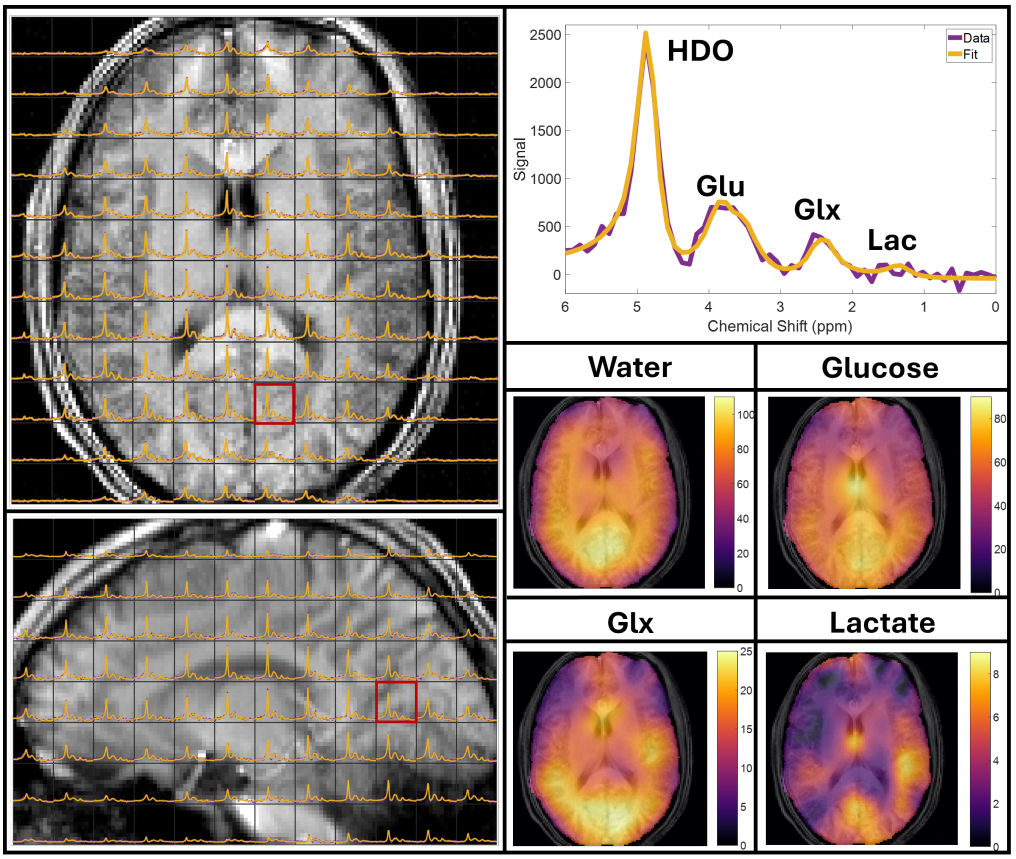

Figure 5.14: *Axial and sagittal slices from a 3D CSI data set (FOV: 180 x 180 x 120 mm^3, 15 mm isotropic resolution) acquired from a participant who had ingested glucose-d_7. Spectra were averaged over six scans and then denoised using a Tucker decomposition and are overlaid on the corresponding slice of the MPRAGE image acquired after ingestion. Experimental data (purple) and fit (yellow) are shown for each voxel. The spectrum from the highlighted voxel is shown in detail in the plot shown upper right. Amplitude maps for each metabolite are also shown, with the colour axis being shared with Fig. 5.13.*

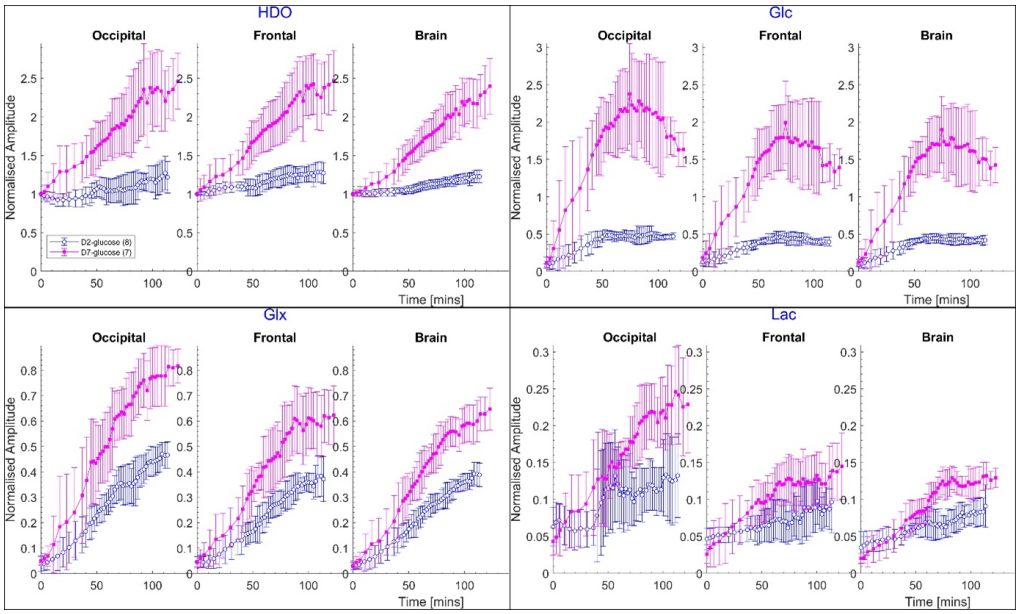

Figure 5.15: *Average time-courses of normalised metabolite signals for the occipital lobe, frontal lobe, and the whole brain from participants who ingested glucose-d_2 (blue, 8 participants) and glucose-d_7 (pink, 7 participants). A running average over a number of the nearest points in time equal to the number of participants was calculated, with error bars representing the standard deviation over the points in the running average. Figures made by Dr. Robin Damion.*

ingestion of glucose. The maximum in the averaged Glc is clearly visible and occurs between 50 and 100 minutes after glucose ingestion. In these plots, it is evident that all metabolite amplitudes from glucose-d_7 ingestion are larger than those from glucose-d_2. It appears the Lac signal does not reach a plateau in the glucose-d_7 occipital lobe time-course compared to the frontal and whole-brain region. However, this is most likely random as the other metabolites time-courses do not vary in the other metabolites and the error on the Lac is high.

The same data, converted to concentrations are shown in Fig. 5.17. These concentrations have been corrected for label-loss, so that the values estimate the concentrations of deuterated molecules that would be observed if no label-loss occurred. The attenuation factor in the concentration calculation corrects for flip-angle and T_1 relaxation. The water content for each tissue is also corrected for: more details on the concentration calculation can be found in Section 5.2.4. As expected, the averaged concentrations of HDO, Glx, and Lac are clearly different between the glucose-d_2 and glucose-d_7 cohorts, with the glucose concentrations appearing similar.

To provide a clearer depiction of the relative metabolite signal amplitudes arising from glucose-d_2 and glucose-d_7 ingestion, Fig. 5.18 shows plots of the ratios of metabolite signals measured from the two glucose isotopologues: Amplitude(glucose-d_7) / Amplitude(glucose-d_2). To calculate the ratio between the averaged glucose-d_2 and glucose-d_7 signals, the data needs to cover similar points in time. Therefore, the glucose-d_2 data is interpolated to the same time series data as the glucose-d_7 data. The error bars are derived from the error bars (standard deviations) of the numerator and denominator using the standard method of combining independent errors of a quotient.

The NA values have been subtracted from the HDO measurements to produce a ratio of the HDO increases above NA. Although there is considerable variability, focusing on the whole-brain ROI (which should have the best SNR), it appears that the ratios are converging to approximately

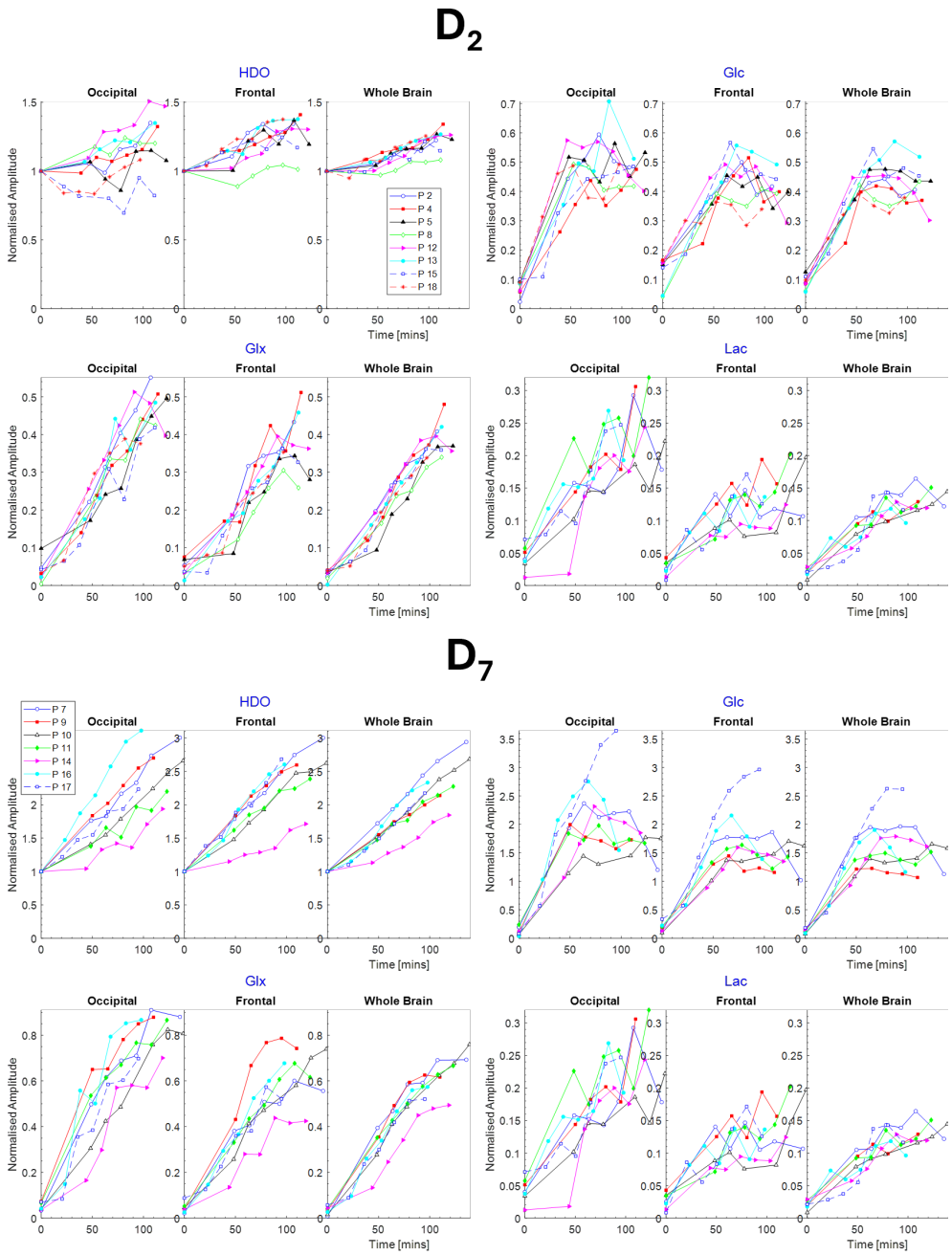

Figure 5.16: *Normalised metabolite signal amplitude time-courses for each participant for glucose-d_2 (top) and glucose-d_7 (bottom) for each ROI: the occipital lobe, frontal lobe, and the whole brain. The results at time = 0 are the results from the pre-ingestion scanning, the HDO results here are used for normalisation. Graphs made by Dr. Robin Damion.*

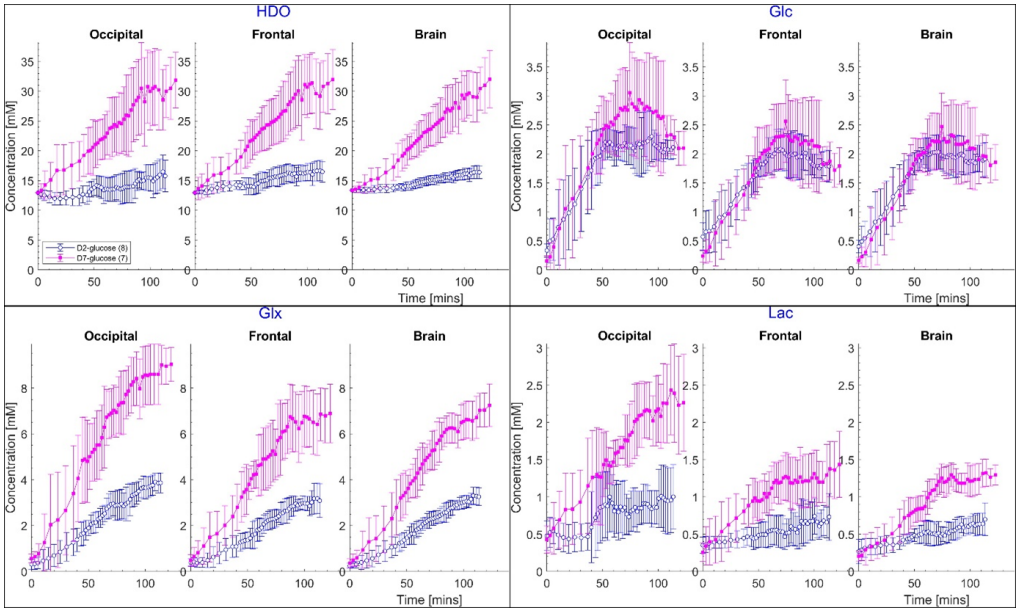

Figure 5.17: *Average time-courses of metabolite concentrations from the occipital lobe, frontal lobe, and the whole brain from participants who ingested glucose-d_2 (blue, 8 participants) and glucose-d_7 (pink, 7 participants). More details on the concentration calculation can be found in Section 5.2.4. A running average over a number of nearest points in time equal to the number of participant was calculated, with error bars representing the standard deviation over the points in the running average. Figure made by Dr. Robin Damion.*

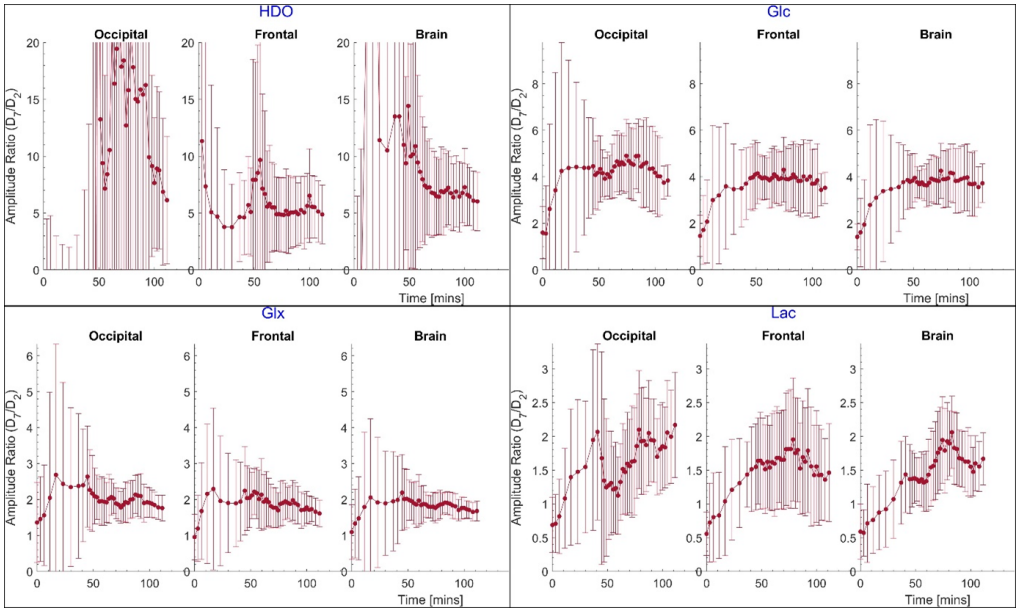

Figure 5.18: *Normalised ratios of signal amplitude for each metabolite following glucose-d_7 and glucose-d_2 for the same regions in Fig. 5.17. The glucose-d_7 data is interpolated (after the moving average in Fig. 5.17. is applied) to the same time-course as the glucose-d_2 data before the ratio is calculated. The amplitude of the errorbars are calculated from the standard deviations of the numerator and denominator using the standard method of combining independent errors of a quotient. Figure made by Dr. Robin Damion.*

constant values, such that for HDO, Glc, Glx, and Lac, the ratios are 5.5 ± 2.5, 3.5 ± 1.0, 1.6 ± 0.4, and 1.5 ± 0.4, respectively. It has been previously suggested that HDO production from the metabolism of glucose-d_7 can be used as a biomarker, that the ratio ΔHDO/(Glx+Lac) of T_1-corrected signal amplitudes (where ΔHDO is the increase in labelled water above NA) has a quasi-stable value of 2.5 [13], calculated by taking account of label-loss from Glx and Lac, and label-gain to HDO.

This value comes from the production of the differing production routes of pyruvate, and how ^{2}H is incorporated into the methyl group of pyruvate. One of the final steps of the formation of pyruvate from glucose is the formation of two three-carbon molecules glyceraldehyde 3-phosphate (GA3P) and dihydroxyacetone phosphate (DHAP), DHAP is then converted into another GA3P and both eventually form pyruvate. During both of these routes alanine aminotransferase (ALT) can influence the loss of ^{2}H labelling. By summing the the HDO, Glx and Lac produced from the two possible routes where ALT is involved and not involved. The ratio of HDO/(Glx + Lac) is then found to be $20/8 = 2.5$. Further details can be found in the paper that first calculated this ratio [13]. The data can then be normalised based on data that looks at ^{2}H and ^{1}H exchange and accounts for the ^{2}H loss in the formation of Glx and Lac [140].

This ratio is shown in Fig. 5.19 as well as similar plots for Glc, Glx, and Lac, for both glucose-d_2 and glucose-d_7. The plots of ΔHDO/(Glx+Lac) for glucose-d_7 appear to also show a quasi-stable region, although at values <2.5. Plots for Glx/(Glx+Lac) appear to show long-time convergence to approximately 0.8 which is similar to what has been shown previously [76], for both glucose-d_2 and glucose-d_7. However, Glc/(Glx+Lac) plots show global maxima at approximately 30 – 70 minutes, which occurs earlier than the maxima of glucose in the plots of Figs. 5.15 and 5.17.

No effect of visual stimulation could be discerned, either in comparison to participants who did not undergo visual stimulation as can be seen in Fig. 5.20 or in comparing metabolite accumulations between frontal and

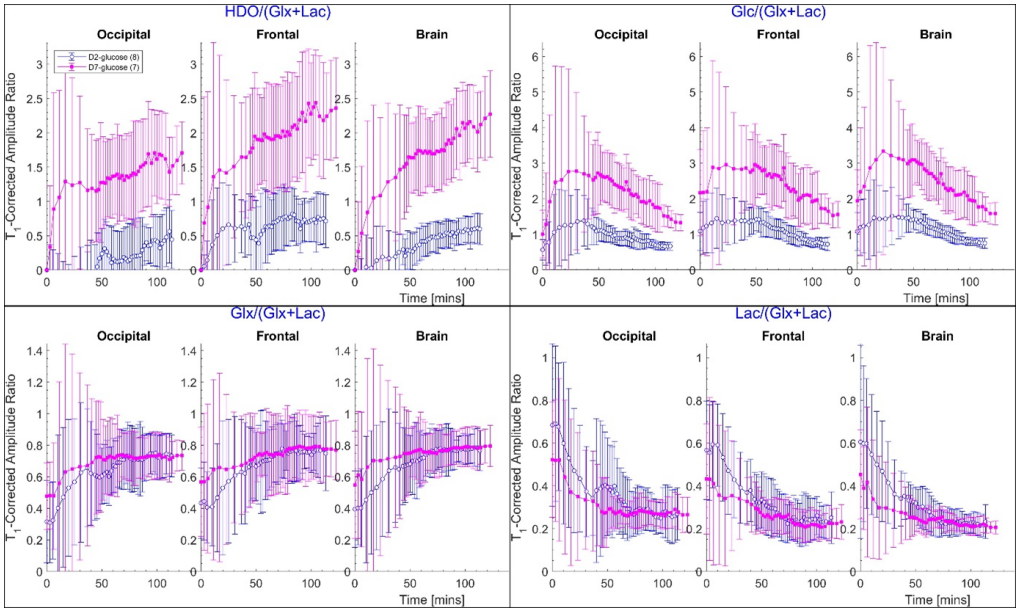

Figure 5.19: *Ratio of each metabolite signal to the sum of downstream metabolites (Glx and lactate) for the same regions shown in Fig. 5.17. The glucose-d_7 data is interpolated (after the moving average in Fig. 5.17. is applied) to the same time-course as the glucose-d_2 data before the ratio is calculated. The amplitude of the errorbars are calculated from the standard deviations of the numerator and denominator using the standard method of combining independent errors of a quotient. Figure made by Dr. Robin Damion.*

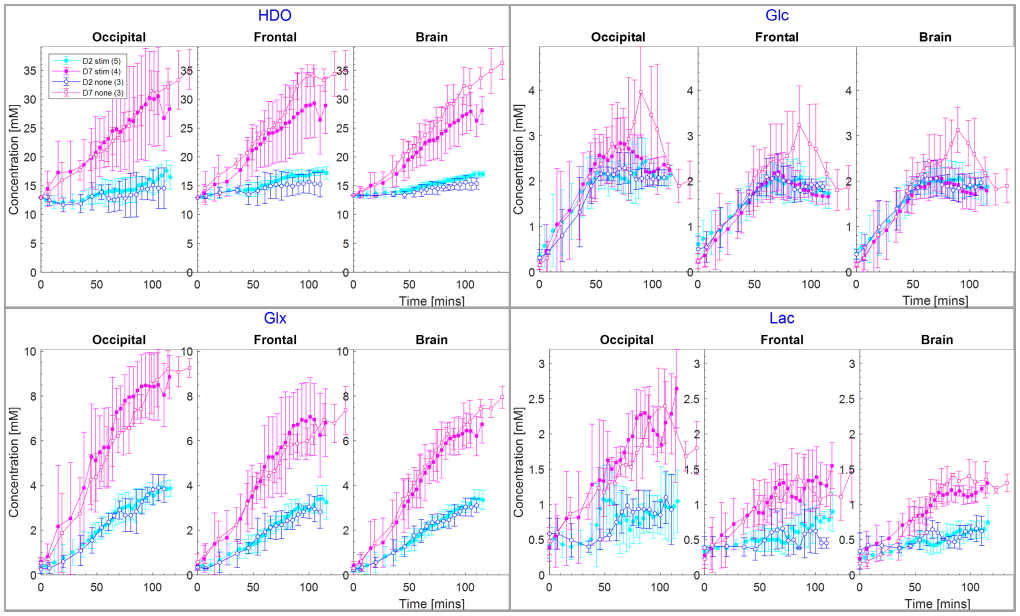

Figure 5.20: *Average time-courses of metabolite concentrations from the occipital lobe, frontal lobe, and the whole brain from participants who ingested glucose-d_2 and had no visual stimulus (blue) and those who were visually stimulated (light-blue) along with those who ingested glucose-d_7 and had no visual stimulus (light-pink) and those were visually stimulated (dark-pink). A running average over a number of nearest points in time equal to the number of participants was calculated, with error bars representing the standard deviation over the points in the running average. Figure made by Dr. Robin Damion.*

occipital lobes as can be seen in Fig. 5.17. An increase in metabolite concentrations, due to an increased metabolism, is expected in the occipital lobe compared to the frontal lobe as the visual cortex lies within the occipital lobe.

5.4 Discussion

^{2}H spectra and CSI data were acquired from fifteen participants, before, and then at 5 or 6 time points after, they had consumed either glucose-d_2 or glucose-d_7 measurements lasted around 90 minutes, with nine of these

participants experiencing visual stimulation during the CSI scans. In all spectra, after glucose ingestion, deuterated water (HDO), non-metabolised deuterated glucose, and Glx were detected for both glucose isotopologues. Lac was also detected in most spectra but was present in lower concentrations, particularly for glucose-d_2, and was generally more challenging to detect, although average time-courses from all participants revealed an unambiguous increase of signal at the lactate frequency (see Figs. 5.15 and 5.17).

Compared to the CSI data, slice-selective deuterium spectra can be acquired in a much shorter time and the higher SNR can provide a more reliable analysis if the magnetic field homogeneity over the slice is good enough to provide a reasonable linewidth. Such spectra are displayed in Fig. 5.11, showing their time evolution from NA to over 100 minutes after glucose ingestion. HDO (4.8 ppm), glucose (approximately 3.8 ppm), and Glx (2.4 ppm) are clearly visible in these spectra, with amplitudes being generally larger for the spectra of the participant who ingested glucose-d_7, especially for the HDO peak. Although possessing a very low SNR, a peak at 1.3 ppm is just visible in some of these spectra and, again, generally appears to be larger in the glucose-d_7 spectra. The fact that it is larger in the glucose-d_7 spectra suggests that it is a result of lactate accumulation but it could also contain a NA lipid component arising from the skull. Examples of spectral fits are shown in Fig. 5.11 for the last time-point spectra in the two displayed data sets. Here it can be seen that spectral components, including the anomeric decomposition of the two glucose isotopologues, have been well fitted with small residuals.

CSI SNR can be improved by increasing the number of averages as opposed to acquiring multiple CSI data sets at different time points. However, by acquiring metabolite time-courses the time point at which the signal from glucose (and other metabolites) is largest can be found. Time-course data can also be used to model the metabolite time-courses. Metabolic modelling has previously been attempted with pre-clinical data [5, 40, 74,

75], and recently modelling been used with human data where glucose-d_2 was ingested orally [36], as opposed to intravenous infusion which is used in animal models. An estimate of the data quality that would have been obtained if only a single CSI was acquired with a higher number of averages can be obtained by combining several of the CSI acquisitions into single data-sets. Figures 5.13 and 5.14 demonstrate the result of doing this for glucose-d_2 and glucose-d_7 data where six consecutive post-glucose-ingestion CSI acquisitions are combined. This would approximately correspond to a single acquisition with 36 averages for a total scan duration of 57 minutes. This duration assumes the full use of acquisition-weighted averaging [133]. Without this, it would take 125 minutes. The spectra shown, from single voxels in the averaged CSI data, have the same essential features as the slice-selective spectra in Fig. 5.11; clear HDO, Glc, and Glx peaks, with small low-SNR peaks where Lac is expected. In this case, it is less likely that these peaks contain a large lipid contribution, which suggests they arise from lactate.

The resolution of the CSI data acquired here is too low to be able to differentiate GM and WM in the cortex after interpolation. ROI-averaged metabolite amplitudes from individual participant data sets were often noisy and their underlying time-dependence could be obscured (see Fig. 5.16). This was more often the case for participants who ingested glucose-d_2, whose metabolite amplitudes were lower, but was also an issue for the Lac signal for both glucose isotopologues. Averaging the data over all participants, however, as presented in Fig. 5.15, delivered a clearer picture of the temporal accumulation of the deuterated metabolites. The glucose time-courses clearly reach a maximum within the timeframe of the experiments, and HDO, Glx, and Lac, all unambiguously show increasing amplitudes over time. The increases in HDO and Glx are as expected from many previous studies, but the observation of an increase in Lac is less common, although it has also been previously reported [76, 114].

No significant difference for any metabolite (HDO, Glc, Glx, and Lac)

was seen between participants that had a visual stimulus applied and those that did not. One could compare the metabolism in the frontal lobe and the occipital lobe, however there was also a difference between the signals from these regions in participants who did not have visual stimulus applied. Because the time-course goes from no detectable signal in Glc, Glx and Lac to a detectable signal it is difficult to compare any other changes above the inter-participant variability which can be larger than 10%. And this variability scales with increased signal from glucose-d_7, which leads to larger standard deviations. However, it is easier to see metabolite changes in response to visual stimulus using other nuclei such as ^{13}C, ^{31}P and ^{1}H as there are already baseline signals making changes easier to detect. Also, even after a long period, the Lac signal is still difficult to detect and fit, so changes in Lac signal amplitude are difficult to detect.

One of the reasons for the large inter-participant variability across all subjects is the evident 'decrease' between NA and the first two time points in all metabolite concentrations, most evidently in HDO. This is because at early time points the metabolism has not had long enough accumulate increased concentrations that would dominate the variability arising from small differences in head position after repositioning in the scanner. The low SNR of the anatomical ^{1}H MPRAGE scan that was acquired could also mean that the ROIs could be better defined and represent the regions more accurately. This is backed up by the largest ROI of the whole brain suffering from this effect the least. Availability of a more sophisticated multi-channel RF coil providing improved SNR for ^{1}H and ^{2}H measurements would help mitigate this problem and allow better definition of ROIs.

One of the main benefits of DMI is the ability to quantify downstream metabolites such as lactate which has been shown to be a useful tool in investigating tumour malignancy [142]. Therefore, the increase in Lac from glucose-d_7 can be useful in future studies. However, the eight times price increase of glucose-d_7 compared to glucose-d_7 along with the increase in analysis difficulty makes glucose-d_2 more clinically viable. With this being

said if the relationship between glycolytic activity and HDO increase was to be investigated further the use of glucose-d_7 could prove to be an invaluable tool in research and in the clinic. It has been shown possible to synthesise deuterated glucose with five labels that is cheaper than both glucose-d_2 and glucose-d_7 [42]. This would make DMI more clinically viable. However, a lot of the complexities of the analysis would not be removed which are mitigated by increases in SNR, therefore it would not be advisable to reduce the dosage to further save on costs.

The differences in the signals in the glucose-d_2 and glucose-d_7 datasets are similar to what has been theorised from animal models [13]. The predicted values are sensitive to exact amounts of label-loss due to ^{1}H - ^{2}H exchange. The increase in HDO signal that is generated from the label loss has been quantified to be approximately six times in glucose-d_7 data compared to glucose-d_2 data. It has already been shown that the increase in HDO for glucose-d_7 is an appropriate measure for metabolism, as the glucose consumption is directly correlated HDO production. However, the reported ratio between HDO and Glx + Lac signals is higher in the literature ($\sim$2.5) than compared to this study ($\sim$1.5) Fig. 5.19. The difference in ratio could come from the difference in infusion techniques, or it could result from differing amount of label loss in the human and rat brain.

5.5 Conclusion

This Chapter reports the first in vivo studies of human participants using glucose-d_7 to track metabolism in the brain. ^{2}H CSI data was acquired over $\sim$90 minutes and changes in metabolite (HDO, Glu, Glc and Lac) were tracked over time and compared to results obtained following similar ingestion of glucose-d_2. De-noising in post-processing was used to enhance SNR for each dataset, acquisition based averaging is also used and could be extended to increase SNR further at the expense of the number of time points measured. Glucose-d_7 has been shown to offer an opportunity to

improve the visualisation of tumour metabolism *in vivo* for patients, by increasing the signal of all available metabolites compared to glucose-d_2.

Chapter 6

Evaluating the Feasibility of Monitoring Lipid Turnover using Heavy Water Loading and ^{2}H Magnetic Resonance

6.1 Introduction

Adipose tissue (more commonly known as body fat) is key for energy storage and can be found either under the skin (subcutaneous fat) or around internal organs (visceral fat) as well as in bone marrow, in breast tissue and around muscles. The cells that make up this tissue are known as adipocytes. They store energy as TriacylGlycerols (TG), and the breakdown/turnover of adipocytes and TG is thought to be a good indicator of metabolic health and homeostasis. Adipose tissue growth is possible through enlargement of existing adipocytes (hypertrophy) as well as by increases in pre-adipocyte and adipocyte numbers (hyperplasia). Adipocyte death is also a vital part of the TG turnover [143]. The differences between these processes in adipose tissue provides vital information on metabolic health [144]. It was originally thought that increases in adipocyte count

only occur during childhood and adolescence [145], and that changes in weight in adulthood are due to adipocyte size changes. However, new studies now show this is not the case [146], indicating the importance of *in vivo* studies into adipose tissue turnover.

In vitro methods using cell cultures can be used to assess adipose/lipid turnover and can provide information about specific adipocyte growth and death [147]. However, results from cell culture experiments do not necessarily provide insight into the turnover of lipids in tissue in the human body. One of the reasons for using *in vitro* methodology is that the half-life of TG *in vivo* in humans has been found to be ∼six months [97], which can make it difficult to measure. However, lipid turnover can be measured by using ^{2}H labelling through D_2O ingestion and invasive tissue sampling (biopsy), with the analysis being performed using mass spectrometry and application of Mass Isotopomer Distribution Analysis (MIDA) [97, 99, 143, 148]. Following heavy water loading, ^{2}H makes its way into the glycerol moiety and fatty acid chains of triglycerides during lipid formation (lipogenesis) making it possible to measure TG synthesis [99]. Using this method differences in the TG synthesis rate between healthy and insulin-resistant individuals [149] and between different races [150] have been evaluated. However, the need for biopsy restricts the range of tissue sites that can be sampled (e.g., making it difficult to sample visceral fat) and causes patient discomfort. Heavy water loading has previously been utilized in conjunction with magnetic resonance imaging and spectroscopy (MRI/MRS) allowing *in vivo* measurement of enhanced ^{2}H MR signals from water in humans and from water and fat in animals [102, 105]. The enrichment of ^{2}H into HDO that can be measured using MRI or MRS has been shown to follow physiological estimates and can therefore be accurately predicted [105]. The enrichment into lipids measured using invasive techniques is much slower [97, 143] but can also be predicted [143].

6.2 Theory

The ^{2}H MR signal that arises from naturally occurring HDO *in vivo* is ∼0.015% (NA). Water turnover in the body involves a balance between water loss through urinating, breathing and sweating and water replenishment through what we eat and drink. The amount of water turning over each day can be written as L. As has already been shown it is possible to increase the *in vivo* ^{2}H abundance by ingesting extra ^{2}H in the form of heavy water (or an aqueous solution of heavy water). The new ^{2}H abundance in a day (A_{t+1} as a percentage) can then be estimated using an iterative calculation, and is relative to a participants total body water (BW) volume as shown here

$$A_{t+1} = A_t + \frac{L[\mathrm{NA} - A_t]}{\mathrm{BW}} + \frac{D}{\mathrm{BW}} \tag{6.1}$$

where the abundance in the previous day is given as A_t, and the amount of ^{2}H consumed in the day is D. This equation is useful when the extra ^{2}H is ingested on a daily basis, the change in ^{2}H abundance with respect to time (dA/dt) can then be calculated as a differential equation shown here

$$\frac{dA}{dt} = \frac{L[\mathrm{NA} - A]}{\mathrm{BW}} + \frac{D}{\mathrm{BW}} \tag{6.2}$$

It is noted that L/BW is the water turnover relative to body weight which can be considered as a rate constant (λ_w). We can estimate $\lambda_w \sim 3/41$, assuming 3 L of fluid turnover and a typical BW of 41 L. It can be beneficial to look at the change in ^{2}H abundance as a multiplicative change compared to NA ($E = A/\mathrm{NA}$). The differential equation then becomes

$$\frac{dE}{dt} = \lambda_w(1 - E) + \frac{D}{\mathrm{BW} \cdot \mathrm{NA}} \tag{6.3}$$

Once the loading period ends ($D = 0$), Eq. 6.3 can be simply solved. Here the enrichment E exponentially decays from E_0, the enrichment at the end of loading, to natural abundance ($E = 1$ at $t = \infty$ and $E = E_0$ at $t = 0$), with a time constant λ_w. The solution is shown empirically here

$$E = (E_0 - 1)\exp(-\lambda_w t) + 1 \tag{6.4}$$

To calculate the enhancement of ^{2}H in water, accurate estimates for L and BW are needed. It is difficult to accurately determine L as it depends on an individual's lifestyle, however BW can be estimated from known formulae. Lines of best fits have been found that relate total body-water to anthropometric measurements (height (H), weight (W), age (A) and gender) [1], equations for the relationships are found here for males

$$\text{BW(litres)} = 2.447 - 0.09516A(\text{years}) + 0.1074H(\text{cm}) + 0.3362W(kg) \tag{6.5}$$

and for females here

$$\text{BW(litres)} = -2.097 + 0.1069H(\text{cm}) + 0.2466W(kg) \tag{6.6}$$

Data from lipid turnover studies looking at the ^{14}C content of fat show that the rate of lipid storage is ∼16 kg/year (44g/day) [151, 152], which gives a time constant (t_f) for lipid turnover of ∼397 days. This estimate assumes a healthy 70 kg individual with a body fat content of 25%, but the value varies depending on the individual's weight, age and height. By making some assumptions about the incorporation of ^{2}H from water into fat we can use the value of t_f to estimate the concentration of ^{2}H in fat during and after a period of heavy water loading. The enhancement of the ^{2}H concentration in fat relative to natural abundance depends on the rate constant ($\lambda_f = 1/t_f$) the number of days of heavy water loading (t), the level of water enhancement (E) and the fraction (f) of H atoms incorporated into CH_2/CH_3 groups from water in newly formed fat. It has been found that ∼20% of stored lipids arise from De Novo Lipogenesis (DNL), compared to triglycerides recycled from fatty acid breakdown. In the case of triglyeride recycling H atoms in CH_2/CH_3 groups do not exchange with water but in the case of DNL 1/3 of the H atoms in CH_2/CH_3 groups come from water, and 2/3 are derived from the metabolite NADPH [153]. Conservatively the

fraction (f) of H atoms in CH_2/CH_3 derived from water can therefore be approximated to a conservative value of 5%. It is important to note that the H in NADPH can undergo catalytic exchange with water which can boost enhancement. If the water enhancement E is approximated at $\times 100$ for 28 days, and assuming a range of f of 5-20% this gives an enhancement of 35-140%. This enhancement should theoretically be detectable using ^{2}H MRS *in vivo* [25].

Assuming the water ^{2}H enhancement E is constant and equal to E_0 the enhancement of ^{2}H in lipids (S) after time t can be estimated using the assumed values for λ_f and f and the following analytical expression

$$S = 1 + f(E_0 - 1)(1 - \exp(-\lambda_f t) \tag{6.7}$$

However, this is not usually the case as often the loading regime will often involve a changing concentration of ^{2}H in water. For example, during rapid loading participants can experience periods of dizziness and nausea [119], and to mitigate this issue, the volume of heavy water consumed per day can be varied during the loading period [97, 105]. Therefore, a more generalised differential equation (Eq. 6.8) is used to estimate the enhancement in fat, which is calculated iteratively and numerically using the temporally varying water enhancement $E(t)$. Now changes in the loading regime can be accounted for before and after the cessation of the loading period. Example loading regimes, HDO enhancements and corresponding signal enhancements in lipids are shown in Fig. 6.4 according to

$$\frac{dS}{dt} = \lambda_f(f(E(t) - 1) + 1 - S) \tag{6.8}$$

Solutions of Eq. 6.8 are used to predict the enhancement of lipid signal that should be detected using ^{2}H MRI/MRS, leading to an estimated increase in fat signal of 30-40%. This level of enhancement should be detectable and could therefore inform on metabolic health.

As a precursor to tracer studies we explored the deuterium spectrum obtained from the lower leg at NA in four healthy human participants,

characterising the T_1 and T_2^* relaxation times of the two spectral lines and demonstrating that measurements are feasible at 3T magnetic field strength on a clinical scanner using a transceive, surface RF coil. We also evaluate whether ^{2}H MR at 3T in conjunction with D_2O loading could be used for non-invasive monitoring of lipid turnover in human subjects as an alternative to a methodology that uses D_2O loading in conjunction with invasive biopsy. Three different healthy male participants were loaded for approximately four weeks and scanned weekly or fortnightly for approximately sixteen weeks using ^{2}H CSI imaging.

6.3 Methodology

6.3.1 NA Scanning

T_1 relaxation times of HDO and lipid signals were measured *in vivo* at 3T in the calf of in four different healthy human participants [116]. Scanning was performed on a 3T scanner (Philips Achieva) using an in-house built surface coil (5 cm diameter) tuned to the deuterium resonance 19.6 MHz. The surface coil was placed under the calf muscle of the left leg. Non-localised Inversion Recovery (IR) spectra were acquired at NA, using a 900 Hz bandwidth adiabatic hyperbolic secant inversion pulse followed by an inversion delay and then a non-selective RF pulse of 90° nominal flip angle. Inversion times were τ: 5, 10, 20, 40, 80, 160, 320, 1000 ms, for a fixed TR: 1200 ms (time between adiabatic pulses). FIDs were collected with 512 samples, NSA: 128, BW: 3000 Hz. FIDs were truncated, zero-filled to 512 points, and line-broadened using a 5 Hz exponential filter.

The data was analysed using code written in MATLAB (MathWorks, Natick, USA). Spectra acquired with a surface coil over a large volume can show peaks with different phases due to the averaging of various RF factors over spatial distributions which are different for the molecules producing the spectral peaks. Therefore, a global zeroth-order phase-correction can-

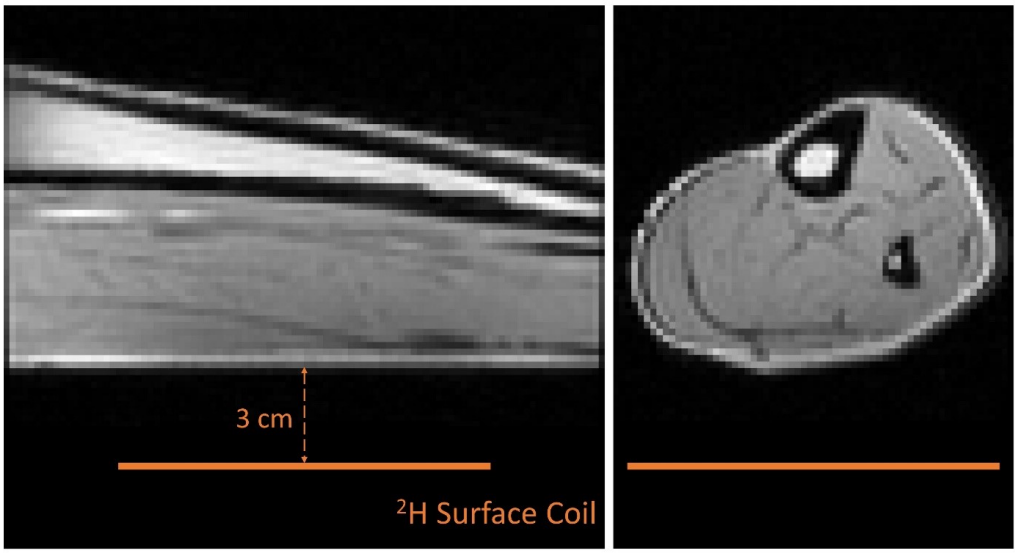

Figure 6.1: *^{1}H images of the calf (FOV: 128 × 128 × 192 mm^3) also showing the position and extent of the ^{2}H surface coil. Left image: mid-sagittal slice. Right image: mid-axial slice. Figure made by Prof. Richard Bowtell.*

not be applied. Instead, the complex spectra were fitted to a sum of two complex Lorentzian lineshape functions employing independent phases for each spectral peak, as well as independent values of amplitude, frequency, and R_2^*. The inappropriateness of a simple phase-correction and the fact that the phases are functions of inversion time (other than the usual phase-shift at the null-point) mean that the inversion-recovery curve also needs to be analysed as a complex function for each resonance as this allows phase to vary with τ and TR. The complex equation used for fitting is shown here

$$M(\tau) = \alpha - \beta \exp(-\frac{\tau}{T_1}) + (\beta - \alpha) \exp(-\frac{T_R}{T_1}) \tag{6.9}$$

where $M(\tau)$ is the complex magnetization (determined by the spectral amplitude and phase) and τ is the inversion time, while B and α are complex coefficients. The T_2^* relaxation times for each peak were obtained from the fit of the Lorentzian and averaged over all inversion delays, the T_1 re-

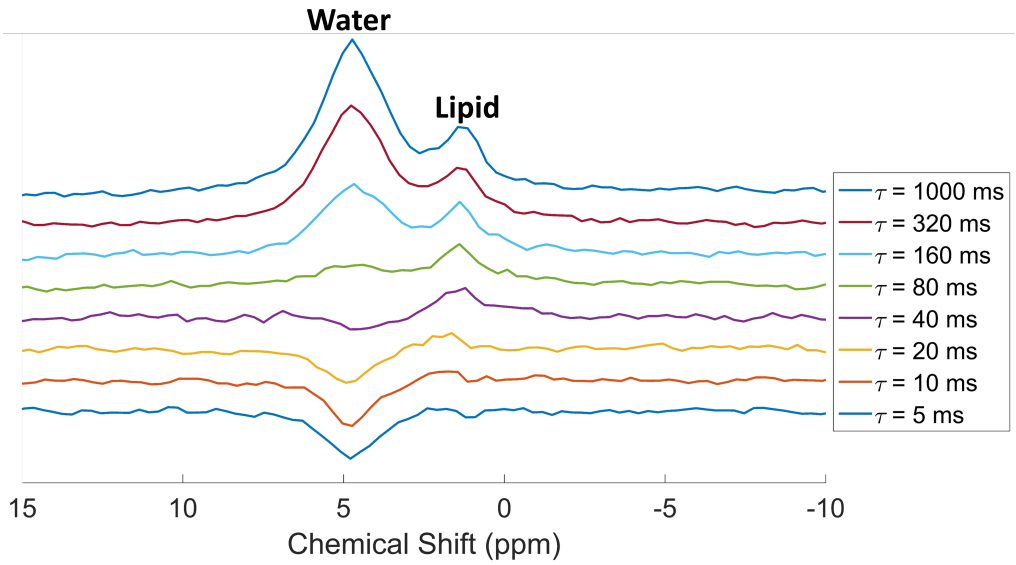

Figure 6.2: *In vivo spectra obtained during an inversion-recovery experiment. At varying inversion times (τ) ranging from 5 to 1000 ms which are given in the legend, in milliseconds.*

laxation time was found from the fit of the IR curve for each peak. Two peaks were consistently measured in all spectra. The chemical shift separation of these peaks was measured to be 3.55 ± 0.12 ppm. An example of the spectra that were acquired at different inversion times can be seen in Fig. 6.2.

Results

The larger peak in Fig. 6.2 corresponds to the HDO present in the calf, whilst the second, smaller peak originates from the CHD groups in adipose tissue (body fat). After correcting for applied line-broadening, mean T_2^* values were obtained for HDO of 8.2 ± 1.6 ms, and 14.0 ± 2.5 ms for lipids (n=4, see Table 6.1). Figure 6.2 shows a set of spectra acquired during an IR experiment. All spectra were globally shifted in reference to the spectrum of longest inversion time. Figure 6.3 shows the complex spectral amplitudes and the fits to Eq. 6.9, for the two peaks (HDO and lipids). Mean T_1 values were found to be 199 ± 34 ms for HDO and 56 ± 10 ms

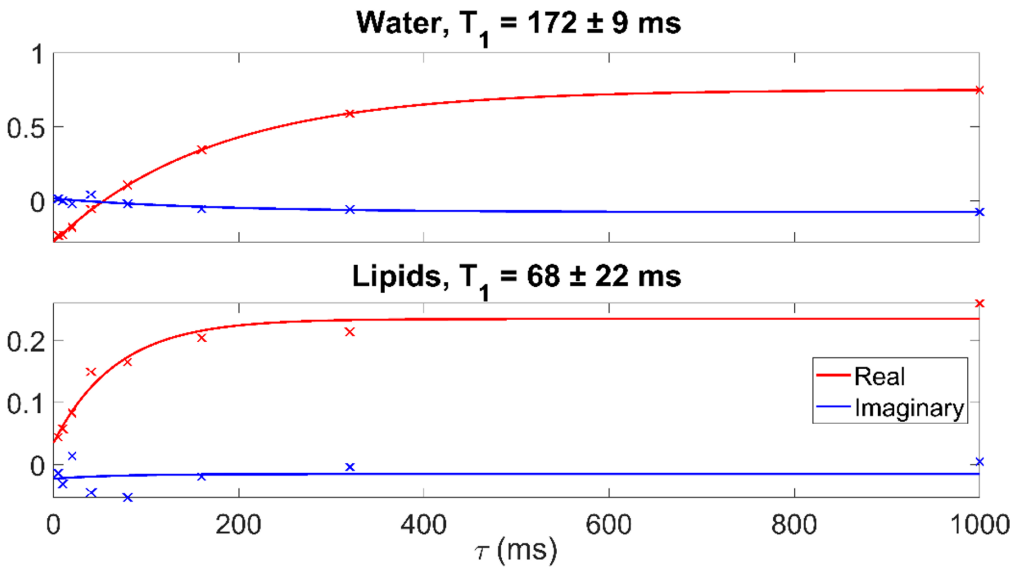

Figure 6.3: *An example of the complex amplitudes and the fitted curves for water and lipids as a function of inversion time, τ.*

for lipids (n=4, see Table 6.1).

6.3.2 Fat Measurements by D_2O Loading

The second study involved measuring ^{2}H signals from the calf and abdomen in three different healthy male participants who underwent 28-days of drinking a mixture of heavy and regular water (D_2O/H_2O: 70/30%). Fig. 6.4 shows the loading schedules that participants followed, plus estimates of the expected changes in water and fat signals over 120 days. During loading the most D_2O that was ingested on a single day was 150 ml. This slowing down of initial ramping of ^{2}H enrichment compared with the regime used in Chapter 4 meant that side effects of the loading were reduced. No reports of dizziness or nausea were reported during initial loading. Using the equations described in Section 6.2 we find that the ^{2}H signal from water, increases to approximately 100×NA in the loading period and then decreases after loading ceases, halving in amplitude every ∼6 days (Fig. 6.4). The fat signal rises more slowly to a maximum of 1.3-1.4 ×NA and then slowly decreases, as also shown in Fig. 6.4.

Subjects	Water		Lipids		Peak Separation
	T_1 (ms)	T_2^* (ms)	T_1 (ms)	T_2^* (ms)	(ppm)
1	172 ± 9	7.83 ± 0.03	68 ± 22	18.1 ± 0.3	3.52 ± 0.01
2	198 ± 10	8.81 ± 0.04	41 ± 12	15.2 ± 0.4	3.59 ± 0.02
3	255 ± 14	10.2 ± 0.4	61 ± 18	11.8 ± 0.2	3.57 ± 0.01
4	172 ± 13	5.85 ± 0.04	57 ± 7	12.4 ± 0.1	3.70 ± 0.01
Mean	**199**	**8.2**	**56**	**14**	**3.55**
SD	**34**	**1.6**	**10**	**2.5**	**0.12**

Table 6.1: *^2H relaxation times of HDO and lipid signals from the calf, and the measured chemical shift separation. Errors on values are the standard deviations obtained from the covariance matrix of the fitting. SD is the sample standard deviation.*

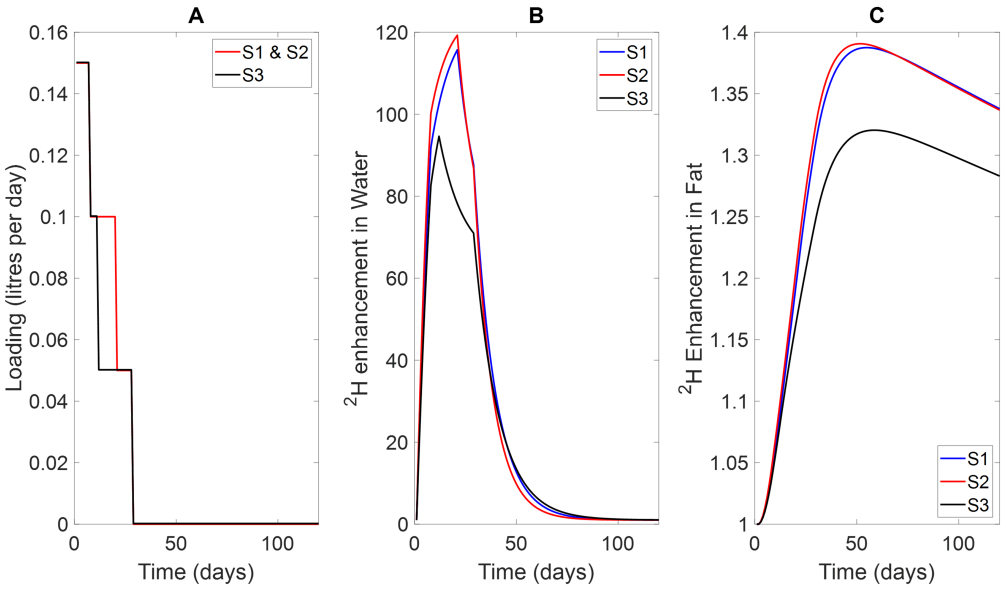

Figure 6.4: *(A) Loading regimes followed by the three subjects (S1, S2 and S3): volume of 70% D2O/30% H_2O ingested per day. (B) Estimated signal enhancement in water signal relative to NA. (C) Estimated signal enhancement in fat relative to NA. These values were estimated using individual subject's weight, height, and age, assuming 3.75 litre water turn-over per day, lipid half-life of 270 days [151, 152]; 5% of hydrogen atoms in fatty acid chains of new lipids derived from water [99].*

Figure 6.5: *Example of the coil positioning for the surface coil used to obtain data from the abdomen. Vitamin/oil pills can be seen on the side of the coil which were used as anatomical landmarks.*

Scans were performed on the same 3T scanner equipped with different in-house built ^{2}H surface coils (5 cm-diameter for calf; 12 cm for abdomen, more information about the RF coils can be found in chapter 3). Measurements were made before loading, to characterise NA signals, and then every ∼14 days during/after loading for a further 8 sessions. Anatomical landmarks were used to position the coils as far as possible over the same region for each scan (under the calf/adjacent to the right abdomen near the liver). An example of the coil positioning used for obtaining data from the abdomen can be seen in Fig. 6.5. Here, the distance from the top of the head to the coil and from the top of the head to the end of the table is measured to characterise the coil position. Before loading started and at the end of the loading period, subjects were scanned multiple times in a session with inter-scan repositioning to allow estimation of fractional signal variation due to positioning errors. A short TR of 50 or 70 ms was used to maximise the SNR of the signal from fat, based on the relaxation

Scan Parameters	Gradient Echo		Bulk Spectra	1D CSI		3D CSI	
Nuclei	^{1}H		^{2}H	^{2}H		^{2}H	
Region	Calf	Abdomen	Both	Calf	Abdomen	Calf	Abdomen
FOV (mm^3)	128x128x192	446x446x250	n/a	300x300x150	300x300x140	150x150x200	140x40x200
Voxel Size (mm^3)	2 mm (isotropic)		n/a	300x300x15	300x300x20	15x15x20	20 mm (isotropic)
TR (ms)	20		50	50		50	
TE (ms)	2.1	1.6	0.37	1.8	1.7	1.7	
BandWidth (Hz)			2000	2000		2000	
Averages			256	1024		36	48
Samples			64	64		64	
Scan Time (s)	122	88	13	136	91	520	420

Table 6.2: *The imaging and spectroscopic scan parameters used to investigate fat signal increases following D_2O loading, for both regions (calf and abdomen). 3D CSI measurements were also obtained with a TR of 70 ms.*

time measurements previously made at NA (see Table. 6.1). A full list of scan parameters can be found in Table 6.2. Some of the scan parameters changed when a TR of 70 ms was used, instead of a 50 ms TR.

Code written in MATLAB (MathWorks, Natick, USA) using the OXSA-AMARES [73] toolbox was used to fit the signal from each voxel to a model incorporating water and fat peaks; in the calf, the water signal was modelled as a doublet with equal amplitudes (due to quadrupolar splitting) [104]. HOSVD [91] with a core matrix of [16 5 5 5] was applied to the 4D data to improve SNR. Water peaks were fitted with a chemical shift ∼4.8 ppm with a lipid peak at ∼1.3 ppm. Both sets of peaks shared the same phase in fitting. To produce single measures of signal enhancement with reduced sensitivity to FOV-positioning, we averaged fat and water signal amplitudes over ROIs ($3 \times 3 \times 3$/$3 \times 5 \times 3$ voxels covering $45 \times 45 \times 60$ / $60 \times 100 \times 60$ mm^3 for the calf/abdomen) positioned relative to the voxel with maximum water signal (i.e., over the centre of the surface coil) to obtain a water value, and shifted 1 voxel closer to subcutaneous fat (right for abdomen, posterior for calf) to obtain a lipid value, as shown in Figs. 6.6 and 6.7.

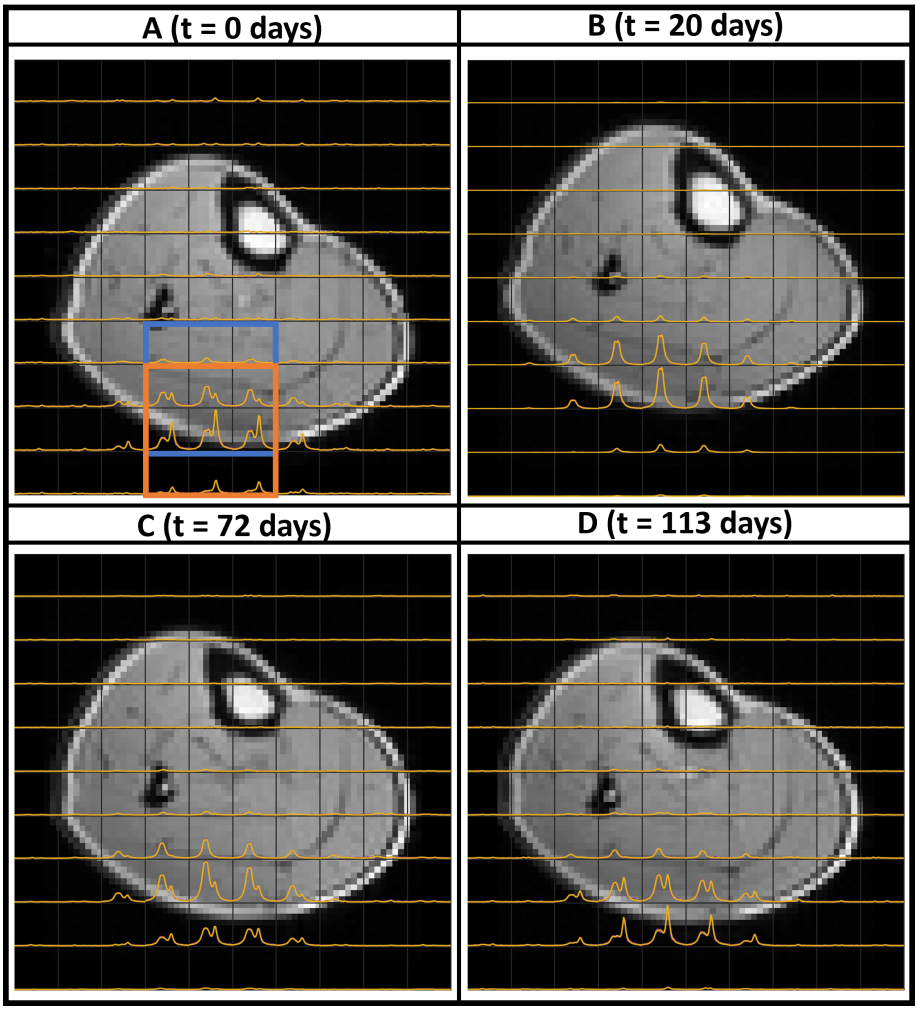

Figure 6.6: *3D CSI spectra in a single axial slice in the calf plus OXSA-AMARES fits with different scalings, overlaid on corresponding ^{1}H GE images. Data was acquired from Subject 1 at four time-points: (A) at NA before loading (t=0 days); (B) at peak loading (t=20-days) where the only peak visible is from HDO; (C) after loading had ceased at t=72 days; (D) at t=113 days. ROI for signal averaging for water (blue) and fat (orange), are shown in (A). The fat ROI was displaced by one voxel towards the surface coil to maximise sensitivity to subcutaneous fat. The peak with the higher chemical shift (appearing furthest left) the other peak is from lipids.*

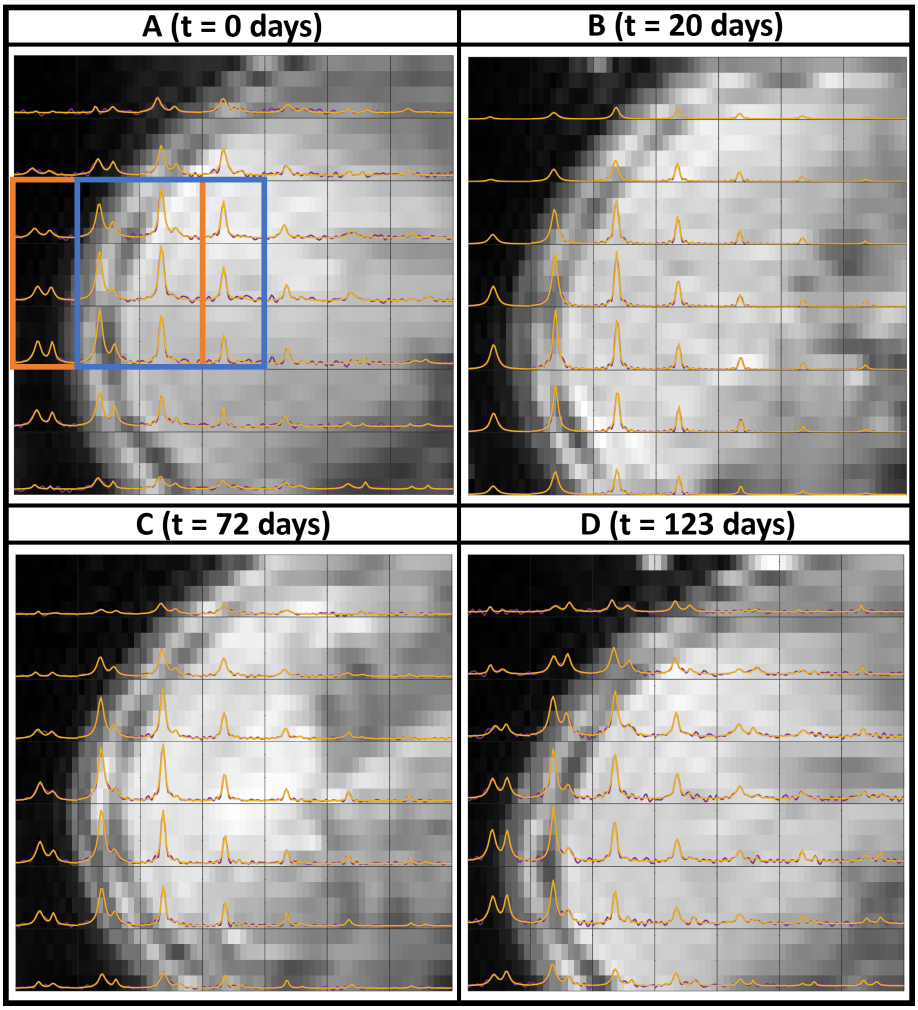

Figure 6.7: *3D CSI spectra in a single sagittal slice in the abdomen plus OXSA-AMARES fits with different scalings, overlaid on corresponding* ^{1}H *GE images. Data was acquired from Subject 1 at four time-points: (A) at NA before loading (t=0 days); (B) at peak loading (t=20-days) where the only peak visible is from HDO; (C) after loading had ceased at t=72 days; (D) at t=123 days. ROI for signal averaging for water (blue) and fat (orange), are shown in (A). The fat ROI was displaced by one voxel towards the surface coil to maximise sensitivity to subcutaneous fat. The peak with the higher chemical shift (appearing furthest left) the other peak is from lipids.*

6.4 Results

Figures 6.6 and 6.7 show 3D-CSI-data acquired from Subject 1 (single transverse/sagittal slice from the calf and the abdomen respectively, overlaid on ^{1}H GE images) at four different time-points. A fat peak is seen in superficial voxels spanning subcutaneous fat close to the surface coil in the NA images (Figs. 6.6 and 6.7A), along with a water peak, which appears over a wider spatial extent and is broadened by quadrupolar splitting in calf muscle (Fig. 6.6).

Superficial fat signals are also evident post-loading (Figs. 6.6 and 6.7 C,D), but during loading are swamped by the ∼100× larger water signal (Figs. 6.6 and 6.7B) making them indistinguishable in appearance and in fitting. A robust and reliable fit to the fat signal could only be achieved at times >50 days when the water signal had decreased to <10×NA (indicated by significantly elevated Cramer-Rao lower bound values at t<50 days).

Figures 6.8 and 6.9 show the temporal variation of the ROI-averaged fat and water signals in calf and abdomen, respectively. As predicted from simulations (Fig. 6.4B) an increase in water signal to nearly ×100 NA is evident, with a lower enhancement in Subject 3 who loaded less (Fig. 6.4A). Although the fat signal shows significant early enhancement (t < 50 days) this tracks the water enhancement and is likely due to poor spectral fitting. Based on the predicted long-term elevation of fat signal (Fig. 6.4C), we focused on the average fat signal enhancement at times > 50 days where fitting was robust (Fig. 6.10).

6.5 Discussion

6.5.1 Comparing other Relaxation Times

From our measurements of the lipid signal's 3.55 ppm chemical shift relative to water, it most likely originates predominantly from deuterium in methylene groups (-CH_2-) of fatty acids, consistent with signals observed

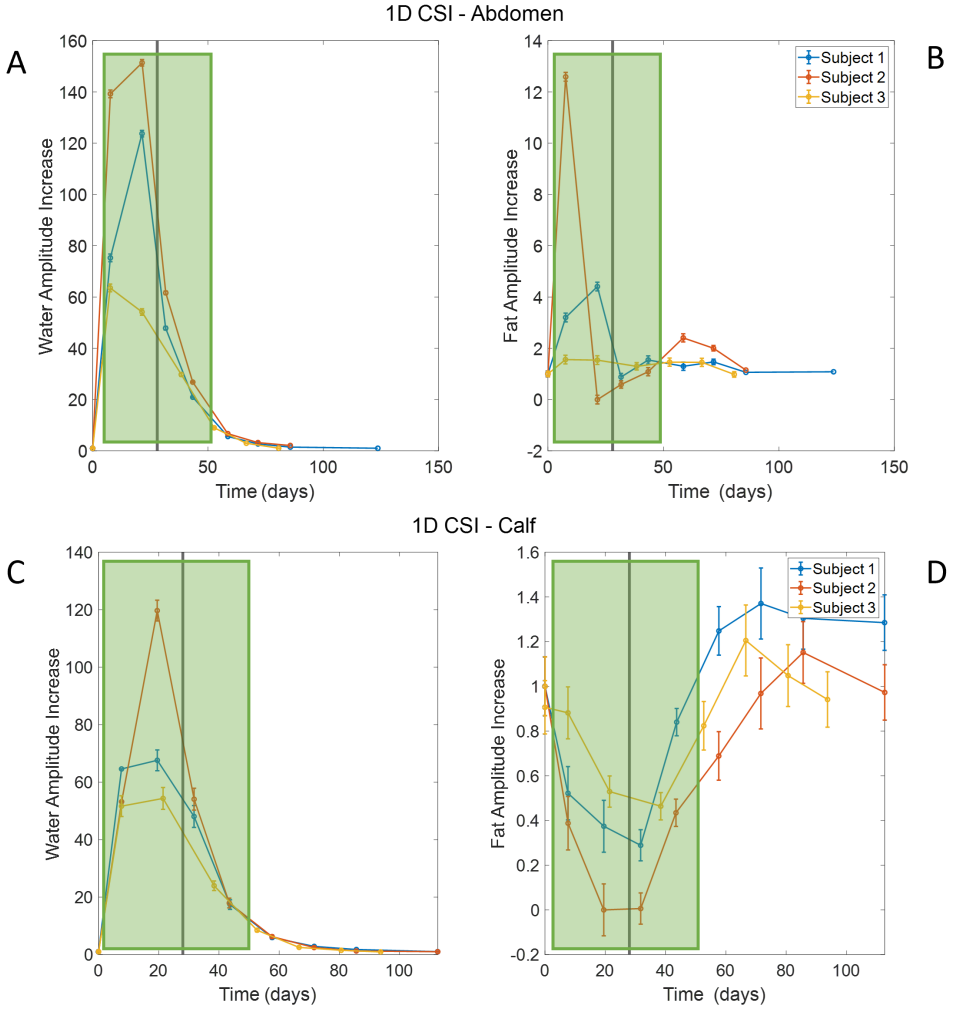

Figure 6.8: *Plots of the temporal variation of the ROI-averaged 1D CSI water and fat signal amplitudes scaled by the measurement at NA for the three subjects. (A) water in Abdomen; (B) fat in Abdomen; (C) water in Calf; (D) fat in Calf. The vertical black line indicates the end of the 28-day loading period. Fat signals are only well characterised by the fitting at t> 50 days (outside green box) when the water signal is < 10xNA. Error bars derived from the relative error measured from repeated experiments at NA. Amplitude increase is relative to a baseline of 1.*

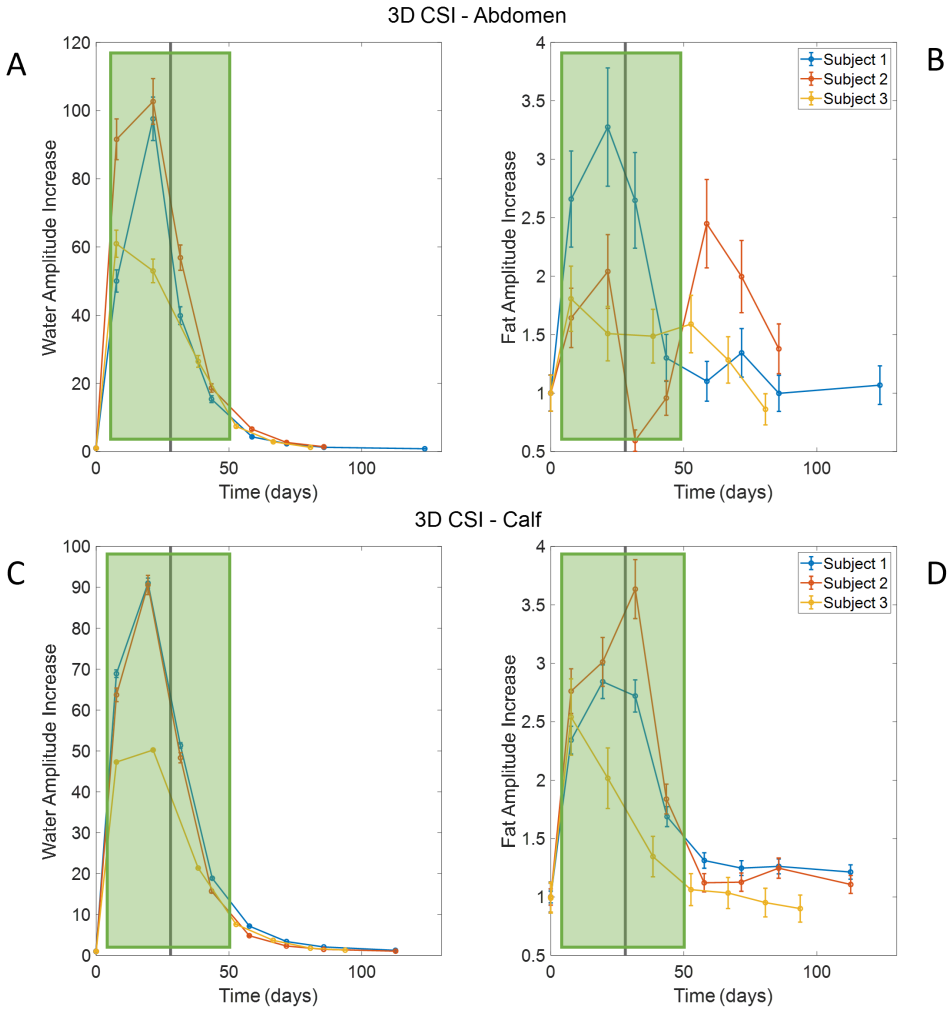

Figure 6.9: *Plots of the temporal variation of the ROI-averaged 3D CSI water and fat signal amplitudes scaled by the measurement at NA for the three subjects. (A) water in abdomen; (B) fat in abdomen; (C) water in calf; (D) fat in calf. The vertical black line indicates the end of the 28-day loading period. Fat signals are only well characterised by the fitting at t> 50 days (outside green box) when the water signal is* $< 10 \times NA$*. Error bars derived from the relative error measured from repeated experiments at NA. Amplitude increase is relative to a baseline of 1.*

		Subject 1	Subject 2	Subject 3
Calf	1DCSI	1.22 ± 0.02 (P<0.05)*	1.85 ± 0.05 (P=0.07)	1.30 ± 0.07 (P=0.10)
	3DCSI	1.26 ± 0.02 (P<0.01)*	1.15 ± 0.03 (P=0.03)*	0.99 ± 0.04 (P=0.61)
Abdomen	1DCSI	1.30 ± 0.07 (P<0.01) *	0.90 ± 0.12 (P=0.70)	1.05 ± 0.08 (P=0.29)
	3DCSI	1.13 ± 0.08 (P=0.09)	1.94 ± 0.31 (P=0.05)*	1.25 ± 0.21 (P=0.18)

Figure 6.10: *Average and standard errors of the fat signal enhancement relative to NA at times of more than 50 days after the start of loading. Values are show for calf and abdomen for the three subjects. P-values for single-sided t-test for difference from NA are also reported.*

previously in proton MRS [154] and in agreement with most previous *in vivo* ^{2}H measurements [102]. In studies that administered D_2O to normal, obese, and diabetic mice, a peak from the deuterated water and a second peak assumed to be CHD groups from adipose tissues were observed [25, 102], and the position of the CHD peak was in the approximate range of chemical shifts of 3.4 ± 0.4 ppm lower than the water resonance. Similarly, experiments on rats produced a lipid signal at approximately 3.4 ppm below the water peak [155]. In contrast, during experiments on the hind limbs of mice with tumour xenografts [90], an HDO peak was observed along with a second peak at 2.8 ppm below the water position. It was suggested [90] that this peak arose from cholesterol (or esters of), which may be actively synthesised in many tumour cells.

Previous deuterium T_1 measurements in muscle water produced values of 130 ± 7 ms (mouse, 9.2 MHz, 25°C) and 160 ± 2.4 ms (rat, 13.7 MHz, *ex vivo*) [156]. Our measured values are higher, possibly due to the higher *in vivo* temperature. A previous measurement of the "CHD group" found T_1: 34 ± 4 ms (mouse abdomen, 30.7 MHz, in vivo) [25], which is smaller than the value measured here. Our longer value could be a consequence of reduced accuracy caused by incomplete inversion of the lipid magnetization because of its short relaxation time [157].

6.5.2 Fat Changes

Previous research in animal models indicated that increases in fat are still observable ∼20 days after loading cessation, although substantial changes in the fat signal occur prior to this point [25], which is supported by this work. Therefore, during our measuring period of > 50 days fat signal should still be increased. Fat signal was increased relative to NA in 5 of the 6 measurements and the increase reached statistical significance ($P<0.05$) in three measurements (Fig. 6.10). These results provide encouraging evidence that ^{2}H MR can be used to detect the increased deuteration of subcutaneous fat resulting from lipid turn-over during long-term heavy water loading.

The wider linewidths of the HDO signals in the calf compared to the liver are due to quadrupolar splitting induced by anisotropic order in the muscle [104], while motion averaging in the liver tissue mitigates this effect. This disparity makes detecting fat changes in the calf more challenging, as the fat peak is more likely to be contaminated by the broader peak from the large HDO signal. The main experimental challenges were in quantifying fat signals in the presence of large water signals and in reproducibly positioning the surface RF coils in repeated experiments. To optimize lipid signal detection in the calf, a smaller coil was used, which is more sensitive to subcutaneous fat, while a 12 cm coil was employed in the abdomen.

6.5.3 Potential Improvements

Previous research has demonstrated the feasibility of using inversion recovery sequences to null the HDO signal which leads to more reliable measures of changes in the fat signal [102], especially when a dominant HDO signal is still present. If the HDO peak was nulled well enough consistently, spectroscopy would not be needed and imaging sequences tuned to the ^{2}H resonance of lipid could be implemented. This could potentially result in higher SNR or higher resolution. This can also be achieved post-processing

through a similar technique that has been used to de-noise MRSI data, Hankel Lanczos singular value decomposition. This technique is similar to HOSVD except now the single values that contribute the most are removed, which reduces SNR. However, this approach can remove overlapping water peaks and has been commonly used in ^{1}H spectroscopy [88, 158].

In future work, higher field could be used to provide better spectral separation of fat and water signals and 3D-printed, individualised coil holders would allow more reproducible coil positioning. This study utilized lower levels of ^{2}H loading compared to previous research (2% abundance of ^{2}H compared to 10%). Studies focused on body composition employ a similar level of heavy water loading to what was used in this study. The results of a similar study could also be combined with better ^{1}H measurements to exclude any change in fat signal amplitude over the experimental time period.

By making all the above improvements it could be possible to detect visceral lipids as well as obtain earlier time-points which would mean functional/kinetic modelling could be employed to distinguish different cohorts of participants. Cohorts could include insulin resistant individuals [159] and between races [150] which have already been investigated using the invasive D_2O loading methodology. These studies would allow comparisons to be made for using *in vivo* MRI/MRS methodology vs invasive biopsy methodology and hopefully therefore provide this new methodology with efficacy.

6.6 Conclusion

Water (HDO) and lipids (probably triglycerides) were identified in the *in vivo* spectra from the human calf. T_1 and T_2^* relaxation times were also measured and were consistent with literature values. Despite poor signal-to-noise ratio at NA and the use of a surface coil for transceive, it was shown that such measurements are possible in a reasonable time period

(approximately 30 minutes), suggesting that tracer-based metabolic studies of, e.g., triglyceride synthesis and turnover are possible in humans, and in such experimental conditions.

This study marks the first instance of heavy water loading being employed to track lipid signals in human participants *in vivo* using MRI/MRS as well as without the need for biopsy. While it has been demonstrated that measuring and fitting fat peaks following D_2O loading in humans is possible, further refinement of HDO signal suppression would enhance accuracy in tracking these signals. Refinement could include higher field strength, improved coil positioning and implementation of water suppression.

Chapter 7

Quadrupolar Effects using Heavy Water

7.1 Introduction

^{2}H possesses an electric quadrupolar magnetic moment ($Q_{deuteron}$ = 0.286 fm^2e) because its nuclear spin (I=1) is larger than 1/2 [160]. This not only shortens the the relaxation times of ^{2}H relative to ^{1}H, but also introduces line splitting which is somewhat similar to the effect of J-coupling or dipolar interactions. The magnitude of separation in the formed doublet is dependent on the effect of ordering on the time-averaged direction of the local electric field gradient, with respect to the magnetic field that is experienced by the ^{2}H nucleus [161, 162]. When performing MRSI, each voxel will contain information from multiple different tissue/water compartments which can therefore complicate spectral appearance due to the superposition of ordered (anisotropic) and disordered (isotropic) signals. The low available MR signal due to the low ^{2}H NA (0.015%) means that quite often studies looking into quadrupolar effects are performed at high field [104] and [163]/or [164] high ^{2}H abundances using D_2O loading. Double quantum filtering (DQF) can be used to simplify the spectral behaviour by eliminating the signals from isotropic compartments [165, 166]. However this generally

reduces the available SNR.

As originally outlined in Chapter 2, spherical tensors are important when describing the quadrupole moment in ^{2}H. Since ^{2}H has a spin $I = 1$, no rank greater than two can be reached, therefore the only multi-quantum coherence level that can be achieved is the double quantum coherence represented by the $T_2^{\pm 2}$ tensors, which only arise in an anisotropic medium. Use of DQF suppresses the single quantum coherences ($T_1^{\pm 1}$) leaving only signal from the $T_2^{\pm 2}$ tensors in anisotropic regions. The use of DQF to measure measure the anisotropy of tissues and fluids in the body such as intervertebral disc tissue [163], brain water [167] and elastin [168] can reveal vital information about tissue structure in health and disease e.g. degenerative disc disease [163]. Sodium (^{23}Na) is an example of other spin $>$ 1/2 nuclei ($I = 3/2$) where multiple-quantum filtered (MQF) scans have been implemented. MQF scans have been used to invesigate ^{23}Na changes in the intracellular sodium environment, and such measurements have the potential to provide a marker of compromised ionic homeostasis in ischemia [169].

7.1.1 Aims

In this work, healthy human participants ingested D_2O to increase their ^{2}H abundance. The dependency of quadrupolar splitting frequency on angular orientation of skeletal muscle in a magnetic field was then measured, using CSI data acquired from the forearm and the calf at 3T with an in-house built saddle coil and Helmholtz coil, respectively. Bulk and CSI data were also obtained with DQF and the effect of muscle orientation on DQF signal was also explored.

7.2 Theory

7.2.1 Quadrupolar Splitting

The quadrupolar moment interacts with the local Electric Field Gradients (EFG) which can be represented as a combination of up to six electric potential tensor elements. These can be simplified to three principal axis elements (V_{xx}, V_{yy} and V_{zz}). By definition the sum of these elements is 0, as the EFG is a traceless tensor. V_{zz} is defined as the largest element and is usually specified as the EFG at the quadrupolar nucleus ($V_{zz} = e \cdot q$) [170]. The difference between V_{xx} and V_{yy} scaled by V_{zz} is referred to as the asymmetry parameter (η).

$$\eta = \frac{V_{xx} - V_{yy}}{V_{zz}} \tag{7.1}$$

By considering the time-independent Hamiltonian (H_Q) of the quadrupolar interaction it is possible to find a mathematical expression in the generalised form

$$H_Q = \frac{eQ}{4I(2I-1)}[V_0(3\boldsymbol{I_z}^2 - I^2) + V_{\pm1}(\boldsymbol{I_\mp I_z} + \boldsymbol{I_z I_\mp}) + V_{\pm2}\boldsymbol{I_\mp}^2] \tag{7.2}$$

V_0, $V_{\pm1}$ and $V_{\pm2}$ are the three complex principal axis elements combined to create new elements, that represent the total EFG. Q is the (scalar) quadrupole moment, e is the charge of an electron, $\boldsymbol{I_\mp}$ is the nuclear spin raising and lowering operators, $\boldsymbol{I_z}$ is the nuclear spin operator in the z-direction and I is the spin quantum number.

When considering the rotational transformation from the molecule's fixed reference frame to the laboratory fixed reference frame [161], along with an assumed value of $\eta = 0$ (uniaxiality), the total Hamiltonian simplifies for ^{2}H ($I = 1$) [165]. The form of this equation, now using its simplified principal axis elements is

$$H = -g\beta_N \boldsymbol{I} \cdot \boldsymbol{H_0} + \frac{eQ(3\cos^2(\theta) - 1)}{8} V_{zz}(3\boldsymbol{I_z}^2 - \boldsymbol{I}^2) \tag{7.3}$$

where g is the g-factor, β_N is the nuclear magneton, $\boldsymbol{H_0}$ is the magnetic field, and θ is the angle between the electric field gradient and the magnetic

field. The perturbed energy levels can be calculated using the simplified total Hamiltonian. The first term describes the Zeeman interaction, whilst the second describes the quadrupolar interaction. There is an associated energy difference and therefore a frequency difference between states $m = -1$ and 0 and 0 and 1 of

$$\nu_Q(\theta) = \frac{3}{2}\left(\frac{e^2qQ}{h}\right)\left(\frac{3\cos^2(\theta)-1}{2}\right) \tag{7.4}$$

where the Residual Quantum Coupling (RQC), which gives the magnitude of the splitting, in this case is given in the first part of this equation

$$\omega_Q/2\pi = \frac{3}{2}\left(\frac{e^2qQ}{h}\right) \tag{7.5}$$

This derivation shows that as a result of the quadrupolar magnetic moment interacting with the EFG, a splitting is observed that is caused by the perturbation of the energy levels. The frequency magnitude of this splitting effect is given by the RQC and depends only on the orientation of the deuterated molecules with respect to the applied magnetic field (Eq. 7.4). In an isotropic structure this splitting effect is not visible due to averaging resulting from molecular motion. In an anisotropic medium such as the skeletal muscle fibres in the calf, the quadrupolar splitting is at a maximum and equal to the RQC value when the muscle fibres are oriented parallel to the magnetic field ($\theta = 0°$). The splitting effect can also be nulled ($\nu_Q = 0$) if the muscle fibres are oriented at the magic angle $\theta = 54.74°$ ($\cos^2\theta = 1/3$) to the magnetic field.

Therefore it is possible to measure the RQC constant from these NMR spectra which provides information on the anisotropy of the medium being investigated.

It is also possible to look at the ordering of muscle fibres by measuring the frequency splitting due to dipolar coupling from ^{1}H spectroscopy. This has been found to be related to the alignment of muscle fibres to the applied B_0 field [171].

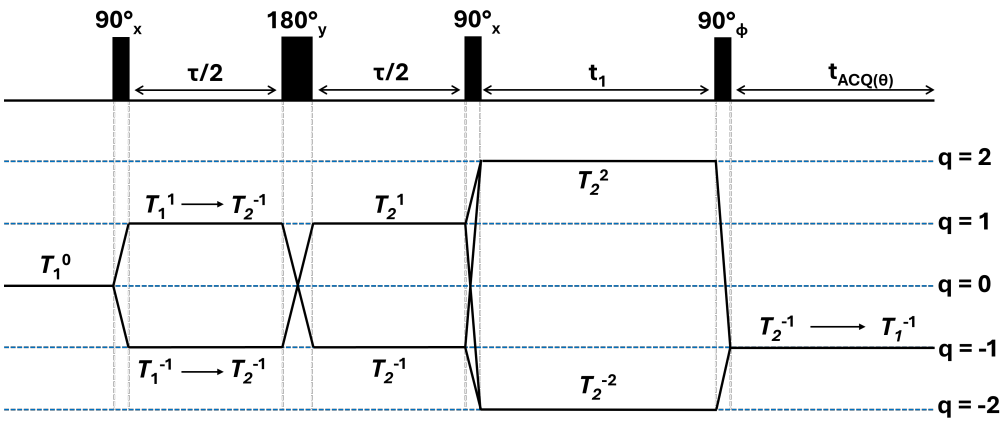

Figure 7.1: *The coherence pathway and the RF pulse sequence used for DQF acquisition. Noting that the tensor T_k^q includes information on the rank (k) and on the coherence (q), which is indicated on the right side. The phase cycling of the last pulse (ϕ) is x, y, -x, -y and the receiver phase (θ) is x, -y, -x, y.*

7.2.2 Quantum Filtering

A pulse sequence that can be used to suppress single quantum coherences and measure signals using from double quantum coherences is shown in Fig. 7.1 [165], where the pulse angles and the wait times are shown below. It is important that the correct phase cycling is used here to suppress unwanted coherences [172]. The transmit phase cycle for the last pulse is x, y, $-x$, $-y$ and the receive phase is cycled as x, $-y$, $-x$, y for this sequence

$$\pi/2 - \tau/2 - \pi - \tau/2 - \pi/2 - t_1 - \pi/2 - t_2 \text{ (Acquisition)} \tag{7.6}$$

This phase cycle suppresses the single quantum coherences and preserves the double quantum coherences meaning only the DQF signal is measured. The obtained FID appears as two anti-phase Lorentzian lines separated by the RQC. If this separation is small the presence of two resonances can be difficult to identify, as the Lorentzian-lineshapes will overlap. An example DQF spectrum with corresponding fitting can be seen in Fig. 7.2.

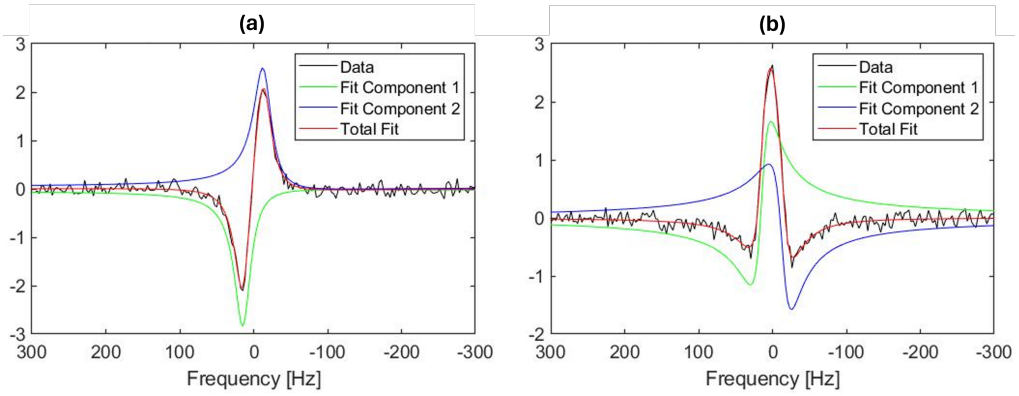

Figure 7.2: *DQF spectrum from an axial 2 cm slice of the lower leg, acquired with τ = 6.5 ms. The plots show the fitting of the two independent Lorentzians to an anti-phase DQF doublet. The imaginary part of the spectrum (absorption) is shown in (a), the real part (dispersion) is shown in (b). The fitting produces a value for the splitting of ν_q = 27.7 Hz, and mean T_2^* = 11.3 ms. In each case the fits to the two signal components are also shown separately. Figure by Dr. Robin Damion.*

The amplitude of the DQF FID follows a damped sinusoid of the form

$$A \sin(2\pi\nu_q\tau) \exp(-2\tau/T_2) \tag{7.7}$$

Here T_2 is the transverse relaxation time, A is the signal amplitude, ν_q is the splitting frequency and τ is known as the creation time and is the time between the first two $\pi/2$ pulses. The form of the signal described in Eq. 7.7 assumes perfect application of the flip angles shown in Fig. 7.1 and that the signal is on-resonance. The coherence transfer pathway with the changing tensor terms can be seen in Fig. 7.1.

Therefore, by performing spatial DQF measurements on a part of the body can inform on the ordering of the tissue present. It has been shown already that the expected quadrupolar splitting in Hz using muscle fibre angles measured using diffusion tensor imaging (DTI) of the calf, approximately agree with splitting frequencies directly measured from ^{2}H MRSI measurements [104]. As the overlapping frequencies can be hard to separate

at lower fibre angles and at lower field strengths, DQF offers an alternative method to measure tissue ordering. Which is explored in this chapter.

7.3 Scanning

Measurements for this work were obtained in two separate investigations that both used the ingestion of D_2O to increase the ^2H concentration. The initial investigation was setup to look at ^2H enrichment in skeletal muscle (see Chapter 4), however in initial experiments quadrupolar splitting was observed across the muscles of the calf (most notably in the tibialis anterior muscle). This motivated us to investigate the effect of quadrupolar splitting in skeletal muscle, quickly in the first investigation and more seriously in the second investigation. The first investigation was used to formulate the second study and improve the parameters chosen and to develop aims. Different loading routines were used in each investigation and both took place at different times. Due to the use of different loading routines the ^2H abundances were different in different subjects and experiments, but the exact SNR was not important for either investigations, as long as it was good enough to allow useful data to be obtained in a reasonable time frame. The loading routine for the first investigation was the same as was used in Chapter 4, and the loading routine used for the second investigation was the same as in Chapter 6. Here only results from the second investigation are shown.

All data was acquired using a Philips 3T Achieva scanner. All ^1H anatomical scans were performed using the built-in body coil using a 3D GE sequence. ^2H data was obtained using in-house built coils details of which can be found in Chapter 3 of Chapter 2.

7.3.1 Quadrupolar Splitting

During the second main study, after the initial D_2O loading period was completed and the participants ^2H enrichment had reached a steady state

level. ^{2}H 3D CSI data were acquired with $10 \times 10 \times 10$ mm^3 voxels, FOV = $120 \times 120 \times 50$ mm^3, TR = 500 ms, TE = 6.2 ms, BW = 750 Hz, samples = 256 and NSA = 2 in the forearm of three healthy human participants using an in-house built Helmholtz coil. Images were acquired in each subject with the forearm at 10 different angles approximately ranging from 0° to 90° to the field.

In order to ensure that the forearm was always in the centre of the field, that a large enough range of angles were covered and that each participant was as comfortable as they could be. Each participant was removed from the scanner between acquisitions of data at different angles, which is why commonly scanning ran over two days. The protocol for each angle included acquisition of a ^{1}H scout scan and GE anatomical images, two bulk spectra and finally a 3D CSI.

Whilst this study was similar to what was performed in the initial investigation, one of the major improvements made was in the analysis routine. It is difficult to estimate the angle of muscles of the forearm relative to the magnetic field. Here a paper printout of a compass attached to the top of the coil helped us to orient the arm in the scanner. In the initial work the angle used in the analysis was estimated from the ^{1}H scout scan. Here the angle of the arm was calculated by measuring the angle of the ulna bone using the Mango software (downloaded from https://mangoviewer.com/download.html), which was found to be different from the angle estimated from the compass, as well as the angle used when planning the scanning. The angle two different members of the group used Mango to calculate the angles of one participants forearms at all angles acquired, and it was found that the largest difference between angles rounded up to 2°. Therefore, this value was used as the error on the angle calculation. Screenshots of using Mango to calculate four angles is shown in Fig. 7.3.

Zero-order phase correction was applied to all spectra, as well as denoising through using HOSVD [91] with a compression core matrix of [64, 6,

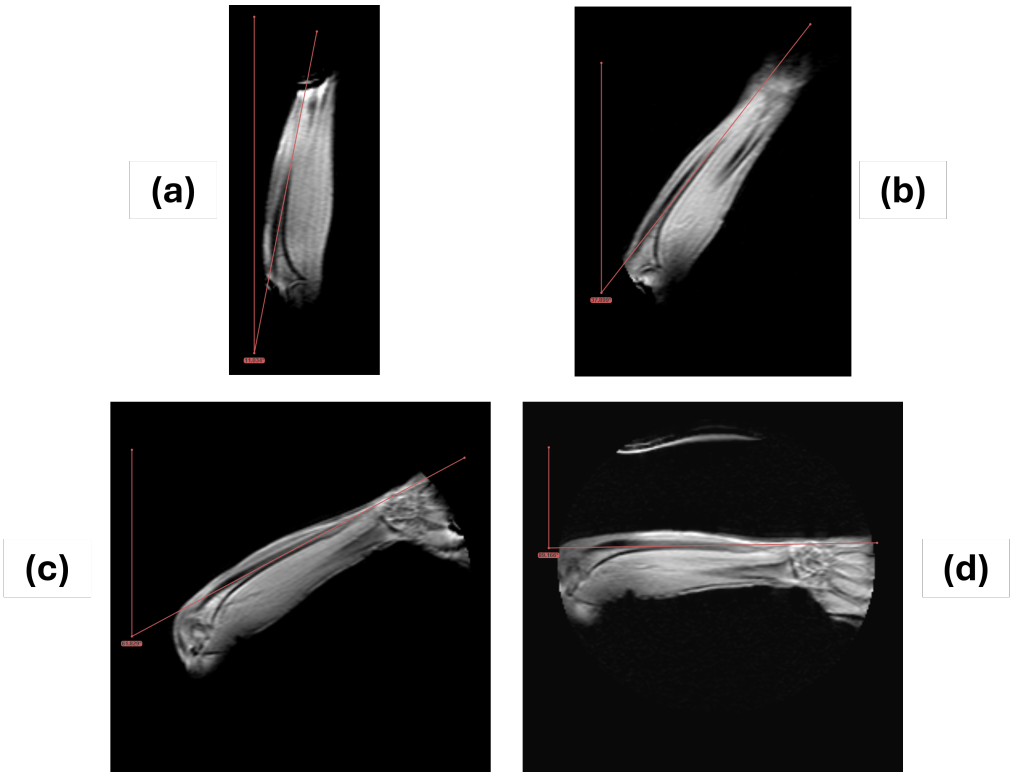

Figure 7.3: *Screenshots of the Mango software being used to calculate the angle of the ulna bone in one participant at what was supposed to be 0° (a), 30° (b), 50° (c) and 90° (d). But was calculated to be 11° (a), 38° (b), 62° (c) and 89° (d).*

6, 3] (spectral, followed by three spatial dimensions). A binarised mask with the same spatial resolution as the CSI data was then constructed, following thresholding of 35% of the maximum spectral signal (the mask was then filled in using imfill). The OXSA-AMARES [73] toolbox in Matlab was used to fit three Lorentzian peaks to each masked voxel. These comprised of a central peak due to any signal from isotropic compartments plus a doublet due to quadrupolar splitting in any anisotropic compartments. Each peak in the doublet has the same linewidth and amplitude and all peaks are fit with the same phase. The initial estimate of the separation of the doublet varied depending on the angle of the arm in the scanner. The separation of the doublet was converted from ppm to Hz and then the values, along with the angle of the arm relative to the magnetic field, was fitted to Eq. 7.4.

7.3.2 Double Quantum Filtering

Bulk DQF ^{2}H non-localised spectra were acquired from a 2-cm axial slice of the forearm in three healthy human participants. Hard pulses were used in combination with OVS for slice selection. Spectra were obtained via an anti-phase DQF sequence [165] whereby the peaks of the doublet acquire a relative phase of 180° to one another. DQF spectra were acquired for a range of values of the creation time, $1 \leq \tau \leq 36$ ms with, TR = 1000 ms, TE = 0.58 ms, BW = 3000 Hz, samples = 1024 and NSA = 56.

^{2}H 2D CSI data were also acquired from single slices in both the lower leg and forearm, using OVS for slice selection with the anti-phase DQF sequence (DQF-CSI) with $\tau = 5$ ms. Each voxel for the CSI was 10 × 10 mm^2 in-plane, TR = 1000 ms, TE = 2 ms, samples = 256, bandwidth = 750 Hz, NSA = 8 with a slice thickness of 2 cm. ^{1}H scout and 3D GE (2 mm isotropic voxels, TR = 20 ms, TE, 2.1 ms, FOV = 128 × 128 × 192 mm^3, NSA = 1) anatomical images were also obtained, along with ^{2}H 2D Single Quantum Filtered (SQF)-CSI data with the same scan parameters as the ^{2}H 2D DQF-CSI scans. The forearm measurements were then repeated

with the arm at a range of angles (0°, 30°, 60° and 90°) to the B_0 magnetic field.

The non-localised spectra were apodised using a 5 Hz exponential line-broadening filter to increase SNR, whilst the CSI data was de-noised using a Tucker decomposition [91] with a core matrix of [32, 6, 6, 2] (time, two spatial and angular dimensions respectively) to increase SNR. All DQF spectra were fit using the OXSA-AMARES [73] toolbox in MATLAB, using two Lorentzian peaks with 180° phase difference, equal linewidths and equal amplitudes. Automatic zeroth-order phase correction was also applied to each spectra. Then signal amplitudes from four voxels from the volar compartment of the forearm were averaged across each subject and all angles and the spectra compared.

7.4 Results

Figure 7.4 shows individual slices from 3D CSI data acquired from the lower leg and forearm, with the limb approximately aligned with the B_0-direction. The fitting is performed on a voxel-wise basis and is the same over the whole ROI and uses the OXSA-AMARES toolbox [73] implementing prior knowledge, and the data has been de-noised. The splitting map has not been interpolated here, and can be seen to the follow the general trend in the underlying anatomical image. Doublets can be observed in many voxels, with residual quadrupolar splittings of 20 to 40 Hz. An increase in the splitting in the Tibialis Anterior (TA) muscle can be seen here, with more homogeneity of splitting values present in the forearm.

Figure 7.5 shows how the CSI spectra from the forearm change as the limb is oriented at different angles to B_0. It can be seen that as the forearm is angled close to the magic angle (54.74°) the quadrupolar splitting vanishes.

Figure 7.6 plots the averaged quadrupolar splitting frequencies against angle of the ulna with respect to the applied field. A fit to the expected

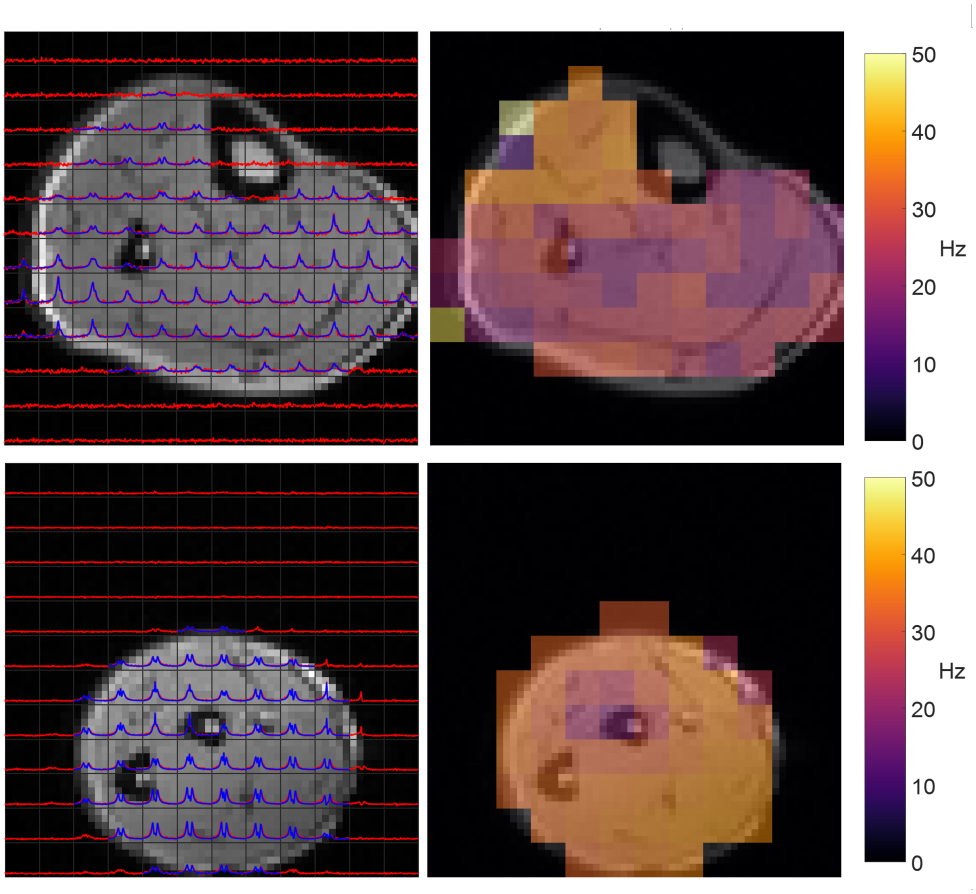

Figure 7.4: *Example slices from 3D CSI of the lower leg (upper panels) and forearm (lower panels), showing spectra (left) and maps of the magnitude of splitting (right). Fits are in blue, CSI data in red. In both cases the limb was approximately aligned with the field.*

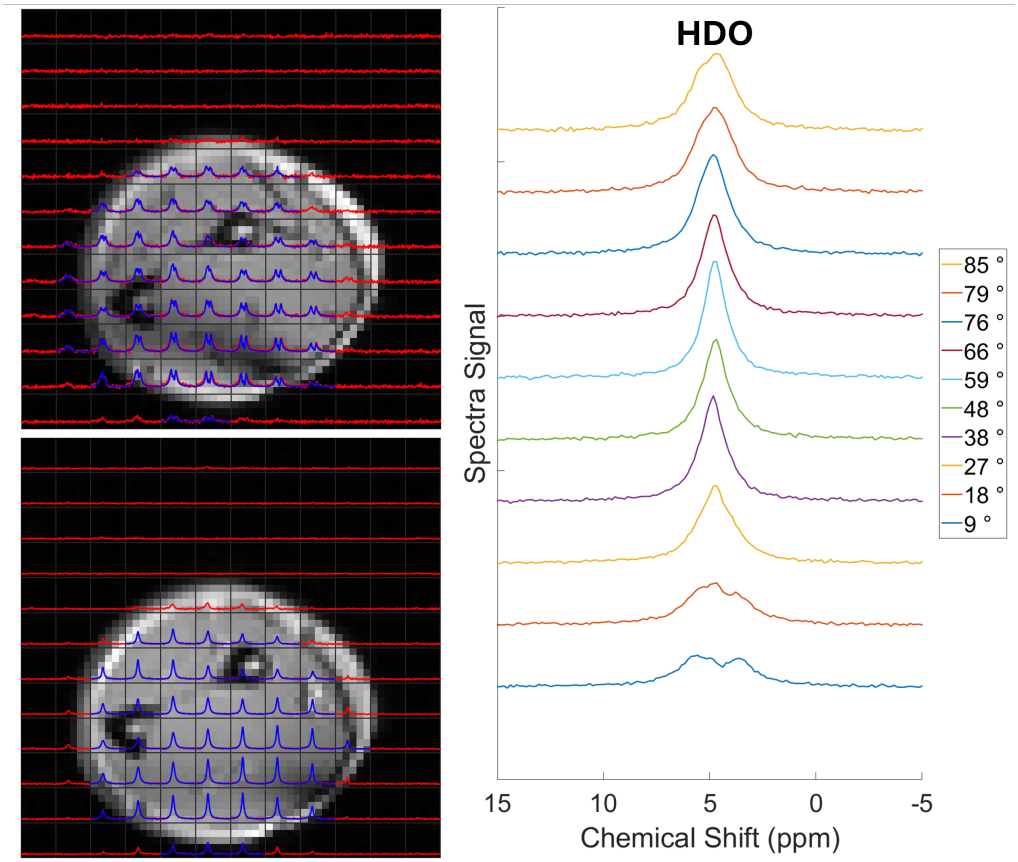

Figure 7.5: *CSIdata from slices of the forearm acquired at two different angles (9°, approximately along the field (upper) and 59° (lower), close to the magic angle) to B_0 (left panels). Averaged spectra are shown for all angles in the right panel. Quadrupolar splitting is evident in the 9° CSI data, but not seen in the 59° CSI data. The average spectra are consistent with quadrupolar splitting that varies with $3\cos^2\theta - 1$ as shown in Eq. 7.4.*

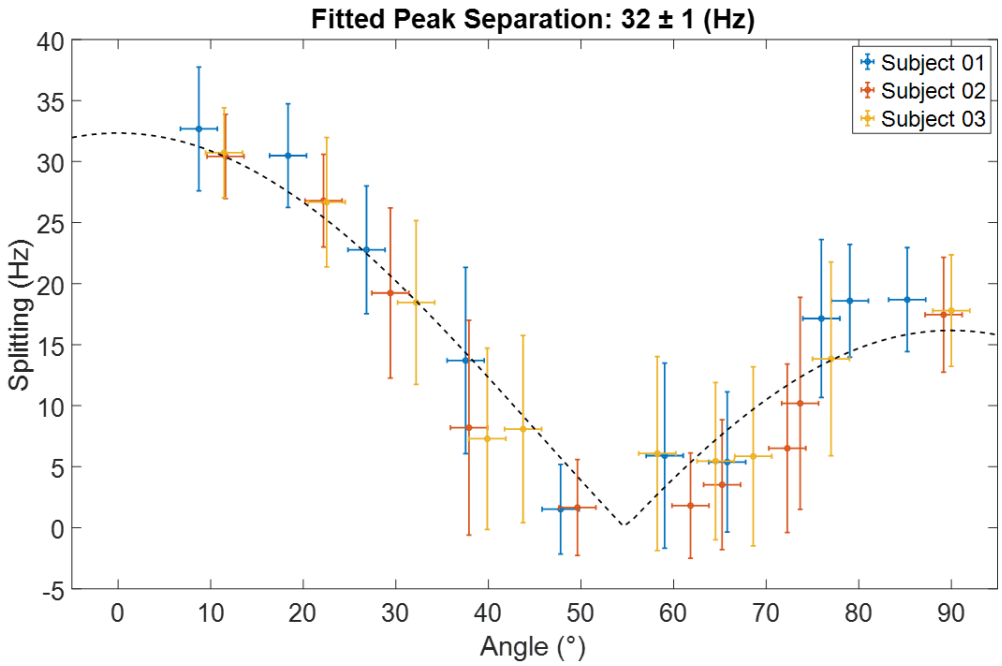

Figure 7.6: *Average quadrupolar splitting frequencies as a function of forearm angle to B_0, fitted to the form of Eq. 7.7. Data points are the average splitting over the forearm in each 3D CSI data set, with data acquired at 10 different angles to the field from 3 subjects. Vertical error bars show standard deviation of the splitting over the volume. Horizontal errorbars are ± 2° due to rounded highest difference between two people analysing the data.*

variation in Eq. 7.4 provided an average value for the splitting amplitude across all voxels and participants of 32 ± 1 Hz.

Non-localised DQF spectra from the forearm of three participants are plotted as a function of creation time (τ) in Fig. 7.7. The biggest differences between participants visible here is the presence of signal at larger τ values. It is expected that the amplitude of the DQF signal varying with τ will follow Eq. 7.7. Where the amplitude of the DQF and the splitting frequency which can be found by fitting the amplitudes to Eq. 7.7, has been shown to be larger in compartments that interact with more ordered structures [173]. Doing this has also been used to show that increased temperature increases the ordering of the water surrounding elastin *ex vivo*, by

looking at the splitting frequency and amplitude of fitting [168].

Figure 7.8 shows a comparison of 2D pulse-acquire CSI and DQF-CSI data along with fits for the lower leg, highlighting spectra in individual voxels in the TA and soleus muscles. With the amplitude

2D DQF CSI spectra for the lower leg at two different angles, (a) 11° and (b) 65°, along with fits are shown in Fig. 7.9. The SNR in data acquired at the angle closer to the magic angle is notably smaller compared to the lower angle CSI, however fitting was still accurate even in the lower angle data. Also shown are the four voxel ROIs that are used for comparison in Fig. 7.10.

In Fig. 7.10 a change in DQF amplitude is obvious across each subject and across all angles with minimums being in the angle closest to the magic angle which is consistent with Eq. 7.7. The SNR is notably lower in subject three's spectra compared to subjects one and two, however it still exhibits the same behaviour with fitting still being possible.

7.5 Discussion

7.5.1 Quadrupolar Splitting

The residual quadrupolar splitting of the HDO spectrum, seen in Fig. 7.4, is evidence of local ordering of the tissue, which been previously observed in muscle, tendon, cartilage, and nerves [104, 162, 165, 166]. All measurements of angular dependencies in this work were made on the forearm due to ease of scanning at multiple specific angles. Other work has performed similar scanning on the lower leg and found magnitude of splittings for different muscle groups. That work was based on NA ^{2}H signals, but used higher field strength (7T) and measurements at just two different angles (0° and 45°) [104]. The splitting map observed in the calf in Fig. 7.4 is similar to what has been found previously at ∼0°. Because of the inhomogeneous spatial splitting in the lower leg, separate ROI's for each muscle

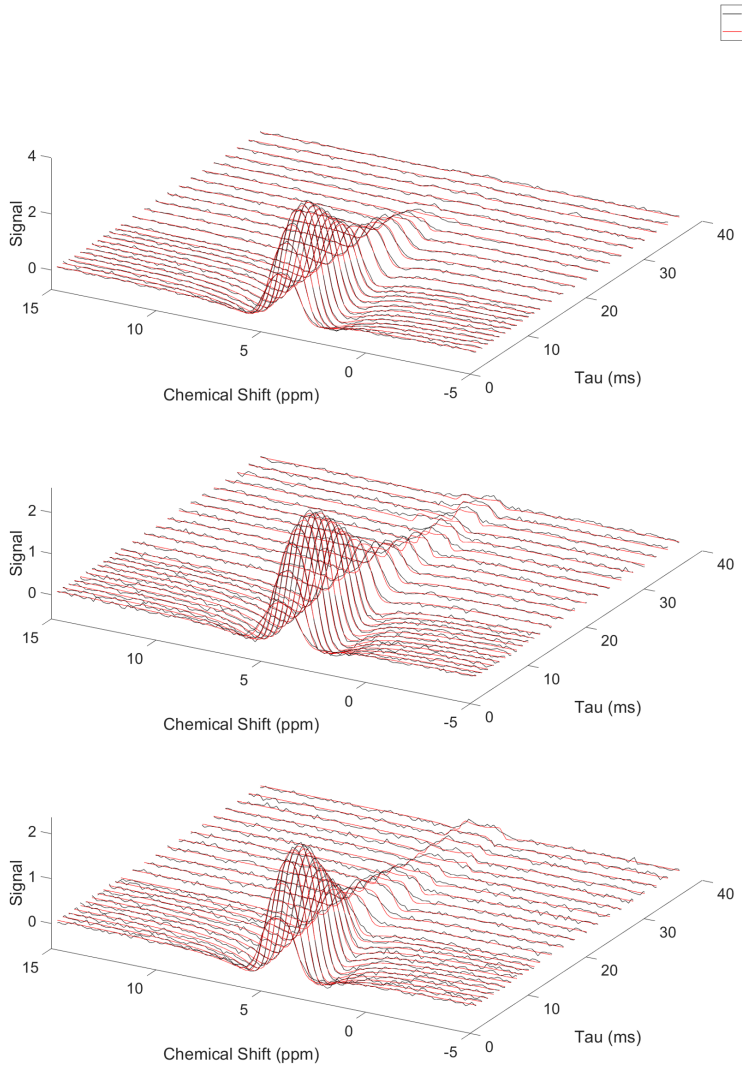

Figure 7.7: *DQF spectra obtained from a 2 cm axial slice across the forearm (aligned approximately with B_0), as a function of the anti-phase DQF sequence creation time, τ. Dispersion mode spectra are shown for three subjects, so that the anti-phase doublets produce a symmetric spectrum with maximum amplitude at the centre frequency. The average values of ν_q found from fitting to these doublets are 36 ± 7 Hz (top), 31 ± 5 Hz (middle), and 36 ± 5 Hz (bottom).*

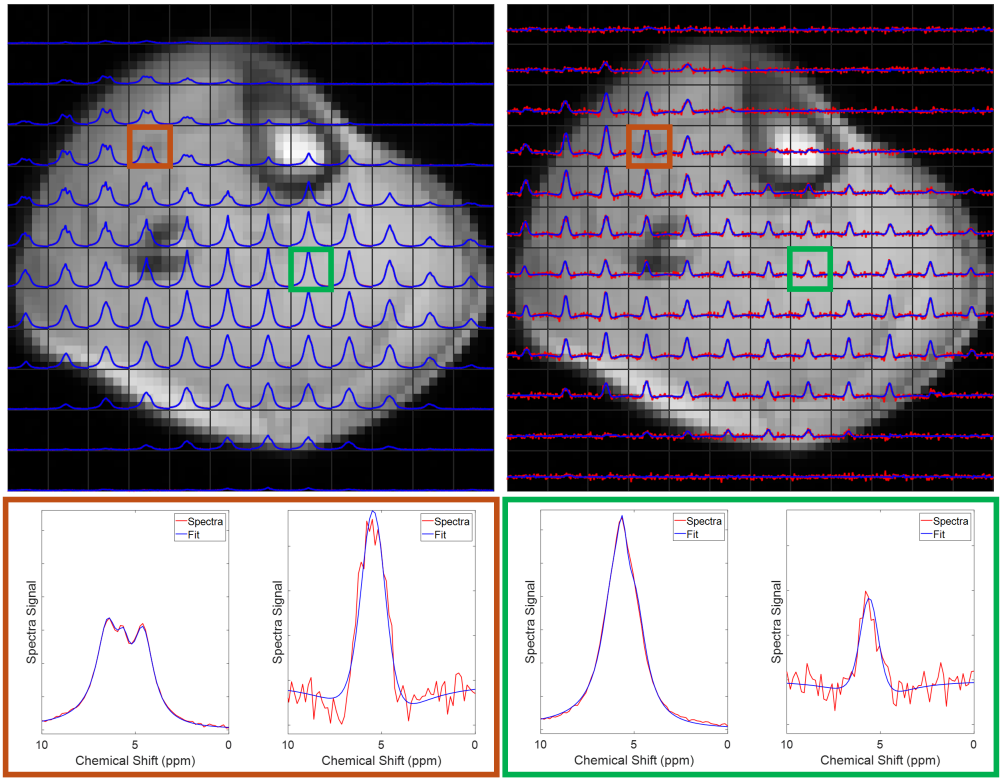

Figure 7.8: *Slices of the lower leg from a CSI sequence (left) and a DQF-CSI (τ: 5 ms) sequence (right), highlighting selected spectra from two voxels: TA (orange), soleus (green).*

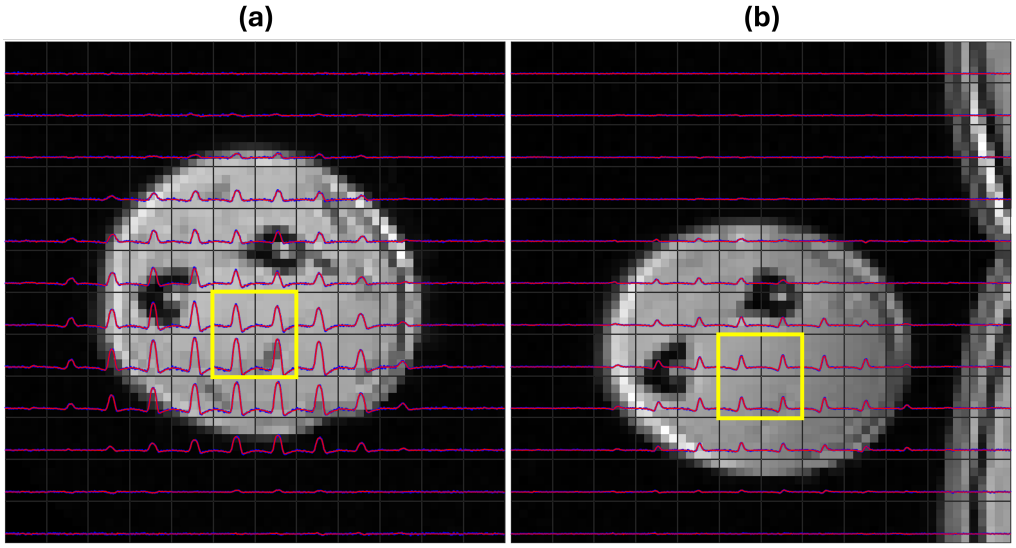

Figure 7.9: *^{2}H 2D DQF CSI obtained from the same subject's forearm using a Helmholtz coil at two different angles to the field, (a) 11° and (b) 65°. The yellow boxes show the ROI used to compare spectra in Fig. 7.10.*

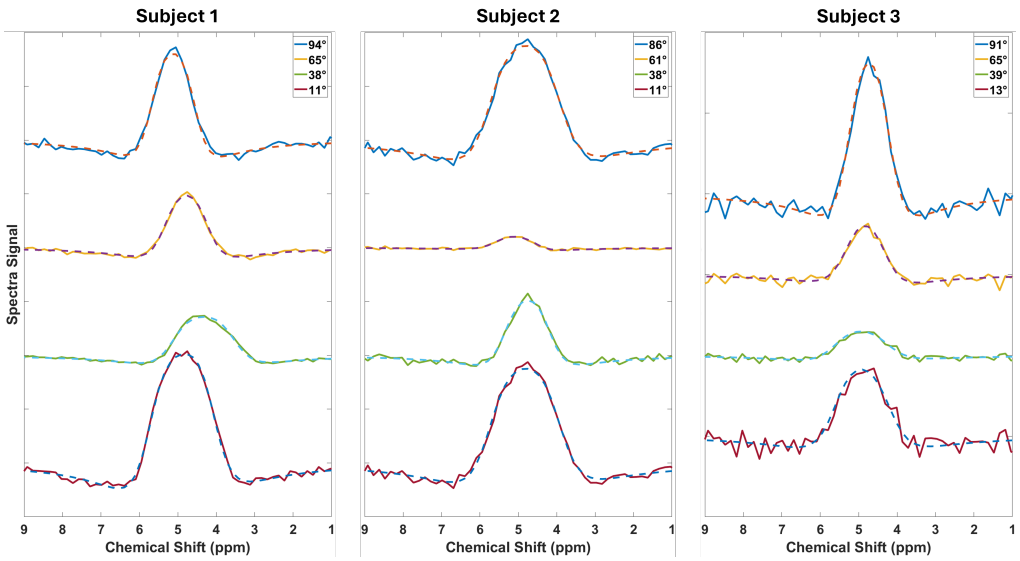

Figure 7.10: *Four ^2H spectra averaged together for four angles across three subject's forearms, obtained from DQF-CSI spectra stacked on top of each other. Angles relative to the B_0 field were measured from the orientation of the ulna bone.*

group had to be used when comparing splitting values. This is not necessary in the forearm (as can be seen in Fig. 7.4) which is why only a single ROI is used here. In the calf the largest splitting arises in the TA muscle group, probably because the fibres of this muscle align closely [104] with the B_0-direction with leg along the field. However this could also indicate a more ordered environment in which the water resides in the TA. Separate ROI analysis in the main three forearm muscle groups (mobile wad, dorsal and volar compartments) would have been interesting to see if any small difference was present. However, due to the large voxels and low SNR from using the built-in body coil for the anatomical images, it was difficult to identify the different muscle groups from the ^{1}H images.

Due to the low spatial resolution of the CSI scans realistically there is a combination of separated doublets and single peaks present which is represented by a three-peak fit. A three-peak fit could be used to fit all voxels as long as each peak is fully resolved, this is often not the case here as the linewidth is often larger than the separation. Therefore in some

cases a three-peak fit is not ideal, which is why the condition of lowest sum of squared residuals is used to choose the apropriate fit. The OXSA-AMARES MATLAB toolbox has already been shown to improve fitting by use of prior knowledge. This has led to increased reliability in fitting here which allows the use of more consistent three-peak fitting in the time domain.

Improving the fitting, de-noising or the change in angle determination (FOV box angle or the angle of the ulna) has increased the fitting accuracy to Eq. 7.4 in Fig. 7.6. It can not be categorically stated which is most responsible for the increased accuracy of fitting. However, due to the fact the angle of the ulna can be significantly different to the angle of the FOV box, it is suspected that this is the driving force for the increase in fitting accuracy.

7.5.2 DQF

As is seen with the DQF filtered CSI data it can be difficult to identify where the regions of maximum DQF signal are present due to the lack of discrimination of the anti-phase peaks.

However, in Fig. 7.8 an increase in the signal in the TA and gastrocnemius muscle and a decrease in the soleus muscle is visible which is consistent with separation maps from pulse-acquire SQF results in Fig. 7.4. This confirms that the strength of DQF signal depends on the degree of tissue ordering, as the magnitude of the quadrupolar splitting has already been shown to depend on tissue ordering in Eq. 7.4.

Increasing the number of τ values in investigation two to what is used in Fig. 7.7 in a similar range to what has been used previously, a more complete evolution of the DQF signal in the forearm is possible. By using OXSA-AMARES [73] more reliable and accurate fitting is possible even at larger τ values with lower SNR. From having a more complete model extra features are visible in the amplitude changes in Fig. 7.7, such as extra signal that is not an exponential decay, as shown in Eq. 7.7.

By using the forearm as opposed to the calf, the partial voluming of multiple splittings is minimised. The τ evolution in Fig. 7.7 has not been modelled in detail as it is clear that a more complicated model is needed, involving off resonance and flip angle effects. Difficulties in fitting this data arise from poor flip angles due to RF inhomogeneity, off resonance effects and contributions from multiple splitting frequencies [165].

Whilst the signal evolution with τ could not be correctly modelled, the angular response of DQF signal has been explored in Fig. 7.10. A full response curve similar to Fig. 7.6 was not possible as only four angles have been measured. However, it is enough to see that the data approximately follows Eq. 7.4 with minimum signal around the magic angle (54.74°) and maximum with a straight arm (0° to the B_0 field).

7.5.3 Future and Limitations

These are the first results using ^{2}H for *in vivo* DQF spectroscopy in human subjects, and as such there are areas for improvement and developing the technique further. By using dual-tuned coils it would be possible to acquire high resolution anatomical ^{1}H images as well as ^{2}H data, which would allow improved segmentation and ROI analysis. In this case it would allow separation of specific muscle groups and DQF signals to be identified. An improved RF coil with multiple channels for the ^{2}H would also increase SNR, which would allow for better spatial resolution, and reduce effects from multiple quadrupolar separations.

On the topic of RF coil improvements, if the B_0 field strength is increased say from 3T to 7T this would decrease the individual peak linewidths. Whilst the splitting frequency does not vary with field strength, minimised linewidths means the peaks will be better resolved which can lead to improved fitting. The SNR will also improve with field strength, and therefore scan time can potentially be reduced, which could lead to improved dynamic scanning.

Whilst the HDO DQF peaks overlap which creates one strong central

signal, a DQF imaging sequence could be used instead of a spectroscopic sequence. This would reduce scan time which could allow for more averaging to improve SNR, improve spatial resolution on CSI acquisitions or acquire more dynamic data ie. with more angles or more τ values.

7.6 Conclusion

Here the first *in vivo* ^{2}H DQF datasets from human subjects have been reported. These will potentially allow crucial information on the ordering of local tissue to be obtained. Experiments have been performed at a clinical field strength of 3T which shows that in the future (with more improvements to study protocol). This technique could be used to investigate effects of diseases that have so far only been shown on *ex vivo* data [163, 165, 166, 168]. The quadrupolar separation has also been quantified in different muscle groups in the lower leg and in the calf as a whole, as well as the angular dependence on this behaviour. By improving the RF coil used, increasing the field strength and using imaging sequences this technique shows potential for uncovering useful information about tissue ordering.

Chapter 8

Conclusion

In this thesis MRI and MRSI tuned to the ^{2}H resonance at 3T and 7T have been used to explore some important ^{2}H MR parameters such as T_1 relaxation times. The metabolic behaviour of ^{2}H glucose has also been investigated *in vivo* using DMI at 7T. Due to this work not being performed on human scanners *in vivo* at the SPMIC previously, some of the hardware used, such as RF coils, were in-house built and the details of designing and building of these coils have also been described here. ^{2}H MRSI with ^{2}H glucose is now being used to investigate metabolic diseases such as brain cancer due to the increased CNR from metabolite concentration maps.

The aim of this work is to successfully lay the ground for future studies at the SPMIC to investigate brain tumours in patients using DMI at 7T *in vivo*. At the time of writing this conclusion the first DMI scan was performed in a patient with a brain tumour using ingestion of glucose-d_7 at 7T *in vivo*, which was performed by our group at the SPMIC. In a preliminary analysis, the data has been fitted using the OXSA-AMARES toolbox [73] (Fig. 8.1), metabolite fitting amplitudes have been obtained and tracked over time and can be seen in Fig. 8.3, Fig. 8.4 and 8.5. The overlayed heatmap on Fig.8.1 represents the location of the tumour, on each slice of the MPRAGE the tumour is manually segmented and the masks are averaged over all slices that cover the CSI slice (ten slices). A value of one in the heatmap means that the voxel is present in the tumour

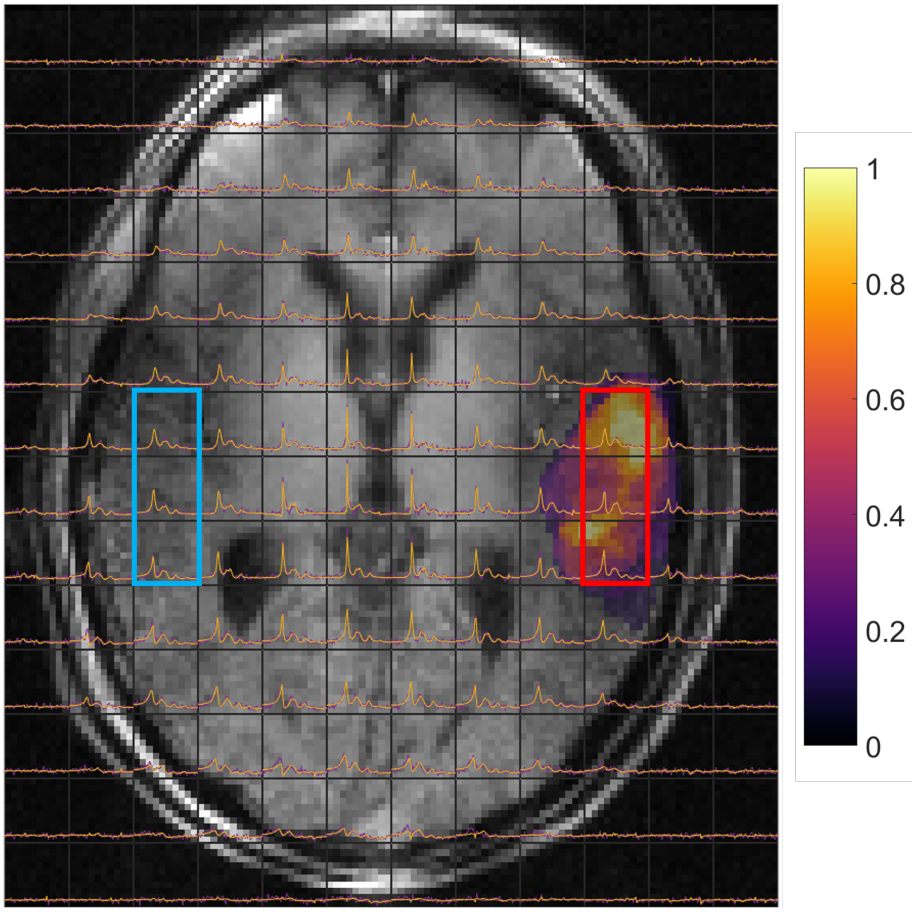

Figure 8.1: *Final ^2H CSI data acquired in ∼12.5 minutes (purple) along with corresponding fits (yellow). In tumour voxels (red) and contralateral voxels (blue). Along with an overlayed heatmap that represents the location of the tumour averaged over ten slices that cover the CSI slice, each individual slice has a mask value of one.*

in all ten slices, and a value of zero means that the voxel is not present in the tumour in any of the slices. It is important to note that the mask here is not drawn by a trained radiographer, instead it is drawn by the author and assessed by a clinical doctor (Dr. Milo Hollingworth).

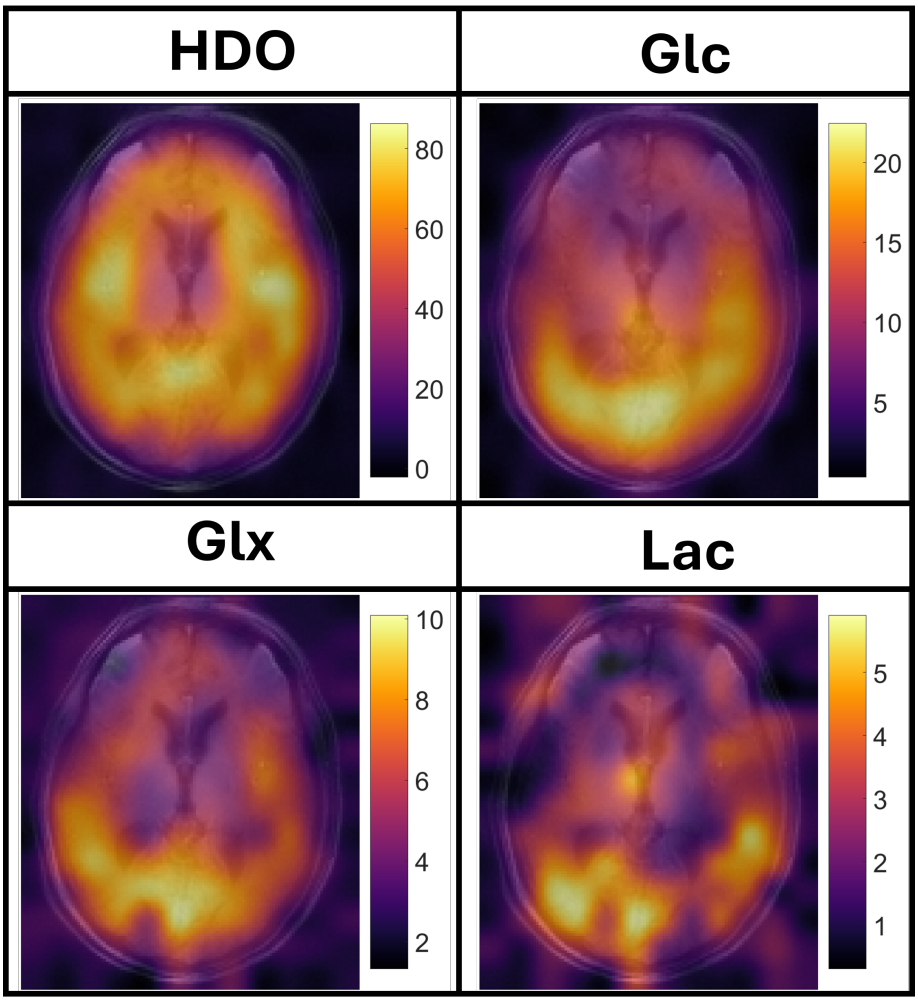

Figure 8.2: Average metabolite maps from the post-ingestion scans from the slice indicating the tumour.

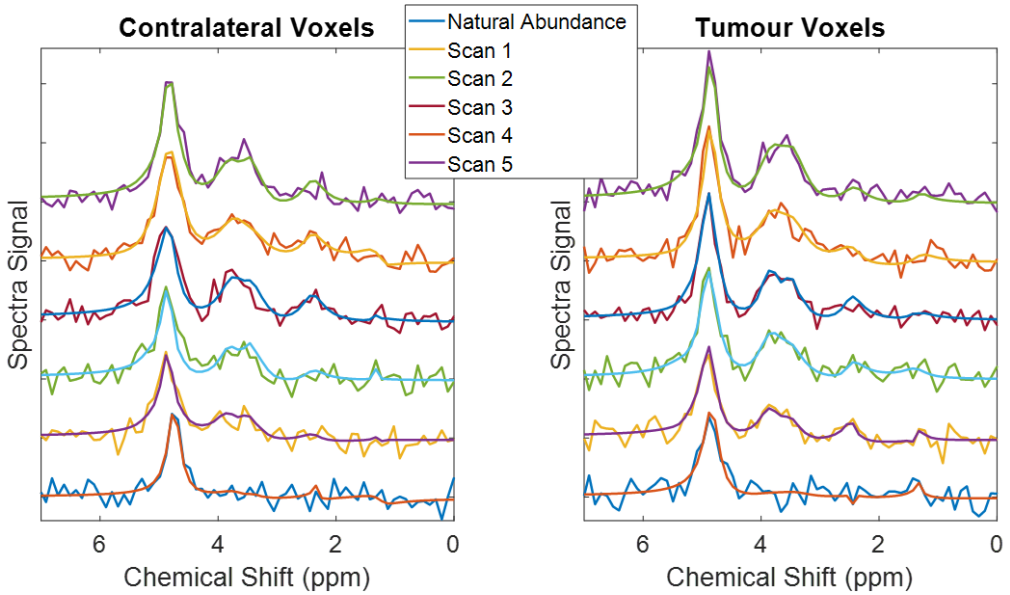

Figure 8.3: *Stacked spectra along with corresponding from the contralateral voxels (left) and of the voxels that cover the tumour region (right). Each spectra is obtained by averaging the three spectra in each ROI, the fitting here is performed before the averaging.*

Decreased Glx was found in tumour voxels compared to contralateral voxels along with increased lactate in the three last scans. This resulted in a statistical increase in Lac/Glx in tumour voxels which is visible in Fig. 8.6, 0.5 ± 0.2 compared to 0.2 ± 0.2 $p<0.05$, the time-course of this ratio is visible in Fig. 8.5. Average metabolite maps from the post-ingestion scans are visible in Fig. 8.2. These are promising preliminary results as it has been recently shown that there is a correlation between PET imaging in Alzheimers patients and the increase in Glx using DMI [174].

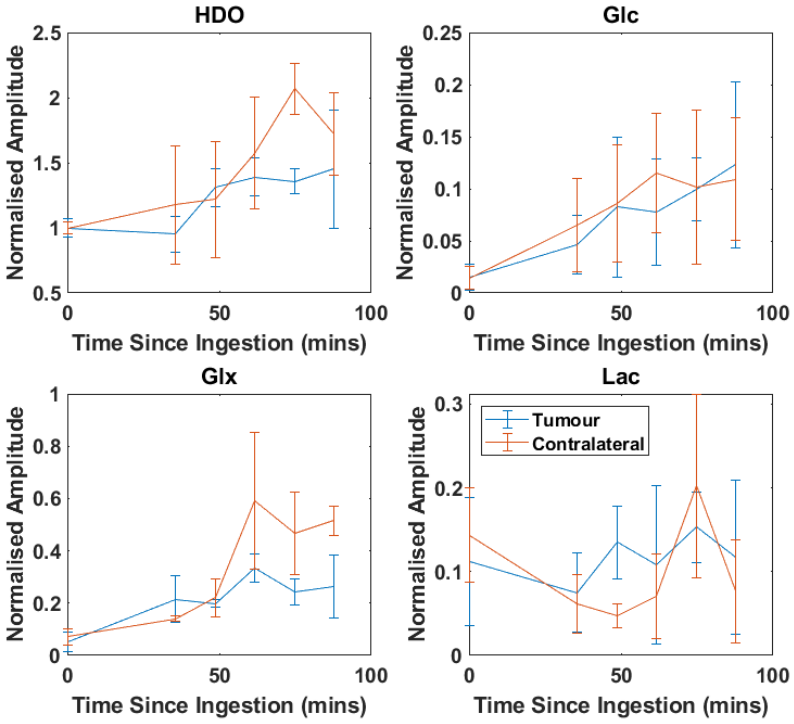

Figure 8.4: Average fitting amplitudes for each metabolite (HDO, Glucose (Glu), Glx and Lac) over the contralateral (red) voxels and the tumour (blue) voxels. For the Natural Abundance Scan (1) and the post-ingestion scans (2 to 6).

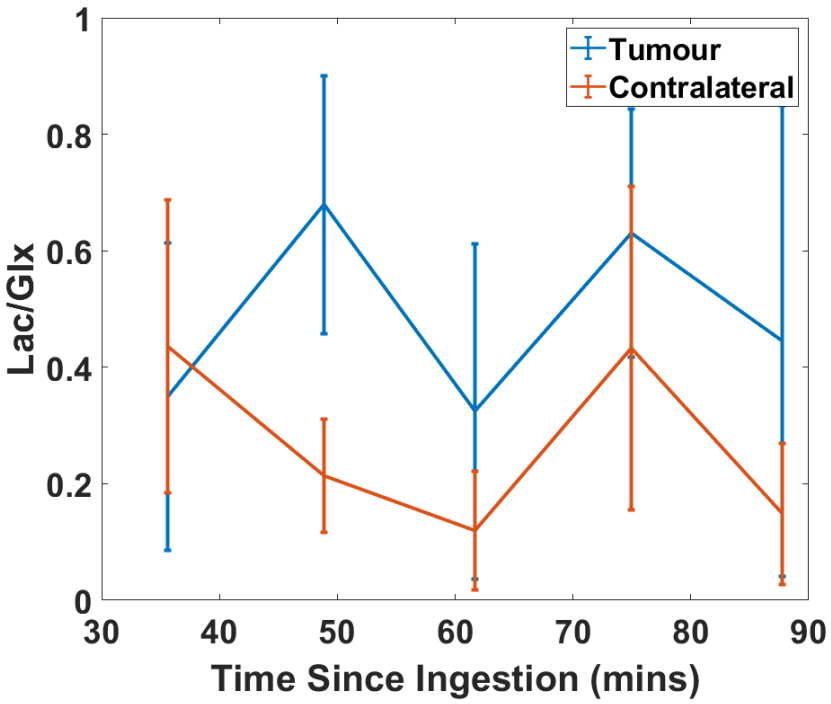

Figure 8.5: The time-course of the average ratios of fitting amplitudes of Lac/Glx for the voxels covering the tumour (blue) voxels and the contralateral (voxels). The error here is the propagated error from the standard deviations used in Fig. 8.4.

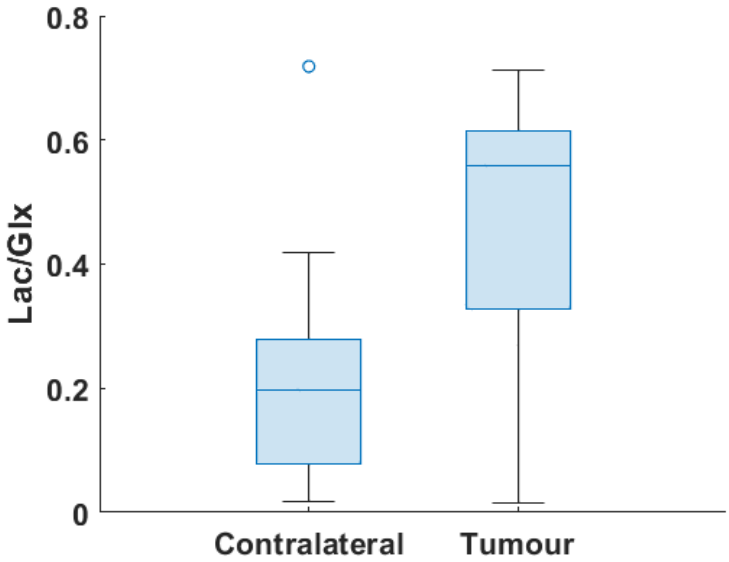

Figure 8.6: Box plots for the average Lac/Glx ratios in the tumour and the contralateral voxels indicating an increase in the tumour region ($p<0.05$). For the final three post-ingestion scans where the Glx and Lac signals appear to have reached a steady state.

8.1 Chapter Overviews

To obtain a complete understanding of this relatively new technique (DMI) it is important to describe the background and history of the technique. This is done in Chapter 1. The basic biology underlying metabolism and the pathways that ^{2}H in a labelled compound that is ingested will take through the body are also described. The historic use of ^{2}H in MR research is described in this chapter, spanning its discovery, to its use in heavy water in the 1980's in animal models and its current, most popular use in the form of ^{2}H labelled glucose.

The physics that underpins the development of the experimental work in this thesis is outlined in Chapter 2. Initially this describes how NMR data is obtained, going from a microscopic to a macroscopic picture. Most MRI and MRS research is performed by tuning to ^{1}H, therefore the differences involved in tuning to the quadrupolar nucleus ^{2}H are explained here.

MRSI techniques are used throughout the work described in this thesis, so the acquisition of MRSI data is explained in detail and the different approaches that can be used to obtain this data are explained. The mathematical approach to analysing ^{2}H spectra is also detailed in this chapter, along with strategies for improving the intrinsically low SNR. Finally the theory behind building RF coils is described here, along with details on the electrical components.

To accurately design and optimise scanning protocols it is important to know the physical properties of the compound being scanned. One of the most important of these is the T_1 relaxation time, which is a key factor in selecting the TR and the flip angle used in measurements. Measurements of the T_1 relaxation times of deuterated water *in vivo* in CSF, GM and WM at 7T are described in this chapter. Participants who were undertaking a study into cell proteomics ingested heavy water, giving rise to a hundred fold increase in the ^{2}H concentration. MEGE images with a range of TR's were acquired allowing joint analysis of signal variation with TE and TR to provide values of T_2^* and T_1. These results were used to improve the accuracy of later concentration quantification and to improve later study/scan designs. Two of the participants were also scanned when they first began ingesting heavy water at regular intervals so that the time course of the increase in ^{2}H levels could be explored, the results were found to be similar to estimates derived from simple dilution.

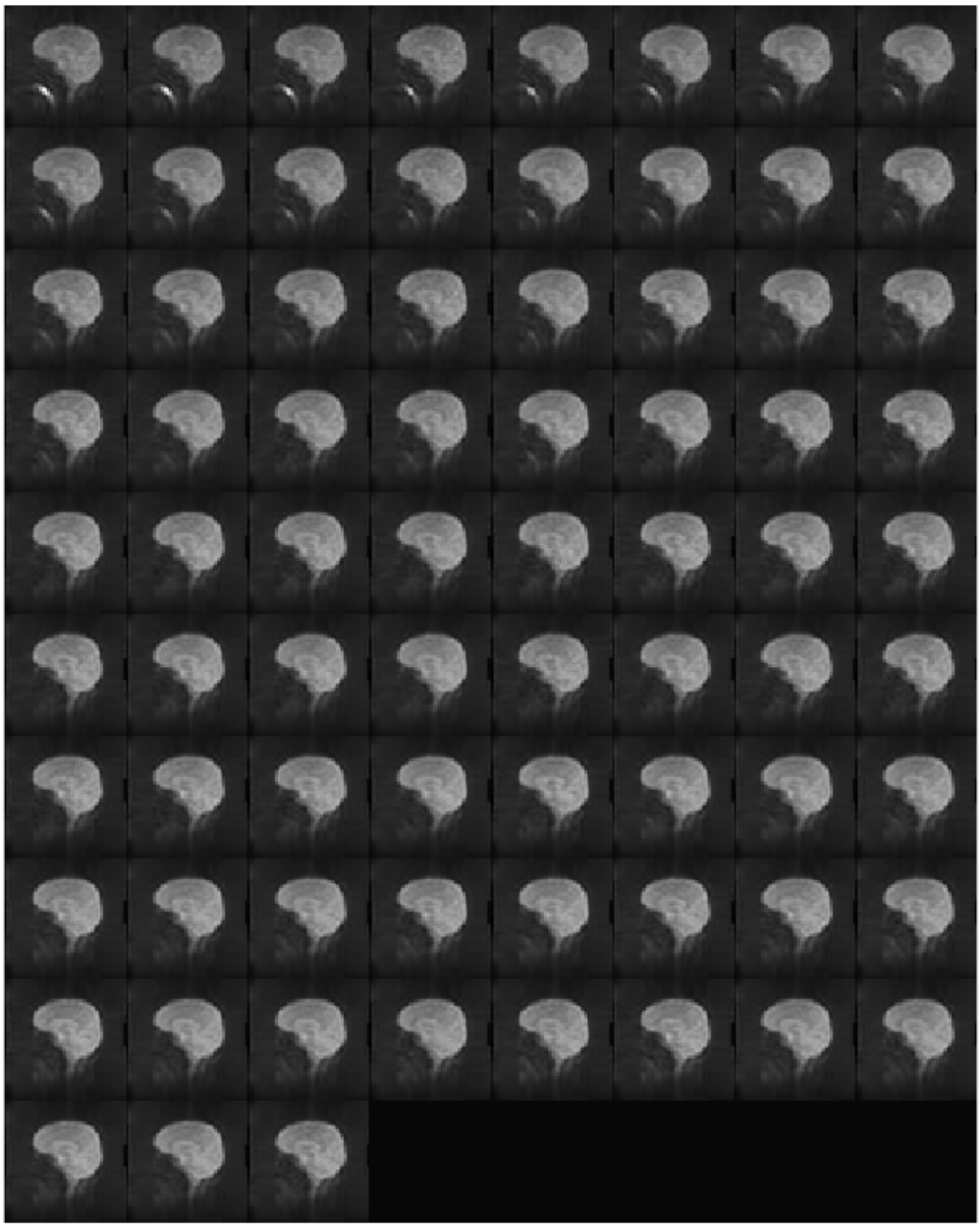

Figure 8.7: *Time-course from the five centre averaged sagittal slices of a healthy human brain in vivo, during the steady-state of D_2O loading, acquired using an EPI acquisition with 75 dynamics, tuned to the ^2H resonance at 7T.*

To demonstrate the potential of ^{2}H imaging a ^{2}H EPI acquisition has been used for faster scanning during heavy water loading, allowing 75 3D image dynamics to be acquired in 48 minutes of scanning (∼38 s each). A healthy human participant was scanned at 7T with a FOV = 288 × 288 ×

240 mm^3, voxel size = 6 × 6 × 10mm^3, TR = 250 ms, TE = 13.8 ms, flip angle = 70°, 75 dynamics, EPI factor = 23. The participant was taking part in the studies in Chapter 6 and 7 at the time of scanning and therefore followed the loading regime outlined there. The participant had completed the initial loading and was in the steady-state period. Immediately prior to scanning their 50 ml daily top-up was ingested. Traces of heavy water in the mouth and throat can be seen in the first few dynamics of Fig. 8.7. The data was de-noised using a Tucker decomposition with a core matrix size of [24, 24, 12] afterwards the slices shown were averaged over the centre five sagittal slices. Each individual slice is shown after averaging all the temporal dynamics in Fig. 8.8, here no de-noising is applied.

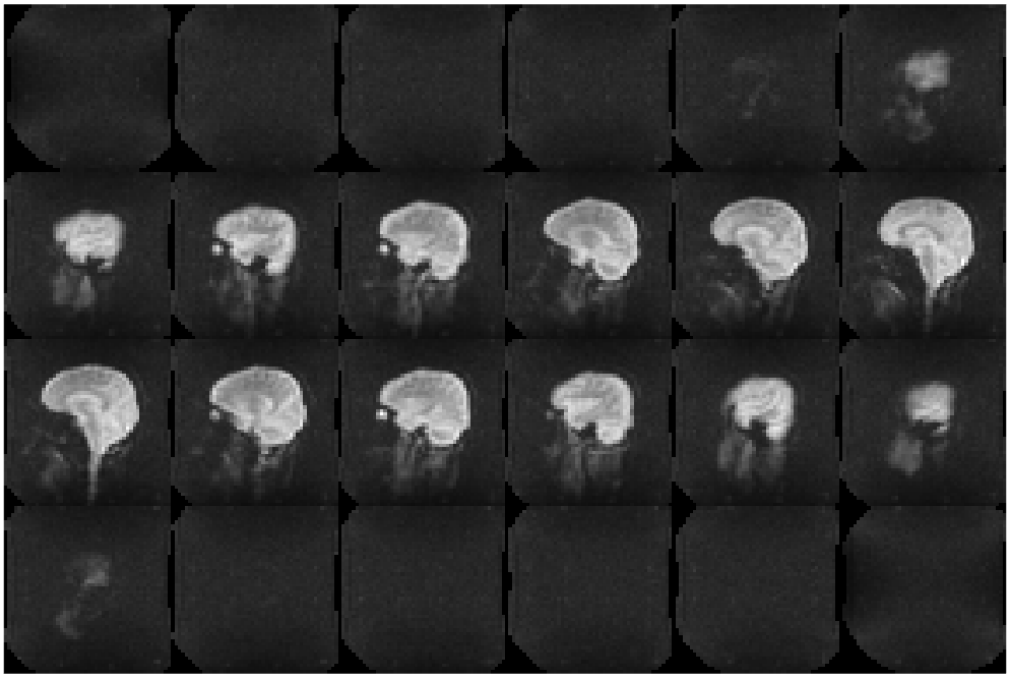

Figure 8.8: *Individual sagittal slices of a healthy human brain in vivo, during the steady-state of D_2O loading, using an EPI acquisition averaged over all 75 dynamics, tuned to the ^2H resonance at 7T.*

Before any work on patients can be undertaken it is important that initial measurements that involve healthy human participants are performed. This ensures that scanning protocols can be optimised for comfort and that the required scan time can be minimised. Such measurements are described

in Chapter 5. Healthy participants ingested glucose-d_2 or glucose-d_7 and concentration maps were subsequently obtained for HDO, Glc, Glx and lactate. The change of signal and concentration with time was characterised and a considerable gain in SNR when using glucose-d_7 versus glucose-d_2 for each metabolite was demonstrated.

Investigation of lipid metabolism can provide useful insights in studying metabolic diseases including diabetes, currently one of the most popular methods for such investigations involves performing invasive biopsies following heavy water ingestion. Chapter 6 reports the first results using ^{2}H-tuned MRSI to investigate increased lipid signals following ingestion of D_2O. Statistically significant increases in the lipid ^{2}H signal from two out of three participants in the abdomen and in 1 out of 3 in the calf were shown. This work is very new and therefore there are many ways in which a study like this can potentially be improved. These include use of water-suppression during scanning and/or post-processing. the first T_1 relaxation time measurements at 3T of HDO in skeletal muscle and of deuterated lipid are also reported in this chapter.

One of the different characteristics of ^{2}H compared to ^{1}H is its quadrupolar moment which can cause spectral broadening/splitting in ordered tissue such as the muscle. The magnitude of quadrupolar splitting in both the forearm and the calf was quantified in different muscle groups (where possible) in Chapter 7 and the relationship between the DQF signal and splitting magnitude was explored. The evolution of DQF with varying creation time (τ) was also investigated. This was made possible due to the increased SNR obtained from participants ingesting D_2O. This is the first time DQF measurements have been attempted using ^{2}H resonance in humans *in vivo*. Accurate time-course analysis was not possible here due to potential flip angle errors and partial voluming, therefore this needs further exploration.

8.2 Future Directions

A common theme throughout the whole thesis is the use of some element of de-noising. Whilst apodisation/line-broadening has already been shown to be useful for increasing SNR it can be problematic in causing overlap of spectral lines and can also negatively impact quantification. To avoid this issue HOSVD is used throughout this thesis for improving SNR and has been shown to be pivotal in improving fitting accuracy. To the author's knowledge there are currently no guidelines in the MR community on the specific level of rank-reduction that should be applied during multi-dimensional de-noising, such as with HOSVD. Other researchers in multi-nuclear MRS who have implemented HOSVD have given limited justification for the rank-reduction that they have used and have generally cited previous work that has often done the same [3, 75, 129]. It would be beneficial to the field if there was more of a focus on HOSVD as a de-noising tool (as opposed to just a data reduction tool) and how far this method can be pushed without sacrificing spatial/temporal/spectral information. The factors that can affect HOSVD performance also need to be further explored. For example, reshaping data matrices so that all spatial dimensions are combined into one dimension would allow the use of SVD rather than HOSVD. This approach would also reduce the dimensionality of time-course data making further decomposition computationally simpler.

It is important to note that whilst this thesis shows how to obtain and analyse *in vivo* ^{2}H data, this work only sets the foundation. As has been pointed out PET is used for clinical studies but only provides limited metabolic information. ^{2}H has the potential to provide more information. However, this first has to be shown in patient studies, as the usefulness of this technique can not truly be proven until direct comparisons are made with current clinical work. Whilst ^{2}H glucose and Glx are important metabolites in the investigation of brain tumours, arguably the most important metabolite is lactate. Currently it is difficult to optimise

a scan for imaging lactate as signal levels do not reach far above the noise level in scans of healthy participants. Brain tumours cause a significant increase in the lactate produced which can be detected using ^{2}H [175]. Other metabolic diseases such as AD and PD also impair metabolism, which has been shown through PET imaging[15, 16], and therefore could potentially benefit from ^{2}H scanning. It is important to optimise/reduce scan time as patients will struggle with extended periods in an MR scanner.

One of the difficulties when trying to track ^{2}H incorporation into lipids after D_2O ingestion is the overlap of signals. When only one peak in a spectrum is visible this means standard imaging approaches can be used to map the distribution of that specific signal. If the increased HDO signal was able to be nulled only the lipid would be visible, therefore if the same sequence was used to acquire image data more rapid acquisitions could potentially be achieved, this would improve participant/patient comfort whilst scanning or averaging can then be used to increase SNR. However, for this to be possible almost near perfect water suppression is needed which can be difficult to achieve. In the DQF spectra the data suffers from low SNR as well and only has one signal present, therefore this sequence could be made into an imaging sequence which could potentially result in smaller voxels which would hopefully reduce effects from partial voluming. Therefore in the future it would be beneficial to the field if more applications of ^{2}H imaging as opposed to spectroscopy, could be developed when ^{2}H spectra are sparse. This has been implemented already using steady-state free precession (SSFP) combined with an adapted version of Iterative Decomposition of water and fat with Echo Asymmetry and Least-squares estimation (IDEAL) [176]. In doing this they have shown an increase in SNR when compared to the conventional CSI acquisition. It's important to note that this is more technically challenging in DMI experiments due to the multiple metabolite peaks being present beyond the expected three-peaks in IDEAL analysis.

8.3 Closing Remarks

In this thesis it has been shown that it is not only possible to obtain *in vivo* ^{2}H spectroscopic information in a reasonable time frame, in humans, as well as ^{2}H MRI and MRSI at 7T. Whilst recently the use DMI in MR research is becoming more widely popular, this thesis has shown the wide potential of uses for ^{2}H and why this nucleus is becoming more popular. I hope this thesis helps push clinical strategies away from either ionising and/or invasive procedures and helps open up a pathway to more ^{2}H MR research and into a place where ^{2}H capabilities comes as standard in all clinical scanners.

Bibliography

[1] P. E. Watson, I. D. Watson, and R. D. Batt. "Total body water volumes for adult males and females estimated from simple anthropometric measurements". In: *The American Journal of Clinical Nutrition* 33.1 (Jan. 1980), pp. 27–39.

[2] James T. Grist et al. "Quantifying normal human brain metabolism using hyperpolarized [1– 13 C]pyruvate and magnetic resonance imaging". In: *NeuroImage* 189 (Apr. 2019), pp. 171–179.

[3] Jeffrey R Brender et al. "Dynamic Imaging of Glucose and Lactate Metabolism by 13 C-MRs without Hyperpolarization". In: *Scientific Reports* 9.1 (2019), p. 3410.

[4] R E Gordon et al. "Localization of metabolites in animals using 31 P topical magnetic resonance". In: *Nature* 287 (Oct. 1980), pp. 538–551.

[5] Ming Lu et al. "Quantitative assessment of brain glucose metabolic rates using in vivo deuterium magnetic resonance spectroscopy". In: *Journal of Cerebral Blood Flow and Metabolism* 37.11 (Nov. 2017), pp. 3518–3530.

[6] Henk M. De Feyter et al. "Deuterium metabolic imaging (DMI) for MRI-based 3D mapping of metabolism in vivo". In: *Science Advances* 4.8 (Aug. 2018).

[7] Otto Warburg. "On the Origin of Cancer Cells". In: *Science* 123.3191 (Feb. 1956), pp. 309–314.

[8] Valentina Di Gialleonardo, David M. Wilson, and Kayvan R. Keshari. "The Potential of Metabolic Imaging". In: *Seminars in Nuclear Medicine* 46.1 (Jan. 2016), pp. 28–39.

[9] Chengxuan Qiu, Miia Kivipelto, and Eva Von Strauss. *Epidemiology of Alzheimer's disease: occurrence, determinants, and strategies toward intervention*. Tech. rep. 2009, pp. 111–128.

[10] *Cancer Statistics for the UK*. URL: https://www.cancerresearchuk.org/health-professional/cancer-statistics-for-the-uk#heading-Zero.

[11] *Brain, other CNS and intracranial tumours statistics — Cancer Research UK*. URL: https://www.cancerresearchuk.org/health-professional/cancer-statistics/statistics-by-cancer-type/brain-other-cns-and-intracranial-tumours#heading-One.

[12] Susana Romero-Garcia et al. "Tumor cell metabolism: An integral view". In: *Cancer Biology & Therapy* 12.11 (Dec. 2011), p. 939.

[13] Rohit Mahar et al. "Deuterated water imaging of the rat brain following metabolism of [2H7] glucose". In: *Magnetic Resonance in Medicine* 85.6 (June 2021), pp. 3049–3059.

[14] Otto Warburg Berlin-Dahlem. "The Metabolism of Carcinoma Cells". In: *The Journal of Cancer Research* 9.1 (1925), pp. 148–163.

[15] S Shokouhi, D Claassen, and WR Riddle. "Imaging Brain Metabolism and Pathology in Alzheimer's Disease with Positron Emission Tomography". In: *Journal of Alzheimer's disease & Parkinsonism* 4.2 (2014).

[16] Sanne K. Meles et al. "Metabolic Imaging in Parkinson Disease". In: *Journal of nuclear medicine : official publication, Society of Nuclear Medicine* 58.1 (Jan. 2017), pp. 23–28.

[17] Ahmad Almuhaideb, Nikolaos Papathanasiou, and Jamshed Bomanji. "18F-FDG PET/CT imaging in oncology". In: *Annals of Saudi Medicine* 31.1 (Jan. 2011), pp. 3–13.

[18] Harold C. Urey, F. G. Brickwedde, and G. M. Murphy. "A Hydrogen Isotope of Mass 2 and its Concentration". In: *Physical Review* 40.1 (Apr. 1932), pp. 1–15.

[19] Rudolf Schoenheimer and David Rittenberg. "Deuterium as an indicator in the study of intermediary metabolism". In: *Science* 82.2120 (1935), pp. 156–157.

[20] Rudolf Schoenheimer and D Rittenberg. "The Application of Isotopes to the Study of Intermediary Metabolism". In: *Science* 87.2254 (1938), pp. 221–226.

[21] N. Bloembergen, E. M. Purcell, and R. V. Pound. "Relaxation effects in nuclear magnetic resonance absorption". In: *Physical Review* 73.7 (Jan. 1948), pp. 679–712.

[22] Henk M. De Feyter and Robin A. de Graaf. "Deuterium metabolic imaging – Back to the future". In: *Journal of Magnetic Resonance* 326 (May 2021).

[23] Roy C Thompson. "Studies of metabolic turnover with tritium as tracer. II. Gross studies on the rat". In: *J Biol Chem* 200.2 (1953), pp. 731–743.

[24] K. W. Turteltaub et al. "Accelerator mass spectrometry in biomedical dosimetry: relationship between low-level exposure and covalent binding of heterocyclic amine carcinogens to DNA." In: *Proceedings of the National Academy of Sciences* 87.14 (July 1990), pp. 5288–5292.

[25] Ian M. Brereton et al. "Preliminary studies on the potential of in vivo deuterium NMR spectroscopy". In: *Biochemical and Biophysical Research Communications* 137.1 (May 1986), pp. 579–584.

[26] Coleen S Ewy, Joseph J H Ackerman, and Robert S Balaban . "Deuterium NMR Cerebral Imaging in Situ". In: *Magnetic Resonance in Medicine* 8.1 (1988), pp. 35–44.

[27] J. J.H. Ackerman et al. "Deuterium nuclear magnetic resonance measurements of blood flow and tissue perfusion employing 2H2O as a freely diffusible tracer." In: *Proceedings of the National Academy of Sciences of the United States of America* 84.12 (1987), p. 4099.

[28] Michael G Irving et al. *In Vivo Determination of Body Iron Stores by Natural-Abundance Deuterium Magnetic Resonance Spectroscopy.* Tech. rep. 1987, pp. 88–92.

[29] John Eng, Bruce A. Berkowitzt, and Robert S. Balaban. "Renal distribution and metabolism of [2H9]choline. A2H NMR and MRI study". In: *NMR in Biomedicine* 3.4 (Aug. 1990), pp. 173–177.

[30] Kevin D. Barrow, Peter L. Rogers, and Glenn M. Smith. "NMR studies of [1-2H]glucose metabolism in Zymomonas mobilis". In: *European Journal of Biochemistry* 157.1 (May 1986), pp. 195–202.

[31] J B Aguayo, M P Gamcsik, and J D Dick. "High resolution deuterium NMR studies of bacterial metabolism." In: *The Journal of biological chemistry* 263.36 (Dec. 1988), pp. 19552–7.

[32] Michael N. Goodman et al. "Use of deuterium labelled glucose in evaluating the pathway of hepatic glycogen synthesis". In: *Biochemical and Biophysical Research Communications* 159.2 (Mar. 1989), pp. 522–527.

[33] H. Harada et al. "Identification and quantitation by 1H-NMR of metabolites in animal organs and tissues. An application of NMR spectroscopy in forensic science". In: *Forensic science international* 24.1 (1984), pp. 1–7.

[34] S. M. Cohen et al. “Use of 13C NMR for investigation of ethanol metabolism in perfused liver”. In: *Advances in experimental medicine and biology* 132 (1980), pp. 419–431.

[35] D. Sappey-Marinier et al. “Effect of photic stimulation on human visual cortex lactate and phosphates using 1H and 31P magnetic resonance spectroscopy”. In: *Journal of Cerebral Blood Flow and Metabolism* 12.4 (1992), pp. 584–592.

[36] Loreen Ruhm et al. “Dynamic observation of 2H labelled compounds in the human brain with 1H versus 2H magnetic resonance spectroscopy at 9.4T”. In: *bioRxiv* (2022).

[37] Eulalia Serés Roig et al. “Deuterium metabolic imaging of the human brain in vivo at 7T”. In: *Magnetic Resonance in Medicine* (Sept. 2022).

[38] Robin A. de Graaf et al. “On the magnetic field dependence of deuterium metabolic imaging”. In: *NMR in Biomedicine* 33.3 (Mar. 2020).

[39] Milou Straathof et al. “Deuterium Metabolic Imaging of the Healthy and Diseased Brain”. In: *Neuroscience* 474 (Oct. 2021), pp. 94–99.

[40] Laurie J. Rich et al. “1H magnetic resonance spectroscopy of 2H-to-1H exchange quantifies the dynamics of cellular metabolism in vivo”. In: *Nature Biomedical Engineering 2020 4:3* 4.3 (Jan. 2020), pp. 335–342.

[41] Guannan Zhang et al. “[6,6′-2H2] fructose as a deuterium metabolic imaging probe in liver cancer”. In: *NMR in Biomedicine* 36.10 (Oct. 2023), e4989.

[42] Chao Zou et al. “A new deuterium-labeled compound [2,3,4,6,6’-2H5]-D-glucose for deuterium magnetic resonance metabolic imaging”. In: *NMR in Biomedicine* 36.7 (July 2023), e4890.

[43] Walther Gerlach and Otto Stern. "Der experimentelle Nachweis der Richtungsquantelung im Magnetfeld". In: *Zeitschrift für Physik* 9.1 (Dec. 1922), pp. 349–352.

[44] J. Larmor. "LXIII. On the theory of the magnetic influence on spectra; and on the radiation from moving ions". In: *The London, Edinburgh, and Dublin Philosophical Magazine and Journal of Science* 44.271 (Dec. 1897), pp. 503–512.

[45] Pieter Zeeman. "Verslagen van de Gewone Vergaderingen der Wisen Natuurkundige Afdeeling". In: *Koninklijk Akademie van Wetenschappen te Amsterdam* 5 (1896), pp. 181–248.

[46] Ludwig Boltzmann. "Weitere Studien über das Wärmegleichgewicht unter Gasmolekülen". In: *Kinetische Theorie II* (1872), pp. 115–225.

[47] Mark E. Haacke et al. *Magnetic Resonance Imaging: Physical Principles and Sequence Design*. 1st ed. Wiley-Blackwell, 2014, 2014, pp. 1–15.

[48] F. Bloch. "Nuclear Induction". In: *Physical Review* 70.7-8 (Oct. 1946), p. 460.

[49] Jean-Baptiste-Joseph Fourier. *Théorie analytique de la chaleur*. F. Didot père et fils, 1822.

[50] Richard R Ernst, Geoffrey Bodenhausen, and Alexander Wokaun. *Principles of nuclear magnetic resonance in one and two dimensions*. Oxford: Clarendon Press, 1987, p. 152.

[51] Robin A. de Graaf. *In Vivo NMR Spectroscopy*. Third. Wiley, Feb. 2019.

[52] Darach Watson et al. "Identification of strontium in the merger of two neutron stars". In: *Nature 2019 574:7779* 574.7779 (Oct. 2019), pp. 497–500.

[53] C. Patrignani et al. "Review of Particle Physics". In: *Chinese Physics C* 40.10 (Oct. 2016), p. 100001.

[54] Antony Joseph. “Geological timeline of significant events on Earth”. In: *Water Worlds in the Solar System*. Elsevier, 2023. Chap. 2, pp. 55–114.

[55] Franck Hersant, Daniel Gautier, and Jean-Marc Hure. “A Two-dimensional Model for the Primordial Nebula Constrained by D/H Measurements in the Solar System: Implications for the Formation of Giant Planets”. In: *The Astrophysical Journal* 554.1 (June 2001), pp. 391–407.

[56] Gabriel J. Bowen et al. “Isotopes in the Water Cycle: Regional- to Global-Scale Patterns and Applications”. In: *Annual Review of Earth and Planetary Sciences* 47 (May 2019), pp. 453–479.

[57] E. L. Hahn. “Spin Echoes”. In: *Physical Review* 80.4 (Nov. 1950), p. 580.

[58] P. C. Lauterbur. “Image Formation by Induced Local Interactions: Examples Employing Nuclear Magnetic Resonance”. In: *Nature 1973 242:5394* 242.5394 (1973), pp. 190–191.

[59] P Mansfield. “Multi-planar image formation using NMR spin echoes”. In: *J. Phys. C : Solid State Phys* 10.3 (1977).

[60] Travis B. Smith and Krishna S. Nayak. “Reduced field of view MRI with rapid, B1-robust outer volume suppression”. In: *Magnetic resonance in medicine* 67.5 (2012), pp. 1316–1323.

[61] Michael K. Stehling, Robert Turner, and Peter Mansfield. “Echo-planar imaging: magnetic resonance imaging in a fraction of a second”. In: *Science (New York, N.Y.)* 254.5028 (1991), pp. 43–50.

[62] Jamie Near et al. “Preprocessing, analysis and quantification in single-voxel magnetic resonance spectroscopy: Experts’ consensus recommendations”. In: *NMR in biomedicine* 34.5 (May 2021), e4257.

[63] Jeffry R. Alger. “Quantitative Proton Magnetic Resonance Spectroscopy and Spectroscopic Imaging of the Brain: A Didactic Review”. In: *Topics in magnetic resonance imaging : TMRI* 21.2 (Apr. 2010), p. 115.

[64] Hendrik Lorentz. “The Theory of Electrons and Its Applications to the Phenomena of Light and Radiant Heat”. In: *Annalen der Physik* 4.1 (1895), p. 177.

[65] G. H. Golub and V. Pereyra. “The Differentiation of Pseudo-Inverses and Nonlinear Least Squares Problems Whose Variables Separate”. In: *SIAM Journal on Numerical Analysis* 10.2 (Apr. 1973), pp. 413–432.

[66] Leentie Vanhamme et al. “MR spectroscopy quantitation: A review of time-domain methods”. In: *NMR in Biomedicine* 14.4 (2001), pp. 233–246.

[67] Jean Baptiste Poullet, Diana M. Sima, and Sabine Van Huffel. “MRS signal quantitation: A review of time- and frequency-domain methods”. In: *Journal of Magnetic Resonance* 195.2 (Dec. 2008), pp. 134–144.

[68] Gavin Hamilton et al. “Prior knowledge for time domain quantification of in vivo brain or liver 31P MR spectra”. In: *NMR in Biomedicine* 16.3 (May 2003), pp. 168–176.

[69] J. W.C. van der Veen et al. “Accurate quantification of in vivo 31P NMR signals using the variable projection method and prior knowledge”. In: *Magnetic Resonance in Medicine* 6.1 (1988), pp. 92–98.

[70] Marion Stubbs et al. “31P-Magnetic resonance spectroscopy studies of nucleated and non-nucleated erythrocytes; time domain data analysis (VARPRO) incorporating prior knowledge can give information on the binding of ADP”. In: *Biochimica et Biophysica Acta (BBA) - General Subjects* 1291.2 (Oct. 1996), pp. 143–148.

[71] Leentje Vanhamme, Aad Van Den Boogaart, and Sabine Van Huffel. "Improved Method for Accurate and Efficient Quantification of MRS Data with Use of Prior Knowledge". In: *Journal of Magnetic Resonance* 129.1 (Nov. 1997), pp. 35–43.

[72] D. Stefan et al. "Quantitation of magnetic resonance spectroscopy signals: the jMRUI software package". In: *Measurement Science and Technology* 20.10 (Sept. 2009), p. 104035.

[73] Lucian A.B. Purvis et al. "OXSA: An open-source magnetic resonance spectroscopy analysis toolbox in MATLAB". In: *PLOS ONE* 12.9 (Sept. 2017), e0185356.

[74] Rui V. Simões et al. "Glucose fluxes in glycolytic and oxidative pathways detected in vivo by deuterium magnetic resonance spectroscopy reflect proliferation in mouse glioblastoma". In: *NeuroImage: Clinical* 33 (Jan. 2022).

[75] Felix Kreis et al. "Measuring tumor glycolytic flux in vivo by using fast deuterium MRI". In: *Radiology* 294.2 (2020), pp. 289–296.

[76] Joshua D Kaggie et al. "Deuterium metabolic imaging and hyperpolarized 13 C-MRI of the normal human brain at clinical field strength reveals differential cerebral metabolism". In: *NeuroImage* 257 (2022), p. 119284.

[77] Stephen W. Provencher. "Estimation of metabolite concentrations from localized in vivo proton NMR spectra". In: *Magnetic Resonance in Medicine* 30.6 (1993), pp. 672–679.

[78] Abigail T.J. Cember et al. "Integrating 1H MRS and deuterium labeled glucose for mapping the dynamics of neural metabolism in humans". In: *NeuroImage* 251 (May 2022).

[79] Fabian Niess et al. "Reproducibility of 3D MRSI for imaging human brain glucose metabolism using direct (2H) and indirect (1H)

detection of deuterium labeled compounds at 7T and clinical 3T". In: *medRxiv* (2023).

[80] M. Joliot, B. M. Mazoyer, and R. H. Huesman. "In vivo NMR spectral parameter estimation: a comparison between time and frequency domain methods". In: *Magnetic resonance in medicine* 18.2 (1991), pp. 358–370.

[81] Mohammed Goryawala, Molly Sullivan, and Andrew A. Maudsley. "Effects of apodization smoothing and denoising on spectral fitting". In: *Magnetic resonance imaging* 70 (July 2020), pp. 108–114.

[82] R Bartha, D J Drost, and P C Williamson. "Factors affecting the quantification of short echo in-vivo 1 H MR spectra: prior knowledge, peak elimination, and filtering". In: *NMR in Biomedicine* 12.4 (1999), pp. 205–216.

[83] Abas Abdoli, Radka Stoyanova, and Andrew A. Maudsley. "Denoising of MR Spectroscopic Imaging Data Using Statistical Selection of Principal Components". In: *Magma (New York, N.Y.)* 29.6 (Dec. 2016), p. 811.

[84] Hien M. Nguyen et al. "Denoising MR Spectroscopic Imaging Data With Low-Rank Approximations". In: *IEEE transactions on biomedical engineering* 60.1 (2013), p. 78.

[85] William T. Clarke and Mark Chiew. "Uncertainty in denoising of MRSI using low-rank methods". In: *Magnetic Resonance in Medicine* 87.2 (Feb. 2022), pp. 574–588.

[86] Gilbert Strang. "The Singular Value Decomposition". In: *Introduction to LINEAR ALGEBRA*. 5th ed. Wellesley - Cambridge Press, 2016. Chap. 7, pp. 364–392.

[87] W. W.F. Pijnappel et al. "SVD-based quantification of magnetic resonance signals". In: *Journal of Magnetic Resonance (1969)* 97.1 (Mar. 1992), pp. 122–134.

[88] E. Cabanes et al. “Optimization of residual water signal removal by HLSVD on simulated short echo time proton MR spectra of the human brain”. In: *Journal of magnetic resonance (San Diego, Calif. : 1997)* 150.2 (2001), pp. 116–125.

[89] Ledyard R. Tucker. “Some mathematical notes on three-mode factor analysis”. In: *Psychometrika* 31.3 (Sept. 1966), pp. 279–311.

[90] Julian C Assmann et al. “In vivo deuterated water labeling allows tumor visualization via deuterium magnetic resonance spectroscopic imaging of cholesterol”. In: *bioRxiv* (Jan. 2020), p. 809327.

[91] Brett W. Bader and Tamara G. Kolda. “Efficient MATLAB Computations with Sparse and Factored Tensors”. In: *SIAM Journal on Scientific Computing* 30.1 (Dec. 2007), pp. 205–231.

[92] Ching-Nien Chen and D.I. Hoult. “Chapter 4: Signal and Noise”. In: *Biomedical Magnetic Resonance Technology*. 1st. CRC Press, 1989, pp. 117–175.

[93] Bernhard Gruber et al. “RF coils: A practical guide for nonphysicists”. 3. Sept. 2018.

[94] D. M. Ginsberg and Melvin J. Melchner. “Optimum geometry of saddle shaped coils for generating a uniform magnetic field”. In: *Review of Scientific Instruments* 41.1 (1970), pp. 122–123.

[95] Carlos Salmon et al. “Optimization of Saddle Coils for Magnetic Resonance Imaging”. In: *Brazilian Journal of Physics* 36.1A (2006).

[96] INTERNATIONAL ATOMIC ENERGY AGENCY. “Introduction to Body Composition Assessment Using the Deuterium Dilution Technique with Analysis of Saliva Samples by Fourier Transform Infrared Spectrometry”. In: *IAEA Human Health Series No. 12* IAEA.Vienna (2011).

[97] A Strawford et al. “Adipose tissue triglyceride turnover, de novo lipogenesis, and cell proliferation in humans measured with 2 H 2 O”. In: *Am J Physiol Endocrinol Metab* 286 (2004), pp. 577–588.

[98] Daniel J. Wilkinson et al. “Stable isotope tracers and exercise physiology: past, present and future”. In: *Journal of Physiology* 595.9 (May 2017), pp. 2873–2882.

[99] S M Turner et al. “Measurement of TG synthesis and turnover in vivo by 2H2O incorporation into the glycerol moiety and application of MIDA”. In: *J Physiol Endocrinol Metab* 285.4 (2003), pp. 790–803.

[100] Eric J. Lawitz et al. “Elevated de novo lipogenesis, slow liver triglyceride turnover, and clinical correlations in nonalcoholic steatohepatitis patients”. In: *Journal of Lipid Research* 63.9 (Sept. 2022).

[101] F. Diraison, C. Pachiaudi, and M. Beylot. “Measuring lipogenesis and cholesterol synthesis in humans with deuterated water: Use of simple gas chromatographic/mass spectrometric techniques”. In: *Journal of Mass Spectrometry* 32.1 (1997), pp. 81–86.

[102] I. M. Brereton et al. “The use of in vivo 2H NMR spectroscopy to investigate the effects of obesity and diabetes mellitus upon lipid metabolism in mice”. In: *NMR in Biomedicine* 2.2 (1989), pp. 55–60.

[103] P. J. Wright et al. “Water proton T1 measurements in brain tissue at 7, 3, and 1.5 T using IR-EPI, IR-TSE, and MPRAGE: results and optimization”. In: *Magma (New York, N.Y.)* 21.1-2 (2008), pp. 121–130.

[104] Ayhan Gursan et al. “Residual quadrupolar couplings observed in 7 Tesla deuterium MR spectra of skeletal muscle”. In: *Magnetic Resonance in Medicine* 87.3 (Mar. 2022), pp. 1165–1173.

[105] Daniel Cocking et al. “Deuterium brain imaging at 7T during D2O dosing”. In: *Magnetic Resonance in Medicine* 89.4 (2023), pp. 1514–1521.

[106] Matthew M Robinson et al. “Long-term synthesis rates of skeletal muscle DNA and protein are higher during aerobic training in older humans than in sedentary young subjects but are not altered by protein supplementation; Long-term synthesis rates of skeletal muscle DNA and protein are higher during aerobic training in older humans than in sedentary young subjects but are not altered by protein supplementation”. In: *FASEB J* 25.9 (2011), pp. 3240–3249.

[107] Jan A Burger et al. “Leukemia cell proliferation and death in chronic lymphocytic leukemia patients on therapy with the BTK inhibitor ibrutinib”. In: *JCI Insight* 2.2 (2017), p. 89904.

[108] Rohit Loomba et al. “Discovery of Half-life of Circulating Hepatitis B Surface Antigen in Patients With Chronic Hepatitis B Infection Using Heavy Water Labeling”. In: *Clinical Infectious Diseases* 69.3 (2019), pp. 542–547.

[109] Yongyue Zhang, Michael Brady, and Stephen Smith. “Segmentation of brain MR images through a hidden Markov random field model and the expectation-maximization algorithm”. In: *IEEE Transactions on Medical Imaging* 20.1 (Jan. 2001), pp. 45–57.

[110] Stephen M. Smith. “Fast robust automated brain extraction”. In: *Human Brain Mapping* 17.3 (Nov. 2002), pp. 143–155.

[111] Mark Jenkinson and Stephen Smith. “A global optimisation method for robust affine registration of brain images”. In: *Medical Image Analysis* 5.2 (June 2001), pp. 143–156.

[112] Mark Jenkinson et al. “Improved Optimization for the Robust and Accurate Linear Registration and Motion Correction of Brain Images”. In: *NeuroImage* 17.2 (Oct. 2002), pp. 825–841.

[113] Alexis Roche et al. “The Correlation Ratio as a New Similarity Measure for Multimodal Image Registration”. In: *LNCS* 1496 (), pp. 1115–1124.

[114] Loreen Ruhm et al. “Deuterium metabolic imaging in the human brain at 9.4 Tesla with high spatial and temporal resolution”. In: *NeuroImage* 244 (Dec. 2021).

[115] Andrew M. Peters et al. “T2* measurements in human brain at 1.5, 3 and 7T”. In: *Magnetic Resonance Imaging* 25.6 (July 2007), pp. 748–753.

[116] Robin A Damion et al. “Natural abundance deuterium MRS of the human calf and T measurements with a surface coil at 3 T”. In: *In Proceedings of the 29th Annual Meeting of ISMRM*. Virtual, 2021, p. 3836.

[117] Simon Davies, Patrik Spanel, and David Smith. *Rapid measurement of deuterium content of breath following oral ingestion to determine body water*. Tech. rep. 2001, pp. 651–659.

[118] François Péronnet et al. “Pharmacokinetic analysis of absorption, distribution and disappearance of ingested water labeled with D2O in humans”. In: *European Journal of Applied Physiology* 112.6 (June 2012), pp. 2213–2222.

[119] K. E. Money and W. S. Myles. “Heavy water nystagmus and effects of alcohol”. In: *Nature* 247.5440 (1974), pp. 404–405.

[120] Anu E. Meerwaldt et al. “In vivo imaging of cerebral glucose metabolism informs on subacute to chronic post-stroke tissue status – A pilot study combining PET and deuterium metabolic imaging”. In: *Journal of Cerebral Blood Flow and Metabolism* 43.5 (May 2023), pp. 778–790.

[121] M. J. Kushner et al. “Cerebral metabolism and patterned visual Stimulation”. In: *Neurology* 38.1 (Jan. 1988), pp. 89–89.

[122] Alexandria Béland-Millar and Claude Messier. "Fluctuations of extracellular glucose and lactate in the mouse primary visual cortex during visual stimulation". In: (2018).

[123] James Prichard et al. "Lactate rise detected by 1H NMR in human visual cortex during physiologic stimulation." In: *Proceedings of the National Academy of Sciences* 88.13 (July 1991), pp. 5829–5831.

[124] Carolina C. Fernandes et al. "Measurement of brain lactate during visual stimulation using a long TE semi-LASER sequence at 7 T". In: *Nmr in Biomedicine* 33.4 (Apr. 2020).

[125] Yan Lin et al. "Investigating the metabolic changes due to visual stimulation using functional proton magnetic resonance spectroscopy at 7 T". In: *Journal of Cerebral Blood Flow and Metabolism* 32.8 (Aug. 2012), pp. 1484–1495.

[126] Navjeet Chhina et al. *Measurement of Human Tricarboxylic Acid Cycle Rates During Visual Activation by 13 C Magnetic Resonance Spectroscopy*. Tech. rep. 2001, pp. 737–746.

[127] Peter C.M. van Zijl and Kevin M. Brindle. "Spectroscopic measurements of metabolic fluxes". In: *Nature biomedical engineering* 4.3 (Mar. 2020), pp. 254–256.

[128] Petr Bednarik et al. "Deuterium labeling enables non-invasive 3D proton MR imaging of glucose and neurotransmitter metabolism in the human brain". In: *Research Square* (2021).

[129] Cornelius von Morze et al. "Comparison of hyperpolarized 13C and non-hyperpolarized deuterium MRI approaches for imaging cerebral glucose metabolism at 4.7 T". In: *Magnetic Resonance in Medicine* 85.4 (Apr. 2021), pp. 1795–1804.

[130] Tao Wang et al. "Noninvasive assessment of myocardial energy metabolism and dynamics using in vivo deuterium MRS imaging". In: *Magnetic Resonance in Medicine* 86.6 (Dec. 2021), pp. 2899–2909.

[131] Henk M. De Feyter et al. "Deuterium Metabolic Imaging (DMI) of glucose metabolism in mouse brain". In: *In Proceedings of the 28th Annual Meeting of ISMRM*. 2020, p. 4713.

[132] Rohit Mahar, Patrick L. Donabedian, and Matthew E. Merritt. "HDO production from [2H7] glucose Quantitatively Identifies Warburg Metabolism". In: *Scientific Reports* 10.1 (Dec. 2020).

[133] Rolf Pohmann and Markus Von Kienlin. "Accurate phosphorus metabolite images of the human heart by 3D acquisition-weighted CSI". In: *Magnetic resonance in medicine* 45.5 (2001), pp. 817–826.

[134] Stephen M. Smith et al. "Advances in functional and structural MR image analysis and implementation as FSL". In: *NeuroImage* 23 Suppl 1.SUPPL. 1 (2004).

[135] Andersson J, Smith S, and Jenkinson M. "FNIRT-FMRIB's non-linear image registration tool". In: *Organization for Human Brain Mapping (OHBM)*. 2008.

[136] Varanavasi Govindaraju, Karl Young, and Andrew A Maudsley. "Proton NMR chemical shifts and coupling constants for brain metabolites". In: *NMR in Biomedicine* 13.3 (2000), pp. 129–153.

[137] Jeffry M. Leitch and Anthony Carruthers. "α- and β-Monosaccharide transport in human erythrocytes". In: *American Journal of Physiology - Cell Physiology* 296.1 (Jan. 2009), p. C151.

[138] R. Hagemann, G. Nief, and E. Roth. "Absolute isotopic scale for deuterium analysis of natural waters. Absolute D/H ratio for SMOW". In: *Tellus* 22.6 (Jan. 1970), p. 712.

[139] Ana Maria Oros-Peusquens et al. "A Single-Scan, Rapid Whole-Brain Protocol for Quantitative Water Content Mapping With Neurobiological Implications". In: *Frontiers in Neurology* 10 (Dec. 2019).

[140] Robin A. De Graaf et al. “Characterization of kinetic isotope effects and label loss in deuterium-based isotopic labeling studies”. In: *ACS chemical neuroscience* 12.1 (Jan. 2021), p. 234.

[141] Alexander M. Funk et al. “The rate of lactate production from glucose in hearts is not altered by per-deuteration of glucose”. In: *Journal of Magnetic Resonance* 284 (Nov. 2017), pp. 86–93.

[142] F A Howe et al. “Metabolic Profiles of Human Brain Tumors Using Quantitative In Vivo 1 H Magnetic Resonance Spectroscopy”. In: *Magn Reson Med* 49 (2003), pp. 223–232.

[143] Ursula White and Eric Ravussin. “Dynamics of adipose tissue turnover in human metabolic health and disease”. 1. Jan. 2019.

[144] Mercedes R. Carnethon et al. “Serum Insulin, Obesity, and the Incidence of Type 2 Diabetes in Black and White Adults: The Atherosclerosis Risk in Communities Study: 1987–1998”. In: *Diabetes care* 25.8 (Aug. 2002), p. 1358.

[145] L. B. Salans, S. W. Cushman, and R. E. Weismann. “Studies of human adipose tissue. Adipose cell size and number in nonobese and obese patients”. In: *The Journal of clinical investigation* 52.4 (1973), pp. 929–941.

[146] Ursula A. White et al. “Differences in In Vivo Cellular Kinetics in Abdominal and Femoral Subcutaneous Adipose Tissue in Women”. In: *Diabetes* 65.6 (June 2016), p. 1642.

[147] Tamara Tchkonia et al. “Fat depot origin affects adipogenesis in primary cultured and cloned human preadipocytes”. In: *American journal of physiology. Regulatory, integrative and comparative physiology* 282.5 (2002).

[148] Getachew Debas Belew and John G. Jones. “De novo lipogenesis in non-alcoholic fatty liver disease: Quantification with stable isotope

tracers". In: *European Journal of Clinical Investigation* 52.3 (Mar. 2022), e13733.

[149] Candice A. Allister et al. "In vivo 2H2O administration reveals impaired triglyceride storage in adipose tissue of insulin-resistant humans". In: *Journal of Lipid Research* 56.2 (Feb. 2015), p. 435.

[150] Ursula A. White et al. "Racial differences in in vivo adipose lipid kinetics in humans". In: *Journal of Lipid Research* 59.9 (2018), p. 1738.

[151] Peter Arner et al. "Dynamics of human adipose lipid turnover in health and metabolic disease". In: *Nature* 478.7367 (Oct. 2011), pp. 110–113.

[152] Kirsty L. Spalding et al. "Impact of fat mass and distribution on lipid turnover in human adipose tissue". In: *Nature communications* 8 (May 2017).

[153] Zhaoyue Zhang et al. "Chemical Basis for Deuterium Labeling of Fat and NADPH". In: *Journal of the American Chemical Society* 139.41 (Oct. 2017), pp. 14368–14371.

[154] Jimin Ren et al. "Composition of adipose tissue and marrow fat in humans by 1H NMR at 7 Tesla". In: *Journal of Lipid Research* 49.9 (Sept. 2008), p. 2055.

[155] A. V. Kosenkov et al. "The Reversible Effect of Deuteration on Tissue Fluid and Biopolymers in Normal and Tumor Tissues of Mice". In: *Biophysics (Russian Federation)* 63.5 (Sept. 2018), pp. 820–824.

[156] Ronald E Block and Barbara C Parekh. *COMMUNICATIONS Deuterium Nuclear Spin Relaxation in Biological Tissues*. Tech. rep. 1987, pp. 286–289.

[157] Annalise R. Pfaff, Cailyn E. McKee, and Klaus Woelk. "Predicting the effect of relaxation during frequency-selective adiabatic pulses".

In: *Journal of magnetic resonance (San Diego, Calif. : 1997)* 284 (Nov. 2017), pp. 99–103.

[158] Jacobus F.A. Jansen et al. "1H MR spectroscopy of the brain: absolute quantification of metabolites". In: *Radiology* 240.2 (Aug. 2006), pp. 318–332.

[159] Ursula A. White et al. "Association of In Vivo Adipose Tissue Cellular Kinetics With Markers of Metabolic Health in Humans". In: *The Journal of Clinical Endocrinology and Metabolism* 102.7 (July 2017), p. 2171.

[160] N. J. Stone. "Nuclear Magnetic Dipole and Electric Quadrupole Moments: Their Measurement and Tabulation as Accessible Data". In: *Journal of Physical and Chemical Reference Data* 44.3 (June 2015), p. 031215.

[161] Joachim Seelig. "Deuterium magnetic resonance: Theory and application to lipid membranes". In: *Quarterly Reviews of Biophysics* 10.3 (1977), pp. 353–418.

[162] Uzi Eliav and Gil Navon. "Multiple quantum MRS". In: *eMagRes.* Vol. 5. 1. Blackwell Publishing Ltd, 2016, pp. 1061–1076.

[163] Kristopher J. Ooms et al. "Double and zero quantum filtered 2H NMR analysis of D2O in intervertebral disc tissue". In: *Journal of Magnetic Resonance* 258 (July 2015), pp. 6–11.

[164] Robin Damion et al. "Double Quantum Filtered 2H Measurements in Human Subjects Following Deuterium Oxide Loading". In: *In Proceedings of the 30th Annual Meeting of ISMRM.* London, UK, 2022, p. 1351.

[165] Yehuda Sharf et al. "Detection of Anisotropy in Cartilage Using 2H Double-Quantum-Filtered NMR-Spectroscopy". In: *Journal of Magnetic Resonance, Series B* 107.1 (1995), pp. 60–67.

[166] William Perea et al. “2H double quantum filtered (DQF) NMR spectroscopy of the nucleus pulposus tissues of the intervertebral disc”. In: *Magnetic resonance in medicine* 57.6 (2007), pp. 990–999.

[167] Yaniv Assaf, Gil Navon, and Yoram Cohen. “In vivo observation of anisotropic motion of brain water using 2H double quantum filtered NMR spectroscopy”. In: *Magnetic Resonance in Medicine* 37.2 (Feb. 1997), pp. 197–203.

[168] Cheng Sun and Gregory S. Boutis. “Investigation of the dynamical properties of water in elastin by deuterium Double Quantum Filtered NMR”. In: *Journal of Magnetic Resonance* 205.1 (July 2010), pp. 86–92.

[169] Adrian Tsang, Robert W. Stobbe, and Christian Beaulieu. “Triple-quantum-filtered sodium imaging of the human brain at 4.7 T”. In: *Magnetic Resonance in Medicine* 67.6 (2012), pp. 1633–1643.

[170] Stuart J Elliott and Philip W Kuchel. “What Are the Relative Intensities of the Components of NMR Spectral Multiplets from Quadrupolar Nuclei in Uniformly Anisotropic Media?” In: *Concepts in Magnetic Resonance Part A, Bridging Education and Research* 2021 (2021).

[171] Roland Kreis and Chris Boesch. “Liquid-Crystal-like Structures of Human Muscle Demonstrated by in Vivo Observation of Direct Dipolar Coupling in Localized Proton Magnetic Resonance Spectroscopy”. In: *Journal of Magnetic Resonance, Series B* 104.2 (June 1994), pp. 189–192.

[172] Geoffrey Bodenhausen, Herbert Kogler, and R. R. Ernst. “Selection of coherence-transfer pathways in NMR pulse experiments”. In: *Journal of Magnetic Resonance (1969)* 58.3 (July 1984), pp. 370–388.

[173] Gil Navon et al. “Multiquantum filters and order in tissues”. In: *NMR in Biomedicine* 14.2 (2001), pp. 112–132.

[174] Nikolaj Bøgh et al. “Comparison of Deuterium Metabolic Imaging and FDG-PET in Alzheimer’s Disease”. In: *In Proceedings of the 32nd Annual Meeting of ISMRM*. Singapore, 2024.

[175] D. P. Soares and M. Law. “Magnetic resonance spectroscopy of the brain: review of metabolites and clinical applications”. In: *Clinical Radiology* 64.1 (Jan. 2009), pp. 12–21.

[176] Dana C. Peters et al. “Improving deuterium metabolic imaging (DMI) signal-to-noise ratio by spectroscopic multi-echo bSSFP: A pancreatic cancer investigation”. In: *Magnetic Resonance in Medicine* 86.5 (Nov. 2021), pp. 2604–2617.